Investigation of the flow with air-core in hydrocyclones

Yanchen Hu

A thesis submitted in partial fulfilment of the requirements for the degree of

Doctor of Philosophy

The University of Sheffield

Department of Mechanical Engineering

Supervisor: A.F. Nowakowski

April 29th, 2020

Dedication

To my lovely and kind family, even though they live in China far away from me, they still gave me every possible care. Without their Strongly support, I would not be able to live and study so smoothly in another country.

Mother and Father

Acknowledgements

To my parents, who made all things possible

Abstract

The present work focuses on the investigation of the flow with an air-core in hydrocyclones. These are used in many industrial sectors owing to their wide range of applications, including filtration, dewatering, concentrating or separation. Despite their popularity, there is still limited theoretical knowledge that could provide an explanation of the flow physics inside the hydrocyclone. Therefore, research on hydrocyclones is challenging, especially in areas directly related to the creation of the air-core.

The air-core phenomenon appears when the primary fluid is liquid and the outlet is open to the atmosphere. The formation of the air core is hard to capture but may influence the hydrocyclone performance. Therefore, it is important to be able to observe its formation as this should help in designing hydrocyclones. The numerical simulations of hydrocyclone fluid flow offer a major advantage in the device's design process. Computational fluid dynamics simulations enable a wider range of design studies to be performed at a relatively smaller cost when compared to physical experimentation. The current study investigates and consequently implements a new approach for resolution of the flow with air-core in hydrocyclones.

In the present study, the Reynolds Stress Model (RSM) is employed to deal with an anisotropic turbulent flow in hydrocyclones. To tackle the interface, resulting from the air core formation, the computational fluid dynamics approach is required to harness the Eulerian multi-phase model. To this end, a new numerical technique, based on the Volume of Fluid (VOF) interface capturing method, has been employed.

The advantage of this approach is its practicality and simplicity. Unlike previous attempts to apply VOF in hydrocyclones, the present one uses the modified advection term in the volume fraction equation. A customised solver called Multidimensional Universal Limiter for Explicit Solution (MULES) is an integral part of this novel VOF method. It is derived from the Flux Corrected Transport (FCT) technique that guarantees accuracy and boundedness. Additionally, the High-Resolution Scheme (HRS) is applied to optimise the developed VOF method further. This technique helps to eliminate unexpected oscillations and dissipation near strong gradients. The method is used for the first time in the present study to simulate the flow in hydrocyclones.

Two straightforward benchmark simulation studies have been undertaken to verify the feasibility of the numerical tools. First, the RSM turbulence model was successfully used to simulate the single-phase flow in cyclones. The second case study was the simulation of the dam breaking flow. The second study proved that the developed VOF method could successfully simulate the transient stages of the multi-phase flow evolution, showing a clear free-surface between the liquid phase and gas phase. Both benchmark simulations have been validated by comparing the results with available experimental data.

Finally, to simulate the flow with air-core in a hydrocyclone, a combination of the RSM model and the developed VOF method has been implemented. The RSM model is applied to deal with the turbulent flow with large swirls. The new VOF-based interface capturing method is used for the modelling of the air-core. The results of the simulations demonstrated good agreement when compared with experimental data and previous studies.

After the verification and validation procedures for the new methodology, additional simulations were carried out. These were performed for the problems where experimental data were not available, or when it was difficult to acquire such data using experimental techniques. The other objectives of the present study included: Investigating the feasibility of using other common turbulence models for hydrocyclone simulation; Investigating the sensitivity of changing the dimensions of different sections of the hydrocyclone on flow patterns; The application of different interface smearing factors on the simulation result. Finally, the correctness of simplifying assumptions, that ignore the air-core presence, on the simulation of the flow in hydrocyclones was investigated.

The proposed numerical simulation methodology is suggested as a convenient academic tool that could be utilised as the platform for fundamental studies of the flow with air-core in hydrocyclones. It also proved to be a powerful tool that could be exploited in practical industrial studies.

Content

List of Figures

List of Tables

Nomenclature

Roman symbol

t	Time	s
L	Length	m
H	Height	m
P, p	Pressure	Pa
v_θ	Tangential velocity	m/s
r	Radius	m
u	x-direction component of the velocity	m/s
v	y-direction component of the velocity	m/s
w	z-direction component of the velocity	m/s
a	Acceleration	m/s^2
V	Velocity	m/s
F	Force	N
f	Force per volume	N/m^3
k	Turbulent kinetic energy	m^2/s^2
g	Gravitational acceleration	m/s^2
d	Particle diameter	m
f	Weighting factor for linear interpolation	
I	Turbulence intensity	
l	Turbulence length scale	m

R	Reynolds stress	m^2/s^2
Z	Size of the grid near to the wall	m
Eu	Euler number	
n	Normal vector	

Greek symbol

ω	Angular velocity	**rad/s**
ρ	Density	kg/m^3
τ	Shear stress	N/m^2
μ	Viscosity	$\text{kg}/(\text{m} \cdot \text{s})$
Φ	Scalar field	
γ	Interpolation factor	
τ'	Fluctuating shear stress	N/m^2
δ_{ij}	Kronecker delta	
ε	Dissipation rate	m^2/s^3
Ω	Control volume	m^3
α	indicator	
γ	Phase fraction	
λ	Weight factor	
η	Collection efficiency	

Superscript

n	Time step at n	

$n+1$	Time step at $n+1$
$+$	Inflow
$-$	Outflow
L	Low-order schemes
H	High-order scheme
C	Corrected flux
$`$	Fluctuating value

Subscript

i, j, k	Space cell i, j, k
$i - 1/2$	Space cell $i - 1/2$
$i + 1/2$	Space cell $i + 1/2$
t	Turbulence
sgs	Subgrid-scale
p	Particle
l	Liquid phase
g	Gas phase
f	Cell's face
CI	Centre linear interpolation
UI	Upwind interpolation
rot	Rotation
rgh	$\rho g \Delta h$

Acronyms

Re	Reynolds number
FVM	Finite Volume Method
$T.E.$	Truncation Error
SIMPLE	Semi-Implicit Method for Pressure-Linked Equations
PISO	Pressure-Implicit with Splitting of Operators
PIMPLE	PISO-SIMPLE
RNG	Re-Normalisation Group
RSM	Reynolds Stress Model
EVM	Eddy Viscosity Model
LES	Large Eddy Simulation
SGS	Subgrid-scale
RANS	Reynolds Averaged Navier-Stokes
HRS	High-Resolution Schemes
FCT	Flux Corrected Transport
VOF	Volume of Fluid
MULES	Multi-dimensional Universal Limiter for Explicit Solution
Tan	Tangential
NTM	Non-Turbulence Model
CC	Curvature Correction

Declaration

I, the author, confirm that the Thesis is my own work. I am aware of the University's Guidance on the Use of Unfair Means (www.sheffield.ac.uk/ssid/unfair-means). This work has not been previously been presented for an award at this, or any other, university.

Chapter 1. Introduction

1.1 Background and motivation

The hydrocyclone was invented in the late 18th century (Bhaskar et al., 2007) and is still widely used due to its irreplaceable versatility, economy, reliability and simplicity. The versatility of the cyclone separator is reflected in its application within many fields, such as dewatering, concentrating and separation. The economic cost of a cyclone separator is relatively cheaper than other standard units of operations. Due to the absence of moving parts, a cyclone separator has an extended operating life and low maintenance costs compared to other separation methods. The process performance does not deteriorate as a result of the operation time. Nevertheless, in terms of drawbacks, a large amount of waste will be generated during the separation process since the separation efficiency of the cyclone depends on the mass flow rate, which is a difficult parameter to control (Nowakowski, 2008).

The cyclone separator is designed based on simple principles. The centrifugal force, which is generated by the large swirling flow inside the cyclone, can be utilised to separate different materials or convey specific particles through the separator. As Fig. 1.1 presents, the large particles of heavier weight will be discharged from the bottom outlet along the wall. The small particles or fluid with lighter weight will flow out from the top outlet along the vortex finder. In general, the cyclone separator can handle a variety of separation conditions. The multi-phase flow inside the cyclone can be in a gas-solid, gas-liquid, liquid-liquid, liquid-solid or even gas-liquid-solid state. Furthermore, the cyclone separator can be called a hydrocyclone only when the primary fluid is a liquid suspension.

The air-core is a fascinating yet not well-comprehended phenomenon that occurs in hydrocyclones. Since the efficiency of the separation will be influenced by the air-core, it has attracted many studies, which have been undertaken based on different techniques. It is generally acknowledged that the air-core is generated due to the low-pressure area, which is created by the large swirling flow in the centre of the hydrocyclone. When the outlets of the vortex finder and spigot open to the atmosphere, the low-pressure area will cause a backflow in the atmosphere and

eventually form an air-core; this phenomenon is shown in Fig. 1.2. Conversely, if the hydrocyclone forms part of a piping network or is in liquid-liquid separation, the air-core will be suppressed (Davidson, 1988).

Investigating the flow with air-core in hydrocyclones is a challenging task and has been considered by industry and academia. A successful numerical simulation of the cyclone flow requires a substantial amount of knowledge from various disciplines. Not only is it related to physical theories, but it also needs developments in mathematics and computer science. These disciplines are key contributors to the development of computational fluid dynamics used to improve hydrocyclone design.
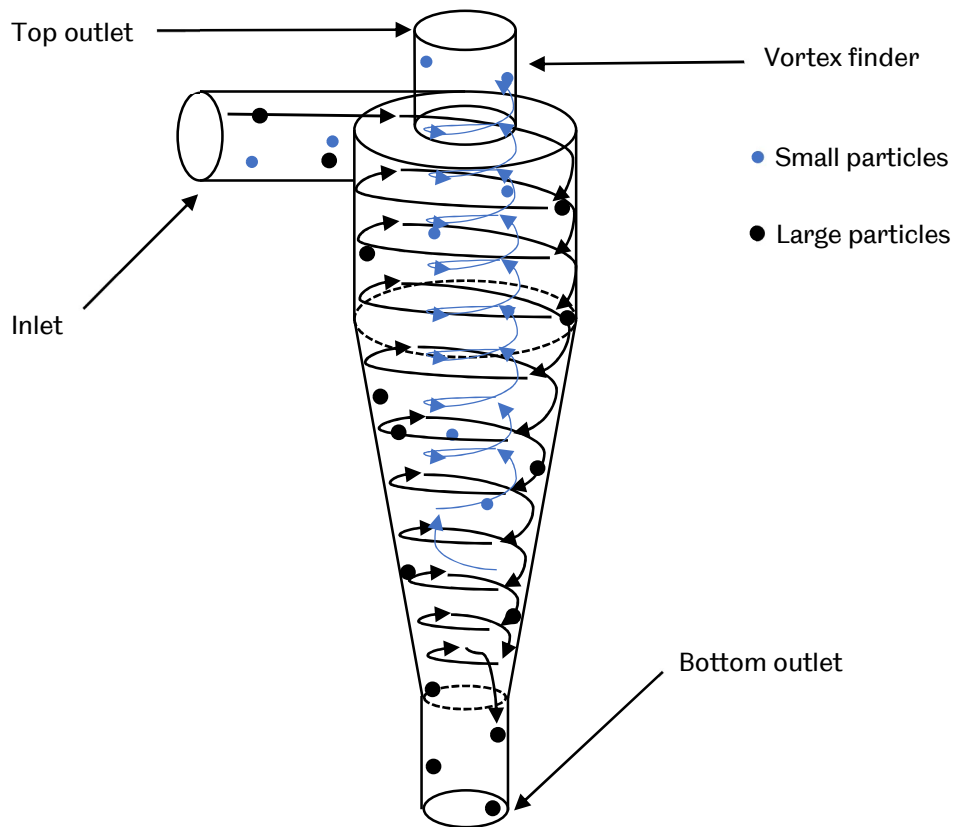
Fig 1.1. The cyclone separator with particles
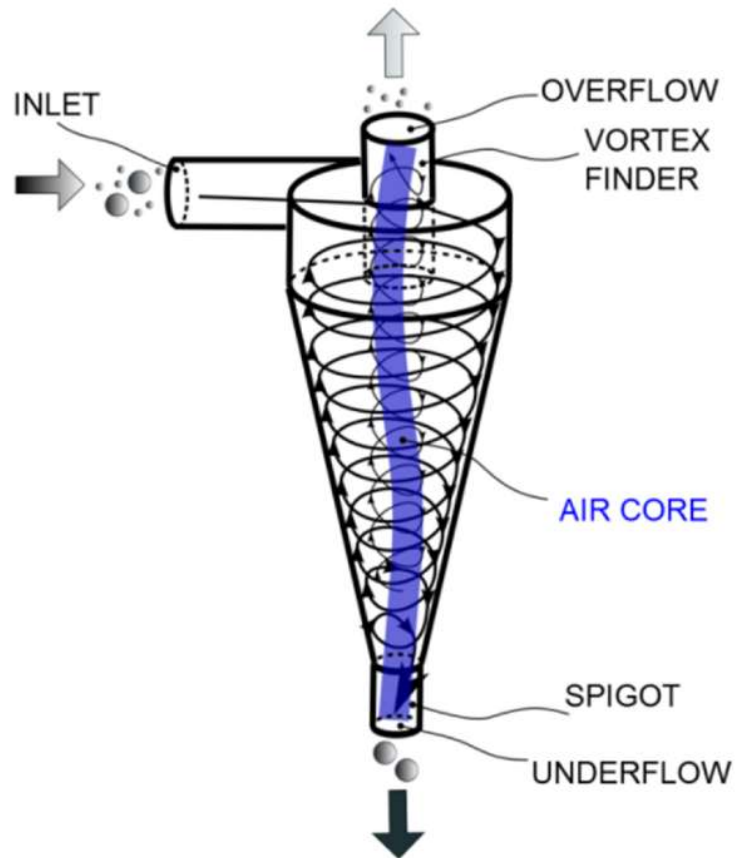
Fig. 1.2. An air-core generated in the hydrocyclone (Rudolf, 2013)

1.2 Aims and objectives

The main aims of this thesis are:

1. To develop a numerical methodology for the simulation of flow with air-core in hydrocyclones.

2. To verify the developed numerical methodology via a series of simulations. These include the single-phase cyclone flow using the RSM turbulence model; the multi-phase dam breaking flow with distinct interfaces using the developed VOF method; the multi-phase hydrocyclone flow using a combination of the RSM turbulence model and the developed VOF method.

3. To investigate the formation of the air-core inside hydrocyclones using the developed methodology with a transient state solver.

4. To analyse the steady flow fields of the flow with air-core in hydrocyclones.

5. To apply the numerical methodology to investigate the challenging problems, in order to benefit the design of hydrocyclones.

The specific objectives required to achieve these aims are:

1. The application of a new approach to Volume of Fluid (VOF)-based interface capturing methods capable of capturing the distinct interface between different fluids.

2. The exploration of an appropriate turbulence model, which is applicable for modelling turbulence effects in a large swirling flow.

3. The employment of the transient state solver to capture the interface between fluids at different times.

4. The application of the developed numerical methodology to obtain the data of the physical properties of the flow in hydrocyclones

5. Verification of the developed approach against previous numerical simulations to demonstrate the performance of the proposed methodology.

6. Validation of the simulation results with reliable experimental data.

7. Comparison of the simulation results using different turbulence models.

8. Investigation of the effect of changing dimensions of different sections of the hydrocyclones on flowing state using the developed methodology

9. The study of the influence of applying different interface smearing factors (used in the new approach to VOF-based interface capturing methods) on the simulation result.

10. Verification of the assumption of simplifying the simulation of the flow in hydrocyclones by ignoring the effects of the air-core.

1.3 Thesis outline

More than half the content of the first chapter is stated above. It presents the background, motivation, aims and objectives of the investigation of the flow with air-core in hydrocyclones. The thesis outline is given in the current section, and the contributions of the present work are listed at the end of **Chapter One**.

Chapter Two presents the previous studies of the flow in cyclones and hydrocyclones. The review focuses on the physical phenomena and numerical methodologies.

Chapter Three demonstrates methodologies for numerical simulations. This includes the introduction of the Navier-Stokes equations, the discretisation method of the differential and integral equations, the interpretation of the pressure-velocity coupling problem and the introduction of the turbulence models that were employed in all simulations.

Chapter Four focuses on introducing the equations and techniques related to the Volume of Fluid (VOF) solver in OpenFOAM®. This solver is optimised through an interface compression scheme (Weller, 2008; OpenCFD, 2008) and is implemented relying on a customised Flux Corrected Transport (FCT) technique, which is called MULES (Multidimensional Universal Limiter with Explicit Solution). The High-Resolution Schemes (HRS) technique is applied for the calculation of the volume fraction equation. An introduction to the FCT and HRS technique is given in this chapter in order to understand the principles of the developed VOF method.

Chapter Five illustrates the essentials of boundary condition setting and mesh generation. The application of each boundary condition is explained in detail. The section on the mesh generation illustrates the geometric dimensions of each study case, and demonstrates the potential defects in the process of generating meshes. The solutions for these defects are also given in this chapter.

Details of the simulation cases are presented from Chapter six to Chapter eight.

Chapter Six introduces the simulation of single-phase flow in a cyclone separator. This simulation is devoted to selecting a suitable turbulence model in the simulation of cyclone flow. The validation process is implemented by comparing the simulation result with Hoekstra's (2000) experiment data.

Chapter Seven presents the simulation of the dam breaking flow. The developed Volume of Fluid (VOF) method was used for this simulation. The investigation by Cruchaga et al (2007) was used for the validation procedure.

Chapter Eight introduces the simulation of flow with air-core in hydrocyclones. It is implemented based on the algorithm, models and solvers introduced and used in the previous studies. The validation procedure is presented by comparing the result

with Hsieh's experimental data (1988). In addition, further studies carried out, based on the new methodology, are introduced. These studies were undertaken to explore whether the developed numerical simulation methodology can be used to change the design of cyclone separators, and to further determine the optimal settings for the new numerical simulation methodology.

Chapter Nine summarises the conclusions of the main study case and provides plans for future studies. The complete work plans and completed objectives are also listed.

1.4 Contributions of the work

The primary contribution of the current work is the application of a new developed numerical simulation methodology (the combination of the RSM turbulence model and the developed VOF method) to analyse the flow with air-core in hydrocyclones. The open source CFD package, OpenFOAM® contains some customised methods and techniques that will produce a different simulation result compared with other commonly used commercial CFD packages. Therefore, the application of the current new methodology provides a new investigation strategy for the study of hydrocyclones in both the academic and industrial aspects.

The following specific original contributions are made throughout this work.

- A simulation of the flow with air-core in hydrocyclones based on the LES method and the developed VOF method.

- The transient flow patterns and formation process of the flow with air-core in hydrocyclones

- A specific analysis of the velocity field, pressure field and other parameters of the flow in hydrocyclones.

- An original study of the influence of applying different turbulence models on the simulation result of the dam breaking flow.

- An original study of the influence of applying different turbulence models on the simulation result of the flow with air-core in hydrocyclones.

- An exploration of the effect of changing dimensions of different sections of the hydrocyclones on flowing state.

- An original study into the influence of applying different interface smearing factors on the simulation results of the hydrocyclone flow.

- A suggestion for simplifying the simulation of the flow in hydrocyclones by ignoring the effects of the air-core.

- Some defects with OpenFOAM® were found during the simulations.

Chapter 2. Characteristics of the hydro-cyclone based on previous studies

2.1 General study

In earlier days, the studies of the cyclone and hydrocyclone are processed focused on the basic working principles. More and more specific phenomenon and theories about the cyclone flow has been revealed since formal researches on the cyclone separator were carried out (Shepherd and Lapple, 1939 and 1940. Ter Linden, 1949. Kelsall, 1952). Shepherd and Lapple (1939 and 1940) investigated the flow pattern, fraction loss and pressure drop of the cyclone dust collector in their experiments. They demonstrated the effects of dust, inlet deflector vane and exit vane on pressure drop. As far as the flow pattern in their research is concerned, the flow inside the cyclone consists of two different kinds of spiral patterns. The outer downward spiral is shaped close to the cyclone's wall, while the other is an inner upward spiral, which occurs near the centre of the cyclone as Fig. 2.1 shows. Furthermore, the research mentioned that for the outer region, the spiral velocity increases approximately with the inverse square root of the radius; and the spiral velocity decreases with decreasing radius when the radius is less than one-third of the cyclone cylinder. Ter Linden (1949) explained a similar flowing pattern in his research. He carried out his experiment in a three-dimensional environment, but the inner part of the cyclone flow was hard to be measured due to the intense turbulence and unsteady. After excluding some inaccurate data from the central area, he founded that the tangential velocity increased as the distance from the centre of the cyclone diminished. The deviation between the total velocity and tangential velocity V_t is inconspicuous. The vertical component V_h is directed downward in the region approaches to the cyclone walls, and the particles will be conveyed out in this region. The radial velocity V_r is directed to the centre of the cyclone in the outer part of the spiral; In contrast, the directions are reversed for the vertical component V_h and radial component V_r in the highly turbulent centre part (Ter Linden, 1949).
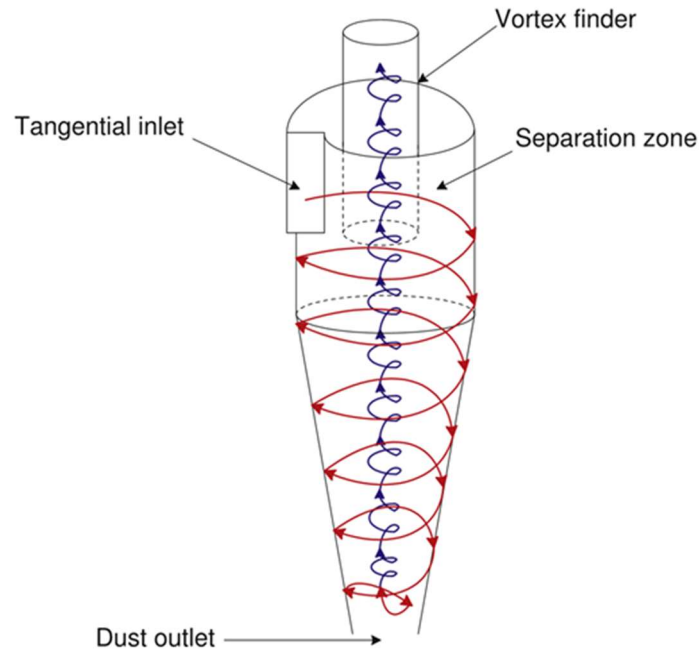
Fig. 2.1. The cyclone separator and the spiral inside the cyclone

(Alahmadi and Nowakowski, 2016)

2.2 Swirl flow in cyclones

Accompany with the advancement of measurement technology and the emergence of Computational Fluid Dynamics, the entire flow pattern of the single-phase cyclone flow becomes apparent. The analysation of the behaviour of the swirl flow in cyclones can be separated into tangential velocity and axial velocity. When a swirling flow emerges in a confined domain, the pattern of the tangential velocity can be defined as a combination of two distinct regions. The inner part close to the centre of the domain is called the solid-body rotation. For the outer part near the boundary, the fluid swirled freely and is named as a free vortex (Hoffmann and Stein, 2008. Alahmadi and Nowakowski, 2016.). The reason for this phenomenon can be attributed to the effect of viscosity. By assuming that the viscosity of the fluid is infinite, the inner part will rotate like a solid body, and the fluid forced to swirl with a constant angular velocity. This phenomenon can be presented in the following equation:

$$v_\theta = \omega r$$

(2.1)

where ω is the angular velocity which can be seen as a constant for the solid rotation part. r is the radius of the domain from the centre to the boundary.

In terms of the outer part of the swirling flow, it is assumed that the fluid has no viscosity in this region, the motions of the fluid elements will not be influenced by each other. Moreover, the flowing behaviour obeys the rule of moment-of-momentum conservation, which means the moment-of-momentum is a constant ($mv_\theta r$). For a mass conserved fluid element, the relationship between radial position and tangential velocity can be written as:

$$v_\theta = \frac{constant}{r}$$

(2.2)

From this equation, it can be found that the tangential velocity is inversely proportional to the radius of the domain. This is consistent with the theory demonstrated in previous literature (Shepherd and Lapple, 1939 and 1940. Ter Linden, 1949.).

Fig. 2.2 presents the tangential velocity curve correspond to the theory and equations mentioned above. The dash lines shown in the figure represent two typical function curves; the straight-line passing through the coordinate origin conforms to the Eqn. 2.1, which illustrates a solid body rotation. The other dash line accord with the Eqn. 2.2 indicate a Loss-free vortex. It can be found that the solid line which represents the velocity curve of the real vortex matches with the dash lines in different parts. The inner part is in line with the forced vortex, and the periphery part agree with the rule of Loss-free vortex. Thus, it can be reputed that the swirl flow is a combination of the forced vortex and the Loss-free vortex; and this phenomenon is also known as the "Rankine vortex". Liu and his colleagues (2006) believe that the primary sources which cause the transportation of the moment-of-momentum between the fluid elements at different radii attribute to the viscose effects and the presence of turbulence (Alahmadi and Nowakowski, 2016).
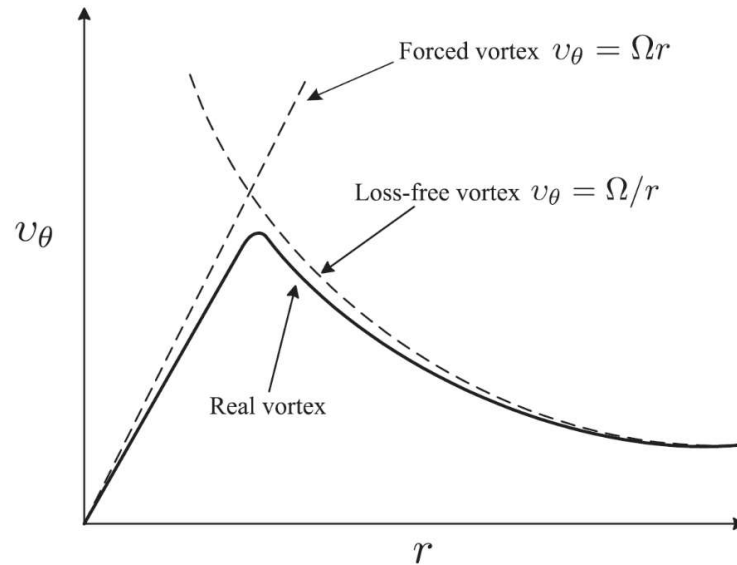
Fig. 2.2. The velocity curve of the tangential velocity in a real vortex and two extreme vortex flow (Alahmadi and Nowakowski, 2016)

In terms of the other component, the axial velocity also plays an essential role when analysing the flowing behaviour of the swirl flow inside the cyclone. The primary fluid, such as gas or liquid, acts as a carrier to deliver particles of different masses or volumes to different tributaries. To be more specific, when the fluid is flowing towards the top outlet of the separator, it has overcome the influence of the gravitation force and presents a velocity vector in the upward axial direction. In terms of the outer part fluid, it flows near the wall of the separator and presents a velocity vector in the downward axial direction (Peng et al., 2002). One of the velocity profiles of the axial component is provided in Fig. 2.3. The near-wall region, which presents a solid line under the zero tick, indicates the axial velocity is directed downward. The solid line with positive value means the axial velocity is directed upward in the core part of the cyclone. Furthermore, the axial velocity curve has a distinct depression at the centre of the cyclone. This depression leads to research about the relationship between the diameter of vortex finder and profile of axial velocity. If the depression exists, the velocity curve illustrates an inverted "W" pattern; otherwise, it gives an inverted "V" pattern curves like the sketches shown in Fig. 2.4. These figures are obtained through the observation point located at the same vertical position below the vortex finder. The cyclone with more extensive vortex finder tends to produce an inverted "W" pattern curves and the curve which takes the form of the "V" pattern generally produced by the cyclone with a smaller

vortex finder. Horvath et al. (2008) investigated this relationship at a deeper level. They introduced a dimensionless diameter D_e/D to predict the pattern of the axial velocity curve as the vortex diameter changes. When this diameter is larger than 0.53, the curve tends to present an inverted "W" pattern. When the ratio is smaller than 0.45, an inverted "V" pattern curves shall be produced. For the ratio between these limiting values, the axial velocity profile is unpredictable due to the unstable state. The low-pressure area which located at the centre of the cyclone is considered as the primary source cause this pattern change. It results in a back-flow phenomenon at the centre of the cyclone. Therefore, the cyclone with larger vortex finder tends to increase the back-flow and illustrates an inverted "W" pattern curve. The above patterns have been captured successfully in the Computational Fluid Dynamics (CFD) area since 1982 (Boysan et al. 1982).
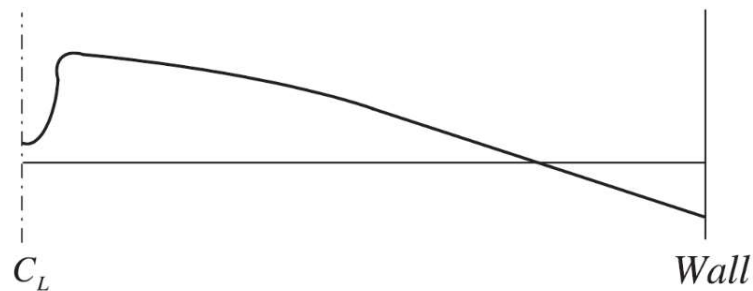
Fig. 2.3. The velocity curve of the axial velocity in a half cyclone.

(Alahmadi and Nowakowski, 2016)
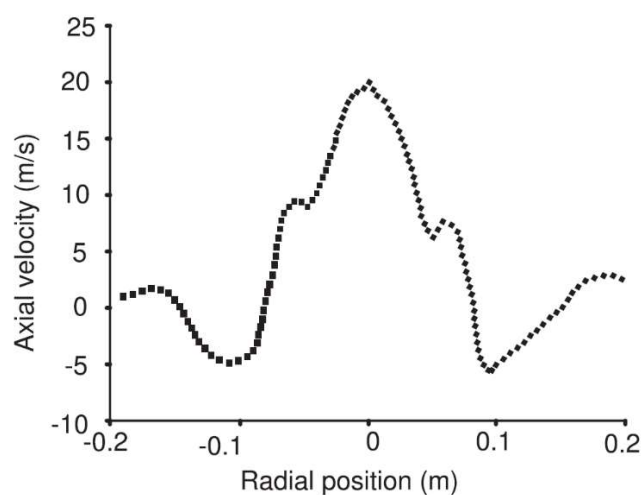
Fig. 2.4a. The velocity curve of the axial velocity in the inverted "V" pattern

(Horvath et al., 2008)
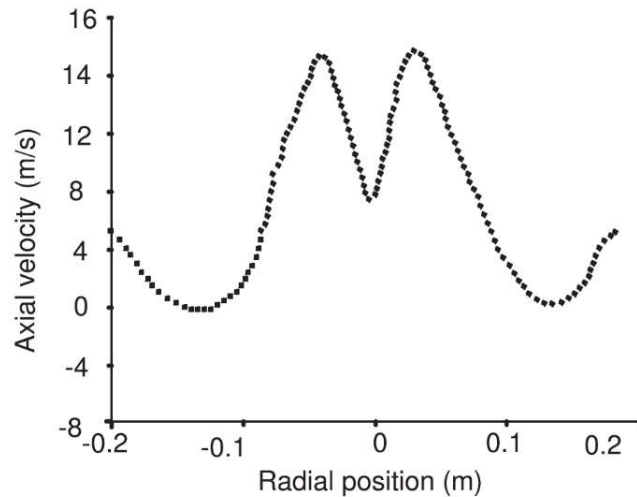
Fig. 2.4b. The velocity curve of the axial velocity in the inverted "W" pattern

(Horvath et al., 2008)

When using the CFD technology to investigate the cyclone flow, the characteristics of the tangential velocity and axial velocity are the basic rules that need to be satisfied. Although the function curves seem uncomplicated as shown in the previous figures, they are hard to be restored due to turbulence and severe rotation problems. Furthermore, the simulations become even more complicated when the multi-phase flow problem being considered. Therefore, these significant challenges are settled for the CFD researchers to overcome, especially in the aspects of turbulence model and multi-phase flow solver.

2.3 Simulation methodology

There are numerous CFD softwares can be used for the numerical simulation, and each one has its advantages. The OpenFOAM® is chosen for the current study since the operation is straightforward if the principles of the CFD have been comprehended correctly. Another advantage of the OpenFOAM® is that the software is free for any researchers to use. Furthermore, their customised code can be added to the original system or equations if they have any new theories or methodologies want to be tried. The operational difference between the OpenFOAM® and Fluent was investigated by Bogdanov and Poniaev (2014) within the problem of the cyclonic separator. The standard $k - \omega$ SST turbulence model was applied for his simulation. The results indicate that the OpenFOAM® performs better on the inner wall of the channel, while the Fluent performs well on the outer wall part. Another

research (Balogh, Parente and Benocci, 2012) was carried out focusing on the ability of OpenFOAM® and Fluent to deal with the turbulence issues. An enhanced $k - \varepsilon$ model was applied for the simulations within the Reynolds averaged Naiver-Stokes (RANS) method. As an essential parameter, the accuracy of the results of the simulations was compared in his study. The time and computational sources required for the operation of the two software were also taken into account.

Governing equation and Turbulence model

The governing equations are the basis of a CFD work. For a particular investigation, the governing equations can be simplified or adjusted to get a more accurate and efficient methodology. Some of the contributions to the investigation of hydrocyclone fluid dynamics were compiled by Nowakowski et al. (2004). The theories and experiences in these investigations are significant and representative for recent researches. For instance, the governing equations of the hydrocyclone problem need to be modelled in a three-dimensional environment. Due to computer capability and the cyclone separator is considered to be axisymmetric geometry, most of the researches were carried out in a two-dimensional environment before the study of Concha et al. (1998). Concha et al. analysed the hydrocyclone flow through a full three-dimensional modelling approach. Later, in order to analyse the separation efficiency more accurately, He et al. (1999) illustrated that the hydrocyclone flow field should be treated as an axial asymmetry problem. Thus, the full three-dimensional modelling is necessary for an accurate simulation of the flow in cyclones.

Another Important subject that scholars are interested in is how to cope with the turbulence in hydrocyclones. As a known condition, the cyclone flow is highly turbulent, accompanied by an intensive swirl. Various turbulence models have been analysed in the past studies, and most of them are applicable to the RANS approach. The other approaches, such as the Large-Eddy Simulation (LES) and the Direct Numerical Simulation (DNS) are also feasible to model the flow fields in hydrocyclones. However, in the early days, due to the limited capabilities of computers, the LES method and DNS method were rarely applied in researches, especially the DNS approach. Nowadays, along with advances in computer technology, the LES method has been widely used in the numerical simulation of

cyclone flow. Even so, the RANS approach still cannot be replaced due to its simplicity and efficiency. More details will be demonstrated in the following content.

RANS

The RANS approach requires a suitable turbulence model, which can accurately present the unknown term of the Reynolds stresses to content the governing equation closure. The models are generated based on the time-averaged equations; they are generally simplified through a rigorous assumption in regard to the physics of the turbulent flow. In concern of the physics phenomenon of the cyclone flow mentioned in the above content, some of the well-known RANS turbulence models are unable to provide practical results during the simulations. For instance, the standard $k - \varepsilon$ model (Harlow and Nakayama, 1968) cannot precisely predict the behaviour of the swirling flow since the viscosity is assumed as isotropic in the model. As one of the most-widely used turbulence model for industrial applications, the $k - \varepsilon$ model is available to produce exact solutions for the fully turbulent flows. The constitution of the $k - \varepsilon$ model is relatively concise comparing with other turbulence models. The turbulence viscosity is assumed can be derived from the turbulent kinetic energy, k, and the dissipation rate, ε. The assumption is conceived directly to the isotropic turbulence flow. Thus, this is the reason why it is improper for the cyclone flow; the Reynolds stresses is highly anisotropic (Petty and Parks, 2001). In order to make the $k - \varepsilon$ model applicable to cope with the anisotropic character of the turbulence flow within a hydrocyclone. Dai et al. (1999) modified the constants $C_{\varepsilon 1}$, $C_{\varepsilon 2}$ and C_u in the standard $k - \varepsilon$ model through their wind tunnel experiments. Unfortunately, this modification still cannot change the situation that the standard $k - \varepsilon$ model is unsuitable for the hydrocyclone flow field. In addition to the $k - \varepsilon$ model, the $k - \omega$ Shear Stress Transport with Curvature Correction (SSTCC) turbulence model was employed by Alahmadi and Nowakowski (2016) to simulate the flow in cyclones. It has been proved that the SSTCC model is available to provide an accurate simulation result and require less computational resources compared with the RSM model and the LES model.

DSM

The commercial CFD package Fluent is commonly used by plenty of research groups since the turbulence models in Fluent are relatively abundant compared with other CFD package in earlier days. When the intensive anisotropic character and

turbulence generation mechanisms of the hydrocyclone flow fields can be noticed during the simulation. The proper choice shall be found between different turbulence models (Cullivan et al., 2003). The full differential stress model (DSM) used in Fluent is considered a reasonable choice considering the accuracy and computational consumption. In order to improve the accuracy of the model, the pressure-strain term in the DSM can be estimated by the high-order model. Instead of accurately describe the effect of the entire turbulence, the Reynolds stress in turbulence is modelled by solving the Reynolds-transport equation.

RSM

In earlier turbulence simulations, most models were designed to be purely dissipative, and the effects of Reynolds stress relaxation were not considered. (Nowakowski and Doby, 2008) This defect was improved in the later designed turbulence model which directly calculate the Reynolds stress through a set of partial differential equations. Those equations are used to estimate the value of each Reynolds stress component. Generally, these Reynolds stress components represent the basic properties of the turbulence. To be more specific, they are stress production, turbulent diffusion, molecular diffusion, pressure-strain, rotation production and dissipation rate, respectively. The pressure-strain term is that the composition expresses the redistribution mechanism. The isotropic characteristic of the turbulence flow emerges when the pressure-strain term equals to zero. This "Reynolds stress model (RSM)" can be adjusted and optimised in different CFD package. In general, there are six partial differential equations for each component and one partial differential equation for the dissipation rate. After this model can be used on most CFD packages, a great number of numerical simulations used this model to explore its range of applications. In the research carried out by Kraipech-Evans et al. (2008), the RSM model was applied for the equation closure within the simulation of turbulence flow. Due to the RSM model has the ability to predict the anisotropic turbulence flow, it was proved to be applicable for the simulation of hydrocyclones (Bhaskar et al. 2007; Wang and Yu 2006). The RSM model estimates the entire stress components with appropriate models and equations; this indicates that the effects caused by the swirling flow in three-dimensional is also taken into account. Although the RSM model has many advantages, it is relatively inefficient compared with other RANS turbulence models. There are at least six equations need

to be solved for the Reynolds stress term, which lead to unstable and substantial time cost during the simulation. Alahmadi and Nowakowski (2016) compared the RSM model with the $k - \omega$ SSTCC turbulence model within the simulation of cyclone flow. They demonstrated that the RSM model takes more time to obtain a simulation result with the same accuracy.

ASM

As the above section mentioned that the RSM model is complicated for calculating, the Algebraic Stress Model (ASM) model was conceived to simplify the solution process of the RSM model; meanwhile, the anisotropy of the RSM model can be preserved as well. The simplified process is achieved by reducing the equations of Reynolds stress transport to algebraic equations. In other words, the convective and diffusive transport terms in the equations are removed or modelled. This ASM model was tested by Chu and Chen (1999) within the simulation of hydrocyclone flow. The simulation result indicated that, compared with the RSM model, the ASM model not only requires less computational resources, but also remains some of the RSM characteristics.

LES

The Large-eddy simulation (LES) approach plays an essential role as the computational technology becomes advanced. Technically, The LES approach is much more accurate than the RANS approach but requires powerful hardware to support its calculation. Different from the RANS approach, the LES approach only models the effects of the eddies with small length scale by using a sub-grid model. Those eddies with large length scale will be simulated directly, thereby the full three-dimensionality and time dependence of the turbulence field can be retained (Zikanov, 2010). Several filter functions can be used to define the size of the small eddies scale length. Thus, the simulation results will be practical only when the mesh is small enough to a certain extent. This requirement became the biggest obstacle for the numerical simulation in earlier days. In concern about the computational costs, the LES approach performs worse than the DSM model (Slack et al., 2000). However, irrespective of time cost and computing resources, the LES approach predicts a remarkably well simulation result in comparison to the Differential Reynolds Stress turbulence model (Brennan, 2006; Brennan et al. 2006). The advantages of the LES method are fully utilised in the simulations of cyclones and

hydrocyclones (Slack et al., 2000; Delgadillo and Rajamani, 2005). The characteristics of the time-dependent vortex oscillations and non-equilibrium turbulence are captured well aimed. Further studies of the LES approach is able to carry out focus on the sub-grid scale models. It can be refined for particular applications such as the simulation of the cyclone and hydrocyclone flow, which concern about the effects of particles and the correlation of different time scales related to collisions and aggregation of particles (Nowakowski and Doby, 2008).

DNS

In the numerical simulation, the direct numerical simulation approach has the highest theoretical precision than the LES approach and RANS approach. Correspondingly, the computational resource required by the DNS approach is significantly greater than the other approaches. The grid size and time scale are the main reasons that cause this discrepancy. They are demanded to be smaller than the smallest length scales and time scale of the energy-carrying dissipative eddies. The Kolmogorov scaling is used to estimate the length scale and time scale in ordinary situations; it is correlated to the Reynolds number in its expressions $(\frac{\eta}{l} \sim Re^{-\frac{3}{4}}, \frac{\tau}{T} \sim Re^{-\frac{1}{2}})$. The Reynolds number of the cyclone in operation is usually higher than 200,000. Therefore, at the current stage, the DNS approach is almost impossible to be used for the simulation of cyclone flow. The applications of the DNS approach are limited to flows at restrained Reynolds number and uncomplicated geometries.

2.4 Air-core

Several approaches are conceived to predict the diameter of the air-core. Dyakowski and Williams (1995) demonstrated that an effective air-core interface viscosity could be used for the prediction. Another approach was introduced by Concha et al. (1998), who estimated the diameter through the application of Young-Laplace's relation. These two approaches provide a feasible solution for estimating asymmetric air-core geometry. Also, the experimental method can be applied to the estimation of the size of the air-core. Hsieh (1988) investigated the flow with air-core in hydrocyclone by the Laser-Doppler Velocimeter (LDV) technique. He provided valuable experimental data for the later investigations of the flow in hydrocyclone. Another technique called Electrical Resistance Tomography (ERT)

was employed by Arugonda et al. (2013) to measure the air-core size. After post-processed by the forward FEM solution and inverse reconstruction algorithms, the three-dimensional air-core size could be estimated.

The characteristics of the air-core were revealed through various researches. Such as the air-core has an oscillatory nature which means the shape of the air-core is not regularised during flowing (Dyakowski and Williams, 1993). Ovalle and Concha (2005) Demonstrated that the inertial waves or the fluctuations in the feed are the main reasons induced the oscillation. The dynamics of the air-core and the velocity field of the fluid was investigated through the LES approach, which was utilised in Delgadillo and Rajamani's (2005) numerical simulation. Another numerical simulation, which was progressed through the finite element method illustrated the relationship between air-core, pressure-field and viscosity (Doby et al., 2008). A set of fluid with different viscosity was examined to prove that low viscosity feeds tend to develop a larger low-pressure area in the centre region of the hydrocyclone than feeds at high viscosity. Fig. 2.5, presents the effect of viscosity on the formation of the air-core. From the above theory and Fig. 2.5, they demonstrated that the air is drawn back into the hydrocyclone from the atmosphere due to the low-pressure formation in the centre area and upper section in the vicinity of the vortex finder. The overall area of the low-pressure field is narrowed with increasing viscosity. As shown on the sketches of the hydrocyclone, the air-core formation presents to begin through both the top outlet and bottom outlet. The air which was drawn from each of the outlets meets in the central part of the hydrocyclone and forms the air-core in final. Kraipech et al. (2008) tried to reduce the energy loss, which is caused by the low-pressure area by inserting the metal rod in the middle of the hydrocyclone. The validation process is implemented by comparing the simulation result with the experiment data. They demonstrated that the air-core area could be represented by the low-pressure area and the characteristics obtained from this numerical simulation are similar to the experimental observation. As Fig. 2.6. shows, the air-core is found to be unstable, and its shape, size and position are unfixed because of the instability of the gas-liquid interface.
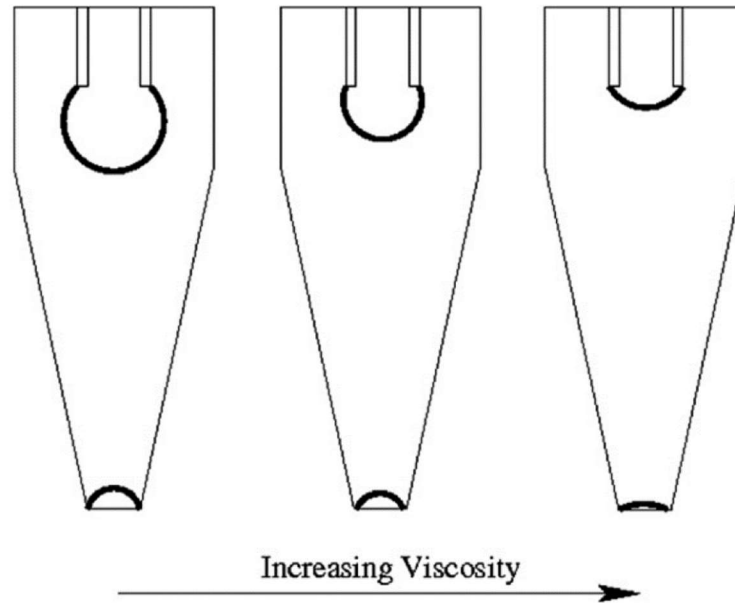
Fig. 2.5. The effect of viscosity on the formation of the air-core. (Doby et al., 2008)

If the position and pattern of the air-core want to be figured out through the numerical simulation, the characteristic of such multi-phase flow requires to be captured. Several kinds of multi-phase-flow solvers are designed to cope with the multi-phase flow within different situations. In general, three approaches are suggested to be used for simulation. First one is the Eulerian-Lagrangian model for fluid-solid simulation. The fluid phase is assumed to be undisturbed by the solid phase and complies with the continuum equations that are solved on a fixed field in the common Eulerian way. The second approach is the Eulerian-Eulerian approach that results in field equations for the flow properties for all phases in the system (Nowakowski and Doby, 2008). Therefore, it requires many extra modelled equations to estimates the unknown terms which represent the interactions between the phases. The third approach called the Volume of Fluid (VOF) method (Hirt and Nichols, 1981), is relatively more straightforward than the previous approaches. This approach introduced a coefficient, α to represents the volume fraction of fluid in each cell. The value of the volume fraction is limited between 0 and 1; these two limited values represent two different fluids, respectively. All of these approaches can be applied for the simulation of the flow in hydrocyclones, but each has its most appropriate situation. Ma et al. (2000) suggested the Eulerian-Lagrangian model mainly employed for dilute systems with a maximum solids volume fraction of 5%. For such cases, the influence due to the particles in a

20

computational grid can be ignored. The Eulerian-Eulerian approach is applicable for the multi-phase flow with larger solids volume fraction (e.g., Davailles et al., 2012). However, the complicated interactions between each phase remain various challenges for modelling process (e.g. Nowakowski et al., 2000). It not only brings a burden to the computer resources but also hard to convergence during the simulation. In theory, Since the VOF approach only concerns about some necessary interaction, the equations between each phase are simplified; it should be suitable for the simulation of hydrocyclones which presents a clear free-surface between different phases. Delgadillo and Rajamani (2005) used the VOF method for calculating the pattern and position of the air-core. In their work, they demonstrated that the RSM model with VOF approach provides an air-core, which is irregular and does not agree with experiment.

In addition to the above three approaches, there are other methods and techniques that can solve the multi-phase flow or capture free-surface. Some researchers had used the mixture model, which is a simplification of the full Eulerian model for the simulation of hydrocyclones (Brennan, 2006; Brennan et al., 2007; Rudolf, 2013). The mixture model requires less computational resources but guarantees accuracy. One of the drawbacks of this method is the numerical diffusion in the area of the free surface. The level set method of Osher and Sethian (1988) is another approach to capture the liquid-gas interface sharply. It is proposed to tackle the air-core problem because of its simplicity and versatility for computing and analysing the motion of an interface in three dimensions (Nowakowski and Doby, 2008) However, the physical meaning of the level set is not as clear as the VOF method, which is not conducive to the analysation of multi-phase flow. Nowakowski and Dyakowski (2003) suggested an interfacial boundary condition to estimate the effect of the air-core without simulating the air-core directly. Natural boundary conditions, relating forces could be advantageous for such simulations.

The modelling of the air-core remains various deficiencies to be refined, even though multi-phase problems in hydrocyclones can be solved through different multi-phase-flow solver. Accompany with diverse schemes and algorithms has been applied to optimise the multi-phase solver, more efficient and accurate modelling approaches for the air-core are expected to be explored. The improvement of the

modelling approaches will benefit the hydrocyclones design because of the flow split between the outlets is influenced by the air-core to a certain degree.
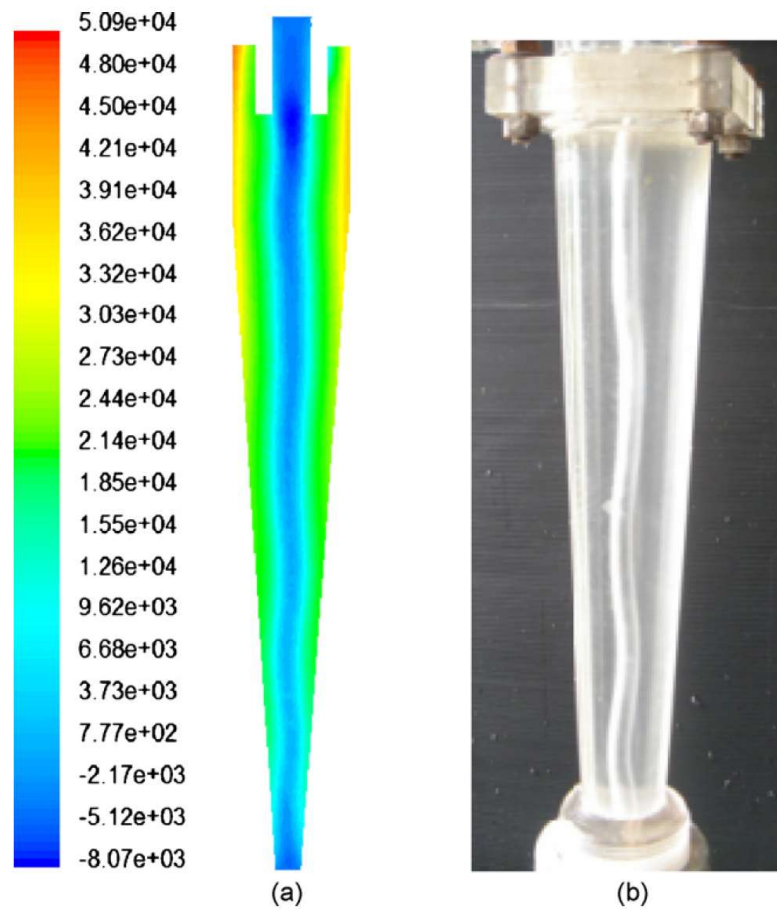
Fig. 2.6. The low pressure area and air-core phenomena (Kraipech et al., 2008)

2.5 Application of numerical simulation in the design of the hydrocyclone

Apart from the CFD package, governing equation, turbulence model and multi-phase solver, the geometry generation is another essential process for the numerical simulations. Especially when a particular cyclone or hydrocyclone wants to be tested by the numerical simulation method, a simple modification to the geometry may cause an unpractical simulation result. The relationship between total cyclone size, cyclone cut-off size and pressure drop in the cyclone flow was investigated by Azadi et al. (2010). They demonstrated that the cyclone cut-off size and pressure drop are reduced as the cyclone size is decreased. Similar research investigated the effect of cyclone length on the efficiency of cyclone separator was carried out by Hoffmann

et al. (2001). They illustrated the performance of the cyclone separator is promoted when the cyclone length is increased. In addition, an optimal length-diameter scale for the cyclone separator was provided in their paper. Lee et al. (2006) indicated that the pressure drop could be reduced by adjusting the diameter of the cylinder body. Moreover, the shape of the core-annulus interface is an essential element, which influences the collection rate and flow pattern. In addition to the main body of the cyclone, the inlet section also affects the performance of the separator. Qiana and Wu (2009) raised an investigation about the inlet section angle of the cyclone separator. They demonstrated that the angle would affect the tangential velocity, pressure drop and separation efficiency. The efficiency would increase rapidly if the angle equals to 45°.

Although the cyclone separator has been used for more than a century, the performance and functions still can be optimised through adding components or changing dimensions. The application of the CFD technology brings time and economy saving comparing with the experimental approach. A practical simulation result can be obtained based on the combination of appropriate turbulence models, suitable solvers, efficient algorithms, advanced computers, and other elements. The present work is one of the researches, seeking a relatively reliable numerical simulation methodology to investigate the flow with air-core in hydrocyclones.

Chapter 3. Numerical methodology

This chapter introduces the numerical methodology which has been used for the simulations. The Navier-Stokes equations in the differential form are recalled since it set the basis for numerical simulations. As the numerical simulation platform (OpenFOAM®) uses the Finite Volume Method (FVM) for discretisation, it is necessary to introduce the integral form of the equations as well. Subsequently, to explain how the computer calculates the equations, discretisation schemes and pressure-velocity coupling algorithms are introduced. Next, the section on the turbulence model provides the derivation of the Eddy Viscosity model (EVM), the Reynolds stress model (RSM) and the Large Eddy Simulation (LES) model. The distinctions between these models are the key features leading to different simulation results. Finally, the Discrete Phase model is introduced in the last section. It was used for the analysis of the particle tracking. The trajectory of a discrete phase particle is predicted by integrating the force implemented on the particle, which is derived in a Lagrangian reference frame.

3.1 Navier-Stokes Equation

The "Navier-Stokes equation" is another name for the continuity equation and momentum equation. Therefore, the following expressions of the Navier-Stokes Equation are the continuity equation and the momentum equation.

Continuity equation:

$$
\underbrace{-\frac{\partial \rho}{\partial t} dx dy dz}_{A} = \underbrace{\left[\left(\frac{\partial \rho u}{\partial x} dx + \rho u\right) - \rho u\right] dy dz}_{B} + \underbrace{\left[\left(\frac{\partial \rho v}{\partial y} dy + \rho v\right) - \rho v\right] dx dz}_{B}
$$

$$
+ \underbrace{\left[\left(\frac{\partial \rho w}{\partial z} dz + \rho w\right) - \rho w\right] dx dy}_{B}
$$

$$
\rightarrow \frac{\partial \rho}{\partial t} + \frac{\partial \rho u}{\partial x} + \frac{\partial \rho v}{\partial y} + \frac{\partial \rho w}{\partial z} = 0
$$

(3.1)

The continuity equation is conceived based on the conservation of mass. Imagine an infinitesimal control volume fixed in three dimensions, then it has,

Term A: The value of the density variety during flowing

Term B: The value of the mass flow across control volume

When the continuity equation is used in an incompressible flow, the equation can be simplified as

$$\frac{\partial u}{\partial x} + \frac{\partial v}{\partial y} + \frac{\partial w}{\partial z} = 0 \rightarrow \nabla \cdot V = 0$$

(3.2)
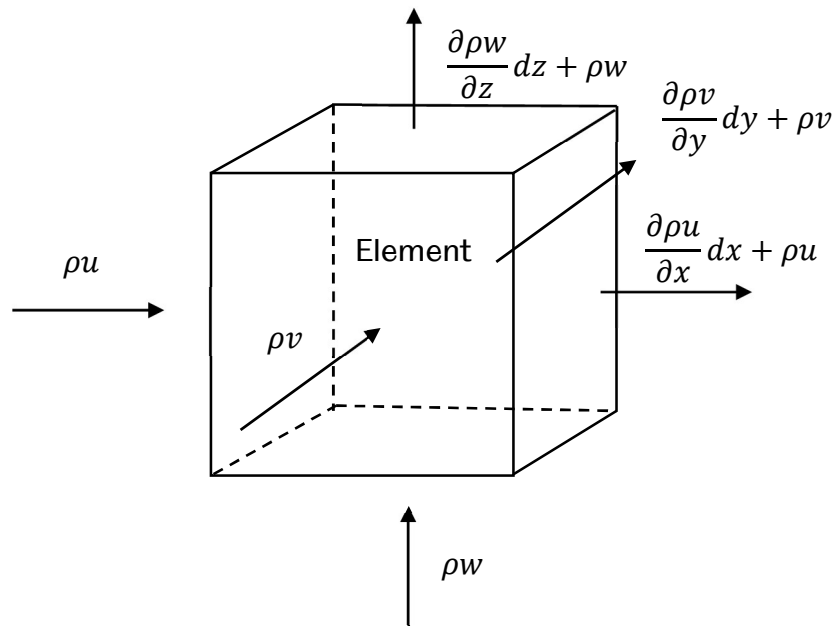
Fig. 3.1. Infinitesimal control volume fixed in three dimensions

Momentum equation:

The momentum equation is generated according to Newton's second law, which states that the rate of change of momentum of a body is equal to the net force acting on it:

$$m\vec{a} = \vec{F} \rightarrow m\underbrace{\frac{D\vec{V}}{Dt}}_{A} = \vec{F}$$

(3.3)

Imagine an infinitesimal element moving within a flow in three dimensions, term A is replaced by the material derivative.

$$m\frac{D\vec{V}}{Dt} = m\left[\frac{\partial\vec{V}}{\partial t} + (\vec{V}\cdot\nabla)\vec{V}\right]$$

(3.4)

In terms of the force term on the right-hand side, generally, two kinds of forces are indicated.

$$F_i = \underbrace{\rho f_i d\Omega}_{A} + \underbrace{\left[\left(\frac{\partial\tau_{ii}}{\partial x_i}dx_i + \tau_{ii}\right) - \tau_{ii}\right]dS_{jk}}_{B} + \underbrace{\left[\left(\frac{\partial\tau_{ji}}{\partial x_j}dx_j + \tau_{ji}\right) - \tau_{ji}\right]dS_{ik}}_{B}$$
$$+ \underbrace{\left[\left(\frac{\partial\tau_{ik}}{\partial x_k}dx_k + \tau_{ki}\right) - \tau_{ki}\right]dS_{ij}}_{B}$$

(3.5)

Where, Ω is the unit volume, S is the unit area.

Term A: represents the body forces acting on the fluid element.

Term B: indicates the pressure and friction forces acting on the interface of the element. The vector field of surface forces is represented by the stress tensor τ_{ij}.

Substituting Eqn. (3.4) and Eqn. (3.5) into Eqn. (3.3), the equation is given as

$$\rho\frac{Du_i}{Dt} = \rho f_i + \frac{\partial\tau_{ii}}{\partial x_i} + \frac{\partial\tau_{ji}}{\partial x_j} + \frac{\partial\tau_{ki}}{\partial x_k}$$

(3.6)

The stress tensor can be separated into the isotropic pressure part and the viscous part. The expression is given as,

$$\tau_{ij} = -P\delta_{ij} + \sigma_{ij}$$

Where

$$\delta_{ij} = \begin{cases} 1 & if \quad i = j \\ 0 & if \quad i \neq j \end{cases}$$

Is the Kronecker delta-tensor

If the fluid is defined as the Newton fluid, then the linear model for the stress tensor is given as

$$\sigma_{ij} = \lambda \delta_{ij}(\nabla \cdot V) + \mu \left(\frac{\partial u_i}{\partial x_j} + \frac{\partial u_j}{\partial x_i}\right)$$

(3.7)

Where $\lambda = -\frac{2}{3}\mu$ for compressible fluids.

Substituting Eqn. (3.7) into Eqn. (3.6), it gives

$$\rho \frac{Du_i}{Dt} = \frac{\partial}{\partial x_j}\left(-\frac{2}{3}\mu\delta_{ij}(\nabla \cdot V) + 2\mu S_{ij}\right) - \frac{\partial P}{\partial x_i} + \rho f_i$$

(3.8)

Where $S_{ij} \equiv \frac{1}{2}\left(\frac{\partial u_i}{\partial x_j} + \frac{\partial u_j}{\partial x_i}\right)$

In addition, for the incompressible fluid ($\nabla \cdot V = 0$) with constant viscosity coefficient μ, the Navier-Stokes equations have the simplified expression,

$$\rho \frac{D V}{Dt} = -\nabla P + \mu \nabla^2 V + \rho f$$

(3.9)

The energy conservation equation is unnecessary for the current study since the fluid is assumed as isothermal.

3.2 Equations in integral form

The integral form of the Navier-Stokes equations is introduced since the Finite Volume Method (FVM) requires such configuration for discretisation. Different from the equation in the differential form, the control volume for the equation derivation is assumed as valuable and fixed in space. For the following equations, the volume is defined as Ω, and the boundary of the volume is defined as S.

Mass conservation equation

$$\frac{d}{dt}\int_{\Omega} \rho d\Omega + \int_{S} \rho V \cdot \mathrm{n} \, dS = 0$$

(3.10)

Momentum equation

$$\frac{d}{dt}\int_{\Omega}\rho u_i d\Omega + \int_{S}\rho u_i V \cdot \text{n dS}$$

$$= \int_{S}\left[(-p + \lambda\nabla\cdot V)n_i + \sum_{j}\mu\left(\frac{\partial u_i}{\partial x_j} + \frac{\partial u_j}{\partial x_i}\right)n_j\right]dS + \int_{\Omega}\rho f_i d\Omega$$

(3.11)

Where n is the normal vector of unit length.

In addition, the general form of the conservation equation for an arbitrary scalar field Φ is given as

$$\underbrace{\frac{d}{dt}\int_{\Omega}\Phi d\Omega}_{A} + \underbrace{\int_{S}\Phi V \cdot \text{n dS}}_{B} = \underbrace{\int_{S}\chi\nabla\Phi \cdot \text{n dS}}_{C} + \underbrace{\int_{\Omega}Q d\Omega}_{D}$$

(3.12)

Term A: indicates the time rate change of the scalar field.

Term B: indicates the convective flux integrals; it represents the transport through the boundary of the control volume by the velocity.

Term C: indicates the diffusive flux integrals; it represents the transport by diffusion through the boundary.

Term D: indicates the volume source integrals; it represents the distributed sources of the conserved quantity within the control volume.

3.3 Discretisation

The discretisation procedure is essential to the process in order to make the above equations capable of computing. The discretisation schemes for differential equations and integral equations are different; both series of schemes are introduced since they have connections during calculating.

3.3.1 Discretisation of differential equations

The discretisation of differential equations is generally used in the finite difference method; it is processed based on the Taylor series expansion. Assume the functions

of the quantity $\Phi(x, y, z, t)$ are sufficiently smooth, so the quantity on neighbouring point $\Phi_{i+1,j,k}$ or $\Phi_{i-1,j,k}$ can be estimated by the quantity on the current point $\Phi_{i,j,k}$ within the Taylor series expansion.

$$\Phi_{i+1,j,k} = \Phi_{i,j,k} + \left(\frac{\partial\Phi}{\partial x}\right)_{i,j,k} \Delta x + \left(\frac{\partial^2\Phi}{\partial x^2}\right)_{i,j,k} \frac{(\Delta x)^2}{2!} + \left(\frac{\partial^3\Phi}{\partial x^3}\right)_{i,j,k} \frac{(\Delta x)^3}{3!} + \cdots$$
$$+ \left(\frac{\partial^n\Phi}{\partial x^n}\right)_{i,j,k} \frac{(\Delta x)^n}{n!} + \cdots$$

(3.13)

Where $\Delta x = (x_{i+1} - x_i)$

$$\Phi_{i-1,j,k} = \Phi_{i,j,k} - \left(\frac{\partial\Phi}{\partial x}\right)_{i,j,k} \Delta x + \left(\frac{\partial^2\Phi}{\partial x^2}\right)_{i,j,k} \frac{(\Delta x)^2}{2!} - \left(\frac{\partial^3\Phi}{\partial x^3}\right)_{i,j,k} \frac{(\Delta x)^3}{3!} + \cdots$$
$$+ \left(\frac{\partial^n\Phi}{\partial x^n}\right)_{i,j,k} \frac{(\Delta x)^n}{n!} + \cdots$$

(3.14)

The above equations can be used to calculate the partial derivative $\frac{\partial\Phi}{\partial x}$.

For instance, moving the partial derivative term to the left-hand side and dividing by Δx, it gives

$$\left(\frac{\partial\Phi}{\partial x}\right)_{i,j,k} = \frac{\Phi_{i+1,j,k} - \Phi_{i,j,k}}{\Delta x} - \left(\frac{\partial^2\Phi}{\partial x^2}\right)_{i,j,k} \frac{\Delta x}{2!} - \cdots - \left(\frac{\partial^n\Phi}{\partial x^n}\right)_{i,j,k} \frac{(\Delta x)^{n-1}}{n!} - \cdots$$

(3.15)

$$\left(\frac{\partial\Phi}{\partial x}\right)_{i,j,k} = \frac{\Phi_{i,j,k} - \Phi_{i-1,j,k}}{\Delta x} + \left(\frac{\partial^2\Phi}{\partial x^2}\right)_{i,j,k} \frac{\Delta x}{2!} - \cdots + \left(\frac{\partial^n\Phi}{\partial x^n}\right)_{i,j,k} \frac{(\Delta x)^{n-1}}{n!} - \cdots$$

(3.16)

Where n is an even number in Eqn. (3.16)

Alternatively, using Eqn. (3.13) minus Eqn. (3.14), and moving the partial derivative term to the left-hand side and dividing by $2\Delta x$, it gives

$$\left(\frac{\partial\Phi}{\partial x}\right)_{i,j,k} = \frac{\Phi_{i+1,j,k} - \Phi_{i-1,j,k}}{2\Delta x} + \left(\frac{\partial^3\Phi}{\partial x^3}\right)_{i,j,k} \frac{(\Delta x)^2}{3!} - \cdots + \left(\frac{\partial^n\Phi}{\partial x^n}\right)_{i,j,k} \frac{(\Delta x)^{n-1}}{n!} - \cdots$$

(3.17)

Where n is an odd number in Eqn. (3.17)

The derivation of the equations is applicable to spatial discretisation in other directions and time discretisation.

The above examples, Eqn. (3.15), Eqn. (3.16) and Eqn. (3.17), can be expressed in the following form

Forward difference

$$\left(\frac{\partial \Phi}{\partial x}\right)_{i,j,k} = \frac{\Phi_{i+1,j,k} - \Phi_{i,j,k}}{\Delta x} + T.E.$$

(3.18)

Backward difference

$$\left(\frac{\partial \Phi}{\partial x}\right)_{i,j,k} = \frac{\Phi_{i,j,k} - \Phi_{i-1,j,k}}{\Delta x} + T.E.$$

(3.19)

Central difference

$$\left(\frac{\partial \Phi}{\partial x}\right)_{i,j,k} = \frac{\Phi_{i+1,j,k} - \Phi_{i-1,j,k}}{2\Delta x} + T.E.$$

(3.20)

Where $T.E.$ represent the truncation error of discretisation of a partial derivative. It contains the rest of the series dropped in Eqn. (3.15) to Eqn. (3.17). The truncation error is a key feature, which decides the accuracy of the discretisation. The magnitude of the truncation error depends on the lowest-order dropped term. Therefore, the forward and backward difference schemes are first-order approximations, while the central difference scheme is a second-order approximation. The size of the mesh will influence the truncation error directly; it can be seen that the error decreases with decreasing Δx.

In addition to the above three discretisation schemes, various schemes have been developed to promote the accuracy of the discretisation. For the simulations mentioned in the present thesis, second-order accuracy should be guaranteed for the discretisation schemes, except for the time derivative term.

3.3.2 Discretisation of integral equations

In the finite volume method, the discretisation is applied directly to the integral equations in a small control volume. Such treatment is relatively advanced when compared with the finite difference method. The most significant advantage is that the equations can be implemented on the corresponding spatial grids without using transform functions. In other words, the finite volume method can be used for complex geometry because the figure of the grids is barely limited (e.g. Fig. 3.2).

Another important advantage is that the discretisation of integral equations has a characteristic of global conservation. It is necessary to recall the conservation equations (Eqn. (3.12)) for an explanation.

$$\underbrace{\frac{d}{dt}\int_{\Omega} \Phi d\Omega}_{A} + \underbrace{\int_{S} \Phi V \cdot n \, dS}_{B} = \underbrace{\int_{S} x\nabla\Phi \cdot n \, dS}_{C} + \underbrace{\int_{\Omega} Q d\Omega}_{D}$$

(3.12)

The volume integral of the quantity Φ is approximated by the product of the cell's volume and the mean value of the integrand $\overline{\Phi}$. The mean value of the integrand $\overline{\Phi}$ can be replaced by the value at the centre of the grid point (shown in Fig. 3.2) when the cell-centred arrangement of the grid points is used. Thus, it has,

$$\int_{\Omega} \Phi d\Omega = \overline{\Phi}|\Omega| \approx \Phi_{P}|\Omega|$$

(3.21)

This approximation generates a second-order truncation error; the approximation is sufficient when the accuracy of the finite volume scheme is designed as second-order.

In terms of the surface integral approximation, this is approximated by the product of the area of the interface and the mean value of the integrand $\overline{\Phi}$. This mean value can be evaluated by the value of the integrand at the midpoint of the interface. (shown in Fig. 3.2)

$$\int_S \Phi V \cdot \mathrm{n} \, \mathrm{d}S = \overline{\Phi V \cdot \mathrm{n}} S_{AB} \approx (\Phi V \cdot \mathrm{n})_e S_{AB}$$

(3.22)

$$\int_S x \nabla \Phi \cdot \mathrm{n} \, \mathrm{d}S = \overline{x \nabla \Phi \cdot \mathrm{n}} S_{AB} \approx (\chi \nabla \Phi \cdot \mathrm{n})_e S_{AB}$$

(3.23)

Where e is the midpoint and n is the normal vector of the interface S_{AB}.
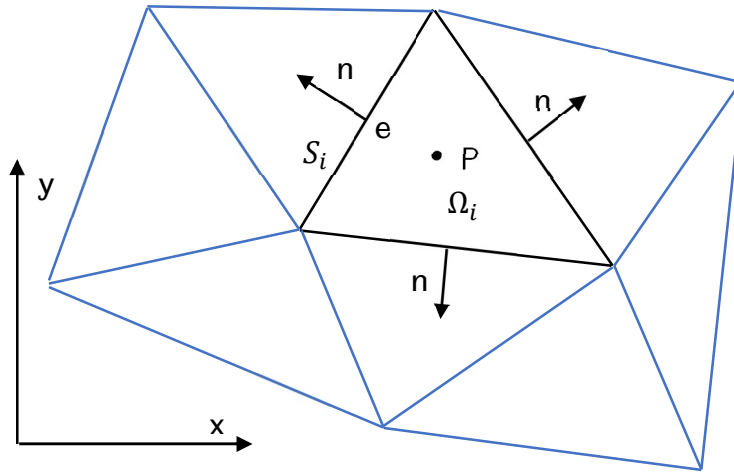
Fig. 3.2. Unstructured finite volume grids

To be more specific, if the mesh is structured and the boundary is drawn parallel to the axis of the Cartesian coordinate (see Fig. 3.2), it gives

$$(\Phi V \cdot n)_e = (\Phi V_i)_e, \quad (\chi \nabla \Phi \cdot n)_e = (\chi \, \partial \Phi / \partial x_i)_e$$

Otherwise, the mesh is unstructured and the boundary is unparalleled to the axis (see Fig.3.2). The surface integral needs to be evaluated by separating the vectors into two (for two-dimensional problems) or three (for three-dimensional problems) components.

The normal vector is perpendicular to the vector of the interface and has a unit length. If the interface vector is defined as

$$S = AB = S_x i + S_y j$$

It provides the normal vector n

$$n = \frac{1}{S_{AB}}(S_y i - S_x j)$$

Therefore, the surface integral is approximated by Eqn. (3.25) and Eqn. (3.26)

$$\int_S \Phi V \cdot n dS \approx \Phi_e \left(V_{x_e} S_y - V_{y_e} S_x \right)$$

$$\int_S x \nabla \Phi \cdot n dS \approx \chi_e \left((\partial \Phi / \partial x)_e S_y - (\partial \Phi / \partial y)_e S_x \right)$$
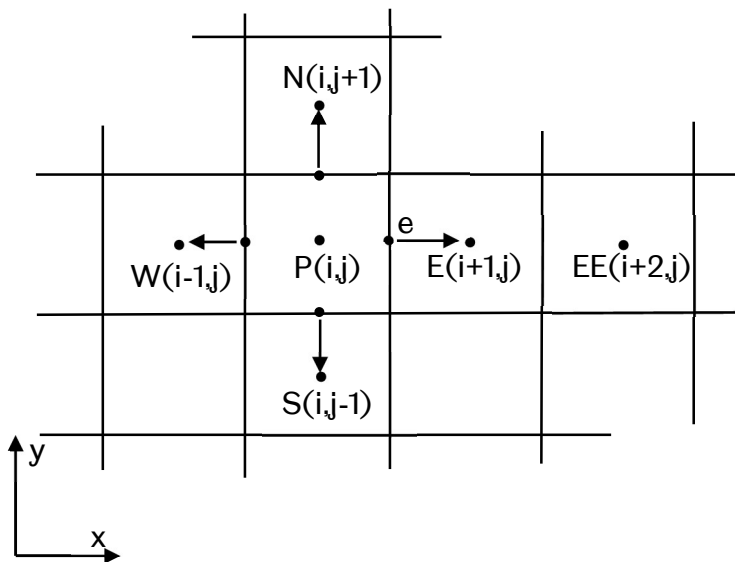
Fig. 3.3. Two-dimensional structured grids used to illustrate interpolation methods

Methods of Interpolation

As can be found from Eqn. (3.25) and Eqn. (3.26), the quantity Φ_e at the midpoints of the cell face cannot be obtained directly. It is necessary to introduce the methods

of interpolation to approximate the value on the cell face. The expression of the linear interpolation method is given as

$$\Phi_e = \gamma \Phi_P + (1 - \gamma)\Phi_E$$

Where $\gamma = |eE|/|PE|$ is the interpolation factor (see Fig. 3.3). When the factor equals 0.5, this interpolation is known as centre linear interpolation; it guarantees the second order of accuracy. This can also be proved by the Taylor series expansion. Recall Eqn. (3.13) and Eqn. (3.14)

$$\Phi_{i+1,j,k} = \Phi_{i,j,k} + \left(\frac{\partial \Phi}{\partial x}\right)_{i,j,k} \Delta x + \left(\frac{\partial^2 \Phi}{\partial x^2}\right)_{i,j,k} \frac{(\Delta x)^2}{2!} + \left(\frac{\partial^3 \Phi}{\partial x^3}\right)_{i,j,k} \frac{(\Delta x)^3}{3!} + \cdots$$

$$+ \left(\frac{\partial^n \Phi}{\partial x^n}\right)_{i,j,k} \frac{(\Delta x)^n}{n!} + \cdots$$

(3.13)

$$\Phi_{i-1,j,k} = \Phi_{i,j,k} - \left(\frac{\partial \Phi}{\partial x}\right)_{i,j,k} \Delta x + \left(\frac{\partial^2 \Phi}{\partial x^2}\right)_{i,j,k} \frac{(\Delta x)^2}{2!} - \left(\frac{\partial^3 \Phi}{\partial x^3}\right)_{i,j,k} \frac{(\Delta x)^3}{3!} + \cdots$$

$$+ \left(\frac{\partial^n \Phi}{\partial x^n}\right)_{i,j,k} \frac{(\Delta x)^n}{n!} + \cdots$$

(3.14)

Add the equations together and divide by 2, to obtain

$$\Phi_{i,j,k} = \frac{\Phi_{i+1,j,k} + \Phi_{i-1,j,k}}{2} - \left(\frac{\partial^2 \Phi}{\partial x^2}\right)_{i,j,k} \frac{(\Delta x)^2}{2!} + O((\Delta x)^3)$$

$$\rightarrow \Phi_{i,j,k} = \frac{\Phi_{i+1,j,k} + \Phi_{i-1,j,k}}{2} + O((\Delta x)^2)$$

(3.27)

It can be found that the truncation error term $O((\Delta x)^2)$ is presented with the second-order of accuracy.

Another method of interpolation with a lower order of accuracy is known as the Upwind interpolation. The value of the quantity Φ_e is approximated by the value at a neighbouring grid point, and which side should be chosen is dictated by the direction of the flow.

$$\Phi_e = \begin{cases} \Phi_P & if \quad (V \cdot n)_e > 0 \\ \Phi_E & if \quad (V \cdot n)_e < 0 \end{cases}$$

Although the accuracy of this method is relatively low compared with the linear interpolations, it is being widely used due to the boundedness that can be guaranteed with such a method (Hirsch, 2007). A method of blending a high-order linear interpolation and an Upwind interpolation will be introduced in Chapter 4; it achieves both accuracy and boundedness in simulations.

Discretisation of the temporal term

The discretisation of the temporal term is the key feature that decides the unknowns in equations. Assuming the time derivative at point (x_P, t^n) in Eqn. (3.12) is approximated by the forward difference scheme (Eqn. (3.18)), it provides

$$\frac{\Phi_P{}^{n+1} - \Phi_P{}^n}{\Delta t} + \sum_f \Phi_f{}^n (V_f \cdot n)^n S_f - \sum_f (\chi)_f{}^n (\nabla \Phi \cdot n)_f{}^n S_f = Q V_P$$

(3.28)

As Eqn. (3.28) presents, $\Phi_P{}^{n+1}$ is the unknown. The quantities with subscript f represent the value of the quantities at the midpoint of the interface. The quantities with superscript n represent the known values, which are obtained from the solutions in the previous time step. The schemes used to solve such kind of equations are called explicit schemes.

Another situation is to approximate the time derivative at point (x_P, t^{n+1}) by a backward difference scheme (Eqn. (3.19)), the equation is given as

$$\frac{\Phi_P{}^{n+1} - \Phi_P{}^n}{\Delta t} + \sum_f \Phi_f{}^{n+1} (V_f \cdot n)^{n+1} S_f - \sum_f (\chi)_f{}^{n+1} (\nabla \Phi \cdot n)_f{}^{n+1} S_f = Q V_P$$

(3.29)

Different from Eqn. (3.28), Eqn. (3.29) contains a large number of unknown values and it requires implicit schemes for solutions.

In addition to the above discretisation schemes, other schemes with a higher order of accuracy exist in OpenFOAM®, such as **crankNicholson** and **backward** scheme (the back-difference method uses two backward time-steps). However, when concerned with the boundness, efficiency and stability, the Backward-Euler scheme, shown as an example in Eqn. (3.29), is used for the simulations in the present thesis.

3.3.3 Iterative linear equations solver

After discretising the governing equation, the equation composed of known and unknown quantities can be simplified and expressed as the following linearised form.

$$\bar{\bar{A}} \cdot \vec{\phi} = \vec{b}$$

In OpenFOAM®, solvers that solve discrete equations can be divided into two categories: non-symmetric iterative linear solvers and symmetric iterative linear solvers. The former is generally used for the equations containing advection, diffusion or reaction terms. Regarding the iterative linear solvers, these are usually used to solve discrete pressure equations or thermal problems. A brief introduction to these solvers is given below (OpenCFD, 2012).

- **Non-symmetric iterative linear solvers**

    1. Preconditioned Bi-Conjugate Gradient (PBiCG) solver

    2. Gauss-Seidel smoother and the Geometric-Algebraic Multi-Grid (GAMG) solver

    3. Gauss-Seidel smoother solver

- **Symmetric iterative linear solvers**

    1. Preconditioned Conjugate Gradient (PCG) solver

    2. Diagonal Incomplete-Cholesky (DIC) solver

    3. Diagonal Incomplete-Cholesky with Gauss-Seidel smoothers (DICGaussSeidel) solver

    4. Symmetric Gauss-Seidel smoother solver

The preconditioners can be applied to improve the performance of the solvers, they are given as

    1. DIC (symmetric)

    2. Faster Diagonal Incomplete-Cholesky (DIC with caching, FDIC)

    3. Diagonal Incomplete-LU (asymmetric, DILU)

    4. Diagonal

5. GAMG

Depending on the problem, using different solvers will save the computing time of the simulation. Thus, the application of the solvers will be discussed separately in each study case.

3.4 Algorithm of pressure-velocity coupling

Generally, the equations can be solved after the discretisation process, which uses the introduced scheme and is matched with an appropriate solver. However, there is still an important component to be considered when solving the Navier-Stokes equation. Comparing Eqn. (3.12) with the momentum Equation (Eqn. (3.11)), it can be found that an essential term was dropped in Eqn. (3.12). The pressure source term introduces a new unknown term, which is essential for calculation. The unknown value of the pressure and velocities suggests being solved at the same time level in order to guarantee the conservation laws. However, this is hard to achieve due to the limitation of the linear solver. It is necessary to employ an algorithm to solve the pressure-velocity coupling problem.

$$\frac{d}{dt}\int_{\Omega} \rho u_i d\Omega + \int_{S} \rho u_i V \cdot n dS$$

$$= \int_{S} \left[(-p + \lambda \nabla \cdot V) n_i + \sum_{j} \mu \left(\frac{\partial u_i}{\partial x_j} + \frac{\partial u_j}{\partial x_i} \right) n_j \right] dS + \int_{\Omega} \rho f_i d\Omega$$

(3.11)

$$\underbrace{\frac{d}{dt}\int_{\Omega} \Phi d\Omega}_{A} + \underbrace{\int_{S} \Phi V \cdot n dS}_{B} = \underbrace{\int_{S} x\nabla\Phi \cdot n dS}_{C} + \underbrace{\int_{\Omega} Q d\Omega}_{D}$$

(3.12)

3.4.1 Pressure-Implicit with Splitting of Operators (PISO)

In current studies, the simulation of the single-phase flow in a cyclone was solved by the PimpleFoam solver, and the simulations of multi-phase flow problems were processed by the interFoam solver. Both solvers utilise an algorithm that combines the Pressure-Implicit with Splitting of Operators (PISO)method and Semi-Implicit

Method for Pressure-Linked Equations algorithm (SIMPLE) for calculation. The PISO algorithm is a non-iterative method for handling the pressure-velocity coupling of the implicitly discretised fluid flow equations and was introduced by Issa (1984). The principle of the algorithm is given below.

The equations in the predictor step and corrector step are derived from the momentum equation (Eqn. 3.11), and mass conservation equation (Eqn. 3.10), the semi-discretised forms of these equations are presented as

$$\frac{\partial \rho}{\partial t}(u_i^{n+1} - u_i^n) = H(u_i^{n+1}) - \nabla_i P^{n+1} + S_i$$

(3.30)

$$\nabla_i \cdot u_i^{n+1} = 0$$

(3.31)

Where $H(u_i^{n+1})$ represents the spatial convective and diffusive fluxes in the momentum equation.

$$H(u_i^{n+1}) = \sum_f u_{i_f}^{n+1}(u_{i_f} \cdot n)^{n+1} S_f - \sum_f (v)_f^n (\nabla u_i \cdot n)_f^{n+1} S_f$$

(3.32)

The non-linear term in Eqn. (3.32) can be solved by the iteration method or sequential iteration method, which are introduced in the textbook by Zikanov (2010).

The pressure gradient term and the continuity equation are discretised by

$$\nabla_i P^{n+1} = \sum_f (P_f \cdot n)^{n+1} S_f, \qquad \nabla_i \cdot u_i^{n+1} = \sum_f (u_{i_f} \cdot n)^{n+1} \cdot S_f$$

The subscript f presents the value at the mid-point of the cells' face. The operator ∇_i is the finite-difference equivalent of $\frac{\partial}{\partial x_i}$. Term S_i presents the body forces.

It can be found that when taking the divergence of Equation. (3.30) to subtract Equation. (3.31), the pressure equation can be obtained. The corresponding pressure equation is given below.

$$\nabla_i^2 P^{n+1} = \nabla_i H(u_i^{n+1}) + \nabla_i S_i + \frac{\partial \rho}{\partial t} \nabla_i u_i^n$$

(3.33)

Regarding the PISO algorithm, the calculation starts from a predictor step. Eqn. (3.30) can be written in the following form.

$$\frac{\partial \rho}{\partial t}(u_i^* - u_i^n) = H(u_i^*) - \nabla_i P^n + S_i$$

(3.30a)

The pressure field prevailing at t^n is used to calculate u_i^* via Eqn. (3.30a). Through several standard techniques, such as iteration methods, the predicted velocity u_i^* can be obtained. However, this predicted velocity will not satisfy the mass conservation equation. Therefore, the second predicted velocity u_i^{**} is used for the first corrector step. Assuming u_i^{**} satisfies the mass conservation equation, which has

$$\nabla_i u_i^{**} = 0$$

(3.31a)

Then

$$\frac{\partial \rho}{\partial t}(u_i^{**} - u_i^n) = H(u_i^*) - \nabla_i P^* + S_i$$

(3.30b)

The pressure equation derived from Eqn. (3.31a) and Eqn. (3.30b) is given as

$$\nabla_i^2 P^* = \nabla_i H(u_i^*) + \nabla_i S_i + \frac{\partial \rho}{\partial t}\nabla_i u_i^n$$

(3.33a)

This a solvable equation for pressure field P^*. Substituting the values of P^* and u_i^* into equation Eqn. (3.30b), the second predicted velocity u_i^{**} can be yielded. However, this result is not accurate enough. In Issa's paper, a second corrector step was required for a more accurate result, and in OpenFOAM®, the number of the correcting procedures is a user-decided parameter, which can be defined by the keyword **nCorrectors**. The third velocity field with its corresponding new pressure field, P^{**}, is formulated. Again, the new value of the velocity and pressure need to satisfy the momentum equation and mass conservation equation.

$$\nabla_i u_i^{***} = 0$$

(3.31b)

$$\frac{\partial \rho}{\partial t}(u_i^{***} - u_i^n) = H(u_i^{**}) - \nabla_i P^{**} + S_i$$

<div align="right">(3.30c)</div>

P^{**} is calculated by

$$\nabla_i^2 P^{**} = \nabla_i H(u_i^{**}) + \nabla_i S_i + \frac{\partial \rho}{\partial t}\nabla_i u_i^n$$

<div align="right">(3.33b)</div>

Similarly, P^{**} is used to calculate u_i^{***} in equation Eqn. (3.30c).

Compared with the exact solution u_i^{n+1} and P^{n+1}, Issa (1984) proved that the corrected value of the pressure field P^{**} and velocity field u_i^{***} is precise enough.

3.4.2 PISO-SIMPLE (PIMPLE) algorithm

Due to the discretisation in the PISO algorithm not being unconditionally stable, the time step setting is still limited by the Courant number. In order to relieve this limitation, another more advanced algorithm is generated based on the PISO algorithm. The PIMPLE algorithm combines the advantages of the SIMPLE algorithm and the PISO algorithm. It is performed with high efficiency, high accuracy and low computer source cost. The PISO algorithm has been mentioned above. In the case of Semi-Implicit Method for Pressure-Linked Equations (SIMPLE) (Caretto et al. 1972), this is a well-known approach that has been introduced in different textbooks (e.g. Zikanov, 2010). A short summary is given below.

1. Set an initial value for the velocity fields and pressure fields in the whole domain. This initial value can also be obtained from the previous iteration. The value of these quantities is presented as v^m, P^m.

2. Solve Eqn. (3.34) to find the predicted velocity, u^*. This equation is derived from the discretisation form of the momentum equation, it has several different forms, but the principle is the same. The left-hand side represents the discretised nonlinear and viscous terms, and the subscript l denotes all neighbouring cells used by the discretisation formulas. The coefficients α_p and $\alpha_{l,p}$ on the left-hand side represent the functions of velocity u, these could be the convection

term and diffusion term in the momentum equation. The coefficients α_p and $\alpha_{l,p}$ need to be evaluated by the approximations of v^m and P^m.

$$\alpha_p\big(u^{(m)}\big)u_{i,p}^* + \sum_l \alpha_{l,p}\big(u^{(m)}\big)u_{i,l}^* = Q_P\big(u^{(m)}\big) - \left(\frac{\delta P^{(m)}}{\delta x_i}\right)$$

(3.34)

3. Solve the approximate pressure equation (Eqn. (3.35)) to find the pressure corrector, P'. This equation is derived from the continuity equation with an incompressible form. The derivation is given as

$$\alpha_p\big(u^{(m)}\big)u_{i,p}^{m+1} + \sum_l \alpha_{l,p}\big(u^{(m)}\big)u_{i,l}^{m+1} = Q_P\big(u^{(m)}\big) - \left(\frac{\delta P^{(m+1)}}{\delta x_i}\right)$$

(3.34a)

Subtracting Eqn. (3.34) by Eqn. (3.34a), it provides

$$\alpha_p\big(u^{(m)}\big)u_{i,p}' + \sum_l \alpha_{l,p}\big(u^{(m)}\big)u_{i,l}' = -\left(\frac{\delta P^{(\prime)}}{\delta x_i}\right)$$

Where, $u_{i,p}' = u_{i,p}^{m+1} - u_{i,p}^*$, $P_{i,p}' = P_{i,p}^{m+1} - P_{i,p}^m$

In the classical SIMPLE algorithm, the second term on the left-hand side is simply removed, so that it has

$$\alpha_p\big(u^{(m)}\big)u_{i,p}' = -\left(\frac{\delta P^{(\prime)}}{\delta x_i}\right) \rightarrow u_{i,p}' = -\frac{1}{\alpha_p(u^{(m)})}\left(\frac{\delta P^{(\prime)}}{\delta x_i}\right)$$

Taking the above equation into an incompressible continuity equation, the pressure corrector equation can be obtained

$$\left(\frac{\delta u^*}{\delta x_i}\right)_P + \left(\frac{\delta u'}{\delta x_i}\right)_P = 0$$

$$\rightarrow \left(\frac{\delta u^*}{\delta x_i}\right)_P - \frac{\delta}{\delta x_i}\left(\frac{1}{\alpha_p(u^{(m)})}\frac{\delta P'}{\delta x_i}\right) = 0$$

$$\rightarrow \frac{\delta}{\delta x_i}\left(\frac{1}{\alpha_p(u^{(m)})}\frac{\delta P'}{\delta x_i}\right) = \left(\frac{\delta u^*}{\delta x_i}\right)_P$$

(3.35)

4. Update velocity and Pressure fields as

$$u'_{i,P} = -\frac{1}{\alpha_p(u^{(m)})}\left(\frac{\delta P'}{\delta x_i}\right)_P$$

(3.36)

$$u_{i,P}^{(m+1)} = u'_{i,P} + u^*_{i,P}, \qquad P_P^{(m+1)} = P'_{i,P} + P_{i,P}^{(m)}$$

5. The last step is to take the new value back into Step 1 and recycle this loop until the value achieves the convergence criterion. More details can be found in Zikanov (2010).

In the PIMPLE algorithm, the flowing state can be considered as a stable state at the end of each time step. The number of the SIMPLE loops is a user-designed number, which can be changed by the **nOuterCorrectors** keyword. Each SIMPLE loop employs the PISO algorithm to replace the pressure correcting procedure, details of which were previously given in Section 3.4.1. As a result, the PIMPLE algorithm will provide a more accurate simulation result and save computer resources in comparison with the SIMPLE algorithm or PISO algorithm.

3.5 Turbulence model

The turbulence model is the key feature of the governing equations when the Reynolds Averaged Navier-Stokes (RANS) method is implemented. Specifically, the turbulence model is generated to evaluate the Reynolds stress tensor in the Reynolds averaged Navier-Stokes equation. The derivation of the averaged equation is given below.

The flow fields are separated into mean and fluctuating parts

$$u_i = \overline{u_i} + u_i', \;\; p = \overline{P} + p'$$

Recalling the continuity equation in the incompressible form

$$\frac{\partial u_i}{\partial x_i} = 0 \rightarrow \frac{\partial}{\partial x_i}(\overline{u_i} + u_i') = 0$$

(3.37)

The result of averaging Eqn. (3.37) is given by

$$\frac{\partial \overline{u_i}}{\partial x_i} = 0$$

Subtracting Eqn. (3.38) from Eqn. (3.37), the continuity equation for the fluctuating velocity is,

$$\frac{\partial u_i{}'}{\partial x_i} = 0$$

According to the momentum equation, the complete expression is

$$\frac{\partial[\rho(\overline{u_i} + u_i{}')]}{\partial t} + \frac{\partial[\rho(\overline{u_i} + u_i{}')(\overline{u_j} + u_j{}')]}{\partial x_j} = \frac{\partial \tau_{ij}}{\partial x_j} - \frac{\partial(\overline{P} + p')}{\partial x_i}$$

The result of averaging is

$$\frac{\partial(\rho\overline{u_i})}{\partial t} + \frac{\partial(\rho\overline{u_i}\,\overline{u_j})}{\partial x_j} = \frac{\partial}{\partial x_j}\left(\tau_{ij} - \rho\overline{u_i{}'u_j{}'}\right) - \frac{\partial \overline{P}}{\partial x_i}$$

As Eqn. (3.40) presents, the new term $\rho\overline{u_i{}'u_j{}'}$, which is known as the Reynolds stress tensor, is derived from the non-linear convection term. In order to close the system, different turbulence models are designed to approximate this Reynolds stress tensor term.

3.5.1 Eddy viscosity hypothesis

One of the most well-known methods is the Eddy viscosity hypothesis. It is assumed that the turbulent transport depends on the mean velocity gradients in the same way as molecular transport depends on the gradients of the full velocity field (Zikanov, 2010). The expression is given as

$$-\rho\overline{u_i'u_j'} = \mu_t\left(\frac{\partial \overline{u_i}}{\partial x_j} + \frac{\partial \overline{u_j}}{\partial x_i}\right) - \frac{2}{3}\rho k\delta_{ij}$$

Where, δ_{ij} is the Kronecker delta

$$\delta_{ij} = \begin{cases} 1 & if \quad i = j \\ 0 & if \quad i \neq j \end{cases}$$

k is the turbulent kinetic energy, which equals the sum of $\frac{1}{2}\overline{u_i'u_i'}$.

$$k = \frac{1}{2}\overline{u_i'u_i'} = \frac{1}{2}\left(\overline{u_x'u_x'} + \overline{u_y'u_y'} + \overline{u_z'u_z'}\right)$$

Substituting Eqn. (3.41) into Eqn. (3.40), the RANS equations can be transformed into the following form:

$$\frac{\partial(\rho\bar{u}_i)}{\partial t} + \frac{\partial(\rho\bar{u}_i\bar{u}_j)}{\partial x_j} = \frac{\partial}{\partial x_j}\left(2(\mu + \mu_t)\bar{S}_{ij} - \frac{2}{3}\rho k\delta_{ij}\right) - \frac{\partial\bar{P}}{\partial x}$$

(3.42)

From this stage, the turbulence model is employed to evaluate the two unknowns left in Eqn. (3.42), μ_t and k.

- **The $k - \varepsilon$ Two-Equation model**

As one of the most widely used turbulence models, the $k - \varepsilon$ Two-Equation model was used in the simulations of the current thesis. It is generated based on the eddy viscosity hypothesis. The expression of the eddy viscosity is

$$\mu_t = \rho\ell_s V_s.$$

Where ℓ_s is the length scale and V_s is the velocity scale. In the $k - \varepsilon$ model, both of them are evaluated by the turbulent kinetic energy k, and dissipation rate ε.

$$\ell_s = \frac{k^{\frac{3}{2}}}{\varepsilon}, V_s = C_\mu k^{\frac{1}{2}}, \Longrightarrow \mu_t = C_\mu \rho \frac{k^2}{\varepsilon}$$

Where, C_μ is a constant, k and ε can be solved from their transport equations.

The transport equations of the kinetic energy k are derived from the momentum conservation equation;

Subtracting Eqn. (3.40) from Eqn. (3.39), gives the expression of the velocity component u_i'.

$$\frac{\partial(\rho u_i')}{\partial t} + \frac{\partial}{\partial x_k}[\rho(u_i'\overline{u_k} + u_k'\overline{u_i} + u_i'u_k')] = \frac{\partial}{\partial x_k}(\tau_{ik}' + \rho\overline{u_i'u_k'}) - \frac{\partial p'}{\partial x_i}$$

(3.43)

The expression of the velocity component u_j' is presented as

$$\frac{\partial(\rho u_j')}{\partial t} + \frac{\partial}{\partial x_k}\left[\rho\left(u_j'\overline{u_k} + u_k'\overline{u_j} + u_j'u_k'\right)\right] = \frac{\partial}{\partial x_k}\left(\tau_{jk}' + \rho\overline{u_j'u_k'}\right) - \frac{\partial p'}{\partial x_j}$$

(3.44)

In the above equations, indicator $\sum_i$ represents Eqn. (3.43), and $\sum_j$ represents Eqn. (3.44), the transport equation (Eqn. (3.45)) can be obtained by averaging the sum of $u_j'\sum_i + u_i'\sum_j$

$$\frac{\partial\left(\rho\overline{u_i'u_j'}\right)}{\partial t} + \frac{\partial}{\partial x_k}\left(\rho\overline{u_i'u_j'u_k}\right) = P_{ij} + T_{ij} + \Pi_{ij} + D_{ij} - \rho\varepsilon_{ij}$$

(3.45)

Where

$$P_{ij} = -\left(\rho\overline{u_j'u_k'}\frac{\partial\overline{u_i}}{\partial x_k} + \rho\overline{u_i'u_k'}\frac{\partial\overline{u_j}}{\partial x_k}\right)$$

$$T_{ij} = -\frac{\partial}{\partial x_k}\left(\rho\overline{u_i'u_j'u_k'}\right)$$

$$\Pi_{ij} = -\left(\overline{u_j'\frac{\partial p'}{\partial x_i}} + \overline{u_i'\frac{\partial p'}{\partial x_j}}\right)$$

$$D_{ij} = \frac{\partial}{\partial x_k}\left(\overline{u_j'\tau_{ik}'} + \overline{u_i'\tau_{jk}'}\right)$$

$$\rho\varepsilon_{ij} = \overline{\tau_{ik}'\frac{\partial u_j'}{\partial x_k}} + \overline{\tau_{jk}'\frac{\partial u_i'}{\partial x_k}}$$

Rewriting the Eqn. (3.45) with $i = j$, and multiplying by $\frac{1}{2}$, the transport equation for the kinetic energy k can be obtained

$$\rho\underbrace{\frac{Dk}{Dt}}_{A} = \underbrace{\rho\overline{u_i'u_k'}\frac{\partial\overline{u_i}}{\partial x_k}}_{B} - \underbrace{\rho\varepsilon}_{C} + \underbrace{\frac{\partial}{\partial x_k}\left[\mu\left(\frac{\partial k}{\partial x_k}\right)\right]}_{D} + \underbrace{\frac{\partial}{\partial x_k}\left(\rho\frac{\overline{u_i^2u_k}}{2} + \overline{u_k p'}\right)}_{E}$$

(3.46)

the meaning of each term is given below

Term A can be decomposed into $\rho\frac{\partial k}{\partial t} + \rho u_j\frac{\partial k}{\partial x_j}$, which is the transient term and convection term of the kinetic energy k.

Term B is the Production term (P_k) approximated from the eddy viscosity hypothesis.

$$\tau_t = -\rho \overline{u_i' u_j'} = \mu_t \left(\frac{\partial \overline{u_i}}{\partial x_j} + \frac{\partial \overline{u_j}}{\partial x_i} \right) - \frac{2}{3} \rho k \delta_{ij}$$

(3.47)

Term C is the Dissipation term $\rho \varepsilon$, which should be solved by the transport equation of the dissipation rate ε.

Term D is the Molecular diffusion term. Term C and Term D are derived from the last two terms of Eqn. (3.45). (Bailly and Comte-Bellot, 2018).

$$D_{ij} - \rho \varepsilon_{ij} = \frac{\partial}{\partial x_k} \overline{(u_i' \tau_{ik}')} - \overline{\tau_{ik}' \frac{\partial u_i'}{\partial x_k}}$$

Where

$$\tau_{ik}' = 2\mu S_{ik}', \qquad S_{ik}' = \frac{1}{2} \left(\frac{\partial u_i'}{\partial x_k} + \frac{\partial u_k'}{\partial x_i} \right), \qquad \frac{\partial u_i'}{\partial x_i} = 0$$

Thus

$$\frac{\partial}{\partial x_k} \overline{(u_i' \tau_{ik}')} - \overline{\tau_{ik}' \frac{\partial u_i'}{\partial x_k}} = \frac{\partial}{\partial x_k} \left[\mu \left(\frac{\partial k}{\partial x_k} \right) \right] - \mu \overline{\frac{\partial u_i'}{\partial x_k} \frac{\partial u_i'}{\partial x_k}}$$

$$= \frac{\partial}{\partial x_k} \left[\mu \left(\frac{\partial k}{\partial x_k} \right) \right] - \rho \varepsilon$$

The last term is the turbulence diffusion term, which is generated by the turbulent motions. A gradient diffusion model is used for the approximation:

$$\frac{\partial}{\partial x_j} \left(\rho \frac{\overline{u_i^2 u_k}}{2} + \overline{u_k p'} \right) \approx \frac{\partial}{\partial x_j} \left(\left(\frac{\mu_t}{\sigma_k} \right) \frac{\partial k}{\partial x_j} \right)$$

(3.48)

Finally, the modelled transport equation of the kinetic energy k is given below.

$$\frac{Dk}{Dt} = \frac{\partial}{\partial x_j} \left(\left(v + \frac{v_t}{\sigma_k} \right) \frac{\partial k}{\partial x_j} \right) - \underbrace{\overline{u_i' u_j'} \frac{\partial \overline{u_i}}{\partial x_j}}_{P_k} - \varepsilon$$

(3.49)

The production term P_k is modified by the eddy viscosity hypothesis and given as

$$P_k = \overline{u_i'u_j'}\frac{\partial \overline{u_i}}{\partial x_j} = 2v_t\overline{S_{ij}}\frac{\partial \overline{u_i}}{\partial x_j}$$

Regarding the dissipation rate ε, the equation is written as:

$$\frac{D\varepsilon}{Dt} = \frac{\partial}{\partial x_j}\left(\left(v + \frac{v_t}{\sigma_\varepsilon}\right)\frac{\partial \varepsilon}{\partial x_j}\right) + C_1\frac{\varepsilon}{k}P_k - C_2\frac{\varepsilon^2}{k}$$

(3.50)

This equation is also derived from the continuity equation and then simplified by some assumptions; the derivation is given in the Appendix.

Finally, the turbulence viscosity is given by

$$\mu_t = C_\mu\rho\frac{k^2}{\varepsilon}, \mu_t = \rho v_t$$

(3.51)

As can be seen from the above equation, there are some constant coefficients that are used to predict the dissipation rate. The value of these coefficients was provided by the experiments. For instance, the value of C_μ and C_1 was obtained from considering the near-wall flow in a local equilibrium; C_2 was derived from grid generated turbulence (He, 2016). The suggested value of these terms is given below (Launder and Spalding, 1974).

$$C_\mu = 0.09, C_1 = 1.44, C_2 = 1.92, \sigma_k = 1.0, \sigma_\varepsilon = 1.3$$

3.5.2 K-epsilon RNG curvature correction model.

Generally, turbulence models based on the viscosity hypothesis cannot be used to predict the flow field of a large swirling flow accurately. But some modified models are exceptional. One of the available turbulence models called the K-Epsilon RNG Curvature Correction (CC) model, is modified based on the Re-Normalisation Group (RNG) method (Yakhot et al., 1992) and the curvature correction function (Spalart and Shur, 1997; Zhao et al., 2017). The K-Epsilon RNG model is designed to account for the effects of smaller scales of motion. In real situations, the eddy viscosity is not only influenced by the length scale at the specified scale but also needs to evaluate the effects caused by the small scales. Thus, the K-Epsilon RNG

method, using a mathematical technique, improves the standard K-Epsilon model by modifying the production terms. The specific expression is given as

The equation for kinetic energy, k,

$$\frac{Dk}{Dt} = \frac{\partial}{\partial x_j}\left(\left(v + \frac{v_t}{\sigma_k}\right)\frac{\partial k}{\partial x_j}\right) - \underbrace{\overline{u_i'u_j'}\frac{\partial \overline{u_i}}{\partial x_j}}_{P_k} - \varepsilon$$

(3.49)

The equation for dissipation rate, ε,

$$\frac{D\varepsilon}{Dt} = \frac{\partial}{\partial x_j}\left(\left(v + \frac{v_t}{\sigma_\varepsilon}\right)\frac{\partial \varepsilon}{\partial x_j}\right) + C_1\frac{\varepsilon}{k}P_k - C_2{}^*\frac{\varepsilon^2}{k}$$

(3.52)

The difference is shown in the dissipation rate equation such that,

$$C_2{}^* = C_2 + \frac{C_\mu\eta^3(1 - \eta/\eta_0)}{1 + \beta\eta^3}$$

(3.53)

Where, $\eta = S\frac{k}{\varepsilon}$, $S = \left(2S_{ij}S_{ij}\right)^{1/2}$ and $S_{ij} = \frac{1}{2}(\frac{\partial \overline{u_i}}{\partial x_j} + \frac{\partial \overline{u_j}}{\partial x_i})$

The turbulence viscosity is calculated by Eqn. 3.51 given in the standard K-Epsilon model.

Regarding the curvature correction function, this is applied to the production term P_k, and modified as,

$$P_k \rightarrow P_k \cdot f_{ro}$$

Where f_{rot} is the rotation function (Spalart and Shur, 1997) and expressed by

$$f_{rot} = (1 + C_{r1})\frac{2r^*}{1 + r^*}[1 - C_{r3}\arctan(C_{r2}\tilde{r})] - C_{r1}$$

(3.54)

r^* and $\tilde{r}$ are defined as follows:

$$\tilde{r} = 2\omega_{ik}S_{jk}\left(\frac{dS_{ij}}{dt}\right)\frac{1}{\omega D^3}$$

$$r^* = \frac{S}{\omega}$$

48

Where,

$$S_{ij} = \frac{1}{2}\left(\frac{\partial \overline{u_i}}{\partial x_j} + \frac{\partial \overline{u_j}}{\partial x_i}\right),$$

$$\omega_{ij} = \frac{1}{2}\left(\frac{\partial \overline{u_i}}{\partial x_j} - \frac{\partial \overline{u_j}}{\partial x_i}\right),$$

$$S = \left(2S_{ij}S_{ij}\right)^{1/2},$$

$$\omega = \left(2\omega_{ij}\omega_{ij}\right)^{1/2} \text{ and}$$

$$D = \left(\max(S^2, 0.09\omega^2)\right)^{1/2}.$$

The constants C_{r1}, C_{r2} and C_{r3} are obtained by the empirical method and are equal to 1.0, 2.0 and 1.0 (Spalart and Shur, 1997), respectively.

3.5.3 Reynolds Stress Model (RSM)

The Reynolds Stress Model (RSM) is another method, that can be applied to calculate the Reynolds stress term. Different from the eddy viscosity model, the calculation of the Reynolds stress is not processed based on the eddy viscosity hypothesis. The eddy viscosity is not introduced into the governing equations, but the Reynolds stress tensor is calculated by using six Reynolds stress components. The averaged momentum and continuity equations have already been given in the previous section (Eqn. (3.38) and Eqn. (3.40)), Eqn. (3.55) is the expression of the RSM, which is used to close the governing equations.

$$\frac{D\rho\overline{u_i'u_j'}}{Dt} = \frac{\partial\rho\overline{u_i'u_j'}}{\partial t} + \frac{\partial\rho u_k\overline{u_i'u_j'}}{\partial x_k} = P_{ij} + D_{T,ij} + D_{L,ij} + \Phi_{ij} + F_{ij} - \varepsilon_{ij}$$

(3.55)

The derivation of Eqn. (3.51) was also given in the previous section (from Eqn. (3.43) to Eqn. (3.45)). The right-hand sides terms are given as

$$P_{ij} = -\rho\left(\overline{u_i'u_k'}\frac{\partial \overline{u_j}}{\partial u_k} + \overline{u_j'u_k'}\frac{\partial \overline{u_i}}{\partial u_k}\right)$$

$$D_{T,ij} = -\frac{\partial}{\partial x_k}\left(\overline{p(\delta_{ik}u_j' + \delta_{kj}u_i')} + \rho\overline{u_i'u_j'u_k'}\right)$$

$$D_{L,ij} = -\frac{\partial}{\partial x_k}\left(\mu \frac{\partial \overline{u_i'u_j'}}{\partial x_k}\right)$$

$$\Phi_{ij} = \overline{p\left(\frac{\partial u_i'}{\partial x_j} + \frac{\partial u_j'}{\partial x_i}\right)}$$

$$F_{ij} = \rho\Omega_k\left(\overline{u_j'u_m'}e_{ikm} + \overline{u_i'u_m'}e_{jkm}\right)$$

$$\varepsilon_{ij} = 2\mu\overline{\frac{\partial u_i'}{\partial x_k}\frac{\partial u_j'}{\partial x_k}}$$

Where, δ_{ij} is the Kronecker delta

$$\delta_{ij} = \begin{cases} 1 & if \quad i = j \\ 0 & if \quad i \neq j \end{cases}$$

Ω_k is the rotation vector, and $e_{jkm} = 1$ if i, j, k are different and in cyclic order; $e_{jkm} = -1$ if i, j, k are different and in anti-cyclic order; and $e_{jkm} = 0$ if any two indices are the same.

It can be found from the above equations that Eqn. (3.55) is similar to Eqn. (3.45). The difference is caused by the rearrangement and adding a new user customised term F_{ij} into Eqn. (3.55). The meaning of each term is given below;

P_{ij} : represents the stress production

$D_{T,ij}$: is the turbulent diffusion term

$D_{L,ij}$: is the molecular diffusion term

Φ_{ij} : is the pressure-strain term

F_{ij} : is the rotation production term

ε_{ij} : represents the dissipation term

The value of the dissipation, ε_{ij}, pressure-strain, Φ_{ij}, and turbulent diffusion, $D_{T,ij}$, cannot be obtained directly. Therefore, they are approximated by modelled equations. The linear-strain model is used to calculate the pressure-strain term

$$\Phi_{ij} = \Phi_{ij,1} + \Phi_{ij,2}$$

(3.56)

Where $\Phi_{ij,1}$ represents the slow pressure-strain and it is modelled as

$$\Phi_{ij,1} = -\rho C_1 \frac{\varepsilon}{k} \left(\overline{u_i' u_j'} - \frac{1}{3} \overline{u_k' u_k'} \delta_{ij} \right)$$

(3.57)

k represents the kinetic energy; the expression is given as

$$k = \frac{1}{2} \rho \overline{u_i' u_i'}$$

$\Phi_{ij,2}$ represents the rapid pressure-strain term, and it is modelled as

$$\Phi_{ij,2} = -\rho C_2 \left(P_{ij} - \frac{1}{3} P_{kk} \delta_{ij} \right)$$

(3.58)

The closure equation for the viscous dissipation term is:

$$\frac{D\varepsilon}{Dt} = \frac{\partial}{\partial x_j} \left(\left(v + C_\mu \frac{k^2}{\varepsilon \sigma_\varepsilon} \right) \frac{\partial \varepsilon}{\partial x_j} \right) + C_{1\varepsilon} \frac{\varepsilon}{k} \overline{u_i' u_j'} \frac{\partial \overline{u_i}}{\partial x_j} - C_{2\varepsilon} \frac{\varepsilon^2}{k}$$

(3.59)

The constant coefficients in the above equations are equal to

$$C_1 = 1.8, \ C_2 = 0.6, \ C_\mu = 0.09, \ C_{1\varepsilon} = 1.44, \ C_{2\varepsilon} = 1.92, \ \sigma_\varepsilon = 1.3$$

The modelled equation of the turbulent diffusion is given as

$$D_{T,ij} = \frac{\partial}{\partial x_k} \left[\frac{C_\mu}{\sigma_k} \frac{k^2}{\varepsilon} \frac{\partial \overline{u_i' u_j'}}{\partial x_k} \right]$$

(3.60)

3.5.4 Large-Eddy Simulation (LES) model

The large eddy simulation (LES) method has made much progress accompanied by the advent of the high-performance computer being widely used. Compared with most turbulence models in RANS methods, models in LES method has higher accuracy, and for the fluid in cyclones, the characteristic of anisotropy can also be correctly captured. Thus, it is worth exploring the performance of the LES model in the current simulation.

The LES method directly calculates the mean flow and the unsteady large-scale and intermediate-scale motions. The effect of small-scale fluctuations on the small eddies is modelled (Zikanov, 2010). In OpenFOAM®, the filter used to distinguish the scale of eddies is called the Top-hat filter. It is equivalent to a box filter and the equation is given as

$$G(r) \begin{cases} 1/\Delta & if \quad r < 1/2 \\ 0 & if \quad r > 1/2 \end{cases}$$

(3.61)

Where, Δ is the filter width of eddies.

The filtered velocity can be obtained by

$$\bar{u}(x,t) = \int G(r,x)u(x-r,t)dr$$

(3.62)

And the filtered incompressible Navier-Stokes equation is

$$\frac{\partial(\rho\bar{u}_i)}{\partial t} + \frac{\partial(\rho\bar{u}_i\bar{u}_j)}{\partial x_j} = \mu\nabla^2\bar{u}_i - \frac{\partial\tau_{ij}}{\partial x_j} - \frac{\partial\bar{P}}{\partial x_i}$$

(3.63)

Where, $\tau_{ij} = \rho\overline{u_i u_j} - \rho\bar{u}_i\bar{u}_j$ is the subgrid scale stress tensor.

A subgrid-scale (SGS) kinetic energy-based model was used to simulate the fields in small eddies, introduced by Yoshizawa and Horiuti (1985; 1986). The model's expressions are given below. (Fumiya, 2016)

The subgrid scale stress tensor τ_{ij} can be approximated by

$$\tau_{ij} \approx \frac{2}{3}k_{sgs}\delta_{ij} - 2v_{sgs}dev(\bar{D})_{ij}$$

(3.64)

Where, v_{sgs} is the subgrid scale eddy viscosity, $(\bar{D})_{ij}$ is the resolved-scale strain rate tensor, which is defined as

$$(\bar{D})_{ij} = \frac{1}{2}\left(\frac{\partial\bar{u}_i}{\partial x_j} + \frac{\partial\bar{u}_j}{\partial x_i}\right)$$

And δ_{ij} is the Kronecker delta.

The subgrid scale kinetic energy k_{sgs} is

$$k_{sgs} = \frac{1}{2}\tau_{kk} = \frac{1}{2}(\overline{u_k u_k} - \bar{u}_k \bar{u}_k)$$

(3.65)

The subgrid scale eddy viscosity is calculated using k_{sgs}.

$$v_{sgs} = C_k \sqrt{k_{sgs}}\Delta$$

(3.66)

Where C_k is a constant with the default value of 0.094 in OpenFOAM®. Δ is the length scale of the subgrid width.

The procedure so far is the same as the Smagorinsky SGS model but there is a difference in the subsequent calculation steps. The method of computing the value of the kinetic energy k_{sgs} becomes a challenge for these models. The Smagorinsky model assumes the local equilibrium to compute k_{sgs} but the one equation eddy viscosity model provides a value by solving the transport equation of k_{sgs} (Huang and Li, 2010).

The remaining transport equation of the subgrid scale kinetic energy k_{sgs} is used to close the model. It is derived to account for the historic effect of k_{sgs} due to production, diffusion and dissipation. The expression is given as

$$\frac{\partial(\rho k_{sgs})}{\partial t} + \frac{\partial(\rho k_{sgs})}{\partial x_j} - \frac{\partial}{\partial x_j}\left[\rho(v + v_{sgs})\frac{\partial k_{sgs}}{\partial x_j}\right] = -\rho\tau_{ij}(\bar{D})_{ij} - C_\varepsilon\frac{\rho k_{sgs}^{3/2}}{\Delta}$$

(3.67)

Where C_ε is a constant equal to 1.048. The meaning of each term in Eqn. 3.67, from left to right, is the time derivative term, convection term, diffusion term, production term, and dissipation term.

The expression of the production term $-\rho\tau_{ij}(\bar{D})_{ij}$ can be rearranged into

$$-\rho\tau_{ij}(\bar{D})_{ij} = \left(-\frac{2}{3}\rho k_{sgs}\delta_{ij} + 2\rho v_{sgs}dev(\bar{D})_{ij}\right)(\bar{D})_{ij}$$

$$= -\frac{2}{3}\rho k_{sg}\frac{\partial\bar{u}_k}{\partial x_k} + \rho v_{sgs}\frac{\partial\bar{u}_i}{\partial x_j}\left(2\bar{D}_{ij} - \frac{1}{3}tr(2\bar{D}_{ij})\delta_{ij}\right)$$

(3.68)

In addition to the above equations, another important setup for the LES method is the filtered function (OpenFOAM®, 2018). The Van Driest filtered function was used to filter the length scale for the subgrid and is given as

$$D = 1 - \exp\left(\frac{-y^+}{A^+}\right)$$

The final length scale is given by:

$$\Delta = \min\left(\frac{\kappa y}{C_s} D, \Delta_g\right)$$

(3.69)

Where Δ_g is a geometric-based delta function, which is approximated by the cube-root volume delta.

$$\Delta_g = c(V_c)^{\frac{1}{3}}$$

The default value of the coefficients is given as

$$c = 1, A^+ = 26, \kappa = 0.41, C_s = 0.158$$

Such a filtered function has been used in the current simulation due to the size of the near wall cell and cell aspect ratio not being strictly limited (OpenFOAM®, 2018).

3.6 Discrete phase model

The Lagrangian Discrete Phase Model (DPM) is a method, that can be used to solve problems including particle separation and classification, spray drying, aerosol dispersion, bubble stirring of liquids, liquid fuel combustion, and coal combustion (Fluent, 2001). For the current study, it was used to evaluate the collection efficiency of the cyclone and hydrocyclone. The procedure for setting up and solving a steady-state discrete phase problem is given as

1. Solve the continuous-phase flow.

2. Create the discrete-phase injections.

3. Solve the coupled flow, if desired.

4. Track the discrete-phase injections, using plots or reports.

The trajectory of a discrete phase particle is predicted by integrating the force implemented on the particle, which is derived in a Lagrangian reference frame. The equilibrium equation represents the balance between the particle inertia and the force acting on the particle, which can be written as

$$\frac{\partial u_p}{\partial t} = F_D\big(u - u_p\big) + \frac{g_x(\rho_p - \rho)}{\rho_p} + F_x$$

<div align="right">(3.70)</div>

Where $F_D\big(u - u_p\big)$ is the drag force per unit particle mass and can be evaluated by

$$F_D = \frac{18\mu}{\rho_p d_p^2} \frac{C_D Re}{24}$$

<div align="right">(3.71)</div>

In the above equations, the subscript p represent the properties of the particle. u is the fluid phase velocity, u_p is the particle velocity, μ is the viscosity of the fluid. ρ is the density of fluid, ρ_p is the density of the particle. d_p is the particle diameter, and g_x is the gravitational acceleration.

The relative Reynolds number, Re is calculated by

$$Re \equiv \frac{\rho d_p |u_p - u|}{\mu}$$

There are several kinds of method to evaluate the drag coefficient, C_D, and in the present work, the formula that accounts for smooth spherical particles (Morsi and Alexander, 1972) was applied to calculate the drag coefficient, C_D.

$$C_D = a_1 + \frac{a_2}{Re} + \frac{a_3}{Re^2}$$

<div align="right">(3.72)</div>

The value of the constant a_1, a_2 and a_3 is given by Morsi and Alexander (1972) and listed in Table 3.1.

The second term on the right-hand side of Eqn. 3.67 represents the force generated by the gravitational acceleration. It is assumed to be $g_x = 9.81$ in the axial downward direction.

The last term on the right-hand side of Eqn. 3.68 represents other forces that may influence the flowing behaviour of the particles. In the current simulations, since the mass fraction of the particles in the continuous phase is sufficiently low, the other forces have not been considered.

Table 3.1 Constants for the equation of drag coefficient

Re	a_1	a_2	a_3
< 0.1	0	24	0
$0.1 - 1$	3.69	22.73	0.0903
$1 - 10$	1.222	29.1667	-3.8889
$10 - 100$	0.6167	46.5	116.67
$100 - 1000$	0.3644	98.33	-2778
$1000 - 5000$	0.357	148.62	-4.75E4
$5000 - 10000$	0.46	-490.546	57.87E4
$10000 - 50000$	0.5191	-1662.5	5.4167E6

Chapter 4. The Volume of Fluid method

In simulations of multi-phase flow, the volume of fluid (VOF) method is generally used for capturing the free-surface between fluids. Although this method can be classified as a Surface Capturing technique, it is different from the Surface Tracking methods, in which free-surface is tracked by the mesh. A phase fraction function is applied to approximate the position of the free-surface in the VOF method (Carrica et al., 2006). Therefore, this chapter focuses on presenting the derivation of the VOF method, and introduces the High-Resolution Schemes (HRS) and the Flux Corrected Transport (FCT) technique used by the OpenFOAM® platform for the new approach to VOF based interface capturing methods.

4.1 Phase fraction function

The phase fraction function is derived from the mass conservation equation. The first step is conceiving a physical domain constituted of a liquid-phase region, R_l and a gas phase region, R_g. The assumption indicates an indicator α, which is given as

$$\alpha(x,t) = \begin{cases} 1 & if \quad x \in R_l \text{ at time } t \\ 0 < \alpha < 1 & if \quad x \in R_{l,g} \text{ at time } t \\ 0 & if \quad x \in R_g \text{ at time } t \end{cases}$$

(4.1)

This function has the characteristic of singular nature. It is appropriate to introduce the integration form of this quantity for the discretisation over the volume corresponding to a computational cell (Ω_i) (Deshpande, 2012). The integration provides a liquid fraction field given by

$$\gamma(x_i,t) = \frac{1}{|\Omega_i|} \int_{\Omega_i} \alpha(x,t) \, dV$$

(4.2)

As a result, this fraction (Eqn. 4.2) equals one when the cells are completely liquid, and equals zero when the cells are completely gas.

The continuity equation based on the conservation of mass is presented as

$$\frac{\partial \rho}{\partial t} + \frac{\partial \rho u}{\partial x} + \frac{\partial \rho v}{\partial y} + \frac{\partial \rho w}{\partial z} = 0$$

$$\frac{\partial \rho}{\partial t} + \nabla \cdot (U\rho) = 0$$

(3.1)

The density fields in Eqn. (3.1) can be modified by adding the indicator function $\alpha(x,t)$

$$\rho(x,t) = \rho_l \alpha(x,t) + \rho_g [1 - \alpha(x,t)]$$

(4.3)

Where, ρ_l is the density of the liquid phase, ρ_g is the density of the gas phase. For the incompressible flow, both of them are constant.

Taking Eqn. (4.3) back to Eqn. (3.1) and replacing the density field, the expression is shown as

$$(\rho_l - \rho_g)\frac{\partial \alpha(x,t)}{\partial t} + \nabla \cdot [(\rho_l - \rho_g)\alpha(x,t)U(x,t)] + \rho_g \nabla \cdot U(x,t) = 0$$

(4.4)

For the incompressible flow, the last term on the left-hand side can be ignored because of $\nabla \cdot U(x,t) = 0$

Integrating Eqn. (4.4) over the computational cell (Ω_i), the equation of a divergence-free flow field is given as

$$\int_{\Omega_i} (\rho_l - \rho_g)\frac{\partial \alpha(x,t)}{\partial t} dV + \int_{\Omega_i} \nabla \cdot [(\rho_l - \rho_g)\alpha(x,t)U(x,t)] dV = 0$$

(4.5)

Applying the definition of the liquid fraction field from Eqn. (4.2), Eqn. (4.5) can be rewritten as

$$\frac{\partial \gamma}{\partial t} + \nabla \cdot (U\gamma) = 0$$

(4.6)

Eqn. (4.6) is the equation of the phase fraction; it is the key feature of the VOF method. However, this equation is not used directly for calculations in OpenFOAM®,

as it needs to be optimised by the HRS and the FCT technique in order to provide better results for simulations.

4.2 Flux corrected transport

In the solution of the phase fraction equation (see Eqn. (4.6)), the characteristic of boundedness needs to be guaranteed. The Flux Corrected Transport (FCT) technique introduced by Boris and Book (1973) is one of the methods that can be applied to achieve such a requirement. Later, the FCT technique was optimised by Zalesak (1979). The application of Zalesak's limiter provides a genuinely multi-dimensional high-resolution scheme (Márquez Damián, 2013).

4.2.1 Theoretical foundation

Rewriting Eqn. (4.6) to the general form by replacing the phase fraction γ with a transported quantity ϕ.

$$\frac{\partial \phi}{\partial t} + \nabla \cdot \vec{F} = 0$$

(4.7)

Where $\vec{F}$ is the flux of the transported quantity ϕ, it can be a linear or nonlinear function of ϕ.

Applying the explicit discretisation scheme for the temporal term (e.g. Eqn. (3.28)), the solution of Eqn. (4.7) is given as

$$\frac{\phi_i^{n+1} - \phi_i^{n}}{\Delta t} V + \sum_f \left(\vec{F}^n \cdot \vec{S}\right)_f = 0$$

(4.8)

Where the subscript i: represents the index of the analysed cell

The superscript n: represents the index of the temporal steps

V: is the volume of the cell.

f: is the index of the i's cell face.

$\vec{S}$: represents the face area vector for the f-th face of the cell i.

Rearranging Eqn. (4.8) by moving the variables with superscript n to the right of the equation, the expression in a one-dimensional equidistant grid is given as,

$$\phi_i{}^{n+1} = \phi_i{}^n - \frac{\Delta t}{V}\left(F_{i+1/2}^n - F_{i-1/2}^n\right)$$

<div align="right">(4.9)</div>

Where $F^n = \left(\vec{F}^n \cdot \vec{S}\right)_f$ is the total flux which depends on the transportive effect of the velocity.

The value of the quantity ϕ at a cell's faces is the key feature that influences the value of the flux F^n. In order to guarantee the boundedness of the temporal solution, modifications can be imposed on the value at a cell's faces or on the face fluxes. For the latter situation, the values of the face fluxes are obtained by combining the solution of the low-order method with the solution of the higher-order method. The low-order method guarantees boundedness and the high-order method guarantees accuracy. The details described by Zalesak (1979) are given below.

1. Compute the transportive flux F^L by a low-order monotonic scheme.

2. Compute the transportive flux F^H by a high-order scheme.

3. Define the anti-diffusive fluxes as $A = F^H - F^L$.

4. Compute the corrected flux $F^C = F^L + \lambda A$, where the weighting factor $0 \le \lambda \le 1$.

5. Solve the equation (e.g. Eqn. (4.9)) by substituting the corrected flux for the original flux.

$$\phi_i{}^{n+1} = \phi_i{}^n - \frac{\Delta t}{V}\left(F_{i+1/2}^C - F_{i-1/2}^C\right)$$

<div align="right">(4.10)</div>

As can be found from the above procedures, the weighting factor λ is the key feature that determines the proportion of the anti-diffusive fluxes. Two extreme situations exist. When $\lambda = 0$, the solution of the equations is obtained by low-order schemes. Conversely, with $\lambda = 1$, the solution is obtained by high-order schemes. The value of the weighting factor is not indicated arbitrarily during calculations. The corrected flux, calculated by the factor needs to satisfy both the boundedness of low-order methods and accuracy of high-order methods.

4.2.2 Zalesak's weighting factor

Further expanding Eqn. (4.10) can be achieved by substituting the expression of the corrected flux F^C into the equation.

$$
\begin{aligned}
\phi_i{}^{n+1} &= \phi_i{}^n - \frac{\Delta t}{V}\left(F^L_{i+1/2} - F^L_{i-1/2}\right) - \frac{\Delta t}{V}\left(\lambda_{i+1/2}A_{i+1/2} - \lambda_{i-1/2}A_{i-1/2}\right) \\
&= (\phi_i^L)^n - \frac{\Delta t}{V}\left(\lambda_{i+1/2}A_{i+1/2} - \lambda_{i-1/2}A_{i-1/2}\right)
\end{aligned}
$$

(4.10)

From Eqn. (4.10) it can be found that the value at time $n+1$ is calculated by two steps. The first step is to estimate the solutions by low-order schemes, and the second step is to add the anti-diffusive flux corrected by the appropriate weighting factor into the equation. However, such a method will produce the risk of unboundedness due to the anti-diffusive flux in the second step. Given this, a new maximum may be created by the inflow and the minimum by the outflow. In order to guarantee the boundedness, the correcting procedure is given as:

1. Defining $P_i^\pm$ represents the flux of inflows and outflows for A

$$
P_i^+ = -\sum_f \left(A_f^-\right), \qquad P_i^- = \sum_f \left(A_f^+\right)
$$

(4.11)

Where A_f^- are the inflows and A_f^+ are the outflows.

2. Defining $Q_i^\pm$ represents the net fluxes limited by the local maximum and minimum.

$$
Q_i^+ = \frac{V}{\Delta t}\left(\phi_i{}^{max} - \phi_i^L\right), \qquad Q_i^- = \frac{V}{\Delta t}\left(\phi_i^L - \phi_i{}^{min}\right)
$$

(4.12)

The relationship between $P_i^\pm$ and $Q_i^\pm$ is shown in Fig. 4.1.
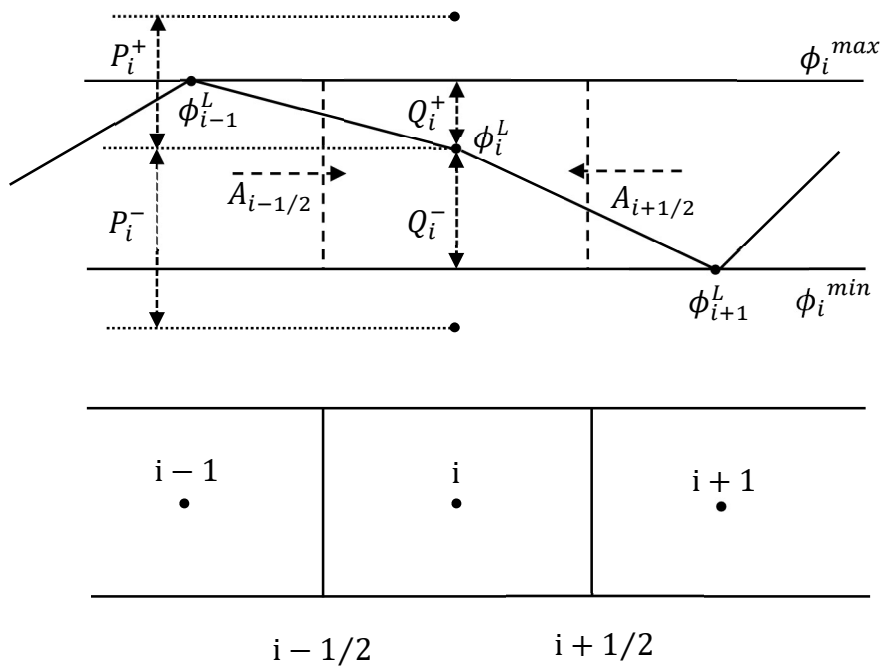
Fig. 4.1. One dimensional geometry and magnitudes for Zalesak's limiter.

(Kuzmin et al., 2003)

Considering fluid flowing through a cell, it has the following situations

- Case 1

  If $P_i^{\pm} = 0$, then it has $\phi_i^{n+1} = (\phi_i^L)^n$, the fluxes do not need to be corrected, and $\lambda_i^{\pm} = 0$.

- Case 2

  If $P_i^{\pm} > 0$, then it means $\phi_i^{n+1} \neq (\phi_i^L)^n$, the anti-diffusive flux is created at the boundaries; the solutions of low-order schemes need to be corrected.

  Because the basic rule of flux correction is to ensure boundedness, then $Q_i^{\pm}$ represents the maximum and minimum anti-diffusive fluxes that can be employed for corrections, as such, it has

  1. $Q_i^{\pm} > P_i^{\pm}$, which means if the corrected value of anti-diffusive flux is within the range, then the solutions will be corrected by $P_i^{\pm}$

  2. $Q_i^{\pm} < P_i^{\pm}$, which means if the corrected value of anti-diffusive flux exceeds the range, then the solutions will be corrected by $Q_i^{\pm}$

These cases can be summarised in an expression

$$\lambda_i^{\pm} = \begin{cases} \min\{1, Q_i^{\pm}/P_i^{\pm}\}, & if\ P_i^{\pm} > 0 \\ 0, & if\ P_i^{\pm} = 0 \end{cases}$$

(4.13)

The weighting factor λ on a cell's faces (e.g. $\lambda_{i+1/2}$) is estimated by taking the value of the weighting factor at the centre of neighbouring cells (e.g. $\lambda_i^{\pm}$ or $\lambda_{i+1}^{\pm}$). For the purpose of guaranteeing boundedness, the smaller value will be applied for calculations.

$$\lambda_{i+1/2} = \begin{cases} \min\{\lambda_{i+1}^+, \lambda_i^-\}, & if\ A_{i+1/2} \geq 0 \\ \min\{\lambda_{i+1}^-, \lambda_i^+\}, & if\ A_{i+1/2} < 0 \end{cases}$$

(4.14)

Finally, as Eqn. (4.12) presented, the local maximum and minimum must be defined for the solution of the equation. Zalesak (1979) provided a straightforward method:

$$\begin{aligned} \phi_i{}^a &= \max{(\phi_i{}^n, \phi_i{}^L)} \\ \phi_i{}^{max} &= \max{(\phi_{i-1}{}^a, \phi_i{}^a, \phi_{i+1}{}^a)} \\ \phi_i{}^b &= \min{(\phi_i{}^n, \phi_i{}^L)} \\ \phi_i{}^{min} &= \min{(\phi_{i-1}{}^b, \phi_i{}^b, \phi_{i+1}{}^b)} \end{aligned}$$

(4.15)

The solution obtained by the above calculations will ensure both boundedness and higher accuracy. Based on the FCT technique provided by Zalesak (1979), some modifications are implemented for OpenFOAM®'s operation.

4.2.3 OpenFOAM®'s weighting factors

The modified FCT technique applied by OpenFOAM® is called MULES (Multi-dimensional Universal Limiter for Explicit Solution). Based on Zelasak's theory, the modification is implemented focused on the calculation of weighting factors λ; an iterative method is used to find the appropriate weighting factors. Another improvement is the introduction of the global extrema, which is a parameter set by the user and is critical for the simulation of multi-phase flows. The procedures of

the MULES solver are summarized by Márquez Damián (2013) and presented in List 4.1.

When calculating the weighting factors of the MULES solver, the net flux of each cell is taken into account. More specifically, different from Zelasak's limiter, the maxima and minima are not only determined by inflows and outflows, respectively. Based on this conservative assumption, both outflows and inflows are used to calculate the limiters for the maxima and minima. It can be proved that when inflows or outflows are insignificant, the values of the weighting factors calculated by the MULES solver will converge to values approximate to Zalesak's ones.

List 4.1 Steps for the MULES solver

---

1. Calculating the local extrema by

$$\phi_i{}^a = \max\left(\phi_i{}^n, \phi_{i,N}{}^n\right)$$

$$\phi_i{}^b = \min\left(\phi_i{}^n, \phi_{i,N}{}^n\right)$$

Where, subscript i, N represent the neighbouring cells adjacent to each face of the $i - \mathbf{th}$ cell.

2. Calculating the inflows and outflows for each cell by Eqn. (4.11)

$$P_i^+ = -\sum_f \left(A_f^-\right), \qquad P_i^- = \sum_f \left(A_f^+\right)$$

(4.11)

Where A_f^- are the inflows and A_f^+ are the outflows.

3. Further narrowing the range of extreme values by introducing user-defined global extrema ϕ^{maxG} and ϕ^{minG}

$$\phi_i{}^{a+1} = \min(\phi^{maxG}, \phi_i{}^a), \qquad \phi_i{}^{b+1} = \max\left(\phi^{minG}, \phi_i{}^b\right)$$

4. Calculating $Q_i^{\pm}$ by

$$Q_i^+ = \frac{V}{\Delta t}\left(\phi_i{}^{a+1} - \phi_i{}^n\right) + \sum_f \left(F_f^L\right), \qquad Q_i^- = \frac{V}{\Delta t}\left(\phi_i{}^n - \phi_i{}^{b+1}\right) - \sum_f \left(F_f^L\right)$$

(4.12)

---

5. Calculating the weighting factor λ on a cell's faces by iterative methods. The number of loops is controlled by **nLimiterIter**, which is a user-defined parameter. At the first iteration step, setting the weighting factor $\lambda_f^{v=1} = 1$ for all faces, the calculation starts with

$$\lambda_{\mp i}^{v+1} = \max\left[\min\left(\frac{\pm\sum_f \lambda_f^{v} A_f^{\pm} + Q_i^{\pm}}{P_i^{\pm}}, 1\right), 0\right]$$

$$\lambda_f^{v+1} = \begin{cases} \min\{\lambda_P^+, \lambda_N^-\}, & \textit{if } A_{i+1/2} \geq 0 \\ \min\{\lambda_P^-, \lambda_N^+\}, & \textit{if } A_{i+1/2} < 0 \end{cases}$$

(4.16)

Similar to Zalesak's limiter, subscript P and N represent the current cell and the neighbouring cell; f represents the shared face of the two cells.

4.3 High-Resolution Schemes Implementation

As Eqn. (4.9) presented, the value of the unknown quantity ϕ_i^{n+1} is calculated by the already known value of the fluxes on cell faces (e.g. $F_{i+1/2}^C$, $F_{i-1/2}^C$). Section 3.3.2 introduced the schemes for calculating these face values. The upwind interpolation method has the characteristic of guaranteed boundedness, but it has only first-order of accuracy. The centre liner interpolation scheme presents second-order accuracy but cannot assure the boundedness when it is used with Courant numbers beyond unity and with high Peclet numbers (Márquez Damián, 2013). As a solution to such a predicament, the High-Resolution Schemes (HRS) is implemented to guarantee boundedness and to work with a higher order of accuracy than first-order schemes. The derivation of the HRS begins with the expression of the basic schemes. Recalling the expression of the linear interpolation method in Section 3.3.2.

$$\Phi_f = f_{xCI}\Phi_P + (1 - f_{xCI})\Phi_N$$

(4.17)

Where $f_{xCI} = d\overline{fN}/d\overline{PN}$ is the weighting factor for linear interpolation. $d\overline{fN}$ and $d\overline{PN}$ are the distance between each point as shown in Fig. 4.2.
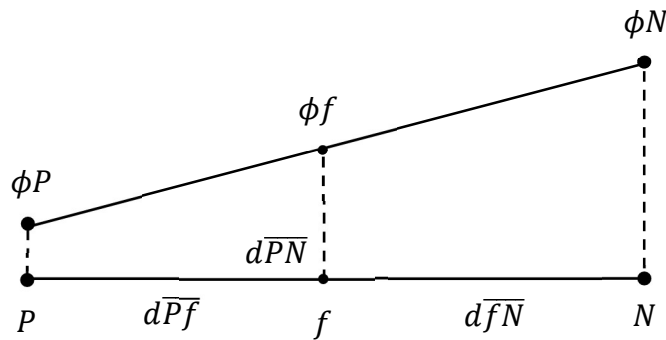

Fig. 4.2. One-dimensional sketches of linear interpolation method.

Assuming P and N are located at the centre of the cells and the distance to the shared face is equal. Eqn. (4.17) can be rearranged to

$$\Phi_{fCI} = f_{xCI}(\Phi_P - \Phi_N) + \Phi_N$$

(4.18)

As presented by Eqn. (4.18), the same expression can be used for upwind interpolation method. This is achieved by defining the weighting factor f_{xUI} equals 1 or 0 (depends on the flowing directions.). As a result,

$$\Phi_{fUI} = \begin{cases} \Phi_P & if \quad (V \cdot n)_f \geq 0 \\ \Phi_N & if \quad (V \cdot n)_f < 0 \end{cases}$$

(4.19)

Combining Eqn. (4.18) and Eqn. (4.19) to obtain the new Blending Interpolation scheme, is written as

$$\Phi_f = (1 - \gamma)\Phi_{fUI} + \gamma\Phi_{fCI}$$

(4.20)

Where γ is the blending factor adjusting the proportion of the solutions based on the upwind interpolation and the centre linear interpolation. Substituting Eqn. (4.18) and Eqn. (4.19) into Eqn. (4.20), it provides,

$$\Phi_f = [(1 - \gamma)f_{xUI} + \gamma f_{xCI}](\Phi_P - \Phi_N) + \Phi_N$$

(4.21)

Simplifying the equation by defining $\lambda = (1 - \gamma)f_{xUI} + \gamma f_{xCI}$,

$$\Phi_f = \lambda(\Phi_P - \Phi_N) + \Phi_N$$

(4.22)

The blending factor γ in the expression of the limited weighting factor λ can be approximated by a constant (Ferziger and Peric, 2002) or calculated on a local basis using a limiter function. The High-Resolution Schemes created based on Total Variation Diminishing (TVD) schemes (Harten. 1983) or Normalized Variable Diagram (NVD) (Leonard, 1991) schemes are used for the solution of the limiter function.

4.3.1 Examples of TVD and NVD

In the operation of OpenFOAM®, the solution of the HRS is implemented based on the TVD schemes. Thus, the schemes created based on the NVD diagram have to be transferred into TVD form. It is necessary to illustrate this transformation by presenting examples of TVD and NVD schemes.

Similar to Eqn. (4.22), Darwish and Moukalled (2003) provided an equation to evaluate the face value.

$$\Phi_f = \frac{1}{2}\psi(r_f)(\Phi_P - \Phi_N) + \Phi_N$$

(4.23)

It can be found that the difference between Eqn. (4.22) and Eqn. (4.23) is that the limited weighting factor λ is replaced by the Sweby's function $\lambda = \frac{1}{2}\psi(r_f)$ (Sweby, 1984). In the case of TVD limiter, the value of the function depends on the ratio of consecutive gradients of the solution r_f, which is given as

$$r_f = \frac{\Phi_P - \Phi_U}{\Phi_N - \Phi_P}$$

(4.24)
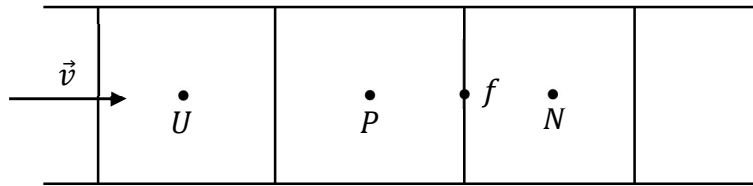
Fig. 4.3. One dimensional schematic of the mesh with neighbour cells and face f.

Distributions of the points are presented in Fig. 4.3.

A better expression of the ratio of consecutive gradients is given by Darwish and Moukalled (2003). This expression, shown in Eqn. (4.25), can be applied to simulations that employ unstructured meshes

$$r_f = \frac{2\vec{\nabla}\Phi_P \cdot \vec{d}_{PN}}{\Phi_N - \Phi_P} - 1$$

(4.25)

Where $\vec{\nabla}\Phi_P$ is the gradient of Φ in a given cell.

In terms of NVD schemes, multiple expressions of the consecutive gradient are used to calculate the NVD functions. They are expressed in the following equations. (Leonard, 1991; Jasak et al., 1999)

$$\widetilde{\Phi}_C = \frac{\Phi_P - \Phi_U}{\Phi_N - \Phi_U}, \qquad \widetilde{\Phi}_f = \frac{\Phi_f - \Phi_U}{\Phi_N - \Phi_U}$$

(4.26)

These variables are related by the NVD functions as $\widetilde{\Phi}_f = f(\widetilde{\Phi}_C)$, where $f(\widetilde{\Phi}_C)$ is a function applied in the NVD diagram. As mentioned at the start of this section, the limited weighting factor cannot be calculated directly by the NVD diagram; a transformation is required to translate the limiter expression in terms of r_f and $\psi(r_f)$. An equivalence formula given by Hirsch (2007) is expressed as

$$\widetilde{\Phi}_f = \left[1 + \frac{1}{2}\psi'(r')\right]\widetilde{\Phi}_C \rightarrow \frac{1}{2}\psi'(r') = \frac{\widetilde{\Phi}_f}{\widetilde{\Phi}_C} - 1$$

(4.27)

Where r' is defined as

$$r' = \frac{\Phi_N - \Phi_P}{\Phi_P - \Phi_U}$$

(4.28)

$\psi'(r')$ represents the expression of the Sweby's function of a limited weighting factor in terms of r'. A conversion equation introduced by Darwish and Moukalled (2003) is applied to replace $\psi'(r')$ by $\psi(r_f)$

$$\frac{1}{r'}\psi'(r') = \psi(r_f)$$

(4.29)

Substituting Eqn. (4.27) into Eqn. (4.29), gives

$$\psi(r_f) = 2\frac{\frac{\widetilde{\Phi}_f}{\widetilde{\Phi}_C} - 1}{r'}$$

(4.30)

In Hirsch (2007), the expression of the ratio of consecutive gradients r' is given as

$$r' = \frac{1}{\widetilde{\Phi}_C} - 1$$

<div align="right">(4.31)</div>

Taking the expression of the ratio r' into Eqn. (4.30), the translated Sweby's function is presented as

$$\psi(r_f) = 2\frac{\dfrac{\widetilde{\Phi}_f}{\widetilde{\Phi}_C} - 1}{\dfrac{1}{\widetilde{\Phi}_C} - 1}$$

<div align="right">(4.32)</div>

Finally, returning to Eqn. (4.23), the OpenFOAM®'s TVD framework based on NVD formulation is expressed as

$$\lambda = \frac{1}{2}\psi(r_f) = \frac{\dfrac{\widetilde{\Phi}_f}{\widetilde{\Phi}_C} - 1}{\dfrac{1}{\widetilde{\Phi}_C} - 1}$$

<div align="right">(4.33)</div>

$$\Phi_f = \frac{\dfrac{\widetilde{\Phi}_f}{\widetilde{\Phi}_C} - 1}{\dfrac{1}{\widetilde{\Phi}_C} - 1}(\Phi_P - \Phi_N) + \Phi_N$$

<div align="right">(4.34)</div>

4.4 Solver implementation

Volume fraction equation

Sections 4.2 and 4.3 introduced the principle of FCT and HRS. These techniques are used to optimise the VOF method in OpenFOAM®. In order to explain the details, it is necessary to recall the equation of the volume fraction (Eqn. (4.6))

$$\frac{\partial \gamma}{\partial t} + \nabla \cdot (U\gamma) = 0$$

(4.6)

Discretising the above equation by the finite volume method, then the integral form of the equation has to be presented.

$$\int_{\Omega_i} \frac{\partial \gamma}{\partial t} \, \mathrm{d}V + \int_{\partial \Omega_i} \gamma U \cdot n \mathrm{d}S = 0$$

(4.35)

The discrete equation is expressed by

$$\gamma_i^{\,n+1} = \gamma_i^{\,n} - \frac{\Delta t}{|\Omega_i|} \sum_{f \in \Omega_i} \left(F_f^C\right)^n$$

(4.36)

Where, $\left(F_f^C\right)^n$ is the total flux on cell faces.

It can be found that Eqn. (4.36) is similar to Eqn. (4.9). The variable ϕ_i in Eqn. (4.9) is replaced by the volume fraction field γ_i.

Implementing the FCT technique (Section (4.2)) to Eqn. (4.36), gives

$$\left(F_f^C\right)^n = \left(F_f^L + \lambda_M A_f\right)^n$$

(4.37)

The meaning of the flux terms F_f^L and A_f was explained in Section (4.2) and here

it is expressed by

$$F_f^L = \phi_f \gamma_{f,\text{upwind}}$$

<div align="right">(4.38)</div>

Where ϕ_f represents the volume flux; it is assigned by

$$\phi_f = U_f \cdot S_f$$

<div align="right">(4.39)</div>

$\phi_f \gamma_{f,\text{upwind}}$ is calculated by lower-order schemes, such as the first-order upwind scheme, and

$$A_f = \phi_f \gamma_f + \phi_{rf} \gamma_{rf} (1 - \gamma)_{rf} - F_f^L$$

<div align="right">(4.40)</div>

Where $\phi_f \gamma_f$ is calculated by higher-order schemes. The second term on the right-hand side of Eqn. (4.39) is the interfacial compression flux term, which is used to reduce the numerical diffusion at the interface and preserve sharpness for the volume fraction field. The value of the weighting factor λ_M is evaluated by the MULES solver, which was introduced in List 1.

When $\lambda_M = 0$

$$F_f^C = \phi_f \gamma_{f,\text{upwind}}$$

<div align="right">(4.41)</div>

When $\lambda_M = 1$

$$F_f^C = \phi_f \gamma_f + \phi_{rf} \gamma_{rf} (1 - \gamma)_{rf}$$

<div align="right">(4.42)</div>

Deshpande et al. (2012) demonstrate the weighting factor λ_M is equal to zero away from the interface and to one near it; this theory is shown in Fig. 4.4.
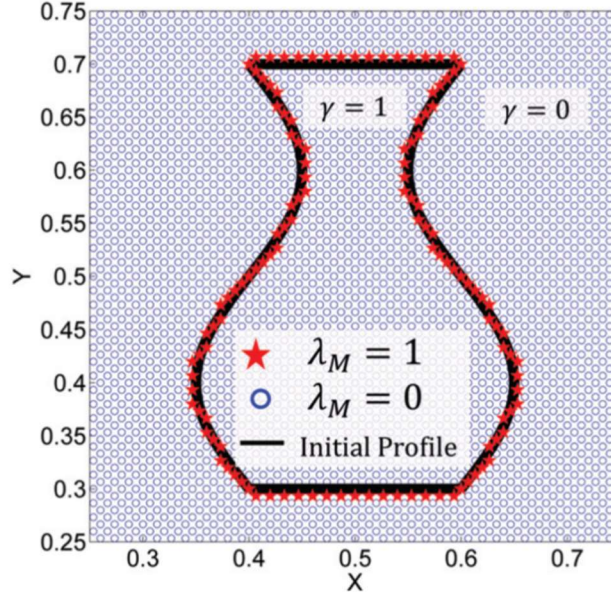
Fig. 4.4. The MULES limiter equals to one near the interface and zero away from it

(Deshpande et al., 2012)

By utilising the functions of FCT and interfacial compression flux, the solution of the volume fraction equation guarantees boundedness, reduces numerical diffusion at the interface and demands fewer computational resources by confining the higher-order treatment to the interfacial region.

When calculating the value of the quantities on cell faces, the face velocity U_f can be evaluated by the linear interpolation scheme directly. The expression is given by

$$U_f = f_{xCI}(U_P - U_N) + U_N$$

(4.43)

This expression is similar to Eqn. (4.18), which replaces velocity U by variable Φ.

Regarding the solution of the face values for the volume fraction field, applying High-Resolution Schemes (HRS) is required to ensure the boundedness and accuracy of the results. Recalling the expression of blending the interpolation scheme and replacing Φ by volume fraction γ_f.

$$\gamma_f = (1 - \lambda_\gamma)\gamma_{fUI} + \lambda_\gamma\gamma_{fCI}$$

(4.44)

Where λ_γ is the blending factor corresponding to the blending factor γ in Eqn. (4.20). Other variables are evaluated by

$$\gamma_{fCI} = f_{xCI}(\gamma_P - \gamma_N) + \gamma_N \text{ and } \gamma_{fUI} = \begin{cases} \gamma_P & if \quad \phi_f \geq 0 \\ \gamma_N & if \quad \phi_f < 0 \end{cases}$$

(4.45)

For central linear interpolation, $f_{xCI} = 0.5$.

Substituting Eqn. (4.45) into Eqn. (4.44), the solution of the face-centred volume fraction field γ_f can be calculated by

$$\gamma_f = \gamma_P + \frac{(\gamma_N - \gamma_P)}{2}[1 - \varsigma(\phi_f)(1 - \lambda_\gamma)]$$

(4.46)

Where $\varsigma(\phi_f)$ is a step function assigned by

$$\varsigma(\phi_f) = \begin{cases} 1 & if \quad \phi_f \geq 0 \\ -1 & if \quad \phi_f < 0 \end{cases}$$

(4.47)

The blending factor λ_γ is calculated by the TVD limiter as previously mentioned.

In regard to the interface compressive flux, $\phi_{rf}\gamma_{rf}(1 - \gamma)_{rf}$, the term ϕ_{rf} in Eqn. (4.40) is calculated by

$$\phi_{rf} = \min\left[C_\alpha \frac{|\phi_f|}{|S_f|}, \max\left(\frac{|\phi_f|}{|S_f|}\right)\right](n_f \cdot S_f)$$

(4.48)

Where C_α represents the interface smearing factor, which can be defined by the user. The maximum operation is executed over the entire simulation domain, and the minimum operation is performed locally at each face $f \in \partial\Omega_i$ (Deshpande et al., 2012). From Eqn. (4.48), it can be found that the sharpness of the interface depends to a large extent on the value of the interface smearing factor. When it is equal to zero, the compressive flux is removed. However, it is unrealistic to expect that by increasing the factor the result will improve. Rather, it will exacerbate errors in the interfacial curvature and result in an unstable solution when the factor exceeds the optimal value. Thus, the default value of the smearing factor is defined as equal to

one, and it is necessary to explore the optimal value in particular cases. In addition, the artificial compressive flux should only be applied to the normal direction to the free-surface. Thus, the direction of the compressive flux depends on the gradient of γ_{rf}. The quantity n_f in Eqn. (4.48) represents the face-centred interface normal vector and is evaluated by

$$n_f = \frac{(\nabla \gamma)_f}{|(\nabla \gamma)_f|} = \frac{\left[\frac{(\nabla \gamma)_P + (\nabla \gamma)_N}{2}\right]}{\left[\left|\frac{(\nabla \gamma)_P + (\nabla \gamma)_N}{2}\right|\right]}$$

(4.49)

The value of the last unknown quantity γ_{rf} in Eqn. (4.40) is obtained using the **interfaceCompression** Scheme (OpenFOAM®, 2008). The term $(1-\gamma)_{rf}$ is approximated by

$$(1-\gamma)_{rf} = (1 - \gamma_{rf})$$

And

$$\gamma_{rf} = \gamma_P + \frac{(\gamma_N - \gamma_P)}{2}\left[1 - \varsigma(\phi_f)(1 - \lambda_{r\gamma})\right]$$

(4.50)

Where the limiter $\lambda_{r\gamma}$ is calculated by the **gammarScheme**, which is given as

$$\lambda_{r\gamma} = \min\left\{\max\left[1 - \max\left(\left(1 - (4\gamma_P(1-\gamma_P))\right)^2, \left(1 - (4\gamma_N(1-\gamma_N))\right)^2\right), 0\right], 1\right\}$$

(4.51)

Momentum equation

The momentum equation in the VOF method also needs to be modified. The original expression of the momentum equation is given by

$$\frac{\partial(\rho U)}{\partial t} + \nabla \cdot (\rho U U) = \nabla \cdot \tau - \nabla p + \rho f_i$$

(4.52)

Where, term $\nabla \cdot \tau$ is the diffusion term and in OpenFOAM®'s VOF method, the viscous stress tensor τ is defined as

$$\tau = \mu(\nabla U + \nabla U^T)$$

Where μ is the effective viscosity, defined as $\mu = \rho(\nu_{mean} + \nu_t)$

And the viscous term is rewritten as

$$\nabla \cdot \tau = \nabla \cdot (\mu \nabla U) + \nabla \cdot \mu (\nabla U)^T$$

Regarding the source term ρf_i, the gravity force and surface tension need to be taken into account. Thus, the gravity force term is given by ρg.

In the case of the surface tension term, the Young-Laplace equation introduces the relationship between surface tension and the pressure difference across the fluid interface. The expression is given as

$$P_1 - P_2 = -\sigma \nabla \cdot \hat{n}$$

(4.53)

$P_1 - P_2$ is the pressure difference across the fluid interface, σ is the surface tension coefficient, $\hat{n}$, is the united normal vector, which can be calculated by a mollified colour function, $\tilde{c}(x)$, (Brackbill et al., 1990).

$$\hat{n} = \frac{\nabla \tilde{c}(x)}{|\nabla \tilde{c}(x)|}$$

(4.54)

Subsequently, the function $-\nabla \cdot n$ is defined as the local interfacial curvature, κ.

$$\kappa = -\nabla \cdot \hat{n}$$

(4.55)

The final form of the Young-Laplace equation is

$$P_1 - P_2 = -\sigma \kappa$$

(4.56)

In the context of the continuum surface force (CSF) model (Brackbill, et al., 1990), the surface force per unit interfacial area is introduced as

$$F_{sa} = \sigma \kappa \cdot \hat{n}$$

(4.57)

Imagine there is an interface between two fluids, as Fig. 4.5 shows.

Consider a volume force, F_{sv}, provides the correct surface tension force per unit interfacial area, F_{sa}, as $h \to 0$

$$\lim_{h \to 0} \int_{\Delta V} F_{sv} \, d^3x = \int_{\Delta A} F_{sa} \, dA$$

(4.58)

Where, h, is the thickness of this volume and the volume force should be localised, this means it is zero outside the interface region. The aforementioned indicator, $\tilde{c}(x)$, is used to calculate this surface tension force

$$\int_A F_{sa} \, dA = \lim_{h \to 0} \int_V \sigma \kappa \frac{\nabla \tilde{c}(x)}{[c]} \, d^3x$$

(4.59)

Combining Eqn. (4.58) with Eqn. (4.59), the volume force, F_{sv}, for finite h is identified as

$$F_{sv} = \sigma \kappa \frac{\nabla \tilde{c}(x)}{[c]}$$

(4.60)

Where $[c]$ is the jump in colour, $[c] = c_2 - c_1$, c_1 and c_2 is the character function in fluid 1 and fluid 2 respectively, in general, this is equal to 1 and 0.

Regarding the present work, this CSF model is used to express the surface tension force, and the mollified colour, $\tilde{c}(x)$, is replaced by the volume fraction, γ. Thus, the final form of the surface tension force in the calculation cell is given as

$$\int_V F_{sv} \, dV = \int_V \sigma \kappa \nabla \gamma \, dV$$

(4.61)
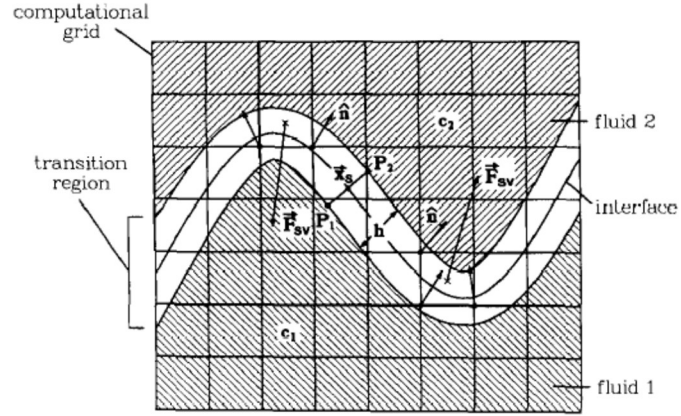
Fig. 4.5. The interface between two different fluids (Brackbill et al, 1990)

Keeping the left-hand side of the equation invariant, then the modified momentum equation is given as

$$\frac{\partial(\rho U)}{\partial t} + \nabla \cdot (\rho UU) = [\nabla \cdot (\mu \nabla U) + \nabla \cdot \mu(\nabla U)^T] - \nabla p + \rho g + \sigma \kappa \nabla \gamma$$

(4.62)

To avoid the numerical integration of the gravity term ρg in the entire computational domain, the pressure term and gravity term are rearranged by

$$p_{rgh} = p - \rho g \cdot h$$

Then, the pressure gradient is expressed as

$$\nabla p_{rg} = \nabla p - \rho g - g \cdot h \nabla \rho$$

$$\rightarrow -\nabla p + \rho g = -\nabla p_{rgh} - g \cdot h \nabla \rho$$

Such a modification provides more accurate results when the mesh quality is poor (Amini Afshar, 2010). The new source term $g \cdot h \nabla \rho$ takes into account the restoring force when the free-surface is deformed from the hydrostatic equilibrium (Li, 2019)

As a result, the integral form of the modified momentum equation is presented by

78

$$\int_{\Omega_i} \frac{\partial(\rho U)}{\partial t} dV + \int_{\partial\Omega_i} (\rho UU) \cdot n \, dS$$

$$= -\int_{\Omega_i} \nabla p_{rg} \, dV - \int_{\Omega_i} g \cdot h\nabla\rho \, dV + \int_{\Omega_i} \sigma\kappa\nabla\gamma \, dV$$

$$+ \int_{\partial\Omega_i} (\mu\nabla U) \cdot n \, dS + \int_{\Omega_i} \nabla \cdot \mu(\nabla U)^T \, dV$$

(4.63)

Eqn. (4.63) can be discretised by the finite volume method, and the PISO algorithm or the PIMPLE algorithm discussed above can be used for the calculation. One issue that needs to be addressed is that even with the PIMPLE algorithm, the time step setting for the VOF method is rigorous, which is based on empirical conclusions (Gopala and Van Wachem, 2008; Berberovic et al., 2009). The recommendation is to use an adaptive time-step control for the solver. The time step is calculated by

$$\Delta t^n = \min\left\{\frac{Co_{max}}{Co}\Delta t^0, \left(1 + \lambda_1 \frac{Co_{max}}{Co}\right)\Delta t^0, \lambda_2\Delta t^0, \Delta t_{max}\right\}$$

(4.64)

Where $Co = \frac{|\vec{u}_f \cdot \vec{S}_f|}{\Delta x \cdot \vec{S}_f}\Delta t$, is the face-computed Courant number, Δx is the side length of the mesh; Co_{max} and Δt_{max} are user-defined parameters; λ_1 and λ_2 are the factors that limit the gradient of time steps to prevent unstable oscillations, which are equal to 0.1 and 0.2, respectively.

At the end of this chapter, the governing equations for the Weller-VOF method (or developed-VOF method) (Weller, 2008) is summarised as

Continuity equation

$$\frac{\partial\rho}{\partial t} + \nabla\rho \cdot U = 0$$

(4.65)

Momentum equation

$$\frac{\partial(\rho U)}{\partial t} + \nabla \cdot (\rho UU) = [\nabla \cdot (\mu\nabla U) + \nabla \cdot \mu(\nabla U)^T] - \nabla p_{rgh} - g \cdot h\nabla\rho + \sigma\kappa\nabla\gamma$$

(4.66)

Volume fraction equation

$$\frac{\partial \gamma}{\partial t} + \nabla \cdot (U\gamma) + \nabla \cdot \left[U\gamma_{rf}(1-\gamma)_{rf}\right] = 0$$

<div align="right">(4.67)</div>

Where

$$\rho = \gamma \rho_{liquid} + (1-\gamma)\rho_{air}$$

$$\mu = \gamma \mu_{liquid} + (1-\gamma)\mu_{air}$$

<div align="right">(4.68)</div>

Chapter 5. Mesh generation and boundary conditions

Regarding the mesh generation process, it must be ensured that the generated geometry for the numerical simulation is consistent with the equipment used in the experiment. Only in this way can further ensure that the numerical simulation restores the actual situation. However, this is often an idealized situation. Due to the constraints of the mesh, most of the time, the geometries used in simulations are simplified or modified. And in the current article, the geometries and meshes used for the simulations are introduced in the following chapters, the difficulties and solutions encountered are also demonstrated.

Another important feature of the simulation is the setups of boundary conditions. They need to restore the real situation as much as possible. The value of the physical flow fields at each boundary is given in the lists. Besides, the flowing behaviour of the boundary flow cannot be simulated directly by the RANS method. Therefore, it requires using wall functions to model the boundary flow. The principles of the wall functions are given in the section of boundary conditions.

5.1 Geometry and mesh

5.1.1 Data of the geometry and mesh

Case 1. Simulation of the flow in cyclones

The geometry and mesh of the first simulation were generated based on the work of Hoekstra (2000). The geometry sketch is shown in Fig. 5.1; the original geometry sketch is presented in Fig. 5.2; the mesh sketch is expressed in Fig. 5.3 and the dimensions of the cyclone are given in Table 5.1,

The geometry is generated by the third-party software **Gmsh** in three-dimensional circumstance. 247768 hexahedra are used for the generation of the structured mesh.
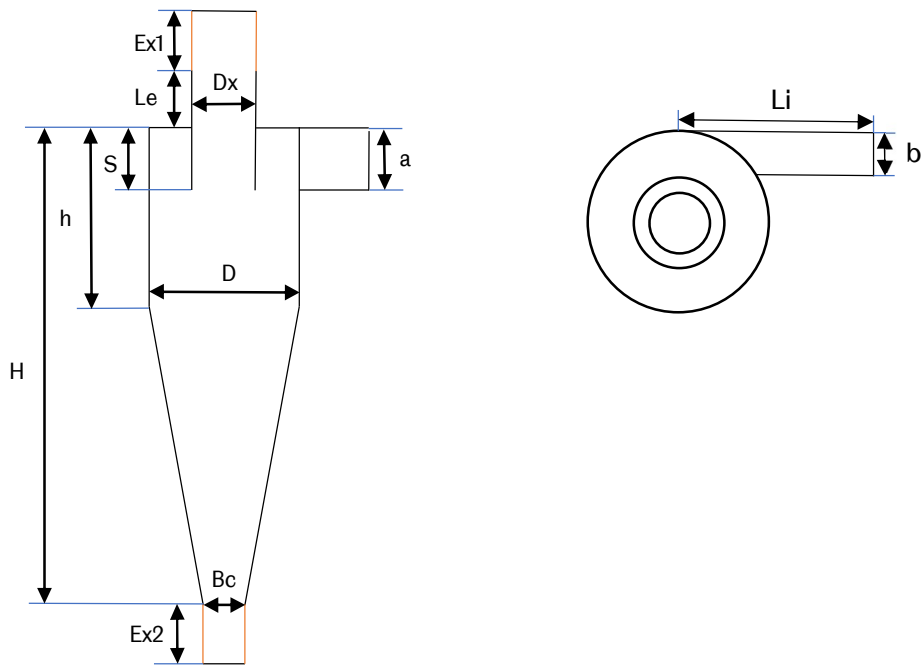
Fig. 5.1. Geometry sketch of the cyclone separator
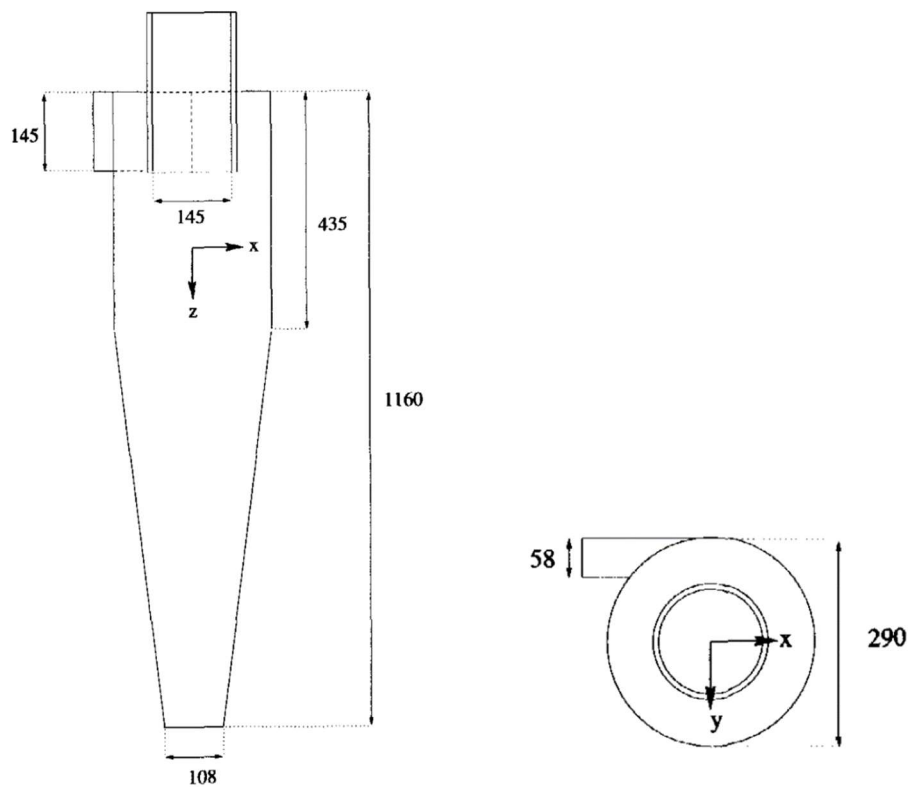

Fig. 5.2. Original geometry sketch of the cyclone separator (Hoekstra, 2000)

(a) Front view
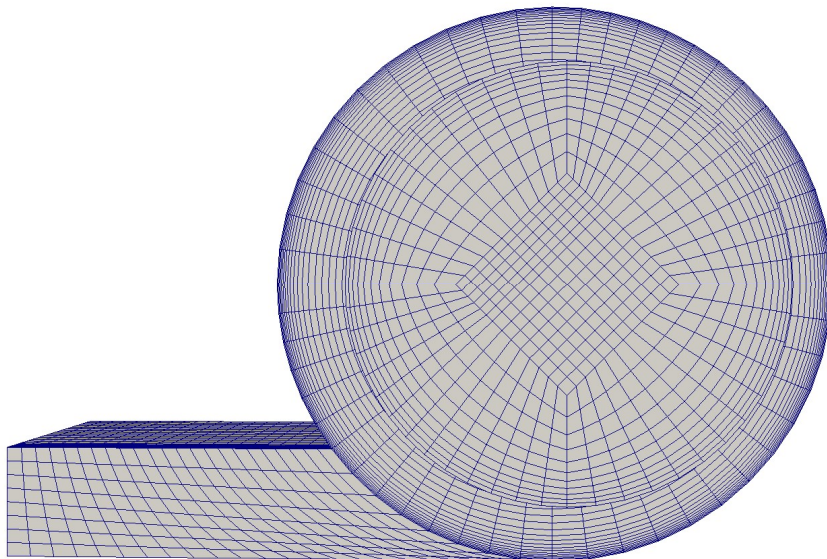
(b) Top view

Fig. 5.3. Mesh sketch of the cyclone separator

Table 5.1 The Dimensions of the cyclone in Fig. 5.1

Dimension	Parameter
Cyclone diameter, D	$0.29m$
Top outlet diameter, $Dx/\boldsymbol{D}$	0.5
Bottom outlet diameter, $Bc/\boldsymbol{D}$	0.375
Inlet height, $\boldsymbol{a}/\boldsymbol{D}$	0.5
Inlet width, $\boldsymbol{b}/\boldsymbol{D}$	0.2
Inlet length, $\boldsymbol{Li}/\boldsymbol{D}$	1
Outlet duct length, $\boldsymbol{S}/\boldsymbol{D}$	0.5
Cylinder height, $\boldsymbol{h}/\boldsymbol{D}$	1.5
Cyclone height, $\boldsymbol{H}/\boldsymbol{D}$	4.0
Extended top outlet, $\boldsymbol{Ex1}/\boldsymbol{D}$	0.5
Extended bottom outlet, $\boldsymbol{Ex2}/\boldsymbol{D}$	0.5

Case 2. Simulation of the dam breaking flow

The geometry and meshes of the second simulation were generated according to the experiment conducted by Cruchage (2007). The simulated geometry sketch is shown in Fig. 5.4; the experimental geometry sketch is presented in Fig. 5.5; the mesh sketch and the initial state of the free-surface are given in Fig. 5.6 and the dimensions of the cube are listed in Table 5.2.

This geometry is created by Openfoam®'s own command execution file in two-dimensional space. The maximum number of structured meshes is 25600 hexahedrons.
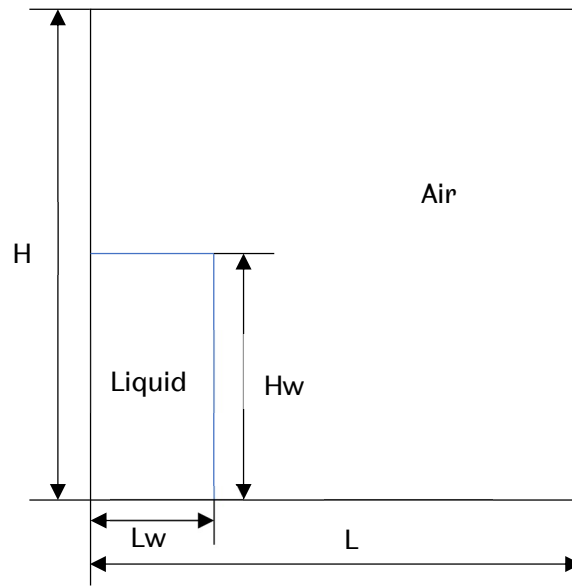
Fig. 5.4 Simulated geometry sketch of the dam breaking flow
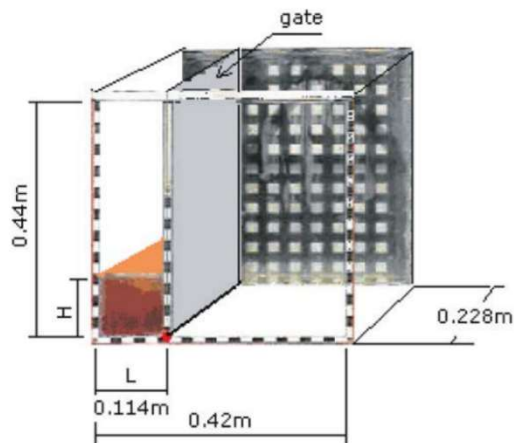
Fig. 5.5 (a) Experimental geometry sketch of the dam breaking flow
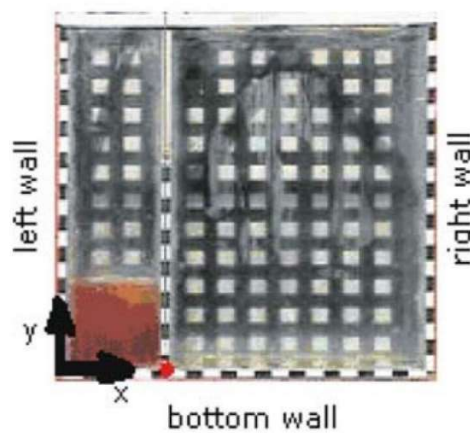
Fig. 5.5 (b) Front view of the experimental geometry sketch of the dam breaking flow (Cruchaga et al., 2007)
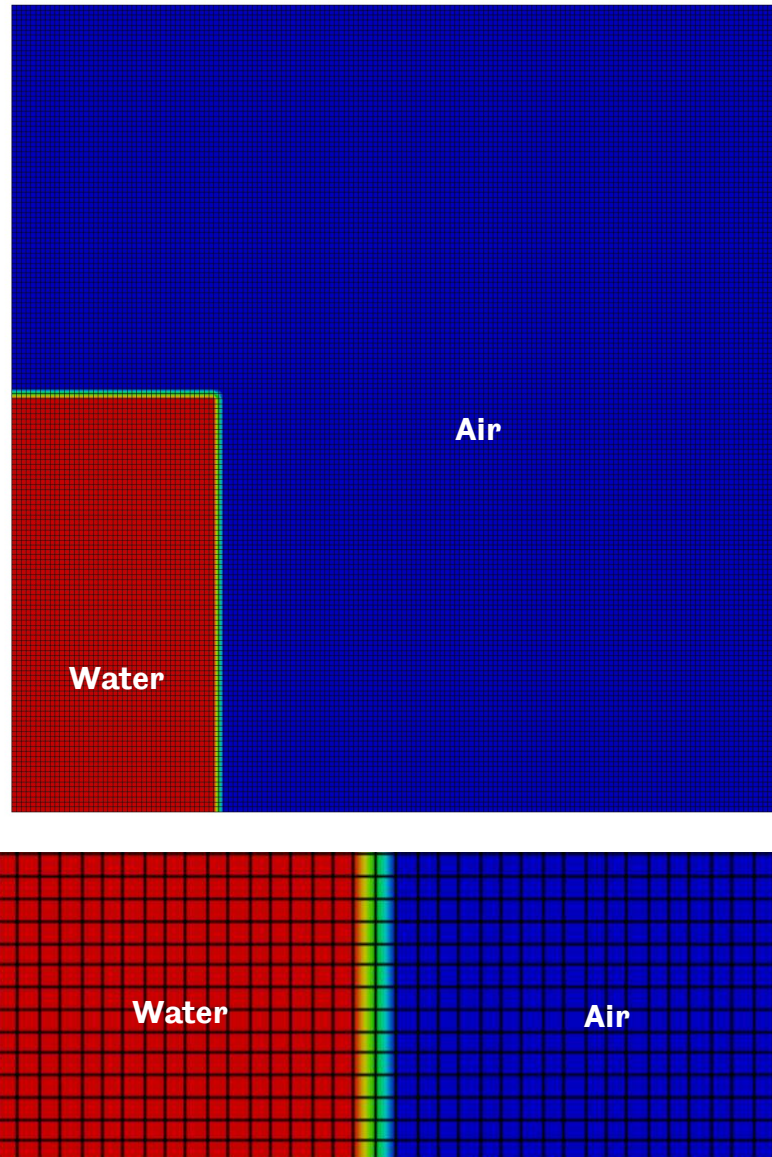
Fig. 5.6. The initial state of the dam breaking simulation with meshes

Table 5.2 The Dimensions of the cube in Fig. 5.4

Dimension	Parameter
Water tank length, L	0.42m
Water tank height, H	0.44m
Initial liquid phase length, Lw	0.114m
Initial liquid phase height, Hw	0.228m

Case 3. Simulation of the flow with air-core in hydrocyclones

The geometry and mesh of the simulation were created based on the experimental data provided by Hsieh (1991). The simulated geometry sketch is shown in Fig. 5.7; the experimental geometry sketch is presented in Fig. 5.8; the mesh sketch is given in Fig. 5.9 and the dimensions of the hydrocyclone are listed in Table 5.3.

The geometry is generated by the third-party software Gmsh in three-dimensional space as well. For the given mesh sketch (Fig 5.8), 325124 hexahedrons are used for the generation of the structured mesh.

Table 5.3 The Dimensions of the hydrocyclone in Fig. 5.7

Dimension	Parameter
Cyclone diameter, D	$0.075m$
Vortex finder diameter, Dx/D	1/3
Bottom outlet diameter, Bc/D	1/6
Inlet height, a	0.022
Inlet width, b	$0.022m$
Inlet length, Li/D	3/4
Vortex finder length, Vt/D	2/3
Cylinder height, h/D	1
Cone angle, Ca	10°
Extended top outlet, $Ex1/D$	3/4
Extended bottom outlet, $Ex2/D$	1/3
Inlet offset, $Ex3$	$0.001m$
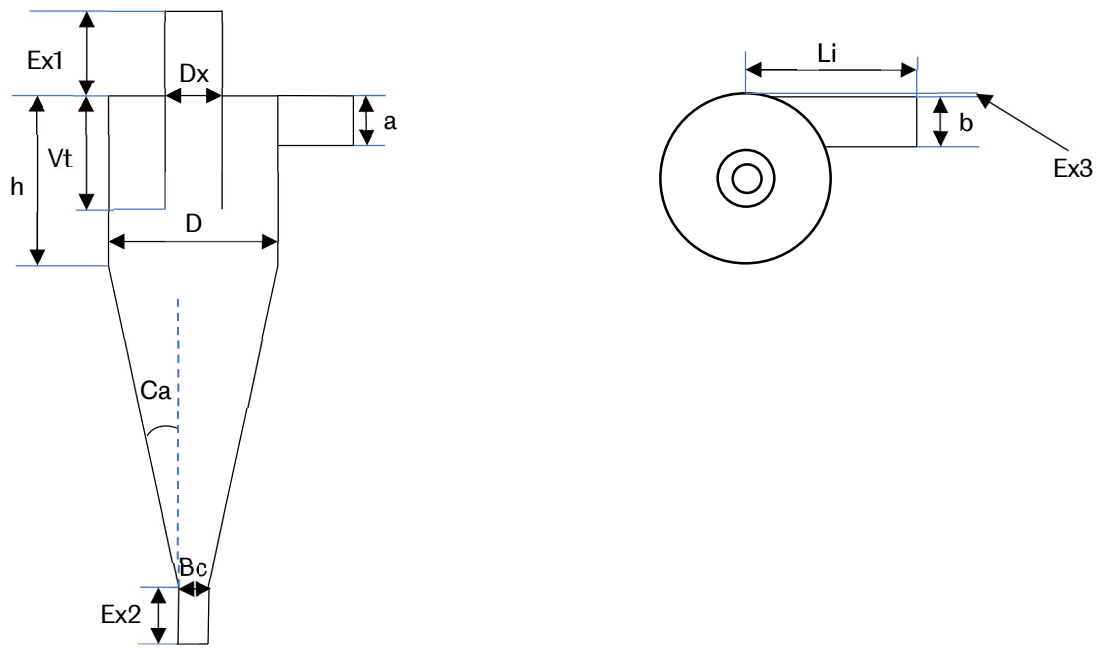
Fig. 5.7. Geometry sketch of the hydrocyclone
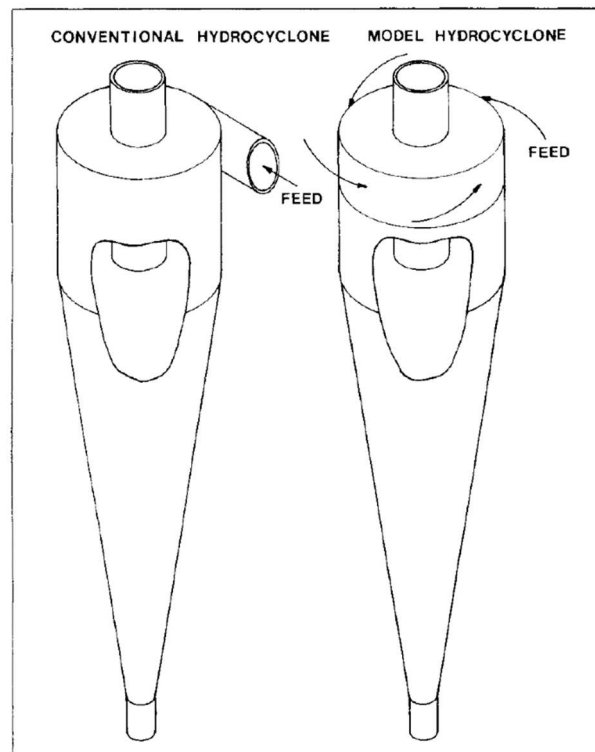
Fig. 5.8. Experimental geometry sketch of the hydrocyclone (Hsieh, 1991)
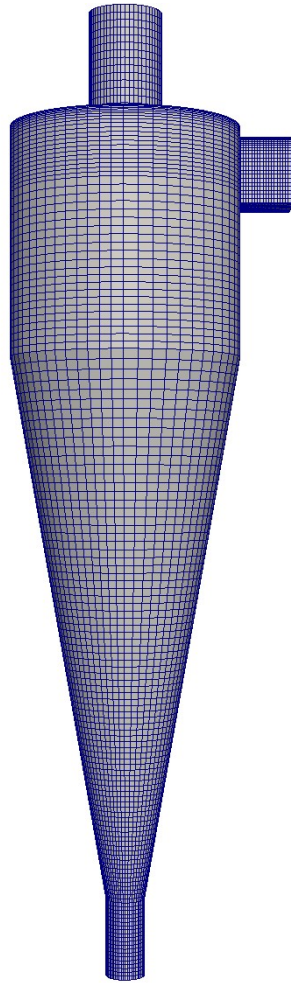
(a) Front view
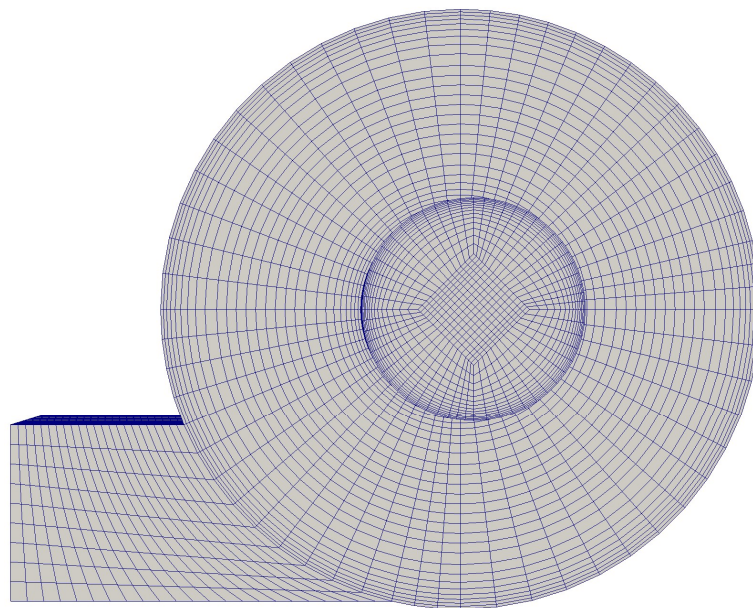
(b)Top view

Fig. 5.9. Mesh sketch of the hydrocyclone

5.1.2 Summarisation of the geometry and mesh

1. Dimension

As can be found from Fig 5.1 and Fig 5.7, the geometry of the cyclone and hydrocyclone has a tangential inlet with asymmetrical distribution. Thus, the hydrocyclone flow field should be treated as an axial asymmetry problem (He. et al.,1999). The full three-dimensional modelling is necessary for an accurate simulation of the cyclone and hydrocyclone flow.

Regarding the dam breaking flows, the problem can be simplified to two-dimensional when the problem focuses on the flow field away from the front wall and back wall. This simplification is considered acceptable because the effects caused by the front and back wall is negligible and requires less computational resources for simulations. A denser mesh can be applied for the geometry in order to sharp the thickness of the free-surface in the VOF method.

2. Structure

The structured mesh is applied to all simulations, and this choice is based on the following advantages

- Applying the structured mesh requires fewer meshes to cover the geometry; this will save computational costs compared with using unstructured mesh.

- When the lower-order schemes are used for discretisation, the simulation result obtained by the structured mesh is less numerically diffusive for flows with a dominant flow direction (see Fig. 5.10).

- Using the structured mesh is more stable during simulating than the unstructured mesh, especially when using high-order discretisation method for simulation.

- For the boundary layer flow, the unstructured mesh is unsuitable because the aspect ratio is hard to control for the meshes near the boundary.

The foremost disadvantage bringing by the structured mesh is the non-orthogonal mesh; it will reduce the accuracy and become one of the factors that cause the calculation results to un-convergence simulating. The treatments for the non-orthogonal mesh are given behind.

3. Quality

In OpenFOAM®, the quality of the mesh can be checked by the **checkMesh** function. The quality of the mesh is assessed from the following aspects

- **Skewness**: The vertex angle of most of the meshes used in the simulations is approach to 90°. Only a few of meshes have a skew angle of more than 70° at the junction of the inlet and the separator, and these meshes are referred to as non-orthogonal meshes.

- **Aspect ratio**: The aspect ratio of most of the meshes is smaller than 5. It is inevitable that the meshes at the boundary layer have an aspect ratio larger than 5, this is acceptable because the rate of change of the variables is not obvious in the direction of the longer side.

- **Smoothness**: In order to guarantee the accuracy of the discretisation schemes, the smoothness of most of the meshes is limited smaller than 1.2.

- **Boundary layer mesh**: The quality of the meshes in boundary layer depends on the yPlus number, which is a dimensionless quantity applied to limits the size of the mesh attached at the boundary, more details are given in the boundary conditions section. The yPlus number of the boundary layer mesh used in the simulations is limited to between 30 and 300 in the RANS method, and less than one in the LES method.

4. Treatments for the Non-orthogonal mesh

As previously mentioned, the non-orthogonal mesh is one of the factors that cause the calculation results to un-converge and will reduce the order of accuracy. Thus, in current studies, two methods have been used to mitigate the defects brought by the non-orthogonal mesh.

The first strategy is to reduce the skew angle of the mesh at the junction of the inlet and the separator by modifying the geometry. Like Fig. 5.11 (part of Fig. 5.3) and Fig. 5.12 (part of Fig. 5.9) presents, the skew angle of the mesh was reduced from 83° to 70°. This one-millimetre offset brings the skew angle from a dangerous level to an acceptable level (OpenFOAM®, 2017).
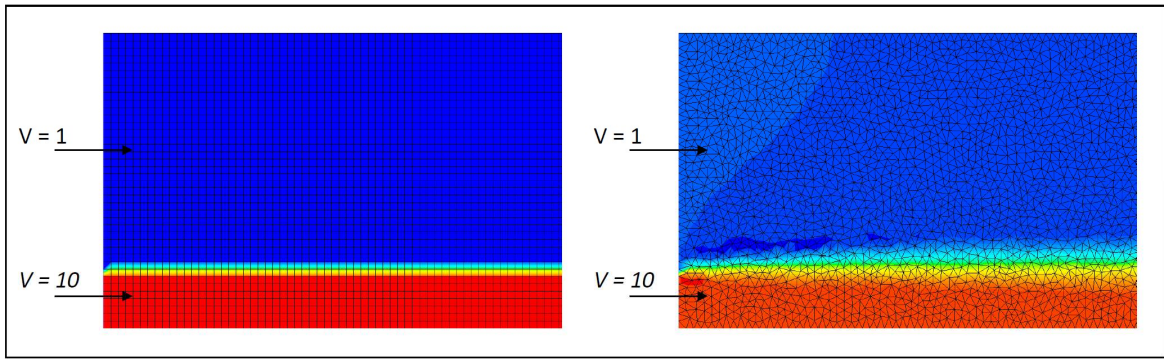
Fig. 5.10 inviscid jet flow (Marzo. et al, 2015)
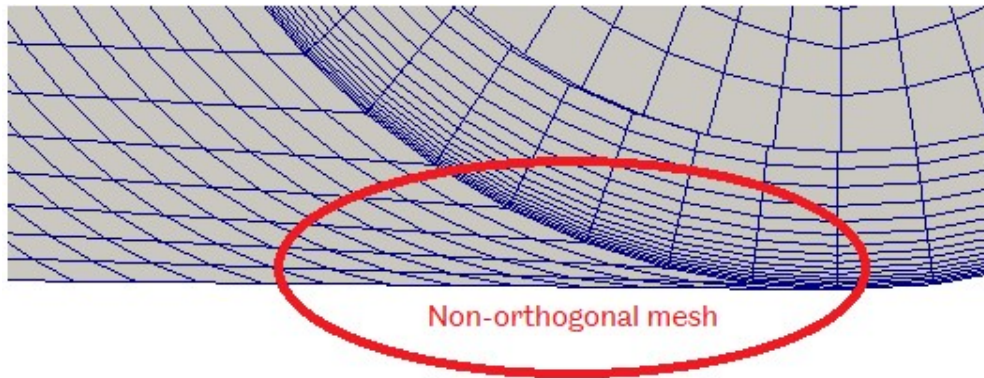
Fig. 5.11 Non-orthogonal mesh from the mesh sketch of cyclone
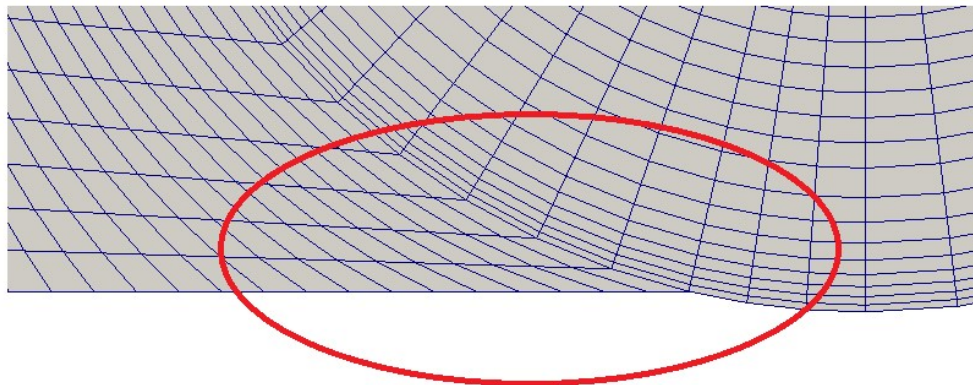
Fig. 5.12 Non-orthogonal mesh from the mesh sketch of hydrocyclone

The second method is reducing the defects by using numerical schemes. The central difference scheme (Eqn. 3.20) cannot provide a second-order approximation of $\left(\frac{\partial \Phi}{\partial n}\right)_{i,j,k}$ when the line between two points (P and E) is not parallel to the normal vector (see. Fig. 5.13). Therefore, the central difference scheme requires to be modified.

The second-order approximation of the gradient operator is given as

$$\left(\frac{\partial \Phi}{\partial x}\right)_P \approx \frac{\int_\Omega (\partial \Phi/\partial x)d\Omega}{|\Omega|}$$

(5.1)

Transforming the integral at the right-hand side using the Gauss' theorem

$$\int_\Omega (\partial \Phi/\partial x)d\Omega = \int_\Omega \text{div}(\Phi i)d\Omega = \int_S (\Phi i \cdot n)dS = \int_S \Phi n_x dS = \sum_j \int_{S_j} \Phi n_x dS$$

(5.2)

Where j is the index represents the cell's faces, and the surface integral over every face can be calculated by the second-order approximation

$$\sum_j \int_{S_j} \Phi n_x dS = \sum_j \Phi_{ej} n_x S_j$$

(5.3)

Where Φ_{ej} is the value of the variety Φ at the corresponding midpoint, which can be calculated through the interpolation scheme. Thus, the second-order approximation of the gradient operator is presented by

$$\left(\frac{\partial \Phi}{\partial x}\right)_P \approx \frac{\sum_j \Phi_{ej} n_x S_j}{|\Omega|}$$

(5.4)
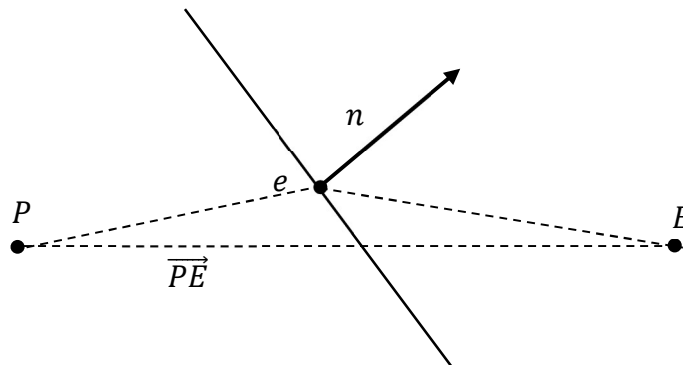
Fig 5.13. Schematic diagram of the Vectors

In OpenFOAM®, a non-orthogonal correction term is utilised to further correct the discretisation on the non-orthogonal mesh. This is achieved by decomposing the factor $(\vec{\nabla}\Phi)_f \cdot \vec{S}_f$ as

$$(\vec{\nabla}\Phi)_f \cdot \vec{S}_f = \underbrace{\vec{\Delta} \cdot (\vec{\nabla}\Phi)_f}_{orthogonal\ contributio} + \underbrace{\vec{k} \cdot (\vec{\nabla}\Phi)_f}_{non-orthogo\qquad correction}$$

(5.5)

As shown in Fig. 5.14 The decomposition of the vector is

$$\vec{S}_f = \vec{\Delta} + \vec{k}$$

Where the vector $\vec{\Delta}$ is parallel to the line $\vec{d}_{PN}$, then the orthogonal contribution can be calculated by the central difference scheme (Eqn. 3.20). Thus, the expression is given as

$$\vec{\Delta} \cdot (\vec{\nabla}\Phi)_f = |\vec{\Delta}| \frac{\Phi_N - \Phi_P}{|\vec{d}_{PN}|}$$

Where, $\vec{\Delta}$ is assigned as

$$\vec{\Delta} = \frac{\vec{d}_{PN}}{\vec{d}_{PN} \cdot \vec{S}_f} |\vec{S}_f|^2$$

Regarding the non-orthogonal correction, OpenFOAM® using the over-relaxed approach to approximate the value (Jasak, 1996; Márquez Márquez Damián et al., 2012). Therefore, Eqn. (5.5) can be expressed as

$$(\vec{\nabla}\Phi)_f \cdot \vec{S}_f = |\vec{\Delta}| \frac{\Phi_N - \Phi_P}{|\vec{d}_{PN}|} + \vec{k} \cdot (\vec{\nabla}\Phi^{v-1})_f$$

Where $\vec{\nabla}\Phi^{v-1}$ is calculated by Eqn. (5.4) with the iterative method, $v-1$ represents the iterator index. Such kind of deferred correction is introduced in Sections 5.6 and 8.6 of Computational Methods for Fluid Dynamics (Ferziger and Peric, 2002). The number of iterations can be set by giving value to **nNonOrthogonalCorrectors** during the same time-step. Although this scheme

takes more time for simulation, it dramatically reduces the impact of non-orthogonal mesh on accuracy and stability.
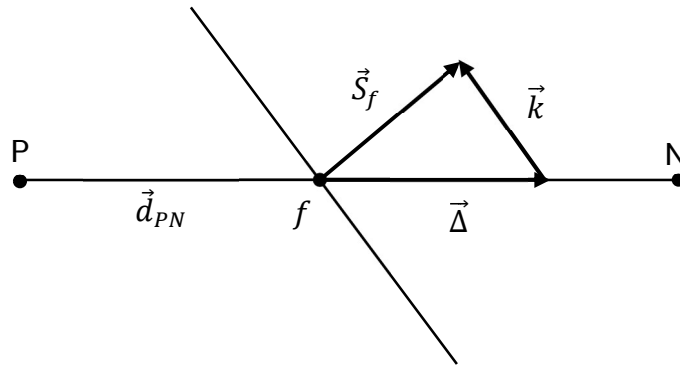

Fig. 5.14. Schematic diagram of the Vector $\vec{S}_f$ and its decomposition vectors $\vec{k}$

and $\vec{\Delta}$

5.2 Boundary conditions

The boundary conditions implemented for each physical quantity in the current simulations are shown in Table 5.4. to Table 5.6

In the followed tables, the turbulence intensity I can be estimated by an empirical value equal to 0.05.

The expression of the Reynolds number is given as

$$Re = \frac{inertial\ forces}{viscous\ forces} = \frac{\rho u d}{\mu} = \frac{u_x d}{v}$$

l represents the turbulence length scale, the value in its initial state can be estimated by

$$l = 0.05d$$

R_{ii} represents the Reynolds stress divided density and the formula is expressed as

$$R_{ii} = \overline{u_i' u_i'}$$

Where u_i' is the fluctuating component of velocity, it can be estimated by

$$u_i' = I u_i$$

C_μ is the constant generally takes $C_\mu = 0.09$..

Table 5.4 The boundary conditions of the cyclone flow

Boundary conditions	Walls	Body wall	Bottom outlet	Top outlet	Inlet
Velocity u (m/s) (u_x, u_y, u_z)	(0,0,0)	(0,0,0)	zeroGradient	zeroGradient	$(U_x, 0, 0)$
Pressure $P(m^2/s^2)$	zeroGradient	zeroGradient	0	0	zeroGradient
Kinetic energy k	0	0	zeroGradient	zeroGradient	$\frac{3}{2} I U^2$
Reynolds stress R	$\begin{pmatrix} 0 & 0 & 0 \\ 0 & 0 & 0 \\ 0 & 0 & 0 \end{pmatrix}$	$\begin{pmatrix} 0 & 0 & 0 \\ 0 & 0 & 0 \\ 0 & 0 & 0 \end{pmatrix}$	zeroGradient	zeroGradient	$\begin{pmatrix} R_{xx} & 0 & 0 \\ 0 & R_{yy} & 0 \\ 0 & 0 & R_{zz} \end{pmatrix}$
Dissipation rate ε	$\varepsilon = \dfrac{C_\mu^{0.75} k^{1.5}}{\kappa z_P}$	$\varepsilon = \dfrac{C_\mu^{0.75} k^{1.5}}{\kappa z_P}$	zeroGradient	zeroGradient	$\varepsilon = \dfrac{C_\mu^{0.75} k^{1.5}}{l}$

Table 5.5 The boundary conditions of the dam breaking flow

Boundary conditions	Left wall	Right wall	Lower wall	atmosphere	Front and back
Velocity u_t (m/s) (u_x, u_y, u_z)	slip	slip	noSlip (0, 0, 0)	pressureInletOutletVelocity uniform (0 0 0)	empty
Pressure P_{rgh} $kg/m \cdot s^2$	fixedFluxPressure uniform 0	fixedFluxPressure uniform 0	fixedFluxPressure uniform 0	TotalPressure $P_0 = 0$	empty
Volume fraction γ	zeroGradient	zeroGradient	zeroGradient	inletOutlet inlet value 0 value 0	empty

Table 5.6 The boundary conditions of the hydrocyclone flow

Boundary conditions	Walls	Body wall	Bottom outlet	Top outlet	Inlet
Velocity u (m/s) (u_x, u_y, u_z)	(0,0,0)	(0,0,0)	pressureInletOutletVelocity uniform (0 0 0)	pressureInletOutletVelocity uniform (0 0 0)	$(U_x, 0, 0)$
Pressure P_{rgh} $kg/m \cdot s^2$	fixedFluxPressure uniform 0	fixedFluxPressure uniform 0	TotalPressure $P_0 = 0$	TotalPressure $P_0 = 0$	fixedFluxPressure uniform 0
Kinetic energy k	0	0	inletOutlet	inletOutlet	$\frac{3}{2} I U^2$
Reynolds stress R	$\begin{pmatrix} 0 & 0 & 0 \\ 0 & 0 & 0 \\ 0 & 0 & 0 \end{pmatrix}$	$\begin{pmatrix} 0 & 0 & 0 \\ 0 & 0 & 0 \\ 0 & 0 & 0 \end{pmatrix}$	inletOutlet	inletOutlet	$\begin{pmatrix} R_{xx} & 0 & 0 \\ 0 & R_{yy} & 0 \\ 0 & 0 & R_{zz} \end{pmatrix}$
Dissipation rate ε	$\varepsilon = \dfrac{C_\mu^{0.75} k^{1.5}}{\kappa z_P}$	$\varepsilon = \dfrac{C_\mu^{0.75} k^{1.5}}{\kappa z_P}$	inletOutlet	inletOutlet	$\varepsilon = \dfrac{C_\mu^{0.75} k^{1.5}}{l}$

The boundary conditions in the above tables have different types; they belong to the Dirichlet and Neumann boundary conditions which corresponding to a fixed value and the gradient normal to boundaries. Fig. 5.15 shows a non-orthogonal mesh that is used to explain the solution process of these two boundary conditions as an example. The vector $\vec{d}_n$ normal to the boundary can be estimated by using the vector $\vec{d}$ joining the cell centre P and face b centre. The expression is given as

$$\vec{d}_n = \frac{(\vec{S}_f \cdot \vec{d})\vec{S}_f}{\left|\vec{S}_f\right|^2}$$

(5.6)
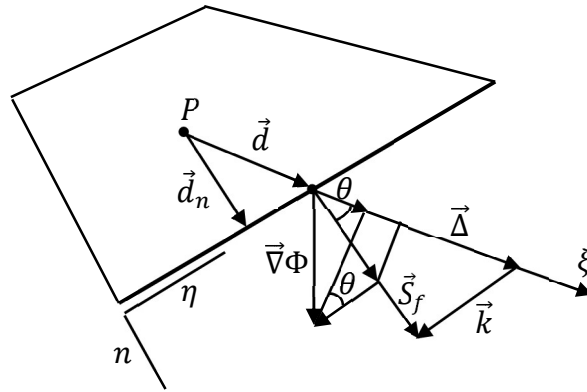
Fig. 5.15. Non-orthogonality treatment in a boundary cell

Dirichlet boundary condition

The Dirichlet boundary condition using the fixed value of $\Phi_f = \Phi_b$ directly determine the boundary condition at face b. Thus, the convective term in governing equations is discretized by

$$\int_S \Phi V \cdot \mathrm{n}\, \mathrm{d}S = \sum_f \Phi_f(\vec{V}_f \cdot \vec{S}_f) = \sum_f \Phi_f F_f$$

The value of Φ_f at the face, b is the given boundary condition and the value of Φ_f at other faces can be calculated by the interpolation schemes.

The diffusive terms in governing equations are discretised by

$$\int_S x\nabla\Phi \cdot \mathrm{n}\, \mathrm{d}S = \sum_f (x)_f (\vec{\nabla}\Phi)_f \cdot \vec{S}_f$$

When the equation is discretised in the non-orthogonal mesh, as previously mentioned, the value of the gradient $\vec{\nabla}\Phi$ at boundaries cannot be estimated by the first-order difference schemes directly. A modification to the scheme is proposed by Mathur and Murthy (1997) and introduced below. The information in Fig. 5.15 contributes to the derivation of the expression.

$$\frac{\partial \Phi}{\partial \xi} = \frac{\partial \Phi}{\partial n}\cos\theta - \frac{\partial \Phi}{\partial \eta}\sin\theta$$

(5.7)

Where θ is the angle between $\vec{d}$ and $\vec{n}$.

The face normal gradient can be obtained by rearranging Eqn. (5.7)

$$\vec{\nabla}\Phi \cdot \vec{n} = \frac{\partial \Phi}{\partial n} = \frac{\partial \Phi}{\partial \xi}\frac{1}{\cos\theta} + \frac{\partial \Phi}{\partial \eta}\tan\theta$$

(5.8)

Since

$$\frac{\partial \Phi}{\partial \xi} = \frac{\Phi_b - \Phi_P}{|\vec{d}|} \quad and \quad \cos\theta = \frac{\vec{d}\cdot\vec{S}_f}{|\vec{d}||\vec{S}_f|}$$

Substituting the expressions into Eqn. (5.8), it gives

$$(\vec{\nabla}\Phi)_b \cdot \vec{S}_f = \frac{|\vec{d}||\vec{S}_f|}{\vec{d}\cdot\vec{S}_f}|\vec{S}_f|\frac{\Phi_b - \Phi_P}{|\vec{d}|} + \frac{\partial \Phi}{\partial \eta}\tan\theta\,|\vec{S}_f|$$

(5.9)

The last term on the right-hand side is null because the value of Φ is constant, then it has $\frac{\partial \Phi}{\partial \eta} = 0$.

Taking Eqn. (5.6) into Eqn. (5.9), the equation can be simplified to

$$\left(\vec{\nabla}\Phi\right)_b \cdot \vec{S}_f = |\vec{S}_f|\frac{\Phi_b - \Phi_P}{|\vec{d}_n|}$$

Neumann boundary condition

Regarding the Neumann boundary condition, a fixed value is assigned to the gradient normal to the boundary face. The expression is given by

$$\left(\frac{\vec{S}_f}{|\vec{S}_f|} \cdot \vec{\nabla}\Phi\right) = g_b$$

Due to the value at boundary face is not given, it has to be calculated by rearranging the formula of first-order difference scheme based on the given gradient g_b, cell-centre value Φ_P.

$$\left(\vec{\nabla}\Phi\right)_b = \frac{\Phi_b - \Phi_P}{|\vec{d}_n|} \rightarrow \Phi_b = \Phi_P + |\vec{d}_n|g_b$$

Then the value of Φ_b can be used to calculate the convective term

In the case of the diffusive term, the value can be obtained directly

Discretising the diffusive term

$$\int_S x\nabla\Phi \cdot \mathrm{n} \, \mathrm{d}S = \sum_f (x)_f \left(\vec{\nabla}\Phi\right)_f \cdot \vec{S}_f$$

At the boundary face b it has

$$\left(\vec{\nabla}\Phi\right)_b = g_b$$

The above tables contain some OpenFOAM®-specific command symbols to set the boundary conditions. The specific meanings and usage of these commands are given below.

- **fixedValue**: Specifies the value of Φ as a fixed value, also known as The Dirichlet boundary condition

- **zeroGradient**: Specifies the value of the normal gradient $\vec{\nabla}\Phi$ equal to zero, this is a kind of Neumann boundary condition.

- **slip**: slip has the same effect as zeroGradient for a scalar magnitude; in case of a vector magnitude, the normal component is specified as a fixed value equal to zero, and tangential components are assigned as zeroGradient.

- **noSlip**: Opposite to slip boundary condition, for a vector magnitude all the components are specified as a fixed value equal to zero at this boundary;

- **pressureInletOutletVelocity**: This boundary condition only can be used for the pressure boundaries where the pressure is specified. The value is set as zero-gradient for outflow. In the case of inflow, the velocity is obtained from the tangential component of the internal-cell value, which is defined by the user.

- **fixedFluxPressure:** The fixedFluxPressure is generally used to replace the zero-gradient boundary condition when the body forces should be considered. This boundary condition is a benefit for convergence.

- **TotalPressure:** This condition specifies

$$P = \begin{cases} P_0 & , & \text{for outflow} \\ P_0 - \dfrac{1}{2}|U^2|, & \text{for inflow (incompressible subsonic)} \end{cases}$$

Where, P_0, is designed by the user.

- **inletOutlet:** The inletOutlet boundary condition is used to treat the situations that there are outflow and inflow (generally backward flow) flowing through this surface simultaneously. The quantities in outflow are assumed as zero-gradient, and a fixed value shall be specified when the flow is inwards.

- **Wall functions**: In the viscous sublayer, the Mean flow velocity has a strong gradient in the immediate vicinity of the wall. The typical length scale of the flow characteristics computed by a RANS model decreases near the walls. Another feature that requires special treatment is that the actual turbulent eddy viscosity becomes smaller as the wall is approached (Zikanov, 2010). These problems are hard to resolve even with a fine grid in the viscous sublayer. Thus, it is necessary to use wall functions to indicate the universal boundary layer behaviour and imitate the effect of a solution corresponding to that behaviour.

Based on the assumption that the flow is in a local equilibrium and the wall-parallel mean velocity satisfies the logarithmic law, one of the wall functions is given as (Zikanov, 2010)

$$\langle u \rangle_P = u_\tau \left[\frac{1}{\kappa} \ln \frac{u_\tau z_P}{\upsilon} + B \right]$$

Where u_τ is the wall shear velocity, which can be used to calculate the viscous shear stress at the wall. The formula is presented by

$$u_\tau = (|\tau_w| \rho^{-1})^{\frac{1}{2}}$$

z_P represents the distance from the wall to the centre of the grid nearest to the wall. κ is the von Karman constant given as $\kappa = 0.41$. B is the empirical constant which takes 5.5 at a smooth flat plate.

As mentioned in the section of mesh quality, wall functions need to fit the appropriate mesh to give correct modelling results. The yPlus number is the standard used to check if the mesh and wall functions match. The expression of the yPlus number is given as

$$y^+ = \frac{u_\tau z_P}{\upsilon}$$

The yPlus number have different limits for different wall functions, and for the standard wall funtion, it has to satisfy $30 < y^+ < 100$.

Finally, the other quantities used in the turbulence model can be calculated by the wall functions. Such as, in the $k - \varepsilon$ model, the kinetic energy and dissipation rate at the grid nearest to the wall is calculated by

$$k_P = \frac{u_\tau^2}{C_\mu^{0.5}} \quad and \quad \varepsilon_P = \frac{C_\mu^{0.75} k^{1.5}}{\kappa z_P}$$

Chapter 6. Simulation of the single-phase cyclone flow

6.1 Case introduction

The simulation of the single-phase cyclone flow was carried out in the RANS method. It is well known that the turbulence model is one of the key features influencing the practicality of the simulation result. Therefore, the main project in the current case is to find an appropriate RANS turbulence model to simulate the flow in a cyclone separator. Given the asymmetry in the distribution of the cyclone inlet, the simulation was performed in a three-dimensional environment. The geometry and mesh are generated by the third-party software Gmsh (see Fig. 5.1 and Fig. 5.3.).

The schemes used for discretisation are the linear-upwind scheme and the centre-linear scheme; both have second-order of accuracy. The iterative linear equations solver used to solve the pressure equation was the Gauss-Seidel smoother and the Geometric-Algebraic Multi-Grid (GAMG) solver. The Gauss-Seidel smooth solver was applied to solve the equations of the velocity, U, kinetic energy, k, dissipation rate, ε, and Reynolds stress, R. Since this study was also interested in the transient state of the cyclone, the transient solver based on the PIMPLE algorithm was used to solve the problem of velocity and pressure coupling.

The two turbulence models used in the present simulation can be considered far different. The $k - \varepsilon$ turbulence model is a typical eddy viscosity model based on the Boussinesq hypothesis. Regarding the RSM turbulence model, although it also applies a modelling method to calculate parts of the stress terms, the value of the Reynolds stress can be evaluated directly.

Since the current case is considered an incompressible problem, the kinetic viscosity of the fluid flowing inside the cyclone is set as a constant, which is equal to $1.57 \times 10^{-5}\ m^2/s$. The inlet velocity is given in the boundary condition section, which equals $15m/s$. Thus, the Reynolds number of the cyclone flow is $Re = u_{in}D/v_{air} = 2.75 \times 10^5$, indicating that the flow is completely turbulent.

The maximum number of meshes used in the simulations is 289702 ununiformed structured hexahedrons, and the minimum number of meshes is 187202

ununiformed structured hexahedrons. The simulation result is illustrated by exhibiting the streamline graph and vector diagrams of the flow field and contour plots of different properties. The validation process of the cyclone flow simulation is achieved by comparing the simulation result with Alahmadi and Nowakowski's (2015) investigation; they validated their works with experimental results from Hoekstra (2000).

6.2 Simulation results

The simulation results of the single-phase cyclone flow are given below.

1. **Streamline graph**

First, the streamline graph is applied to represent the changes in flowing behaviour over time. As the simulation is processed by PimpleFoam solver, the PIMPLE algorithm was used for calculation. The transient state of the cyclone flow can be captured during the simulations; as a result, the streamline graph shows the flowing behaviour of the cyclone flow at six different time points.

The first figure (see Fig. 6.1) shows the fluid just flowed into the cyclone separator. A small vortex was generated near the vortex finder pipe, and most of the fluid inside the cyclone flowed out through the bottom outlet. The second figure (see Fig. 6.2) shows the flowing state at 0.4s; the pattern of the cyclone flow was gradually stabilised. A large swirl appeared at the centre of the cyclone separator, and the velocity magnitude is distributed unevenly along the radius direction. The fluid flowed out through the bottom outlet and top outlet simultaneously. The next three figures show the gradual development of the flow pattern in the cyclone from 0.6 to 1.0 seconds (see Fig. 6.3 to Fig. 6.5). The cyclone flow gradually presents two different swirl patterns. The internal swirl tended to flow out through the top outlet. In contrast, the swirl that approached the wall of the cyclone tended to flow out through the bottom outlet. Furthermore, as the time-step progressed, the maximum value of the velocity magnitude became higher. The last figure (see Fig. 6.6) presents the flow pattern at a stable state. The maximum value of the total velocity has increased to a stable level, and the distribution of the maximum value is concentrated at the boundary of the swirl which has a radius approaching the top outlet radius.

2. **Vector diagrams**

In addition to the streamline graphs, vector diagrams can be used to analyse the flow patterns of cyclones. The following figures (From Fig. 6.7 to Fig. 6.12) show the distribution of the 3D velocity vector in the 2D plane. Similar to the streamline graphs, the analysis of the vector diagrams is performed in transient state. Fig. 6.7 presents the vector diagram at 0.2s. Combined with the streamline graph in Fig 6.1, the overall flow pattern presents the trend of a large swirling flow. A small non-axisymmetric vortex emerged near the vortex finder, and most of the fluid tended to flow out through the bottom outlet. The vector diagram at 0.4s (see. Fig 6.8) exhibits the small non-axisymmetric vortex dissipated, and a vortex appeared near the apex of the conical part. The fluid inside the cyclone tended to flow out through both outlets. From 0.6s to 1.0s (see. Fig. 6.9 to Fig. 6.11), the vector diagram shows a process in which the flow pattern gradually stabilised. The turbulence near the apex of the conical part was fixed, and another turbulence was generated at the bottom of the vortex finder. The reason for these two turbulences can be attributed to the backflow. Lastly, Fig. 6.12 shows the outer swirling flow tended to flow downwards and met the turbulence that appeared near the bottom outlet. The inner swirling flow tended to flow upwards and formed turbulence near the bottom of the vortex finder.

3. **Contour plots**

In terms of the contour plots, the results are divided into three groups for comparison. These are the pressure contour, tangential velocity contour map and axial velocity contour.

● Pressure contour: The figures (see Fig. 6.13 to Fig. 6.15) in the first group present the pressure contours obtained using two different turbulence models and without using turbulence models. In these contour plots, the pressure increases from the core to the wall. The difference shown in these contour plots is that the pressure gradient has a different magnitude. Although the value of the pressure has no practical physical meaning in the results, the pressure gradient is an important feature in the calculation of the Navier-Stokes equations. The change in colour reflects the change in the pressure gradient. Compared with Fig. 6.15, the areas of dark blue to light blue in Fig. 6.13 and Fig. 6.14 are larger, and the areas of orange to bright red are smaller in Fig. 6.14.

- Tangential velocity contour: The tangential velocity contour plots demonstrate an obvious difference in the outer part of the swirling flow. In Fig. 6.16 and Fig. 6.18, the maximum value of the tangential velocity is located at the halfway point between the core and the wall, but Fig. 6.17 shows the maximum value is distributed at the whole outer part of the swirling flow

- Axial velocity contour: In terms of the axial velocity contour, the difference is more conspicuous. The axial velocity contour plot (see Fig. 6.19), obtained without using the turbulence model, shows that the maximum axial velocity is a Y-shaped distribution in the separator. In the upper half of the cyclone, the axial velocity shows an upward trend along the vortex finder tube wall. In the lower half of the cyclone, the maximum axial velocity is concentrated in the central part. Fig. 6.20 presents the axial contour plots obtained using the $k - \varepsilon$ turbulence model. The maximum value of the axial velocity is distributed near the wall of the vortex finder tube. At the main body of the cyclone separator, the value of the axial velocity is distributed evenly, except that the minimum value of the axial velocity is distributed near the wall of the bottom outlet pipe. The RSM turbulence model provides an axial velocity contour plot (see Fig. 6.21), which shows that the maximum value of the axial velocity extends from the top outlet along the vortex finder wall to the bottom outlet. The red stripes formed by the maximum value are distributed in parallel.

(0.2s)	(0.4s)	(0.6s)
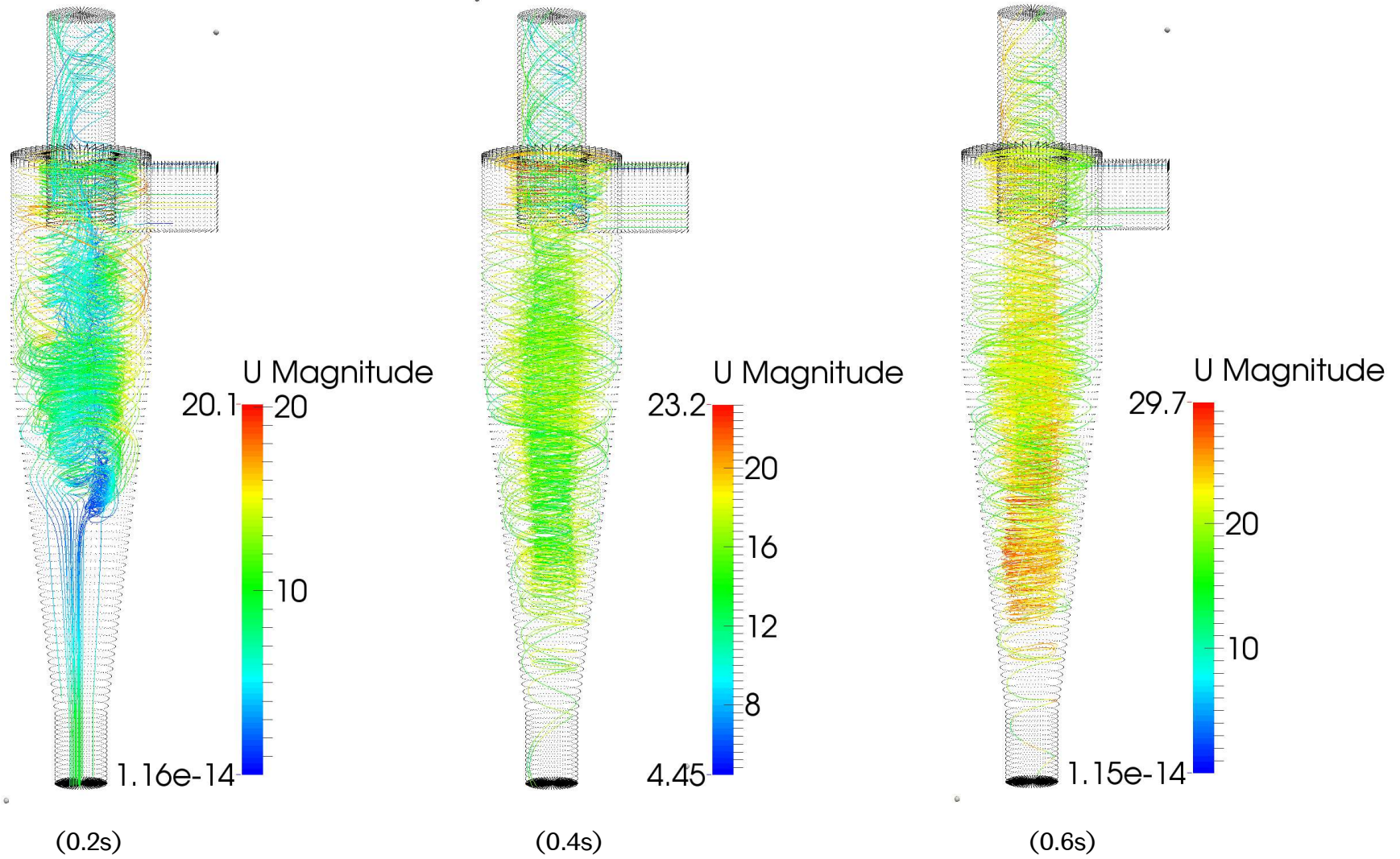
Fig. 6.1 to 6.3. Streamline graph of the cyclone flow at different time step

U Magnitude — 32.7, 30, 20, 10, 0.296

U Magnitude — 35.9, 30, 20, 10, 1.15e-14

U Magnitude — 35.9, 30, 20, 10, 1.15e-14

(0.8s)   (1.0s)   (Steady)
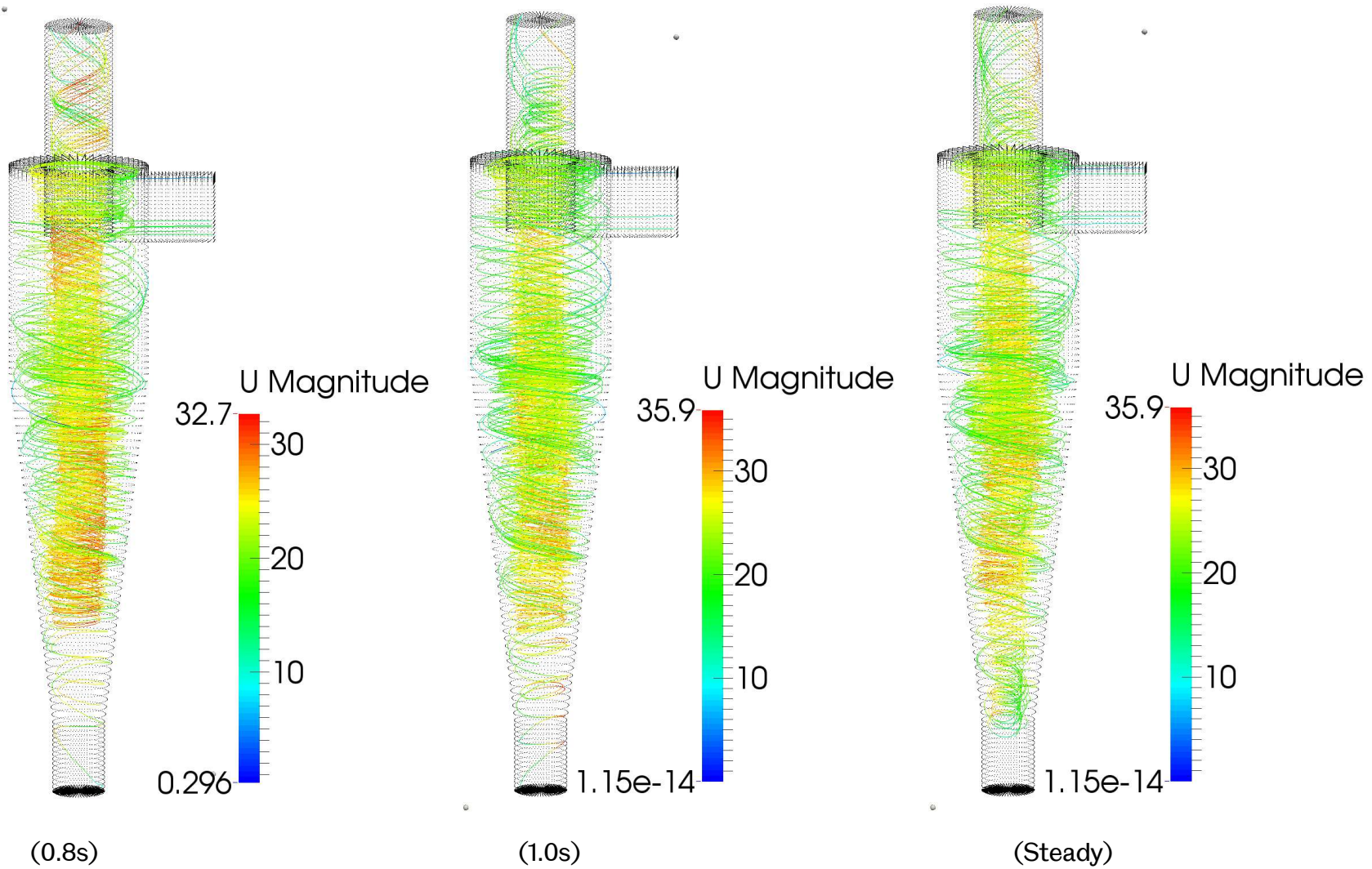
Fig. 6.4 to 6.6. Streamline graph of the cyclone flow at different time step
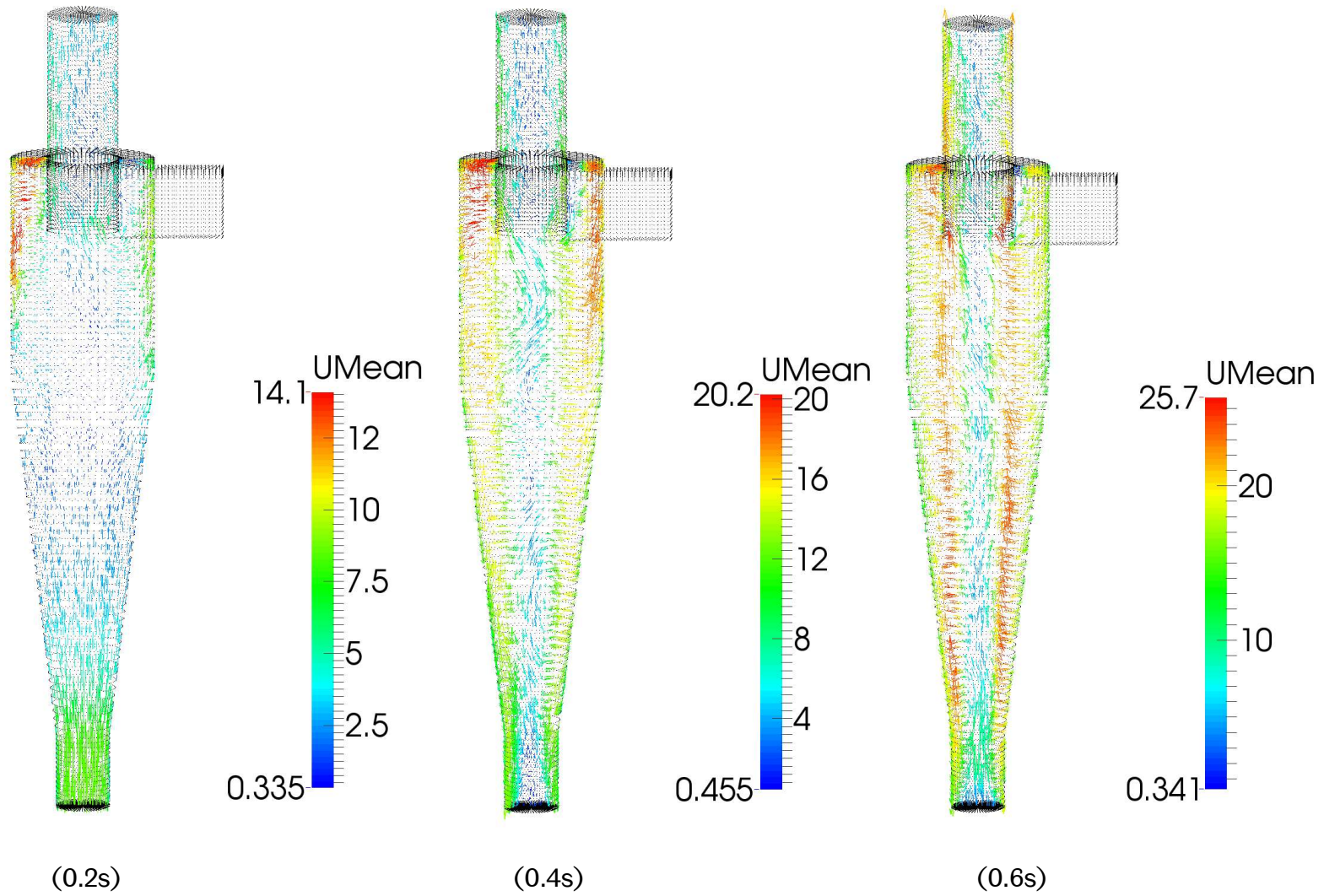
(0.2s)   (0.4s)   (0.6s)

Fig. 6.7 to 6.9. Vector plot of the cyclone flow at different time step (Front view)

(0.8s)   (1.0s)   (Steady)
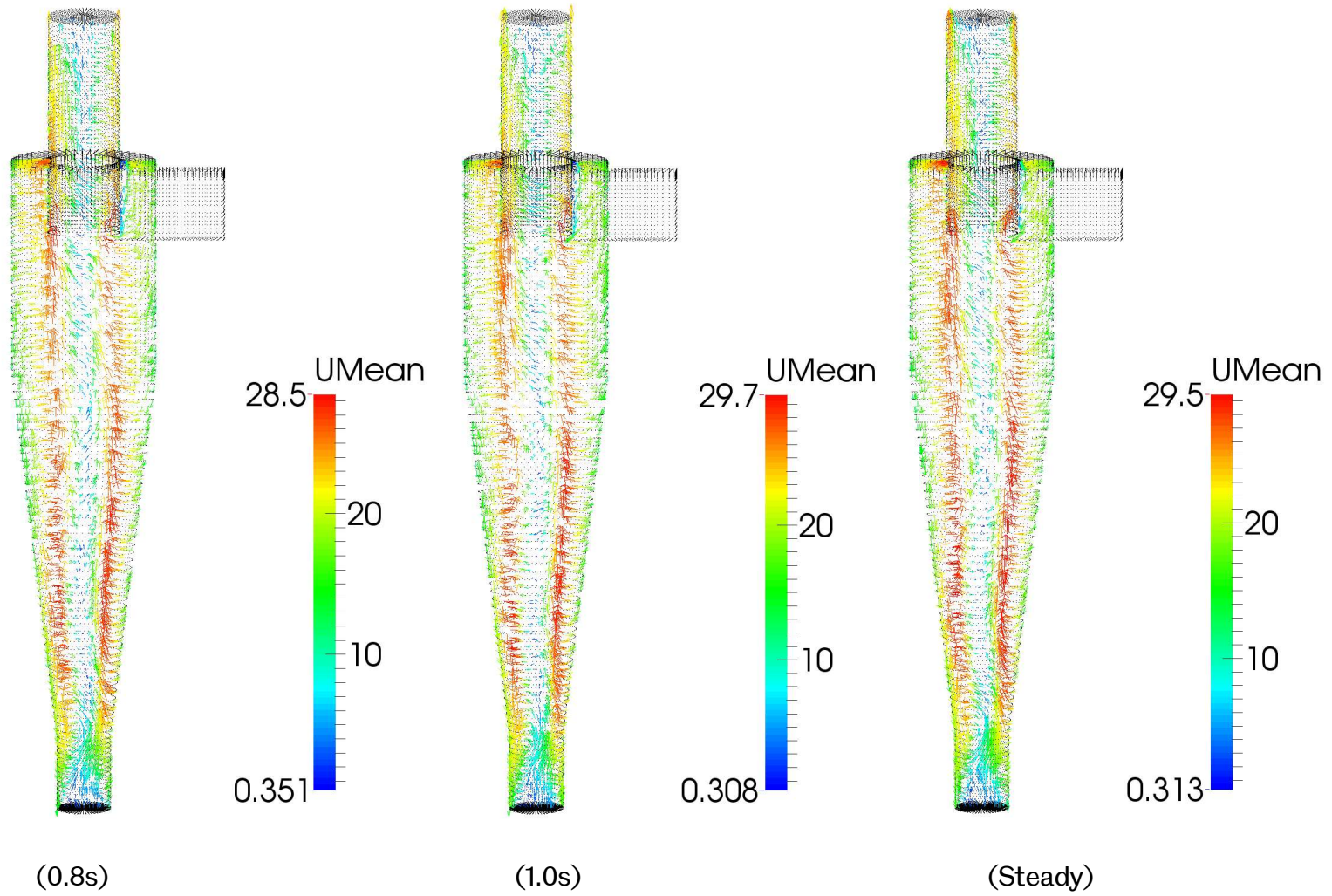
Fig. 6.10 to 6.12. Vector plot of the cyclone flow at different time step (Front view)

(0.2s)

(0.4s)

(0.6s)
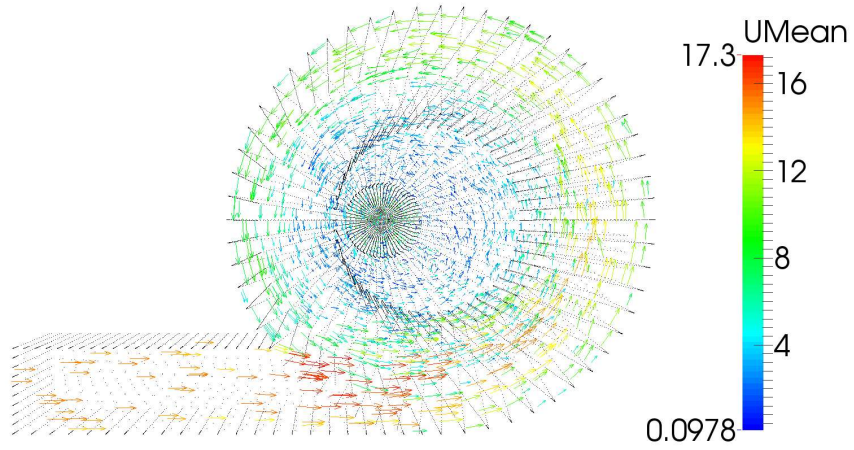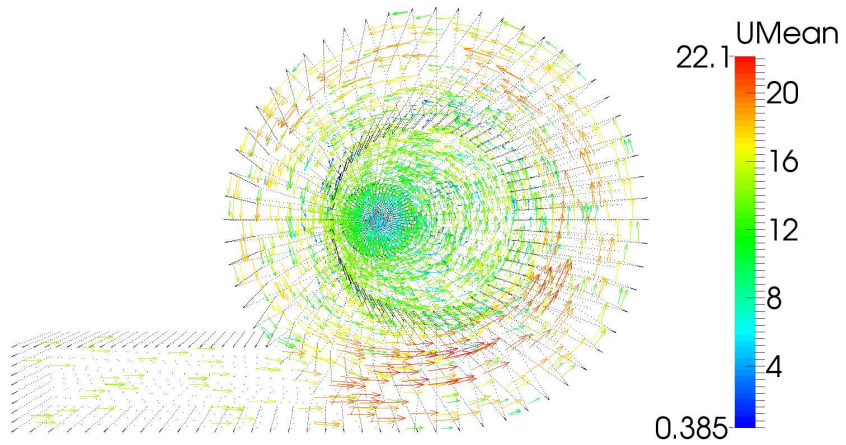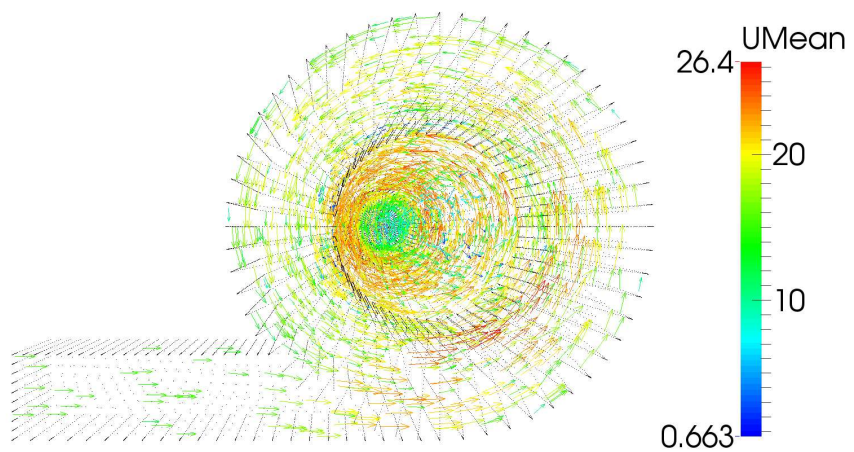
Fig. 6.7 to 6.9. Vector plot of the cyclone flow at different time step (Top view)
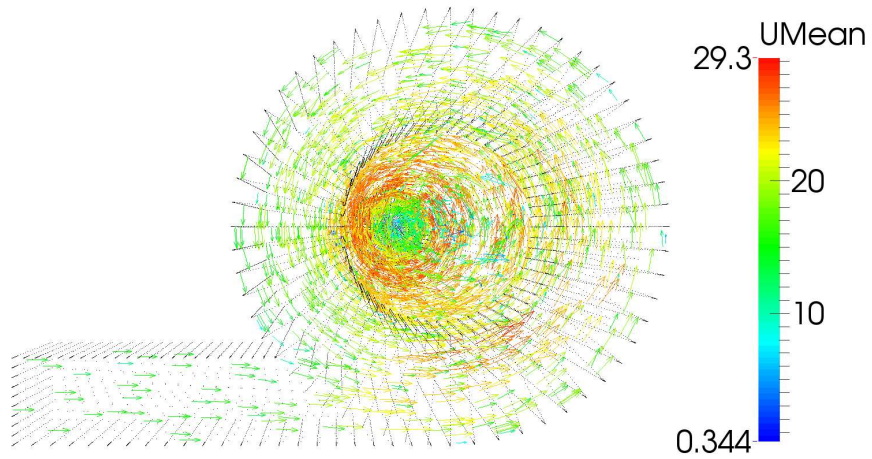
(0.8s)
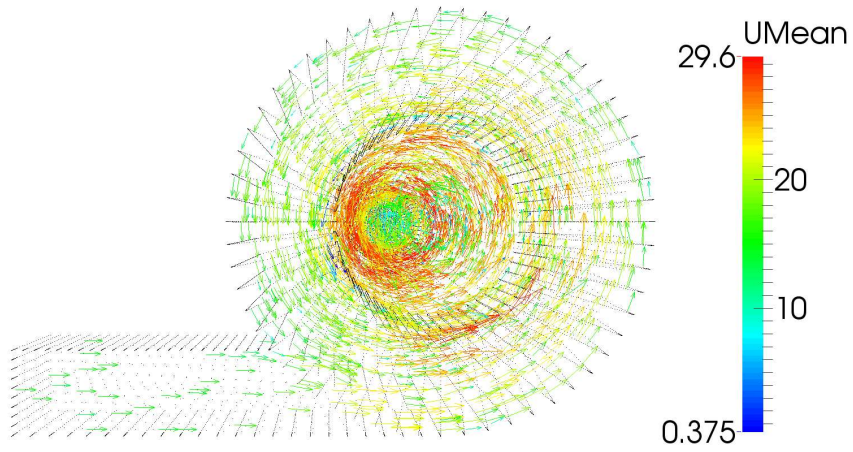
(1.0s)
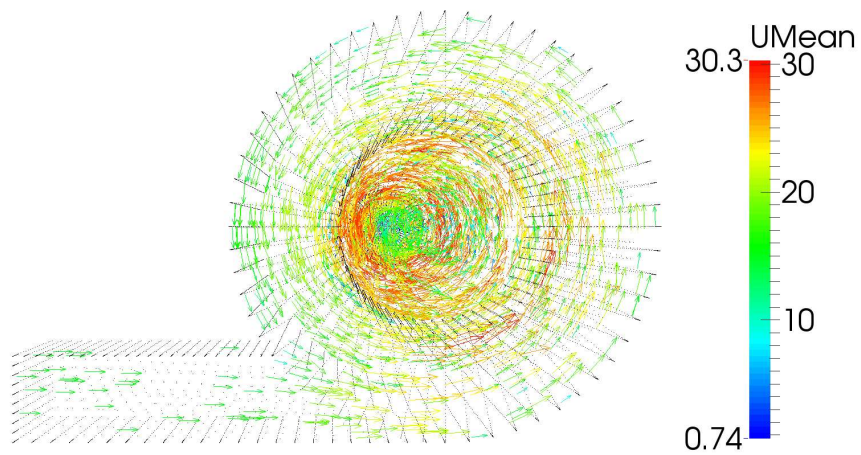
(0.6s)

Fig. 6.10 to 6.12. Vector plot of the cyclone flow at different time step (Top view)
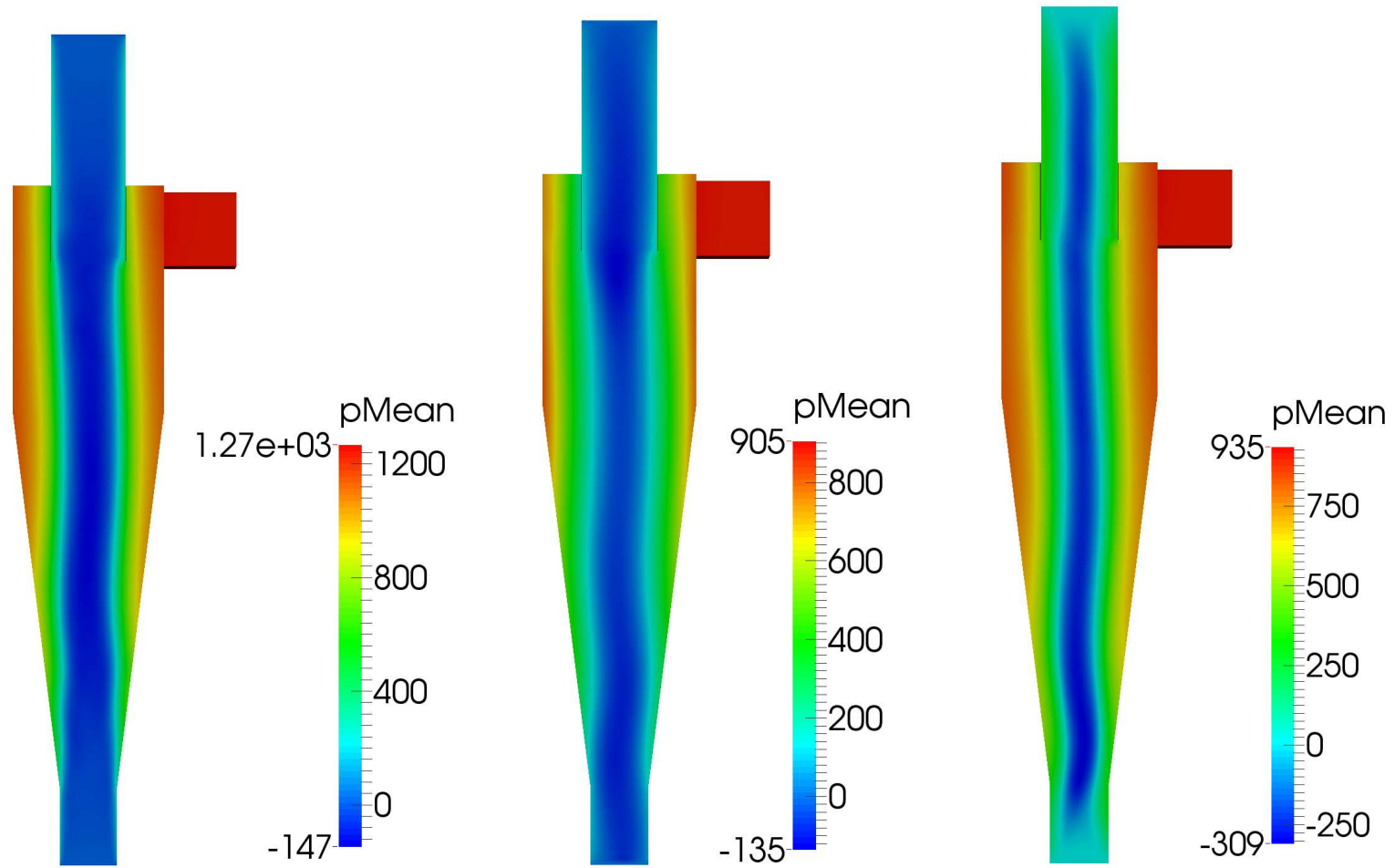
(Non Turbulence model)　　　($k - \varepsilon$ Turbulence model)　　　(RSM Turbulence model)

Fig 6.13 to Fig. 6.15. Contour plots of the pressure field

(Non Turbulence model) $(k - \varepsilon$ Turbulence model)   (RSM Turbulence model)
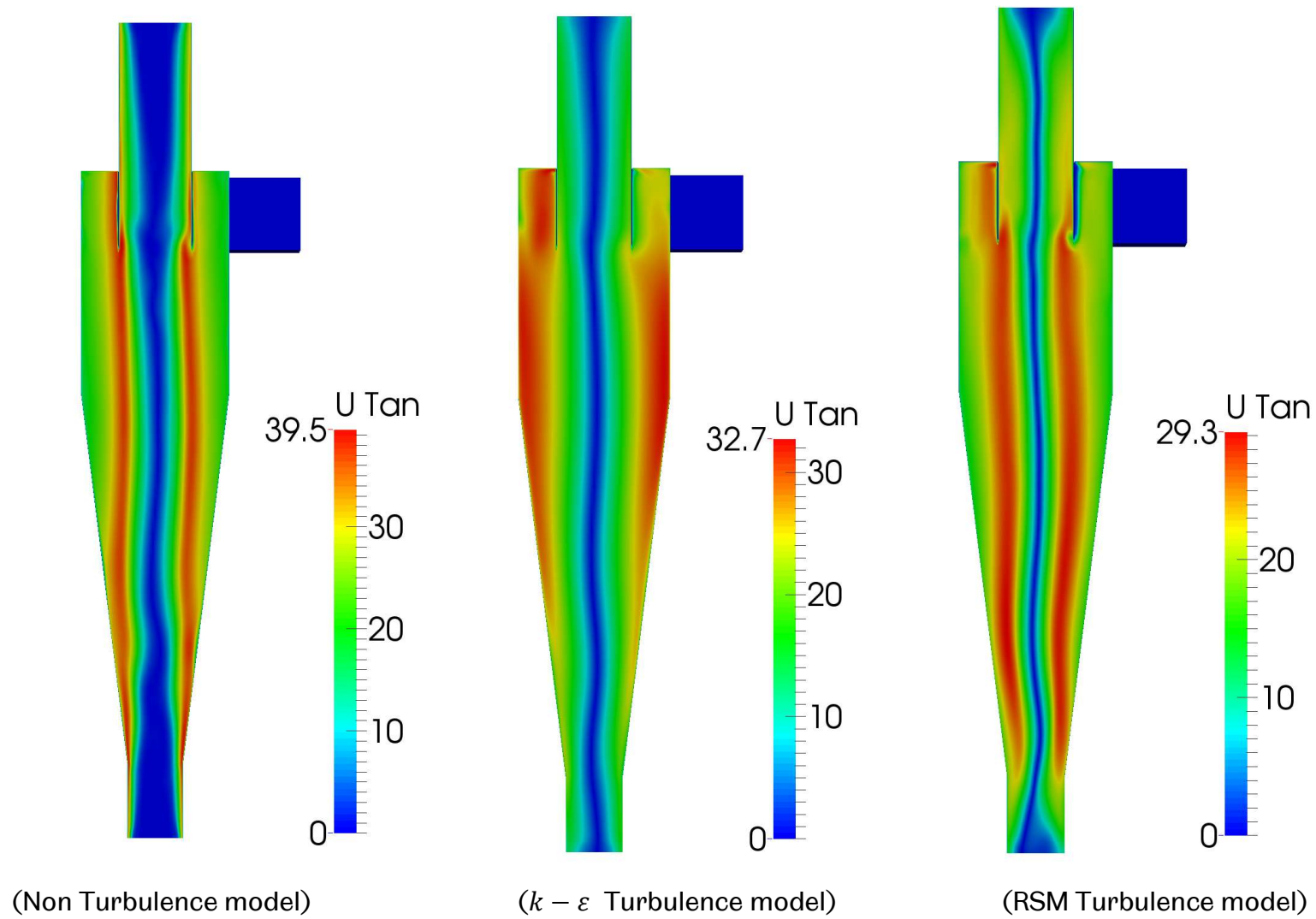
Fig 6.16 to Fig. 6.18. Contour plots of the Tangential velocity field
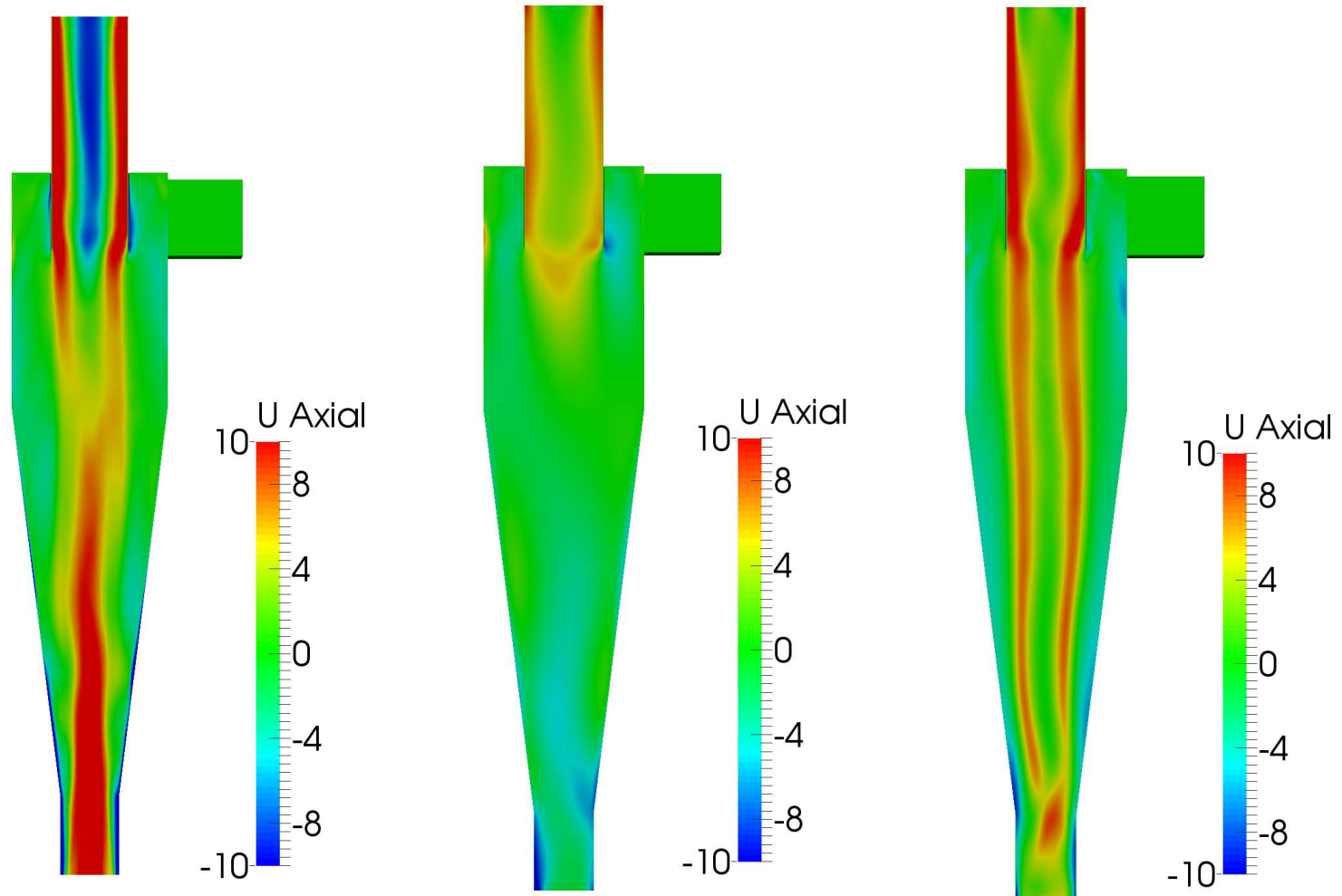
(Non Turbulence model)   ($k - \varepsilon$ Turbulence model)   (RSM Turbulence model)

Fig 6.19 to Fig. 6.21. Contour plots of the Axial velocity field

6.3 Discussion

Using the curve graphs is necessary to compare the simulation results more intuitively. Thus, three physical quantities of the simulation result are used for comparison: pressure, velocity, and kinetic energy. The experimental data used for validation were obtained by Hoekstra (2000). The horizontal position of the observation levels is shown in Fig. 6.22.

1. Pressure

The first group for comparison is the pressure curve graphs. These plots provide a more explicit comparison of the issue of pressure gradients. As per Fig. 6.22, four horizontal observation levels are used for data collection. At the first level $h = 1.5D$ (see Fig. 6.23), the pressure curve obtained by the RSM turbulence model has a larger maximum and a smaller minimum, so the pressure gradient is also larger. It can be seen from the remaining three pressure curve graphs (see Fig. 6.23a to Fig. 6.23d) that as the horizontal level rises, the difference between the maximum and minimum pressures obtained through different turbulence models gradually narrows. However, if the cyclone is divided into an inner ring and an outer ring; it can be seen from the figures (see Fig. 6.23a to Fig 6.23d) that the curve obtained by the RSM turbulence model has a larger value of pressure gradient in the inner ring, whereas the pressure gradient value in the outer ring gradually decreases. The curve obtained by the $k - \varepsilon$ turbulence model shows a nearly fixed pressure gradient value.
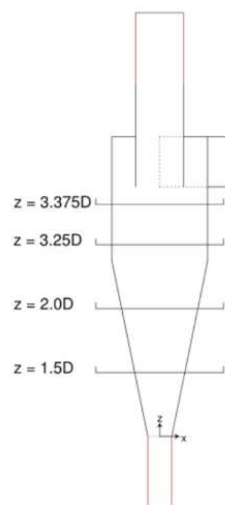

Fig. 6.22 The positions of the observation levels. (Alahmadi and Nowakowski, 2016)
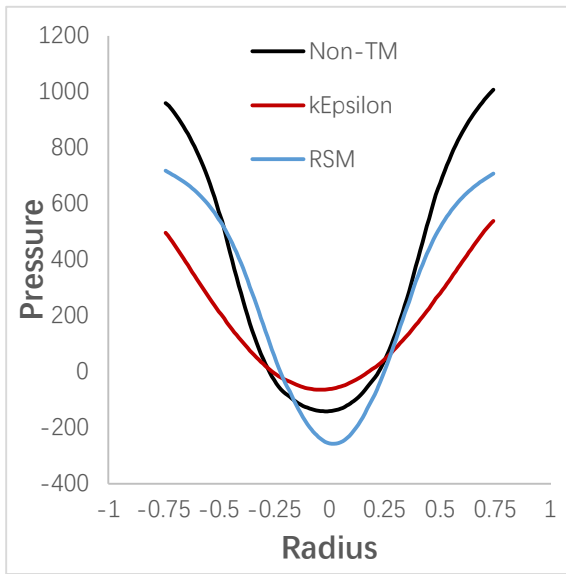
a (z = 1.5D)
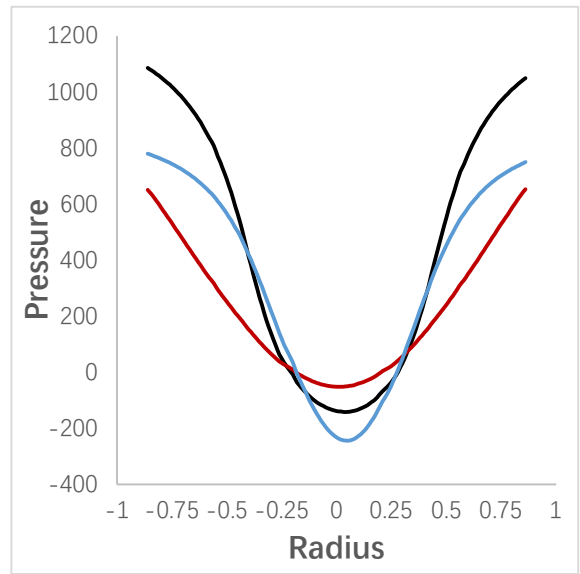
b (z = 2.0D)
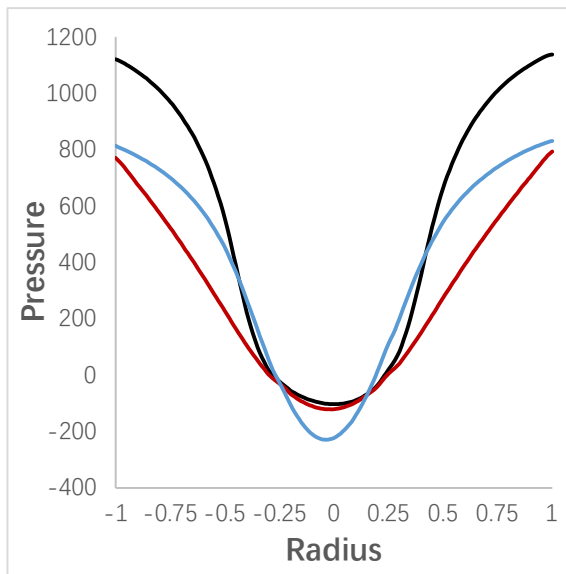
c (z = 3.25D)
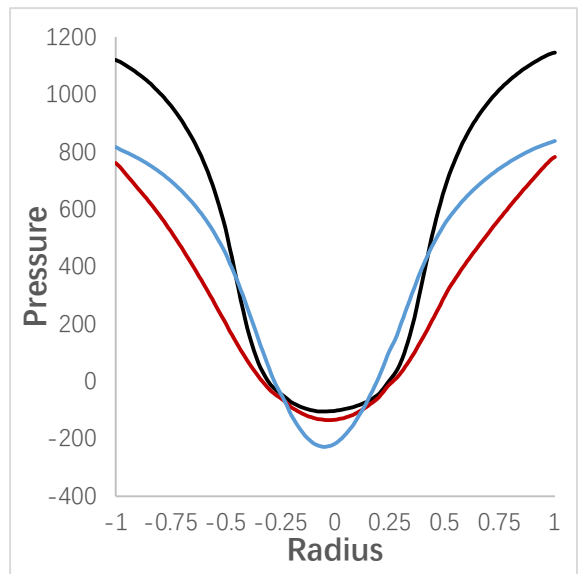
d (z = 3.375D)

Fig.6.23. Profile of the Pressure field at different observation levels.

2. Velocity

The variation patterns of the tangential velocity and axial velocity are presented on the following plots. Comparing the velocity curves obtained by the numerical simulations and experiment (Hoekstra, 2000) in Fig. 6.24 and Fig. 6.25, the following information can be obtained;

- Tangential velocity: The variation pattern of the tangential velocity (Rankine vortex) can be restored by the simulation without using turbulence models, but the value of the tangential velocity has been overestimated.

  The tangential velocity curves, which were obtained using the $k - \varepsilon$ turbulence model are inaccurate in the aspect of variation pattern. The aforementioned "Rankine vortex" cannot be captured by the $k - \varepsilon$ turbulence model. More specifically, at the first and second observation levels ($h = 1.5D$ and $h = 2.0D$), the tangential velocity enlarges gradually from the cyclone's core to the borderline of boundary layer flow. In the third and fourth observation levels, the growth trend of the velocity curves becomes more moderate in the middle position between the core and the wall. Comparing the curve with the experimental results, the middle position between the core and the wall is also the position where the Rankine vortex changes from the solid-body rotation to a free vortex.

  As an extension of the $k - \varepsilon$ turbulence model, the $k - \varepsilon$ RNG model and $k - \varepsilon$ RNGCC model exhibit more accurate tangential velocity curves, especially the $k - \varepsilon$ RNGCC model. Even at the first and second observation level, the obtained tangential velocity curves obey the rule of the "Rankine vortex".

  Finally, the RSM turbulence model provides an accurate prediction in terms of the tangential velocity curves. The curves are well matched with the experimental results at all the observation levels.

- Axial velocity: In terms of the axial velocity, the curves obtained without using the turbulence model are incorrect in the first and second observation levels. The axial velocity curves present an inverted "V" pattern, which does not match with the experimental results. Regarding the third and fourth observation levels, the simulation without using turbulence models produced a reasonable variation

curve. A pit located near the centre of the cyclone and the curve presents an inverted "w" pattern.

The $k - \varepsilon$ turbulence model provides incorrect axial velocity curves at all the observation levels. Although the curves look smoother than the non-TM curves, they cannot match the experimental curves, either in pattern or in value. This inaccurate prediction does not improve much when using the $k - \varepsilon$ RNG model and $k - \varepsilon$ RNGCC model


a (z = 1.5D)   b (z = 2.0D)
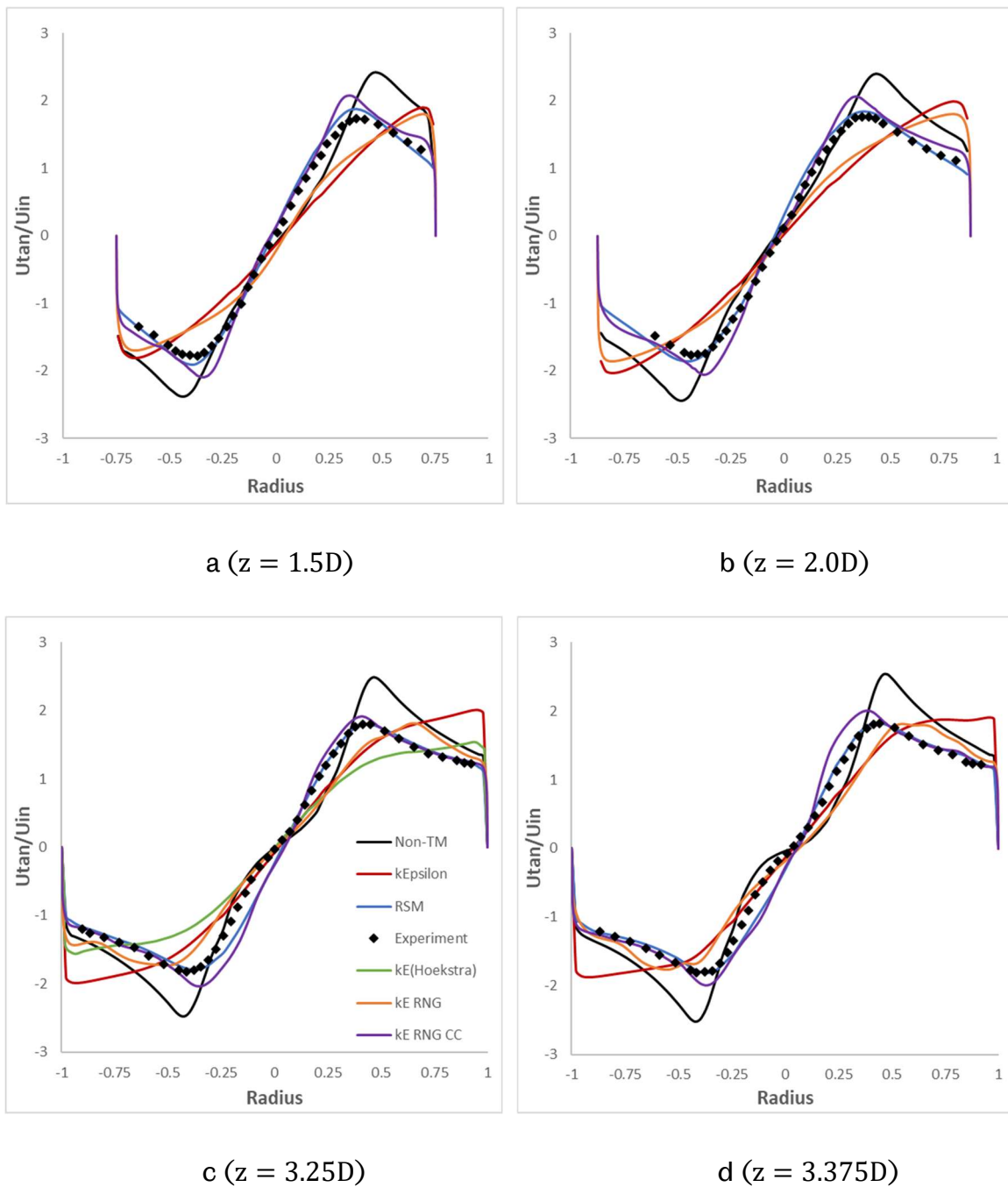
c (z = 3.25D)   d (z = 3.375D)

Fig.6.24. Profile of the tangential velocity field at different observation levels
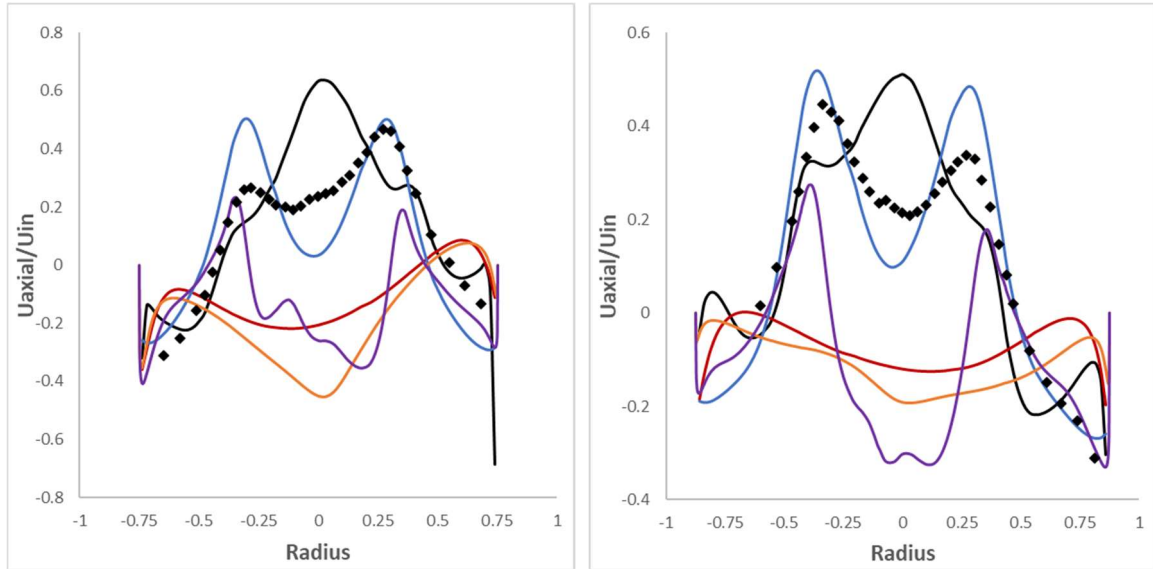
a (z = 1.5D)   b (z = 2.0D)
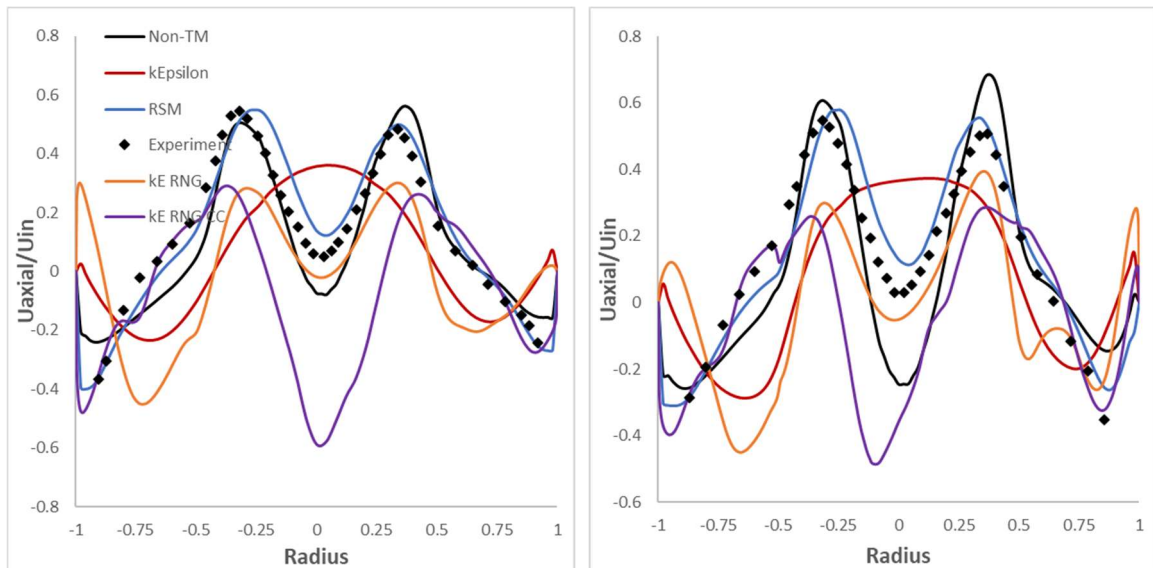
c (z = 3.25D)   d (z = 3.375D)

Fig.6.25. Profile of the axial velocity field at different observation levels

The curves obtained by the RSM turbulence model are much more accurate than the other two methods. The curves match the experimental curves in the aspect of the curve pattern. The only defect shown in Fig 6.25a is that the maximum values are slightly overestimated.

3. Kinetic energy

The kinetic energy k is a physical quantity used to assess the accuracy of turbulence models in the RANS method. It has been discussed that in the RANS method (Section 3.5), the velocity fields can be separated into the mean velocity component and fluctuating velocity component

$$u_i = \overline{u_i} + u_i{'}$$

Furthermore, the kinetic energy is calculated by the fluctuating velocity component in three directions (two directions in a 2D environment).

$$k = \frac{1}{2}\overline{u_i' u_i'} = \frac{1}{2}\left(\overline{u_x' u_x'} + \overline{u_y' u_y'} + \overline{u_z' u_z'}\right)$$

In the $k - \varepsilon$ turbulence model, the kinetic energy is directly used for calculating the turbulence viscosity and Reynolds stress term,

$$\tau_t = -\rho\overline{u_i' u_j'} = \mu_t \left(\frac{\partial \overline{u_i}}{\partial x_j} + \frac{\partial \overline{u_j}}{\partial x_i}\right) - \frac{2}{3}\rho k \delta_{ij}$$

$$\mu_t = C_\mu \frac{k^2}{\varepsilon}$$

However, in the RSM model, the value of the kinetic energy needs to be calculated using the Reynolds stress term

$$R_{ii} = \overline{u_i' u_i'}$$

$$k = \frac{1}{2}\left(R_{xx} + R_{yy} + R_{zz}\right)$$

As a result, the profile of the kinetic energy is given in Fig. 6.29.

From Fig. 6.29(c) and Fig. 6.29(d), it can be found that the kinetic energy curve obtained using the $k - \varepsilon$ turbulence model presents an inverted "W" pattern. The two vertices are located near the midpoint between the centre of the cyclone and the wall.

Compared with the curve obtained by the $k - \varepsilon$ model, the other three curves present irregular curves that are approximately horizontal straight lines. Among them, the value of the kinetic energy obtained by using the $k - \varepsilon$ RNGCC model is the smallest, followed by the RSM model. The values on the three curves are much

smaller than the values obtained by the $k - \varepsilon$ model, and the difference between them is not obvious

The profile of the kinetic energy curve is more diverse at the first and second observation levels (see Fig. 6.29(a) and Fig. 6.29(b)). The curve presented by the $k - \varepsilon$ RNGCC model is close to zero at the centre of the cyclone separator. This indicates that there is almost no turbulence in the solid rotation part.
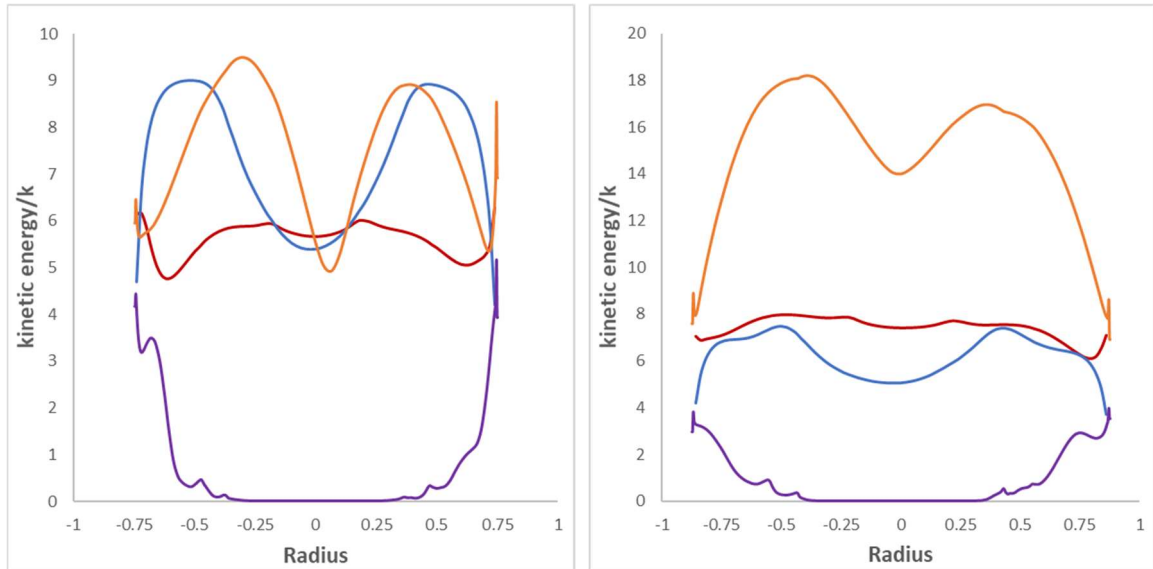
a (z = 1.5D) b (z = 2.0D)
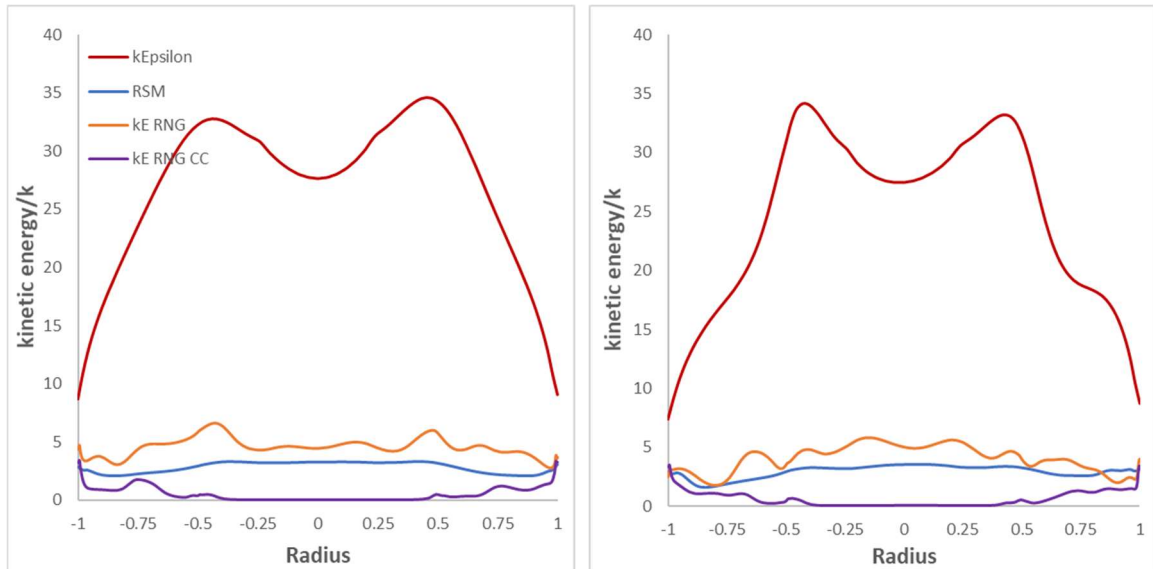
c (z = 3.25D) d (z = 3.375D)

Fig.6.26 Profile of the kinetic energy at the fourth observation level

4. Cyclone performance and efficiency

The parameters of the collection efficiency and the pressure drop are used to demonstrate the performance of the cyclone separator. From Eqn. 3.67, it can be found that the drag force term is the main factor in separating particles in different sizes flowing out from different outlets. The centrifugal force applied to the larger diameter particles causes them to flow downward along the cyclone wall and exit through the bottom outlet. In addition, the centrifugal force and the pressure drop are related to the magnitude of the tangential inlet velocity. Both increase proportionally as the inlet velocity increases. Thus, the design of a cyclone often requires an optimal combination between the parameters of collection efficiency and the pressure drop. The material of the injected particles is defined as limestone, and the simulation result of the current study is verified by Hoekstra's (2000) experiment.

The injected particles are divided into seven levels according to the diameter. The maximum diameter is $3.5E - 6m$ and the minimum is $8E - 7m$. The DPM solver was operated with a total mass flow rate of 0.001kg/s, and the maximum number of steps was 200,000. The efficiency is calculated by the following equation.

$$\eta = \frac{trapped}{injected - suspended}$$

The particles are injected from the tangential inlet, and the particles ejected through the bottom outlet are set as trapped.

From Fig. 6.27, it can be found that the curves of the collection efficiency obtained by the RSM model and the $k - \varepsilon$ RNGCC model are highly consistent with the experimental curves. The curve obtained by the $k - \varepsilon$ RNG model shows that the simulation result underestimates the collection efficiency for larger diameter particles.

The Euler number of the pressure drop obtained by the RSM model and $k - \varepsilon$ RNGCC model are $Eu = 5.4$ and $Eu = 5.8$, respectively, which are acceptable compared with the value $Eu = 5.1$ obtained by the experiment. The formula of the pressure drop Euler number is given by

$$Eu = \frac{\Delta P}{\frac{1}{2}\rho u^2}$$
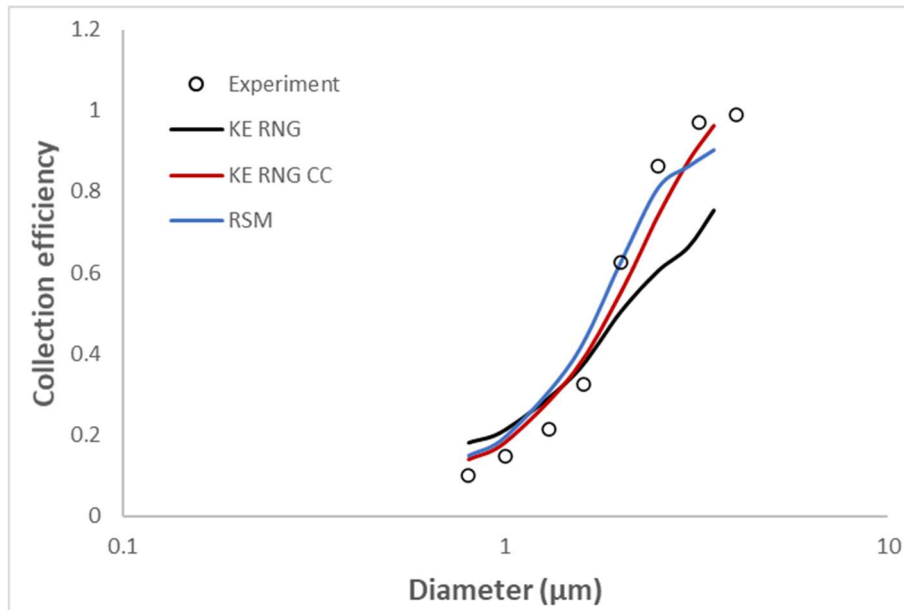
Fig. 6.27 Collection efficiency curves obtained by different turbulence models compared to the experiment measurement.

6.4 Summary

Based on the simulation of single-phase flow in cyclones, some theories and ideas have been verified. These are summarized in following text.

1. The characteristic of the "Rankine vortex" has been captured by the simulation without using turbulence models. Although the value is not accurate enough, it still successfully estimates the position of the maximum and gives an acceptable variation pattern. In terms of the simulation that used the standard $k - \varepsilon$ turbulence model, the curves of the tangential velocity seem smoother. However, it cannot predict a correct variation curve due to an inaccurate simulation result of the turbulence viscosity based on the Boussinesq's hypothesis. Thus, a more accurate calculation of the turbulence viscosity was provided by the $k - \varepsilon$ RNGCC model. The simulated tangential velocity values are acceptable compared with the experimental data. In terms of the results predicted by the RSM model, the tangential velocity curves are accurately matched with the experimental curve.

2. Regarding the axial velocity curve, this should be shown as an inverted "W" pattern. The simulation method without using turbulence models can achieve a similar result at the third (Z = 3.25D) and fourth (Z = 3.375D) observation points, but the maximum value has been overestimated. In the aspect of the first (Z = 1.5D) and second (Z = 2.0D) observation levels, the simulation results produced inverted "V" pattern

curves, which are incorrect. The simulation method with the $k - \varepsilon$ turbulence model cannot predict the proper curves as either. Although the axial velocity curve shows an inverted "W" pattern with two vertices at the first and second observation levels, the location of the maximum value is inaccurate. At the third and fourth observation levels, the results present a regular variation curve, but the concave near the centre was not predicted. The result of the axial velocity obtained by the simulation using the RSM model presents a curve matched with the experimental result. The inverted "W" pattern of the axial velocity curve has been captured, and the value of the axial velocity predicted by the simulation is acceptable.

3. The simulation results of the turbulent kinetic energy can be used to detect whether the turbulence model correctly estimates the value of the perturbation velocity. In the current study, the curve of the kinetic energy obtained by the $k - \varepsilon$ turbulence model presents a different pattern compared with the curve obtained using the RSM turbulence model. In the upper half of the cyclone, the value of the turbulent kinetic energy predicted by the $k - \varepsilon$ turbulence model was overestimated in the solid-rotation region and free-rotation region.

4. The collection efficiency and pressure drop, predicted by numerical simulations, are consistent with the experimentally obtained predicted value at different levels. The result shows that the particle tracking method based on the Lagrangian-Eulerian model is largely affected by the turbulence model. A suitable turbulence model can predict the value of the flow fields accurately in the continuous phase, and the value of flow fields in the continuous phase directly affects the calculation of the particle equilibrium equation.

As the fundamental simulation for the study of the flow in cyclone and hydrocyclones, the simulation of single-phase cyclone flow includes various important physical theories and CFD principles that need to be understood. From the complicated modelling process to the selection of turbulence models, each process needs to be carefully considered. In summary, the current simulation shows that the RSM model is suitable for the simulation of cyclone flows, which involve large swirls and anisotropic flow. Furthermore, the current simulation provides valuable experience in other aspects such as optimization of modelling and selection of algorithms and schemes.

Chapter 7. Simulation of the dam breaking flow

7.1 Case introduction

The simulation of the dam breaking flow is considered to be a suitable fundamental study due to the simulation of the flow with air-core in hydrocyclones also being a multi-phase flow problem. The geometry used in the simulation is easy to build, and it is efficient to test the performance of the multi-phase flow solver. The Reynolds Averaged Naiver-Stokes equation (RANS) method and the developed VOF technique are utilized to cope with the two-phase flow and the free-surface.

The multi-phase solver used for simulations is called interFOAM and used a PIMPLE algorithm for calculations. As it is known that the SIMPLE algorithm in the PIMPLE algorithm is used to simulate the steady state of the flow at each time step, the number of the SIMPLE iteration loop may influence the simulation result. As such, in the current simulation, the number of the SIMPLE iteration loop is set as 20 to ensure the simulation result meets the convergence criterion in each time step. The schemes in the second-order of accuracy are used for the discretisation of the volume fraction equation, continuity equation and momentum equation.

The technologies introduced in Chapter 4 are applied to optimise the solution of the volume fraction equation. They are the Multidimensional Universal Limiter with Explicit Solution (MULES) algorithm and the High-Resolution schemes (HRS) technique.

The final results present the dimensionless vertical position of the free-surface against simulation time. A comparison between the results of the simulations using different mesh sizes and different turbulence models is presented. The number of meshes used in the simulations increased from 1600 cuboids to 25600 cuboids.

The other extended study focuses on the performance of the solver when using different turbulence models. The turbulence models used for simulations are the $k - \varepsilon$ turbulence model and the RSM turbulence model. Due to the fluid flowing inside the tank being a multi-phase flow, the viscosity and density need to be calculated through substituting volume fractions into the equation. The volume

fraction is equal to one for the liquid phase, and it is equal to zero for the air phase. Since the free-surface has the volume fraction with $0 < \alpha < 1$, the density and viscosity of the free-surface are calculated by

$$\rho = \gamma \rho_{liquid} + (1 - \gamma)\rho_{air}$$

$$\mu = \gamma \mu_{liquid} + (1 - \gamma)\mu_{air}$$

The density and viscosity of the liquid is set as $1 \times 10^3 \ kg/m^3$ and $1 \times 10^{-6} \ m^2/s \cdot s$. The density and viscosity of the air is set as $1.2 \ kg/m^3$ and $1.48 \times 10^{-5} \ m^2/s$

7.2. Simulation results

The velocity field and the pressure field are not the key points for the current simulation. The simulation results of the dam breaking flow are presented focusing on the volume fraction field. Due to the simulation being executed based on the PIMPLE algorithm, the transient states of the dam breaking flow are posted in the following figures (see Fig. 7.1 to Fig. 7.4) for investigations. These simulation results are given with aim to determine the position of the free-surface between liquid and gas. The recorded time step is set as one frame per 0.05s, and the end time of the simulation is assigned at 2.5s.

The first group of figures (see Fig. 7.1) demonstrates the simulation result compared with the experiment pictures taken by Cruchaga (2007). The simulation result is obtained through the simulation using 25600 cuboids without using turbulence models. The experiment picture at the initial state presents that the water was segregated by a plant in the tank; this initial state was also restored in the numerical simulation method. After the plant was removed, the liquid fluid flowed to the right wall, reaching the highest point at $t = 0.5s$ and it bounced back to the left wall after 0.5 seconds. Although the free-surface was still raised when it had contact with the left wall, it did not reach the same height, as $t = 0.5s$ shows. After this, the liquid fluid flowed to the right-hand side again. The free surface will be calm after this swinging motion has been repeated many times. Fig. 7.2 presents the simulation results in different mesh sizes. In general, the flowing behaviour is the same, but they still have some differences. Through observing these figures, the detections are summarized below:

- It is obvious that the thickness of the interface between liquid and gas becomes sharper when accompanied with the mesh size growing denser. In addition, the shape of the free-surface becomes more complicated.

- As the grid size decreases, the resolution of the volume fraction distribution picture increases with more bubbles appearing in the liquid phase.

The simulation results, obtained by using the $k - \varepsilon$ turbulence model and the RSM turbulence model, are shown in Fig. 7.3. Compared with the results yielded without using the turbulence model, the results obtained by using the $k - \varepsilon$ turbulence model present different flow patterns and the results obtained by using the RSM turbulence model produce similar flow patterns at each recorded time point.

Fig. 7.4 presents the velocity vector plots of the dam breaking flow at each recorded time step. Using vector plots can help analyse the flow trends of the water phase. In addition, the air phase is also affected by the water phase and causes irregular movements. The topside of the tank is open to the atmosphere, so air and water can flow back from the topside during the dam breaking.

7.3 Discussion

In regard to the mesh convergence study of the dam breaking flow, three different mesh numbers were used; the number of meshes is defined as $40 \times 40, 80 \times 80$ and 160×160. Due to the current simulations being unsteady problems, the results used for the mesh convergence study were selected based on the fixed space and fixed time. Four time-points (0.5s, 1s, 1.5s and 2.0s) were used for comparison. They were chosen because of the water line approach to the highest level at these time points. The space points were assigned according to Cruchaga's (2007) experiment and are located at $x = 0m$, $x = 0.27m$, and $x = 0.42m$.

From these figures and tables, it can be found that the simulation has met the mesh convergence criterion in most situations. The convergence ratio is calculated by

$$R = \frac{\phi_2 - \phi_1}{\phi_3 - \phi_2}$$

Where, ϕ represents the numerical solution of a local or functional variable. The subscripts $1, 2$ and 3 indicate the grid size from fine to coarse.

Some of the convergence parameter, R equals zero, is due to the simulation result being same when mesh numbers are equal to 80×80 and 160×160. Although in Table 7.1b, one of the parameters exceeded the convergence limitation, this excess value can be ignored since the simulation result is close between different mesh sizes. A space-time graph is shown in Fig. 7.6a to Fig. 7.6c. These figures give a more intuitive comparison between the simulation results obtained by using different mesh sizes. Furthermore, the experiment data from Cruchaga's (2007) paper are posted on the graph.

In Fig. 7.6a, the experiment plots indicate the free-surface declined to a lower position and bounced back to the highest level in the first second. This behaviour is also precisely predicted by the numerical simulation. After the free-surface reached the highest point, it dropped back to the lowest level again. A small fluctuation occurred before the second rise of the free-surface around 1.5 seconds. The fluctuation is captured by the numerical simulation when using higher mesh numbers. Between 1.5 seconds and 2 seconds, the free-surface again completed another set of rising and falling processes. Regarding the second upswing process, the simulation results show nearly a 0.3 second delay compared with the experimental data.

The second space-time graph (see Fig. 7.6b) shows the fluctuation of the free-surface at the middle observation point. Three obvious fluctuations appeared between 0s and 2s. All the fluctuations were accurately predicted by the numerical simulation. Compared with the experimental data, the occurrence time of the three fluctuations has a delayed prediction by the numerical simulation, but the dimensionless vertical position of the fluctuations is predicted precisely, especially when using the finest grids.

In regard to the third figure (Fig 7.6c), the same problem is displayed in the graph. Even though the simulation result is reliable in the aspect of the dimensionless vertical position and movement, the prediction of occurrence time is still inaccurate. Two large peaks appear around 0.5 seconds and 1.5 seconds, and there is a small fluctuating movement between them. The simulation results present the lowest dimensionless vertical position of the fluctuation equal to zero, which is different from the experimental result.

The next group of figures (From Fig. 7.7a to Fig. 7.7c) present the simulation result obtained by using different turbulence models. It shows that the plots predicted by using the $k - \varepsilon$ turbulence model differ considerably from the plots predicted by the other models. The plots predicted using the RSM turbulence model are similar to those predicted without using turbulence models.

7.4 Summary

In summary, the simulation of the dam breaking flow based on the developed-VOF method can be concluded as a successful simulation in the following aspects.

1. The dimensionless vertical position of the free-surface has been estimated acceptable in a certain range. The flowing behaviour has been predicted accurately in the whole domain.

2. The mesh size is important for the developed-VOF method. On the one hand, it will influence the accuracy of the simulation result. On the other hand, the thickness of the free-surface is also affected by the mesh size. Although a customised technique has been used to compress the free-surface, the improvement is still conspicuous when the finest grid has been used.

3. The application of turbulence model will affect the simulation results of current research. The RSM turbulence model can predict the flow behaviour of the dam breaking flow and capture the position of the free-surface. When the $k - \varepsilon$ turbulence model is implemented into the developed VOF method, it cannot provide accurate simulation results.

4. The vector plots are useful for analysing the flow behaviour of the dam breaking flow. It can be seen from Fig. 7.4 that the sudden flow of the liquid phase will cause the movement of the gas phase and form vortices and turbulence. The water and air that flow near the free surface have higher velocity amplitudes.

When studying the fluid flow in a hydrocyclone, the problem of using a multi-phase flow solver is inevitably involved. When there is a clear interface between the two phases, such as the phenomenon of air-core in free-surface, the developed-VOF method can be used to solve this type of problem. Therefore, comprehending and correctly using the developed VOF method is essential for simulating multi-phase flow with a clear free surface in hydrocyclones.
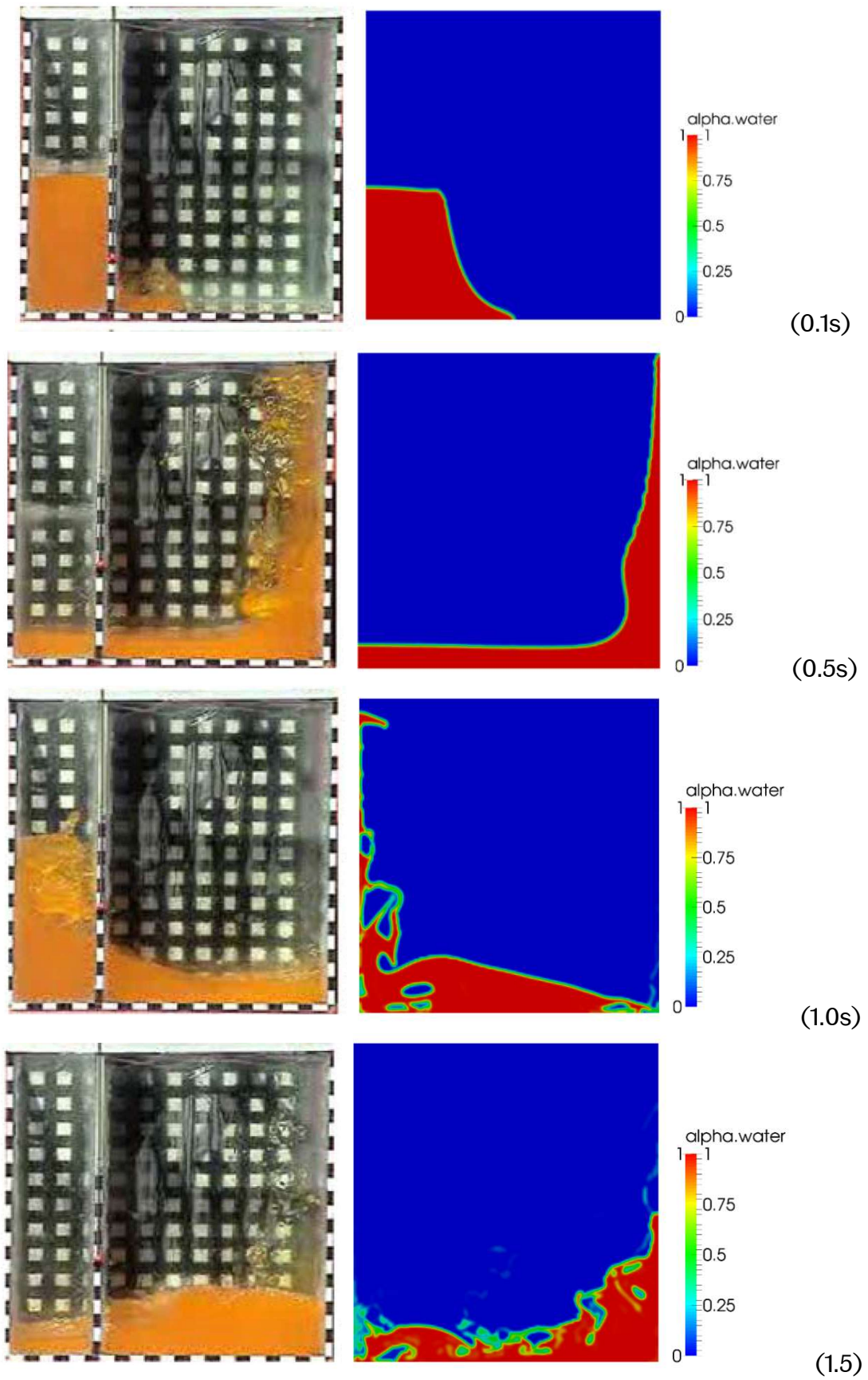
Fig. 7.1. Comparison of volume fraction distribution with experimental photos
(Cruchaga et al., 2007)

(0.0s)

(0.5s)

(1.0s)

(1.5s)

(2.0s)

(a) (40×40) (b) (80×80) (c) (160×160)
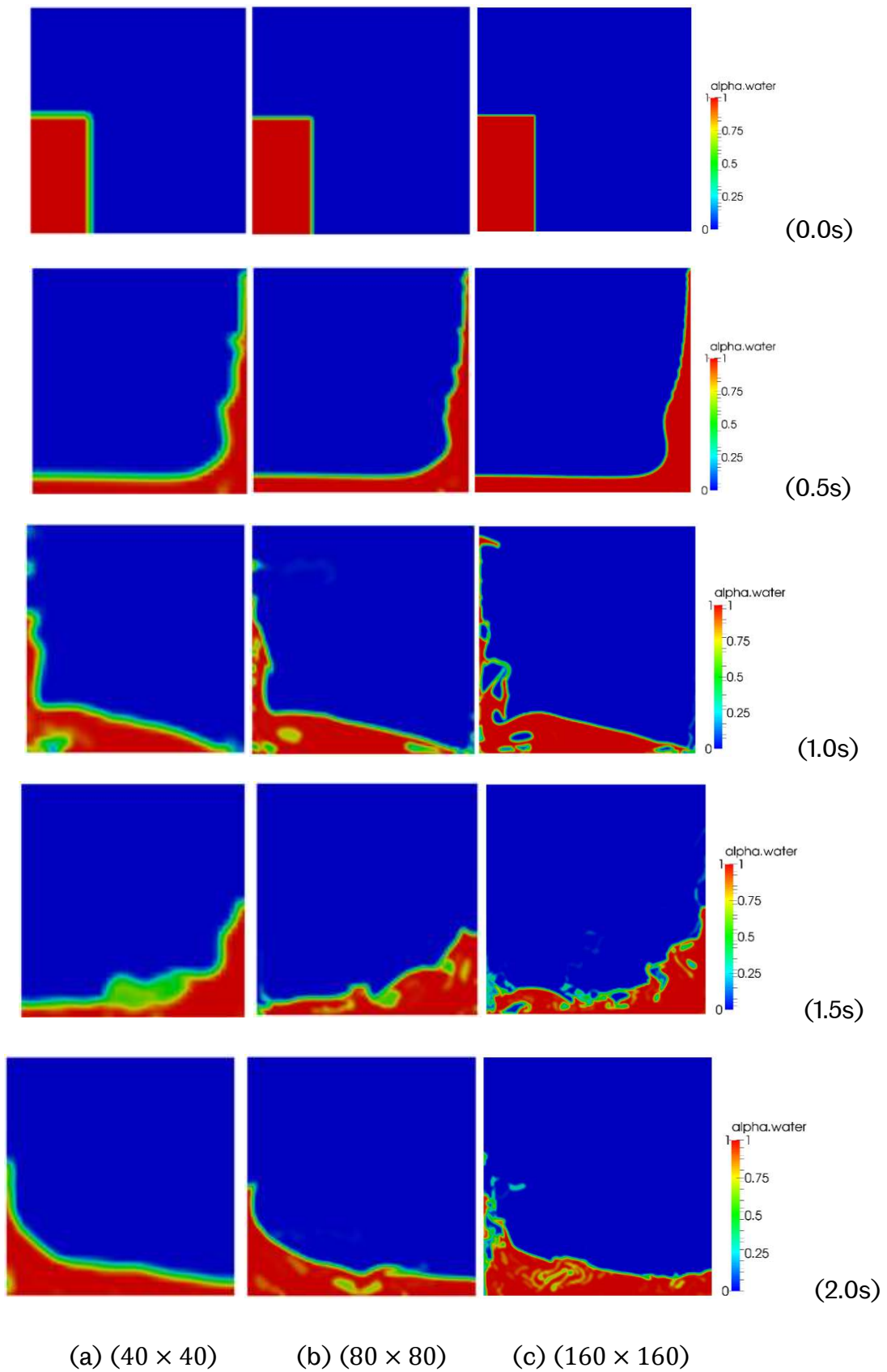
Fig. 7.2. Distributions of the free-surface obtained by different mesh size

(0.1s)

(0.5s)

(1.0s)

(1.5s)

(2.0s)

(Non-TM)   (K-epsilon)   (RSM)
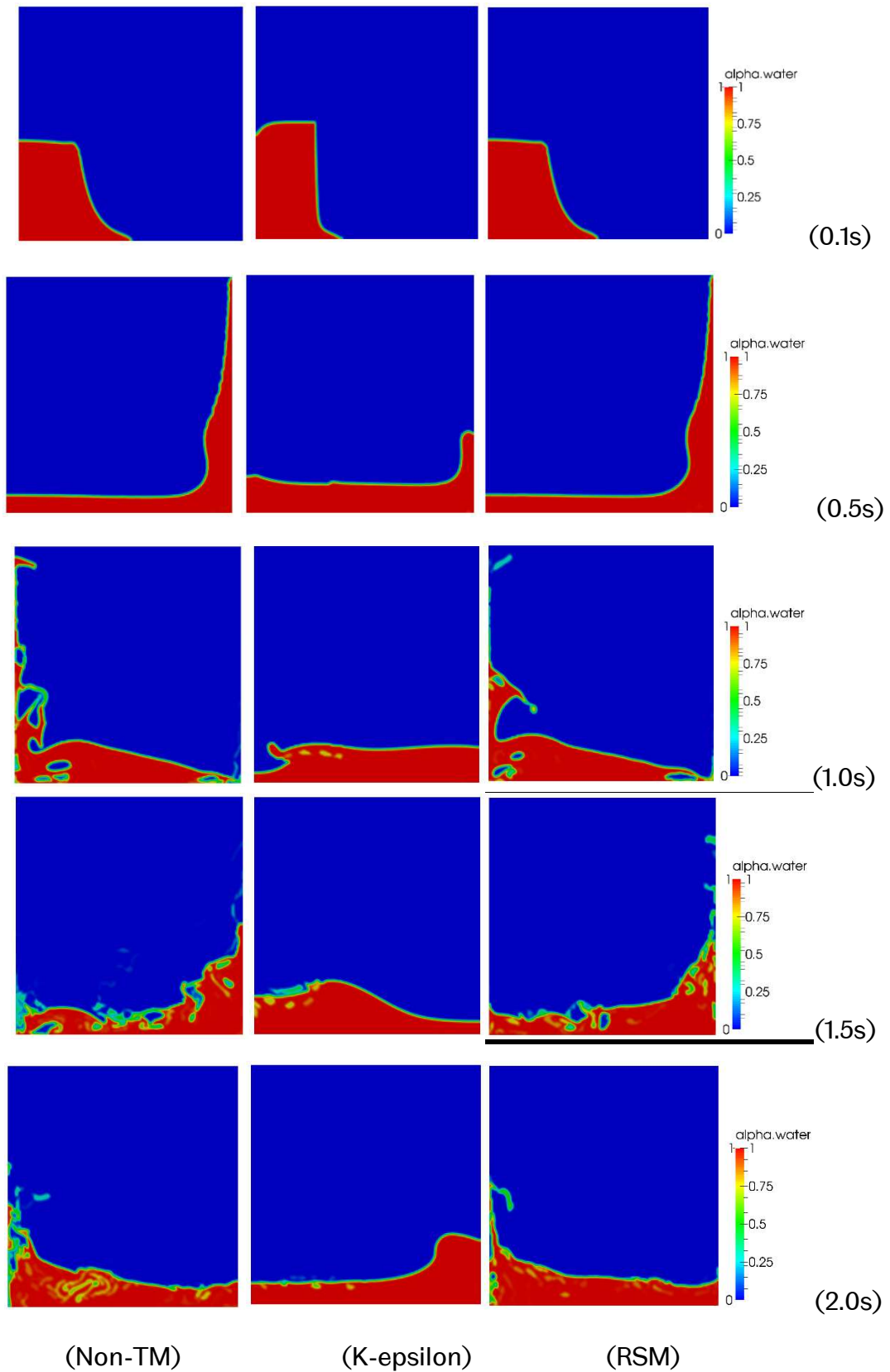
Fig. 7.3. Distributions of the free-surface obtained by different turbulence model

(0.1s)

(0.5s)

(1.0s)

135
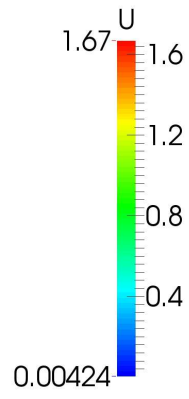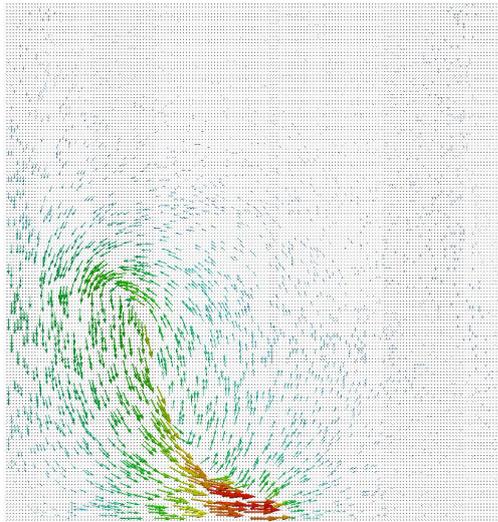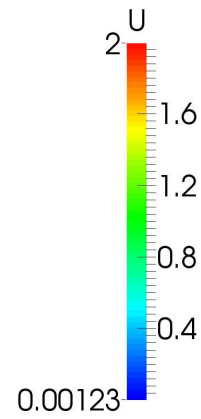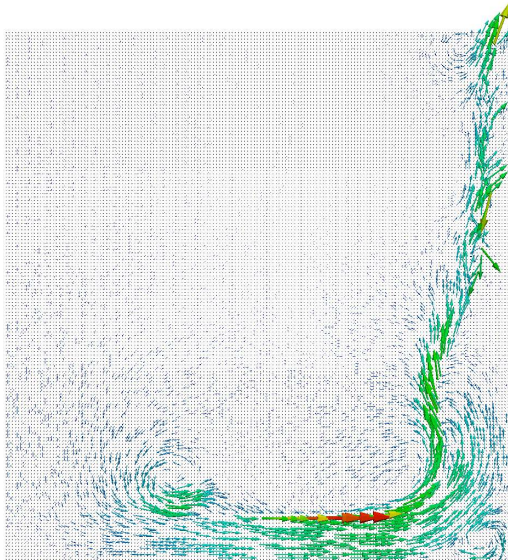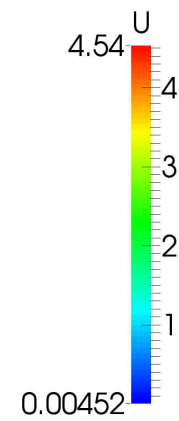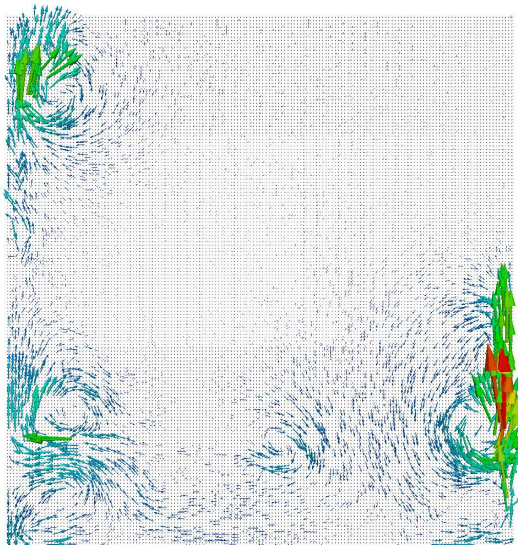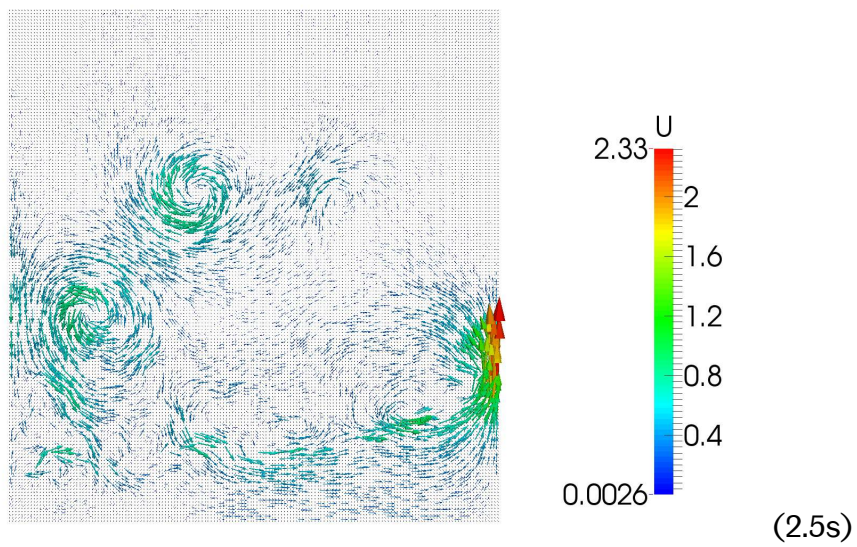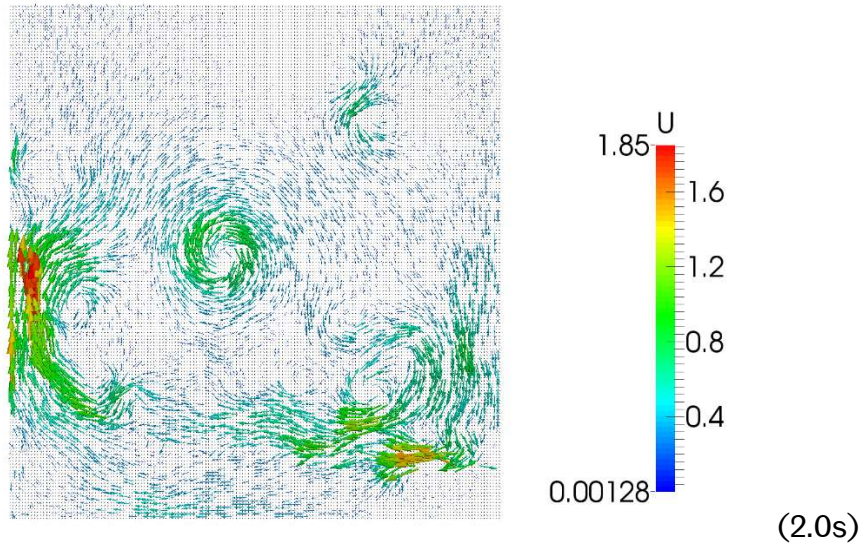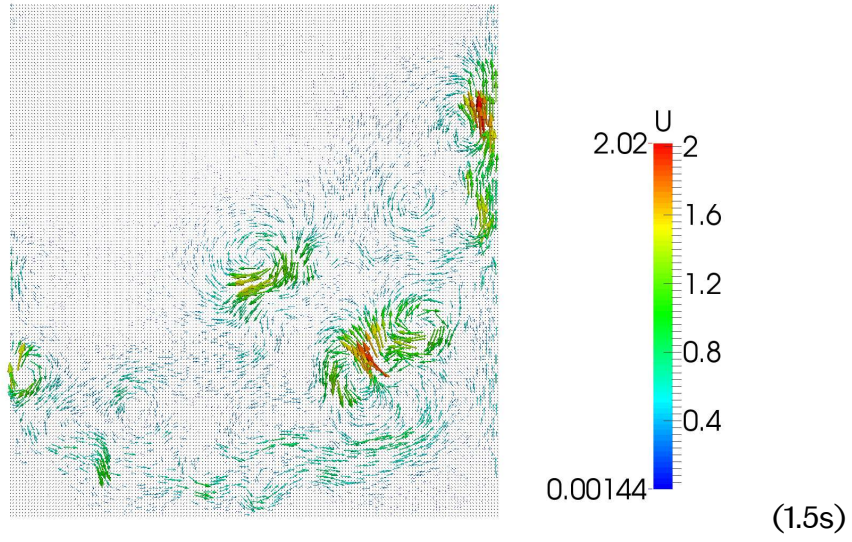
Fig. 7.4. Velocity vector plots of the Dam breaking flow
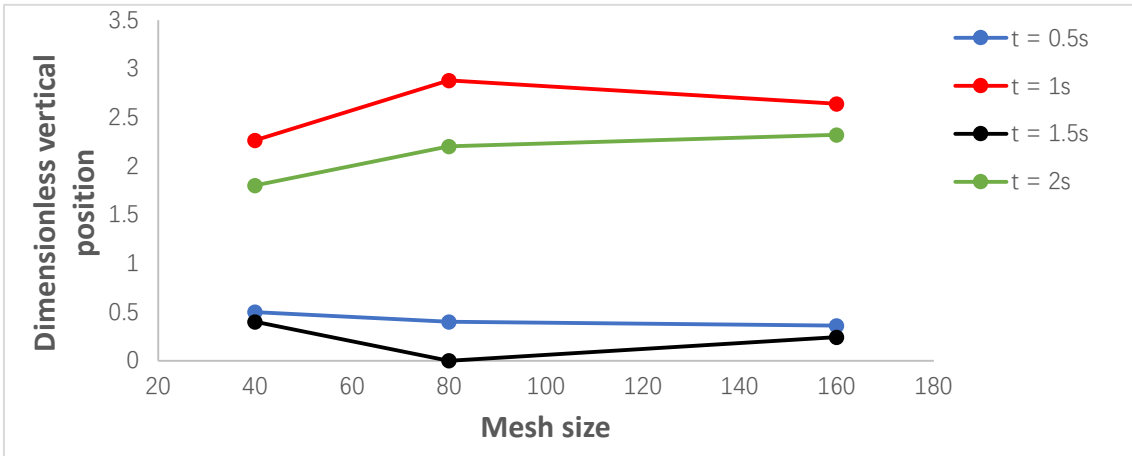
Fig. 7.5a. Mesh convergence study via the position of free-surface at the left wall
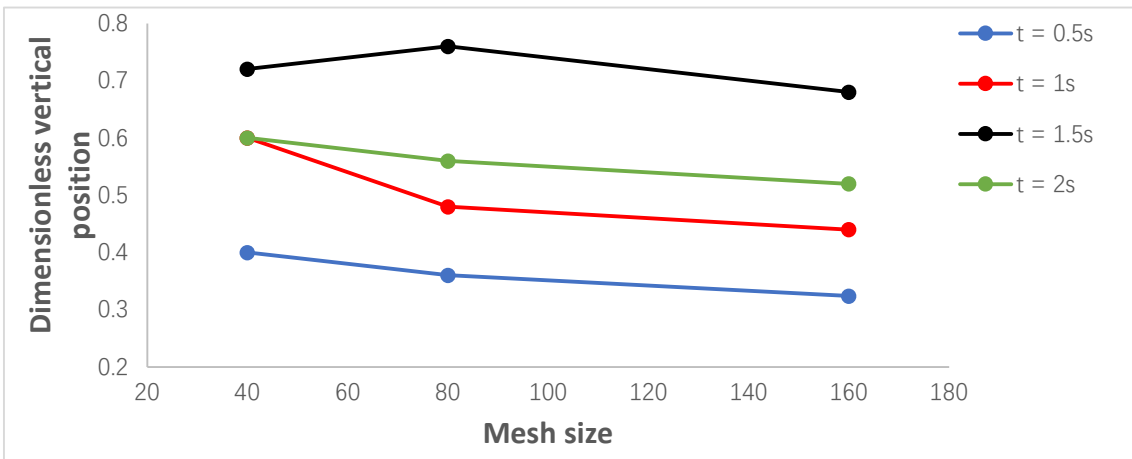
Fig. 7.5b. Mesh convergence study via the position of free-surface at the middle point
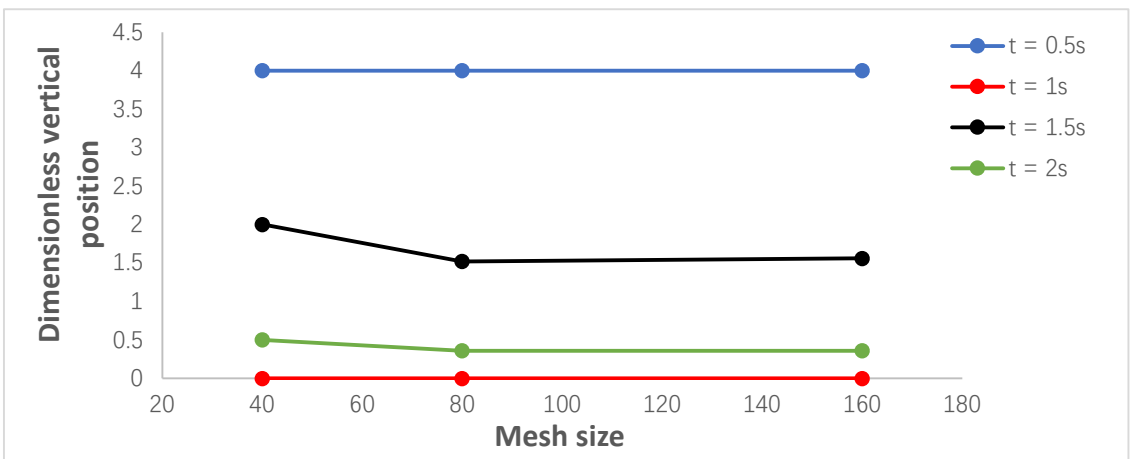

Fig. 7.5c. Mesh convergence study via the position of free-surface at the right wall
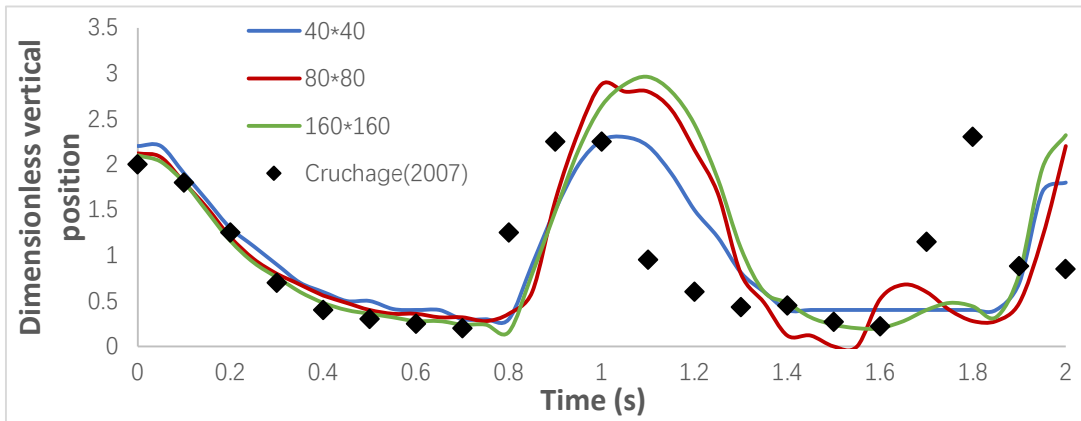
Fig. 7.6a. Dimensionless vertical position of the free-surface at the left wall

(x = 0m)
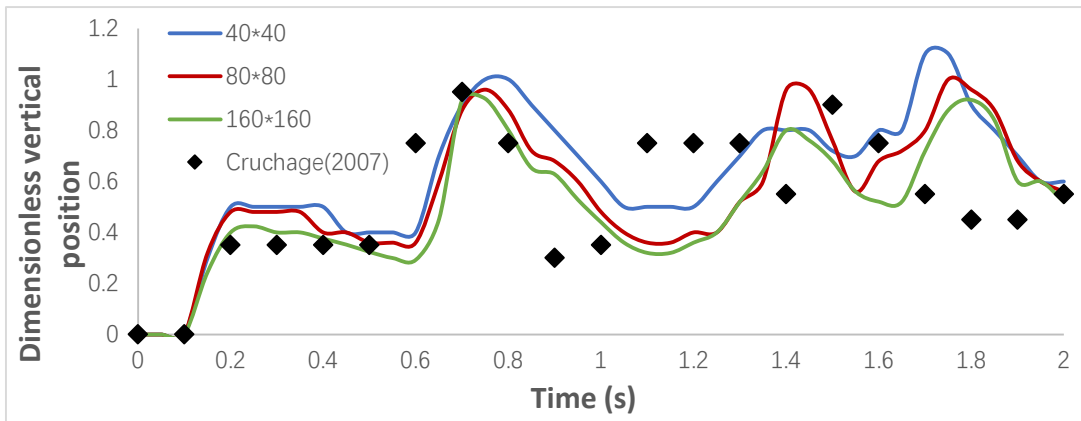
Fig. 7.6b. Dimensionless vertical position of the free-surface at the middle point

(x = 0.27m)
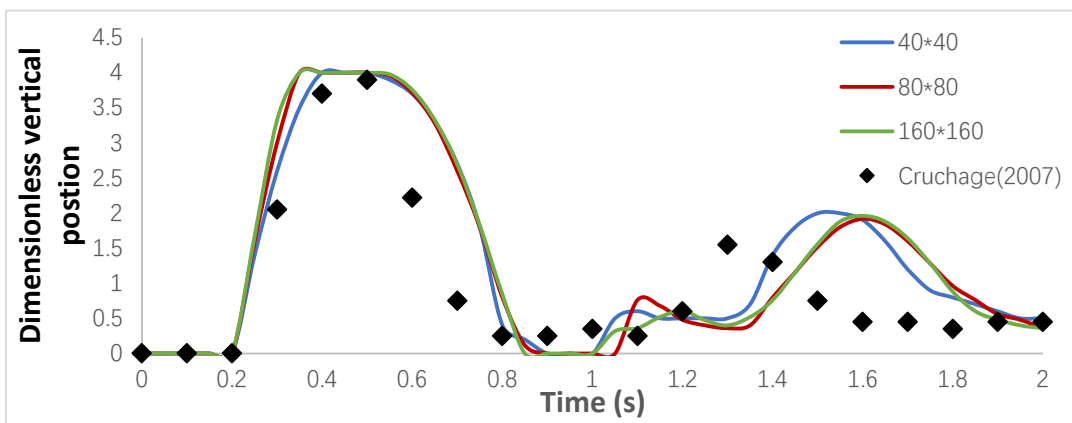
Fig. 7.6c. Dimensionless vertical position of the free-surface at the right wall

(x = 0.42m)

Table 7.1a. The difference of the average velocity between each mesh (left wall)

	0.5s	1.0s	1.5s	2.0s
$\frac{1}{40}$ *and* $\frac{1}{80}$	0.2222	0.2397	-2	0.2
$\frac{1}{80}$ *and* $\frac{1}{160}$	0.10526	0.0870	2	0.0531
R	0.4	-0.3894	-0.6	0.3

Table 7.1b. The difference of the average velocity between each mesh (middle point)

	0.5s	1.0s	1.5s	2.0s
$\frac{1}{40}$ *and* $\frac{1}{80}$	-0.1053	0.2222	0.0541	0.0690
$\frac{1}{80}$ *and* $\frac{1}{160}$	-0.1053	0.0870	0.1111	0.0741
R	0.9	0.3333	<u>-2</u>	1

Table 7.1c. The difference of the average velocity between each mesh (right wall)

|	0.5s	1.0s	1.5s	2.0s
$\frac{1}{40}$ *and* $\frac{1}{80}$	0	0	0.2727	0.32558
$\frac{1}{80}$ *and* $\frac{1}{160}$	0	0	0.0260	0
R	0	0	-0.08333	0
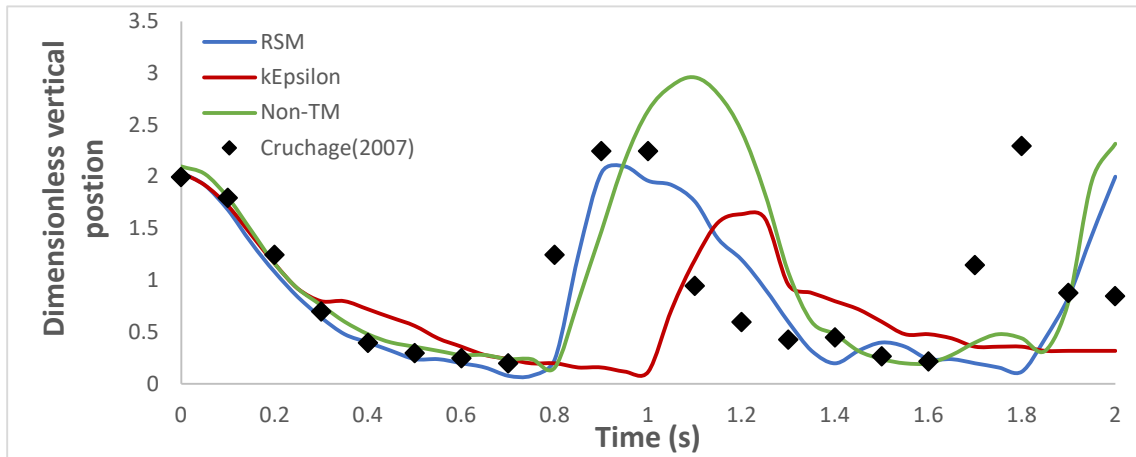
Fig. 7.7a. Dimensionless vertical position of the free-surface at the left wall (x = 0m)
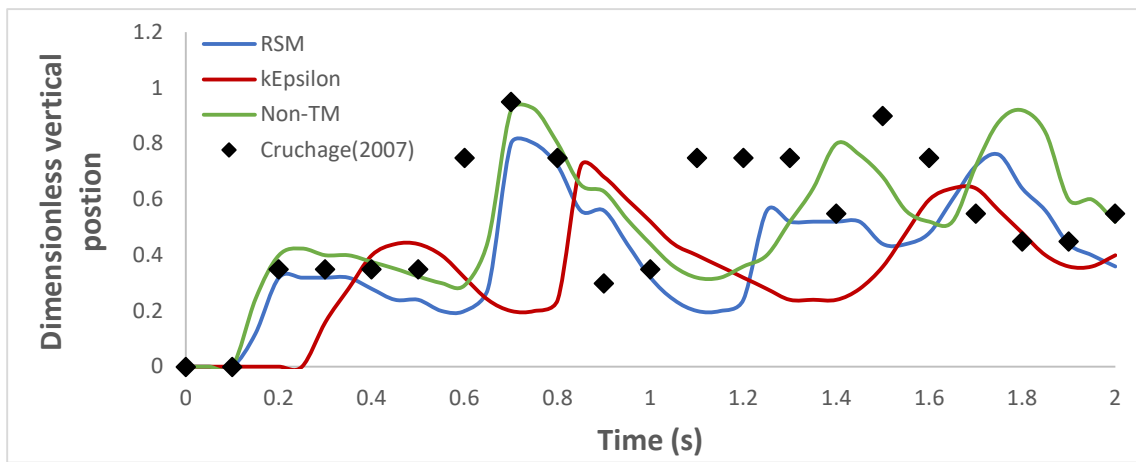

Fig. 7.7b. Dimensionless vertical position of the free-surface at the middle point (x = 0.27m)
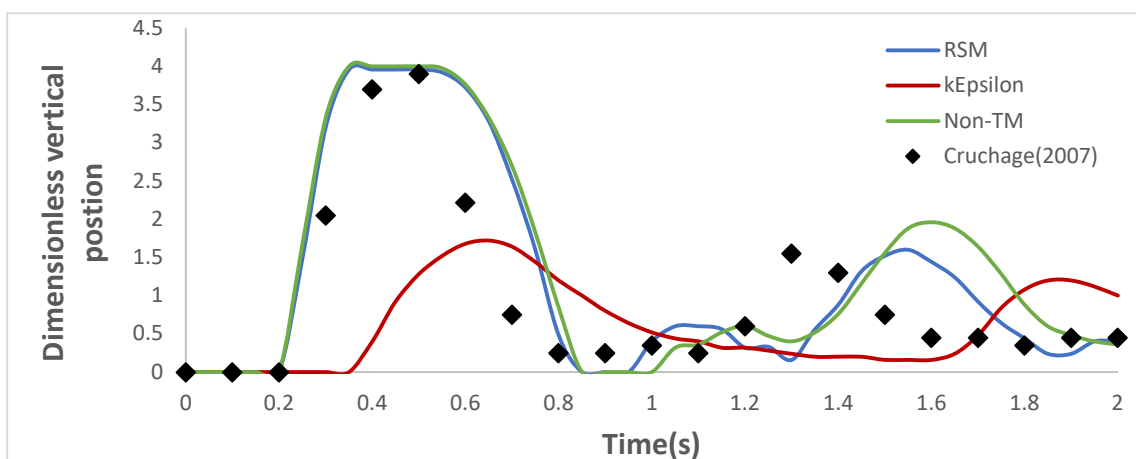
Fig. 7.7c. Dimensionless vertical position of the free-surface at the right wall (x = 0.42m)

Chapter 8. Simulation of the flow with air-core in hydrocyclones

8.1 Case introduction

The simulation of the flow with air-core in hydrocyclones is a challenging problem due to the characteristic of combining the multi-phase flow problem with an intensive swirling flow problem. The simulation not only has to correctly predict the fields of the large swirling flow, such as the "Rankine vortex", but is also required to precisely predict the pattern of the air-core.

The **interFoam** solver is used to solve the problem of gas-liquid multi-phase flow; it works based on the developed VOF method. The customised solver called Multidimensional Universal Limiter for Explicit Solution (MULES) is used for the calculation of this developed VOF method. It is derived from the Flux Corrected Transport (FCT) technique and utilised to guarantee the coexistence of accuracy and boundedness. In addition, the High-Resolution Schemes (HRS) is applied to further optimise the developed VOF method. Such a technique helps to eliminate the unexpected oscillations near a strong gradient, like the value of the volume fraction near the free-surface.

The PIMPLE algorithm is used to solve the problem of pressure-velocity coupling during calculations. Thus, the transient state of the flow in hydrocyclones can be captured. It is possible to analyse the formation process of the air-core by the numerical simulations, which is hard to observe in the experiment.

The schemes in the second-order of accuracy are used for the equation discretization, and these include the center linear scheme and upwind linear scheme. The number of structured meshes used for simulation increased from 223875 hexahedrons to 594728 hexahedrons.

Three different turbulence models have been used for investigations. Two of them are used for the RANS method, namely, the $k - \varepsilon$ turbulence model and the RSM turbulence model. The other turbulence model called the subgrid-scale kinetic energy model is used for the LES method. Finally, the validation process is completed by comparing the simulation result with Hsieh's experimental data (Hsieh,

1988). The density and viscosity of the liquid is set as $1 \times 10^3 \, kg/m^3$ and $1 \times 10^{-6} \, m^2/s$. The density and viscosity of the air is set as $1.2 \, kg/m^3$ and $1.48 \times 10^{-5} \, m^2/s$. The inlet velocity was mentioned in the section of boundary conditions, $U_{in} = 2.3 \, m/s$. Thus, the Reynolds number is approximated by $Re = u_{in}D/v_{water} = 1.73 \times 10^5$, which indicates that the flow is completely turbulent.

8.2 Simulation results

The simulation result is demonstrated by showing the streamline, vector, and contour plots of the velocity, pressure and volume fraction.

● **Volume fraction**

Screenshots of the contour plots of the volume fraction field can be used to analyse the formation process of the air-core in hydrocyclone flows. The screenshot interval is set to 0.1s, and the main formation process of the air-core occurs between 0s and 1s. Fig. 8.2 presents the air-core formed in the hydrocyclone, which is filled with air at the initial state. The results are compared with the snapshot taken by Wang et al. (2015) (see Fig. 8.1) in their experiment. Fig. 8.3 shows the air-core formed in the hydrocyclone, which is filled with water at the initial state. These two groups of screenshots were obtained through the simulation using the RSM turbulence model. They demonstrate two different formation processes of the air-core in hydrocyclone flows.

Fig. 8.2 shows that when the liquid flows into the hydrocyclone, it flows at a high speed against the wall of the separator. The second and third figures show that the liquid rapidly fills the entire cylinder and conical part, then a small amount of liquid flows out from the bottom outlet. Over time, the thickness of the liquid phase gradually increases, and the liquid can be discharged through the upper and bottom outlets simultaneously. In the eighth figure, the hydrocyclone is almost completely filled with water, and a small air-core is formed in the centre of the hydrocyclone. After that, the size of the air-core increases until the flow stabilises.

The first four screenshots of the second group of figures (see Fig.8.3) seem to be roughly the same, but in fact, the liquid flows around the wall of the separator after flowing into the hydrocyclone. The screenshot at 0.4s shows that the airflow flows into the hydrocyclone through the upper and bottom outlets. After that, two airflows

merge at the bottom of the vortex finder and form a small air-core; the size of the air-core increases until the flow stabilizes.

The two groups of screenshots present two different formation processes of the air-core in hydrocyclone flows, nevertheless the profile of the air-core at the steady states is similar.
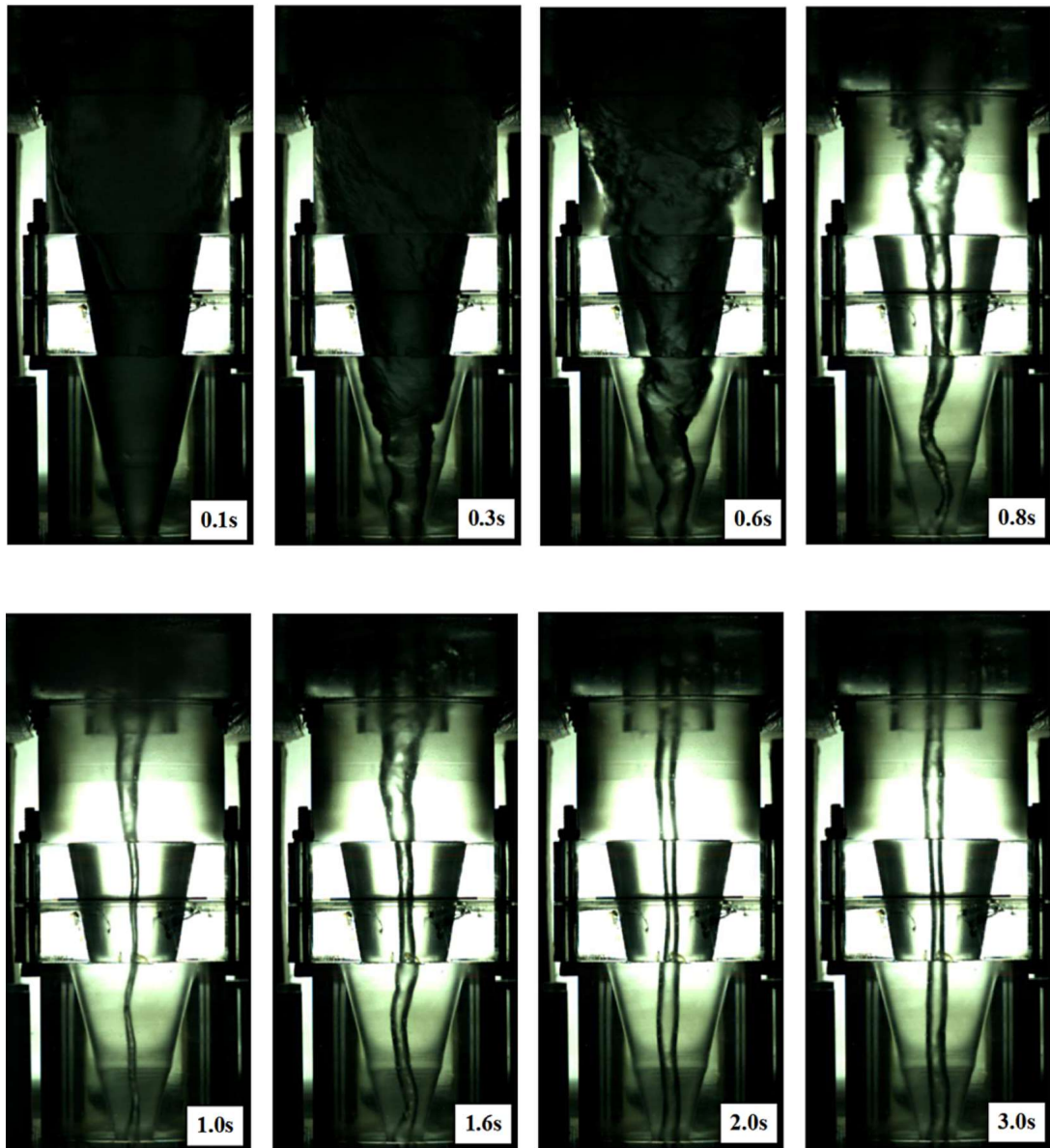

Fig. 8.1. Snapshots showing the formation process of the air-core shot by a high-speed camera.

(Wang et al., 2015)

(0.1s) (0.2s) (0.3s) (0.4s) (0.5s) (0.6s) (0.7s)

(0.8s) (0.9s) (1.0s) (1.6s) (2.0s) (steady)
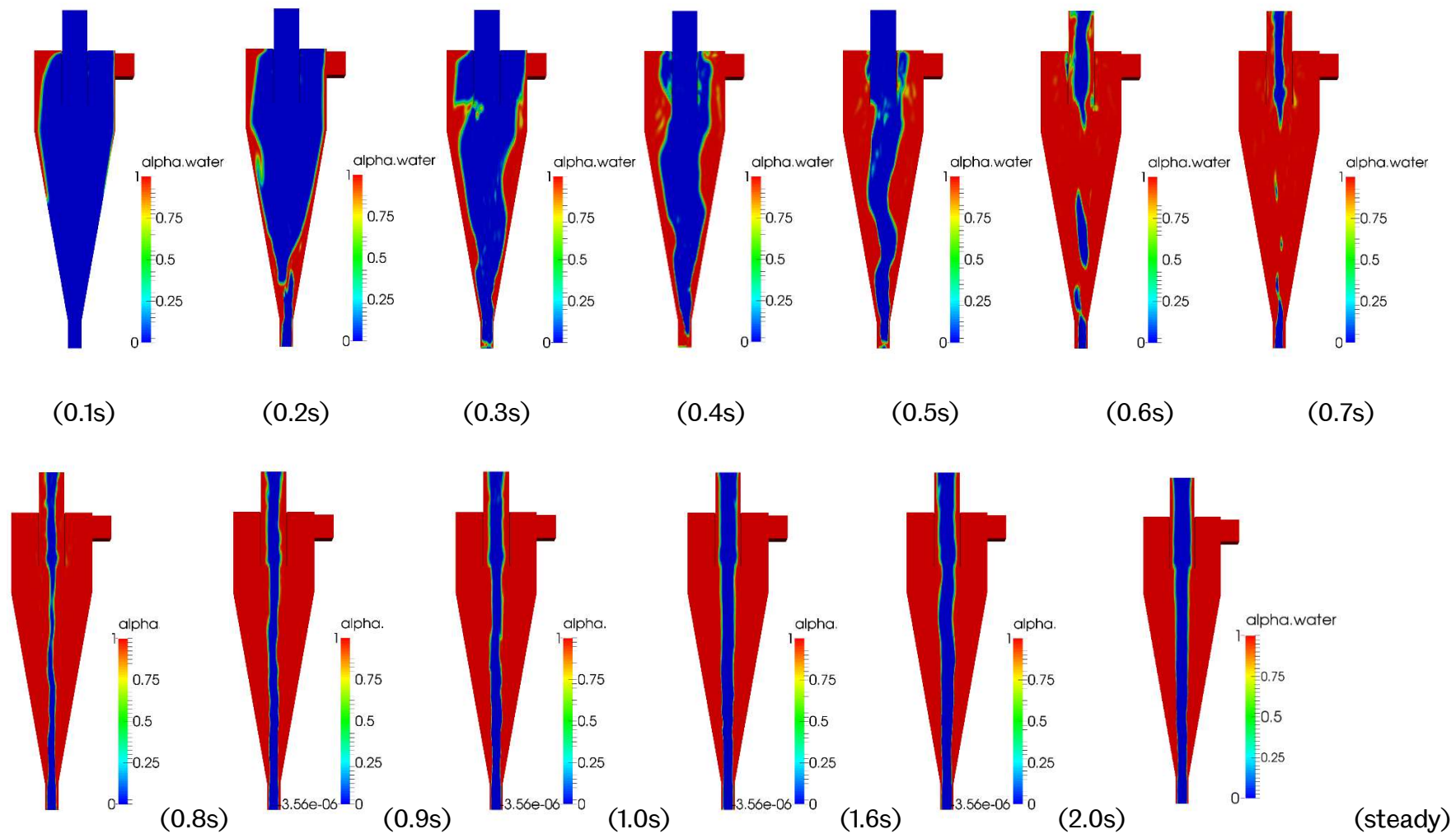
Fig. 8.2. Simulation results showing the formation process of the air-core in the gas-liquid hydrocyclone flow (Air filled)

(0.1s)   (0.2s)   (0.3s)   (0.4s)   (0.5s)   (0.6s)

(0.7s)   (0.8s)   (0.9s)   (1.0s)   (2.0s)   (steady)
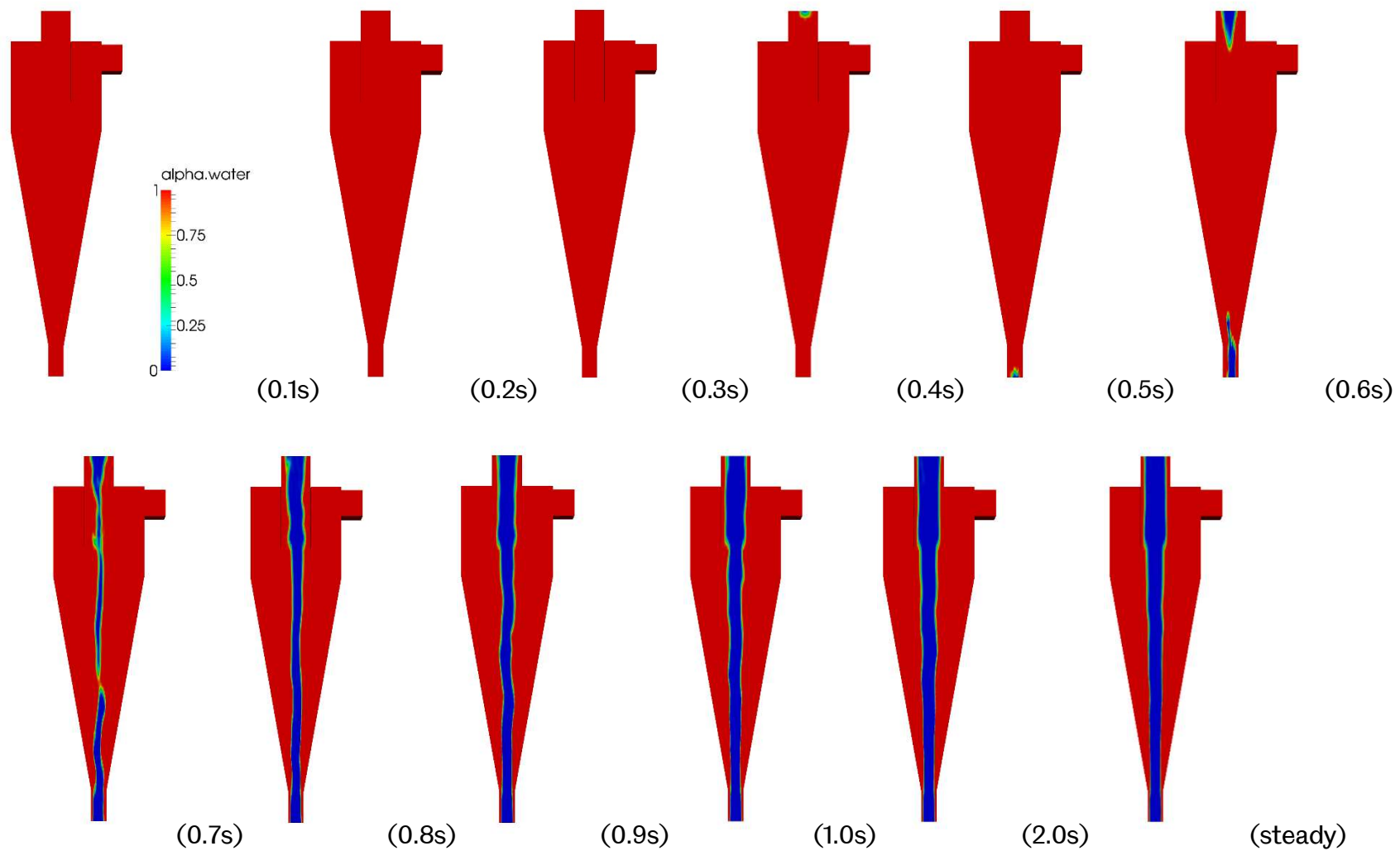
Fig. 8.3. Simulation results showing the formation process of the air-core in the gas-liquid hydrocyclone flow (water filled)

● **Velocity**

The contour plots of the velocity field present the profile of the tangential velocity, and axial velocity of the hydrocyclone flows at steady state. It can be seen that the profile of the tangential velocity provided in the current case (see Fig. 8.4a) is similar to the profile obtained by the simulation of cyclone flows (see Fig. 6.3a). The tangential velocity has an area with maximum value distributed along the extension line of the wall of the vortex finder. From this area to the wall of the separator or the centre of the separator, the value of the tangential velocity gradually decreases. In terms of the axial velocity, the profile shown in the current simulation (see Fig. 8.4b) is different from the profile given in the simulation of cyclone flows (see Fig. 6.3b).

The axial velocity shown in Fig. 8.4b tends to flow upwards at the centre of the conical section, meaning that the airflow is drawn from the atmosphere and flows into the cyclone through the bottom outlet. In the centre of the vortex finder, the blue area shows that the axial velocity tends to flow downward, indicating that the airflow is drawn from the atmosphere and flows into the hydrocyclone through the upper outlet. The water flowing out along the wall of the upper outlet exhibits an upward axial velocity, while the water flowing out along the bottom outlet duct exhibits a downward axial velocity.

Fig. 8.5 presents the velocity streamline graph and vector plots of the simulation of hydrocyclone flows. This helps to illustrate the flowing behaviour of the airflow and water flow at steady state. In general, the fluid flow in the hydrocyclone is relatively regular. The water flow swirls around the wall of the separator and forms an outer swirling flow on the periphery. The airflow rotates in the air-core to form an inner swirling flow. Furthermore, the inner swirl flow can be divided into two branches, where the branch flowing through the upper outlet directs downward, and the one flowing through the bottom outlet directs upward. The axial contour, streamline and vector plots demonstrate that the two branches meet each other at the bottom of the vortex finder.
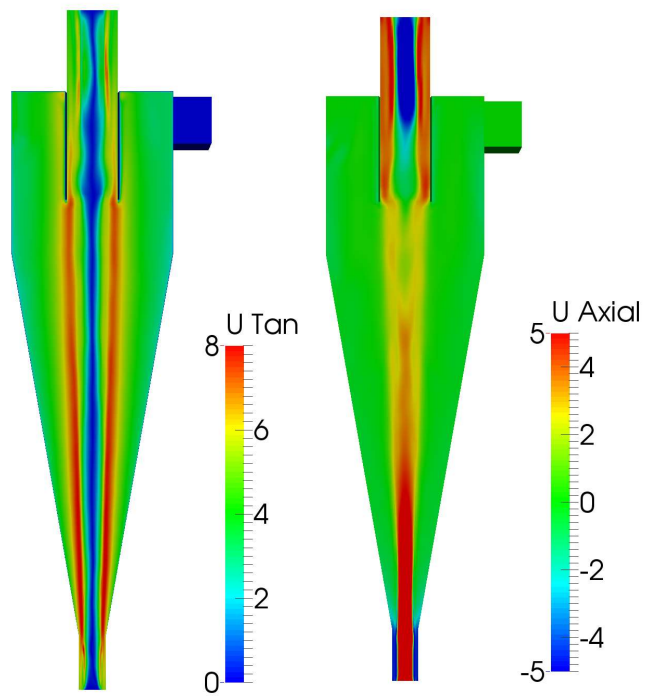
(a) Tangential velocity   (b) Axial velocity

Fig 8.4. Velocity contour plots of the gas-liquid hydrocyclone flow

Vortex finder

and   top

Bottom

outlet and

pipe
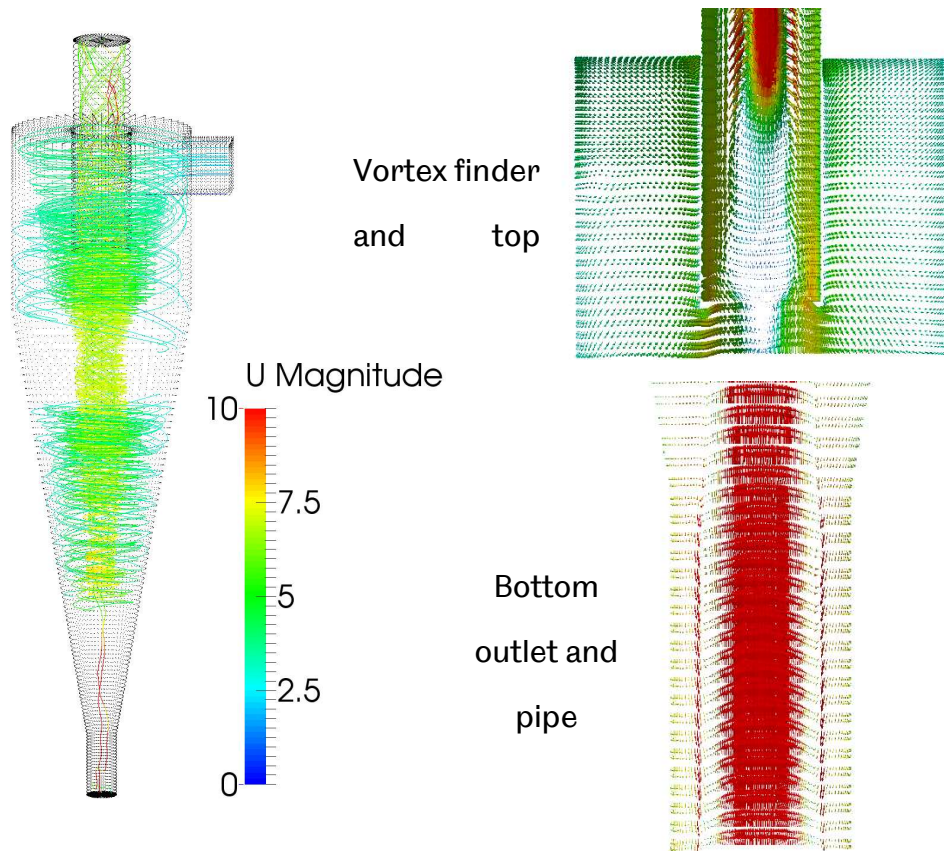
Fig 8.5. Streamline and vector plots of the gas-liquid hydrocyclone flow

- **Pressure**

The contour plots of the pressure field (see Fig. 8.6) present the profile of the pressure in hydrocyclones at steady state. It can be found that because the current simulation is a multi-phase problem, the low-pressure area in the centre of the hydrocyclone presents a different colour distribution compared with the contour plots shown in the simulation of single-phase cyclone flow. The actual pressure value in the entire dark blue low-pressure region is almost equal, which is lower than the given pressure in the atmosphere. Thus, it provides a source that prompts the airflow back into the hydrocyclone. The scale of the low-pressure area is similar to the size of the air-core; research by Kraipech-Evans (2008) states that the low-pressure area could represent the air-core in terms of the sizes. For the other area, the pressure gradually increases from the low-pressure area in the centre to the wall of the hydrocyclone.
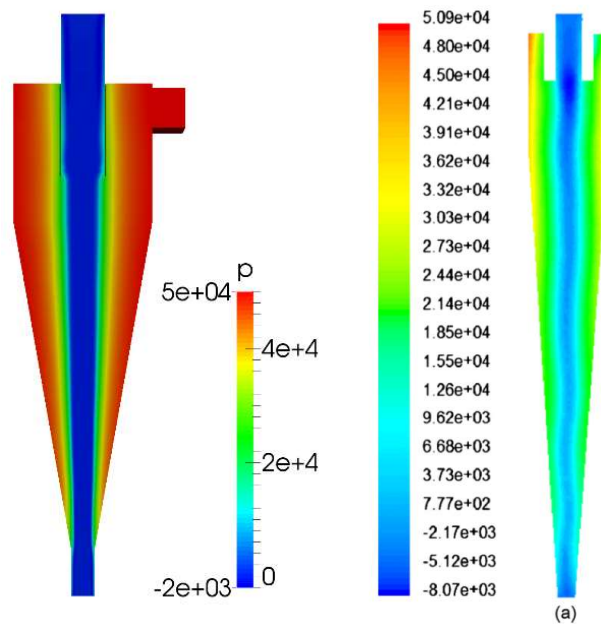
(Current simulation)（Kraipech-Evans, 2008）

Fig. 8.6. Pressure contour plot of the gas-liquid hydrocyclone flow.

8.3 Discussion

The curves' plots of the velocity field are obtained by the simulation using the Develop VOF method and the RSM turbulence model. These plots are used for the

validation process, which compares the simulation results with experimental data obtained by Hsieh (1988 and 1991) and simulation results obtained by Rudolf (2012).

The first group of figures (see Fig. 8.8) presents the curve of the tangential velocity against the length of lines located at three observation levels (see Fig. 8.7), they are $d = 60mm$, $d = 120mm$ and $d = 170mm$, respectively. The second group of figures (see Fig. 8.9) presents the curve of the axial velocity against the length of those lines. From Fig. 8.8, it can be seen that the curve obtained by the current simulation shows a reasonable curve matched with the experimental data. The characteristic of "Rankine vortex" has been captured and the inflexion points of all tangential velocity curves are located at almost the same radius position. However, the curves obtained by the current simulation show that the value of the tangential velocity has been overestimated, especially at the outer swirling flow. In addition, the curves obtained by previous simulations show that the maximum value of the tangential velocity has been underestimated. Regarding the curves of the axial velocity, the current simulation provides a curve that almost matches the experimental data. Compared with previous simulations, the results of the current simulation ensure a higher accuracy, especially near the free-surface.
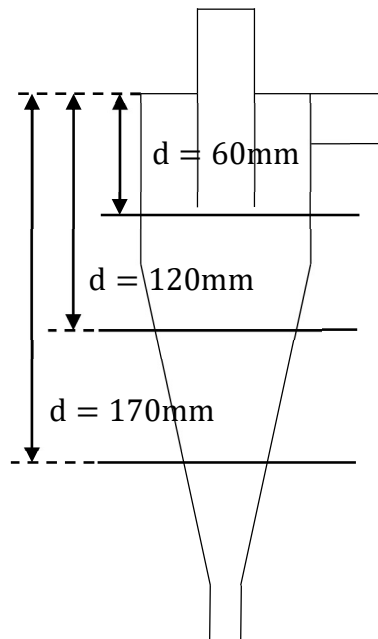
Fig. 8.7. The data collection line located at three different levels.
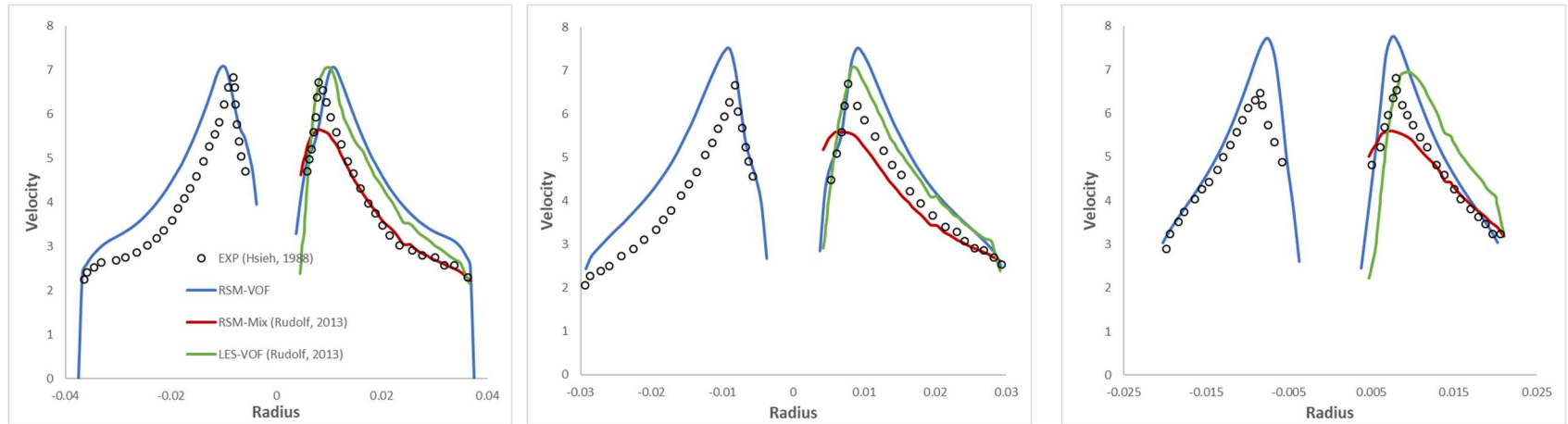
Fig. 8.8. Profile of the tangential velocity curve against three observation lines (d = 60, 120, 170mm)
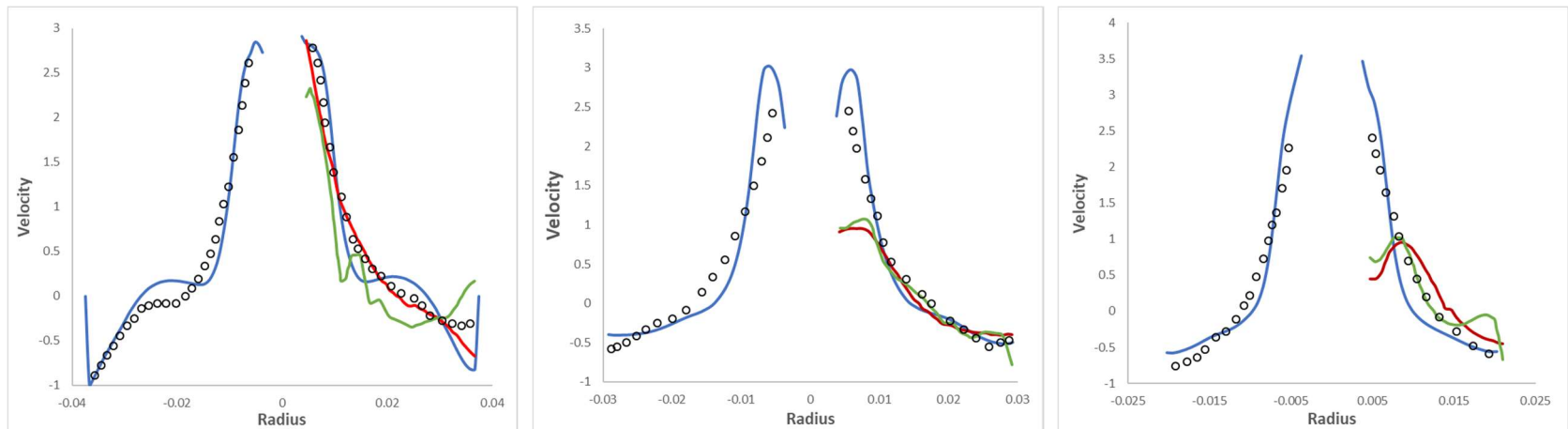
Fig. 8.9. Profile of the axial velocity curve against three observation lines (d = 60, 120, 170mm)

8.4 Further studies

After the verification and validation procedure for the new methodology, additional simulations were carried out. The focus of these simulations is to further optimize the contribution of numerical methods to the simulation of air flow in hydrocyclones and to optimize the dimensions of the hydrocyclone. The first study was simulated using the $k - \varepsilon$ turbulence model and the subgrid-scale kinetic energy model, which were applied in the RANS method and LES method, respectively. The second case is the influence of changing the dimensions of different sections of the hydrocyclone on flow patterns. The third simulation investigated the influence of applying different interface smearing factors on the simulation result. Finally, the assumption of simplifying the simulation of the flow in hydrocyclones, by ignoring the effects of the air-core, was verified. Aside from those specific parameters (e.g. turbulence model, dimension and smearing factor) in each extended study that needed to be adjusted, other settings (e.g. algorithms and solvers) were consistent with the settings used in the previously verified simulation.

## 8.4.1 Simulations based on different turbulence models

Fig. 8.10 presents the contour plots of the volume fraction obtained by using the simulations with the $k - \varepsilon$ turbulence model and the subgrid-scale kinetic energy model. It can be found that the contour plot obtained by using the simulation with the $k - \varepsilon$ turbulence model presents an entirely different profile with the volume fraction contour plots shown before (see Fig. 8.10). Even if the airflow appears at the top and bottom outlets, the characteristics of the air-core cannot be predicted.

The contour plot (see Fig. 8.10) obtained by using the simulation with the subgrid-scale kinetic energy model presents a similar air-core profile compared to the contour obtained by the RSM model. An inconspicuous different is shown in the plots, in that the size of the air-core obtained by the subgrid-scale kinetic energy model is smaller than the air-core obtained by the RSM model.

Fig. 8.11 shows the tangential velocity contour plots yielded by the three models. The tangential velocity distribution predicted by the $k - \varepsilon$ turbulence model shows a gradually increasing trend from the centre to the wall of the separator, while the

tangential velocity distribution obtained by the subgrid-scale kinetic energy model shows a pattern similar to the one obtained using the RSM model. Fig. 8.12 presents the axial velocity contour. The plots obtained by the $k-\varepsilon$ turbulence model do not show a clear upward axial velocity in the lower half of the separator. The pressure contour plots are shown in Fig. 8.13, demonstrating the source that forms the air-core. The plots obtained by the $k-\varepsilon$ turbulence model again present a different profile.

The curve graph of the tangential velocity and axial velocity can be used to provide a more intuitive comparison. The velocity curves obtained through the experiment are compared with the simulation result at each observation level. Fig 8.14 shows that the tangential velocity curve obtained by the $k-\varepsilon$ turbulence model cannot predict the pattern of the "Rankine vortex". The subgrid-scale kinetic energy model is able to capture the characteristic of the "Rankine vortex" but the maximum value of the velocity has been underestimated. The axial velocity curve obtained by the $k-\varepsilon$ turbulence model and the subgrid-scale kinetic energy model has different degrees of deviation.
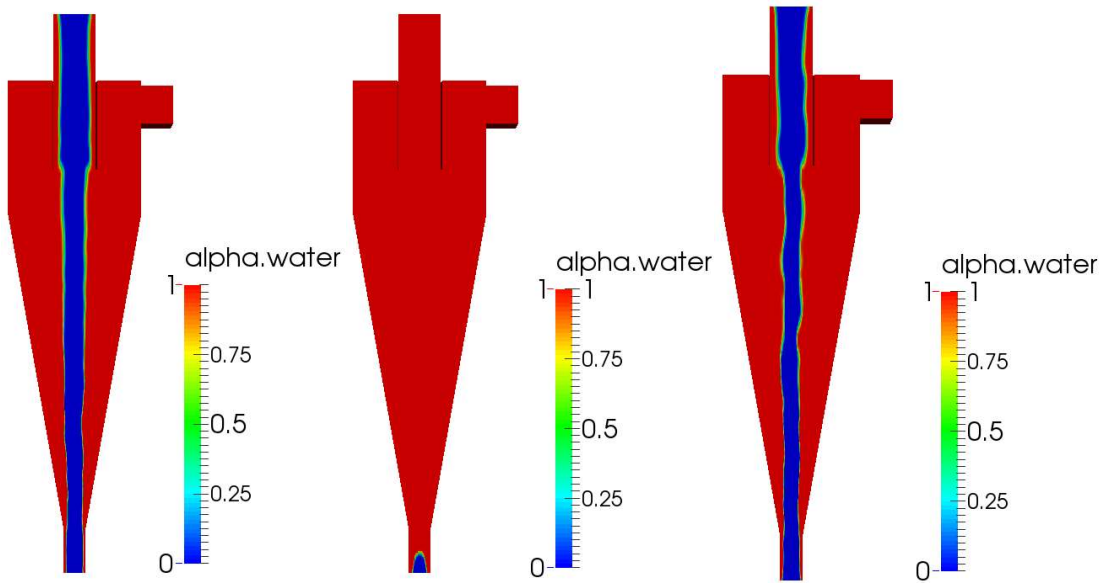
(the RSM model) (the $k - \varepsilon$ model) (the LES model)

Fig. 8.10. Profile of the air-core obtained by different turbulence model (TM)
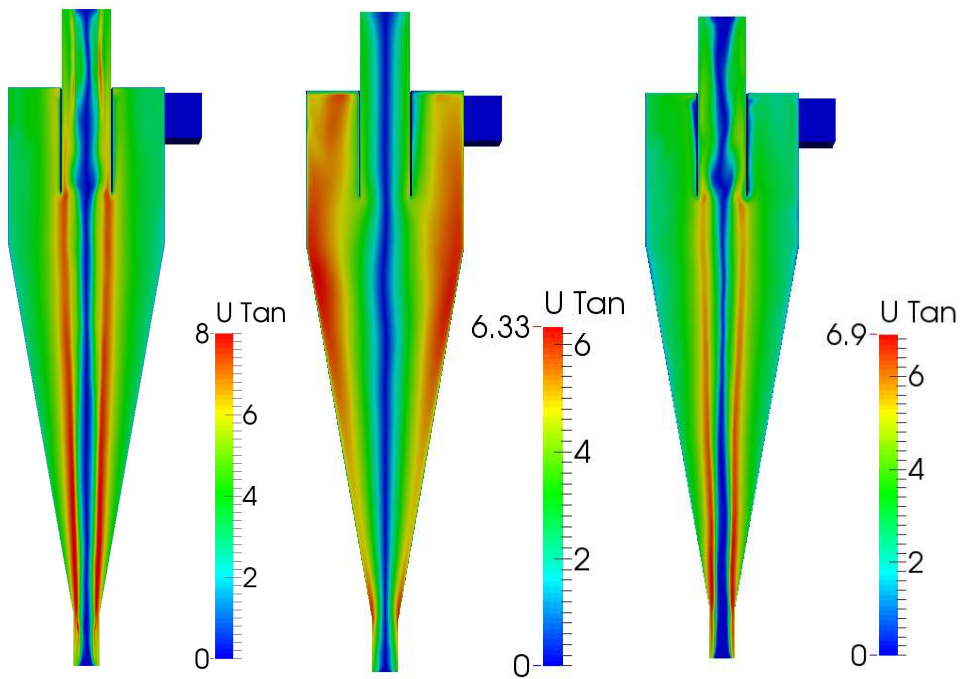
(the RSM model) (the $k - \varepsilon$ model) (the LES model)

Fig. 8.11. Contour plots of the tangential velocity obtained by different TM
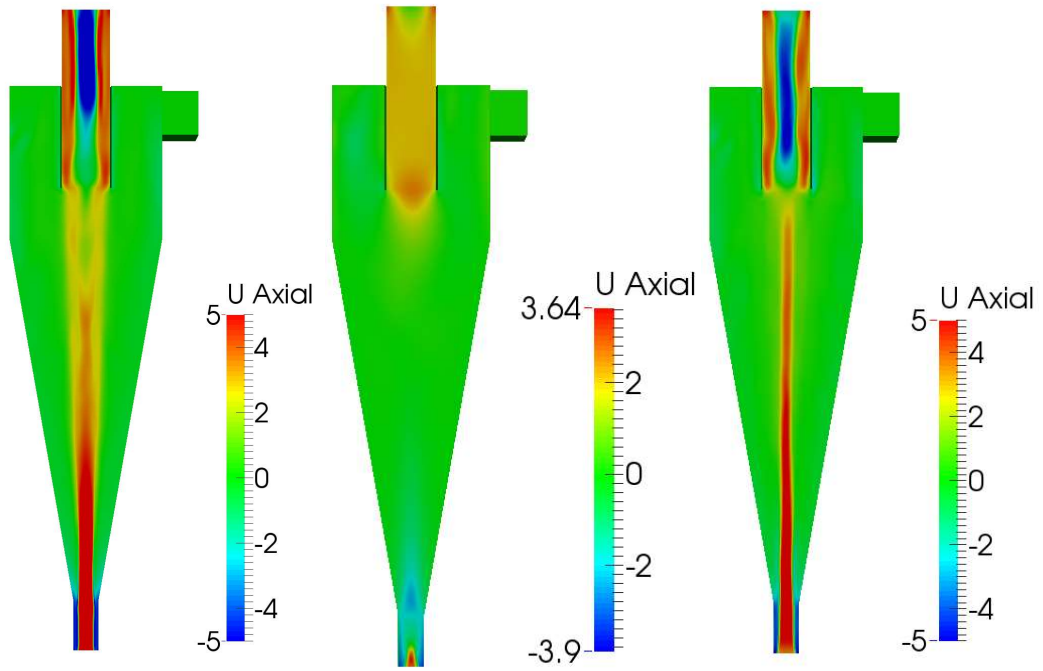
(the RSM model)   (the $k - \varepsilon$ model)   (the LES model)

Fig. 8.12. Contour plots of the axial velocity obtained by different TM.
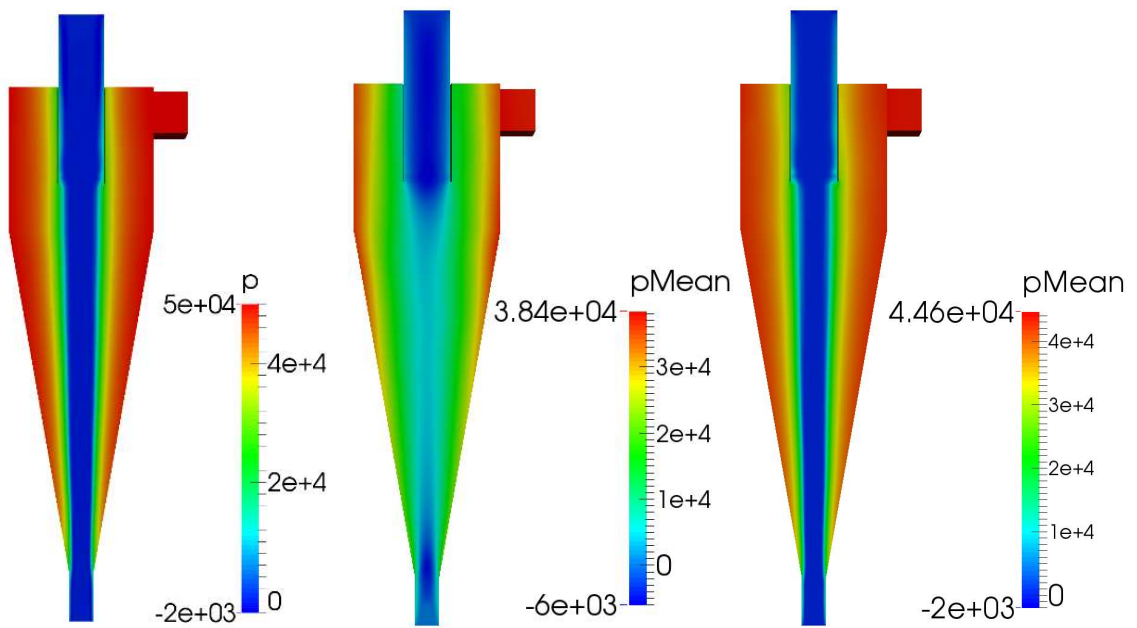
(the RSM model)   (the $k - \varepsilon$ model)   (the LES model)

Fig. 8.13. Contour plots of the pressure field obtained by different TM.

154
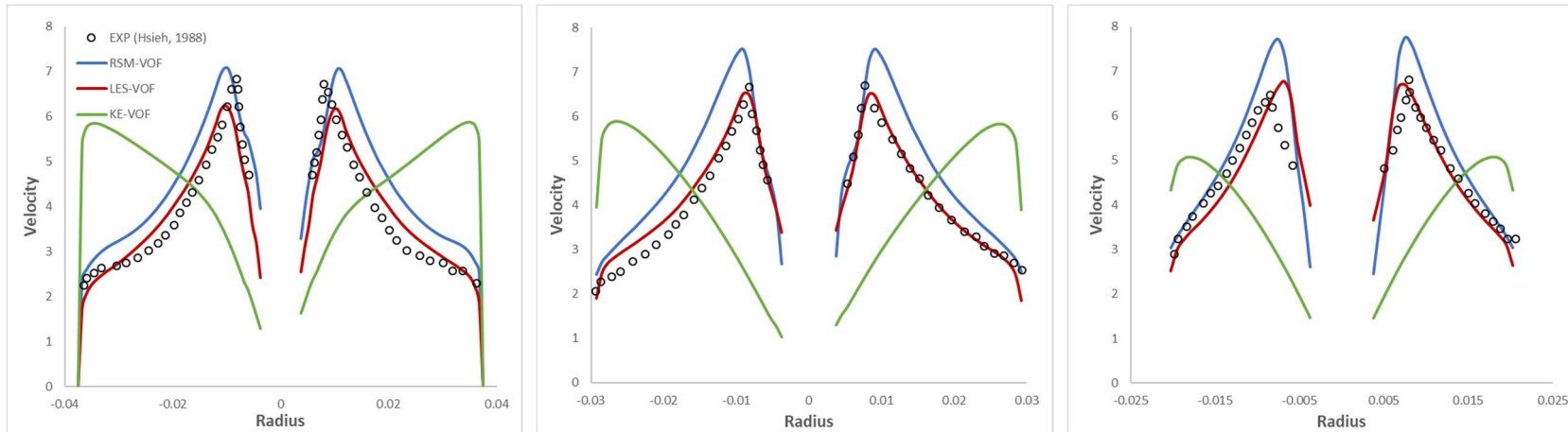
Fig. 8.14. Profile of the tangential velocity curve obtained by different TM against three observation lines ($d = 60, 120, 170$mm)
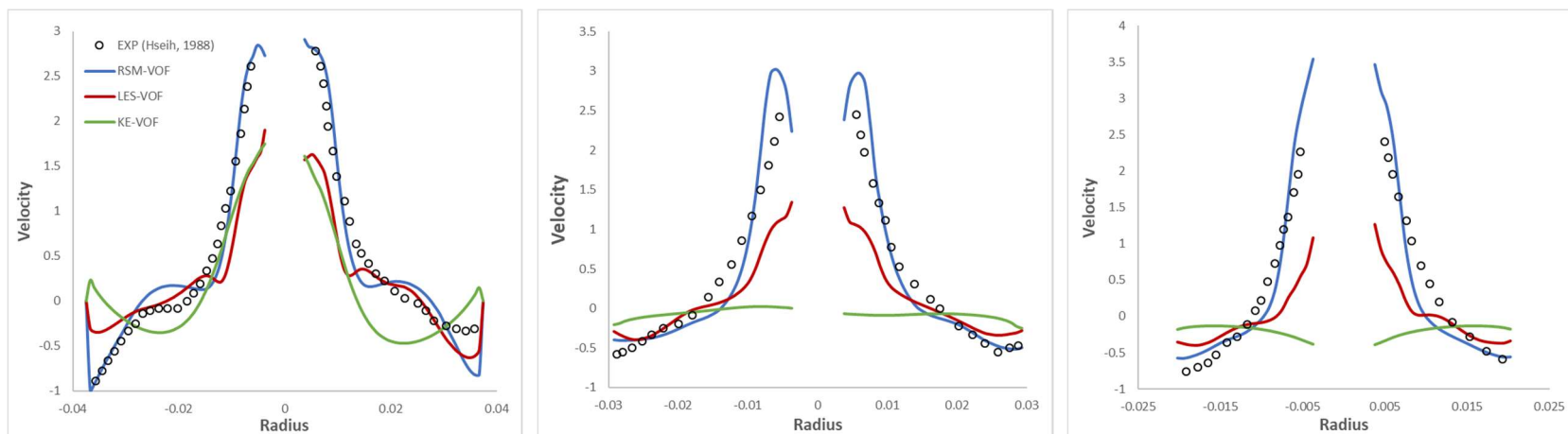

Fig. 8.15. Profile of the tangential velocity curve obtained by different TM against three observation lines ($d = 60, 120, 170$mm)

8.4.2 Simulations based on different hydrocyclone dimensions

The second study focuses on the problem of the influences of hydrocyclone dimensions on the flow behaviour inside the hydrocyclone. As introduced in Chapter 2, the diameter of the top outlet will influence the profile of the velocity curve in cyclones. Therefore, the current simulation not only studies the effect of changing the size of the top outlet on the flows in hydrocyclones, but also the effect of changing the size of the bottom outlet and the cone angle on the flows in hydrocyclones.

Fig. 8.16 presents the contour plots of the volume fraction. This helps to analyse the influence of the hydrocyclone dimensions on air-core sizes. The most apparent difference is that the size of the air-core increases as the diameter of the top outlet and bottom outlet increases. Fig. 8.17 presents the tangential velocity contour plots obtained by the simulations using hydrocyclones in different sizes.

The first set of figures compares the tangential velocity contour plots obtained using the hydrocyclones with different bottom outlet diameters (d 11mm, 12.5mm, 13mm and $d = 15$mm). The difference is not obvious and shows the characteristic of "Rankine vortex".

The second group of figures presents the simulation results predicted using the hydrocyclones with top outlet diameters equal to $d = 20$mm, $d = 25$mm and $d = 30$mm, respectively. It can be seen from the plots that the distribution of the area with the maximum tangential velocity is related to the diameter of the top outlet, the maximum value area distributed along the extension line of the wall of the vortex finder.

The third group of figures illustrates the simulation result yielded using the hydrocyclones with different cone angles ($CA = 18°, 20°, 22°$). They exhibit similar tangential velocity distributions. Fig. 8.18 shows the axial velocity contour plots obtained by the simulations using hydrocyclones in different sizes. They all present a similar profile, which shows a "Y" pattern for the axial velocity direct upward. The downward axial velocity appears at the centre of the vortex finder and the wall of the bottom outlet pipe. The pressure contour plots (see Fig. 8.19) exhibit similar

profiles, presenting that the low-pressure area is located in the air-core region, and the value of pressure gradually increases from the centre to the wall of the hydrocyclones.

The curve graphs are illustrated in Fig. 8.20 to Fig. 8.25. The observation levels are chosen based on the experiment. These graphs show that changing the size of the hydrocyclone will affect the flow velocity profile to varying degrees. The most obvious difference in the velocity curves is caused by changing the top outlet diameter of the hydrocyclone. When the diameter of the top outlet is reduced, the maximum value of the tangential velocity becomes larger and moves closer to the centre of the hydrocyclone. The maximum upward axial velocity decreases near the free-surface. In the other sets of comparisons, the difference is not obvious. However, it can also be seen that as the diameter of the bottom outlet decreases, the maximum value of the tangential velocity decreases and the axial velocity increases near the free-surface. Regarding the cone angle, as it increases, the maximum value of the tangential velocity increases, and the axial velocity hardly changes.

Another important criterion to distinguish the performance of the cyclone separator is the water split ratio. In the current study, the water split ratio is calculated by the value of **phiAlpha**, which is given as

$$\text{phiAlpha} = \phi \times \alpha$$

where phi, ϕ, is the velocity value through the surface and α is the value of volume fraction. Thus, the value of **phiAlpha** can be used to calculate the volume flow rate and mass flow rate of the water-phase flow. The post-process function called **patchIntegrate** is used to integrate the value of **phiAlpha** on the specific patch. Furthermore, the water split ratio is obtained by

$$\text{water split ratio} = \frac{\text{phiAlpha}_{Bottom\ outlet}}{\text{phiAlpha}_{inlet}}$$

and the value of the water split ratio of each hydrocyclone in different dimensions is given in Table 8.1.

It is generally agreed that a better cyclone separator has a lower water split ratio. This is because in the case of separating a liquid-solid two-phase flow, the less water

being discharged from the bottom outlet, the higher the concentration of solid particles is in the fluid separated from the bottom outlet. Unmodified Geometry:

(Bottom outlet =12.5mm, Top outlet =25mm and Core angle = 20°)

Bottom outlet =   (11mm)   (13mm)   (15mm)

Top outlet =   (20mm)   (30mm)
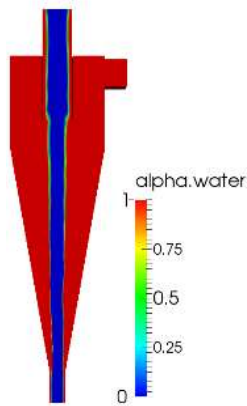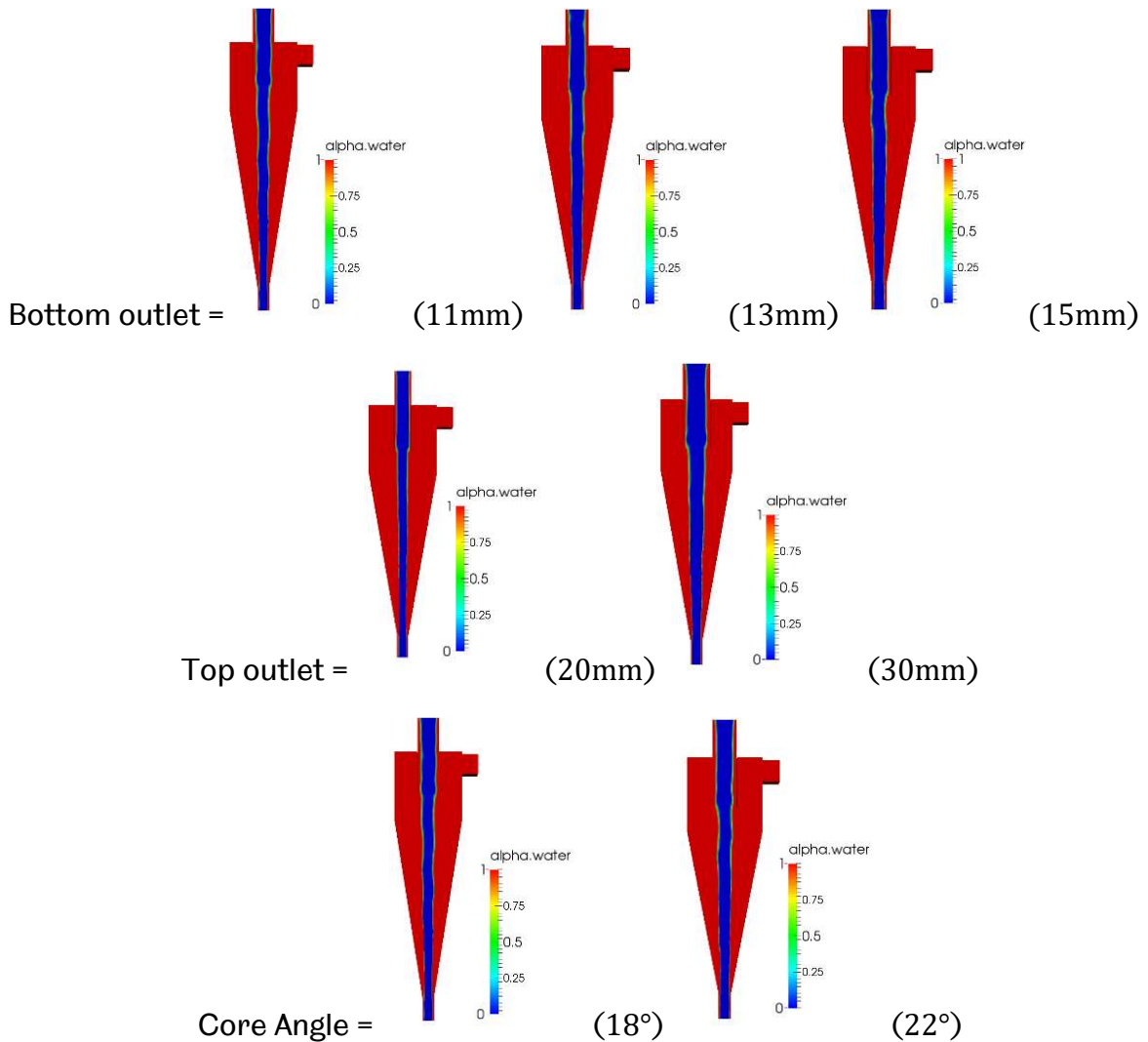
Core Angle =   (18°)   (22°)

Fig. 8.16. Contour plots of the volume fractions

Unmodified Geometry:

(Bottom outlet =12.5mm, Top outlet =25mm and Core angle = 20°)

Bottom outlet =   (11mm)   (13mm)   (15mm)

Top outlet =   (20mm)   (30mm)
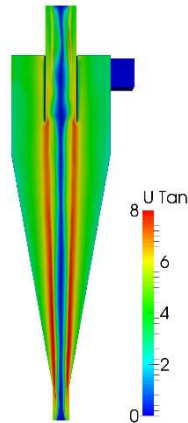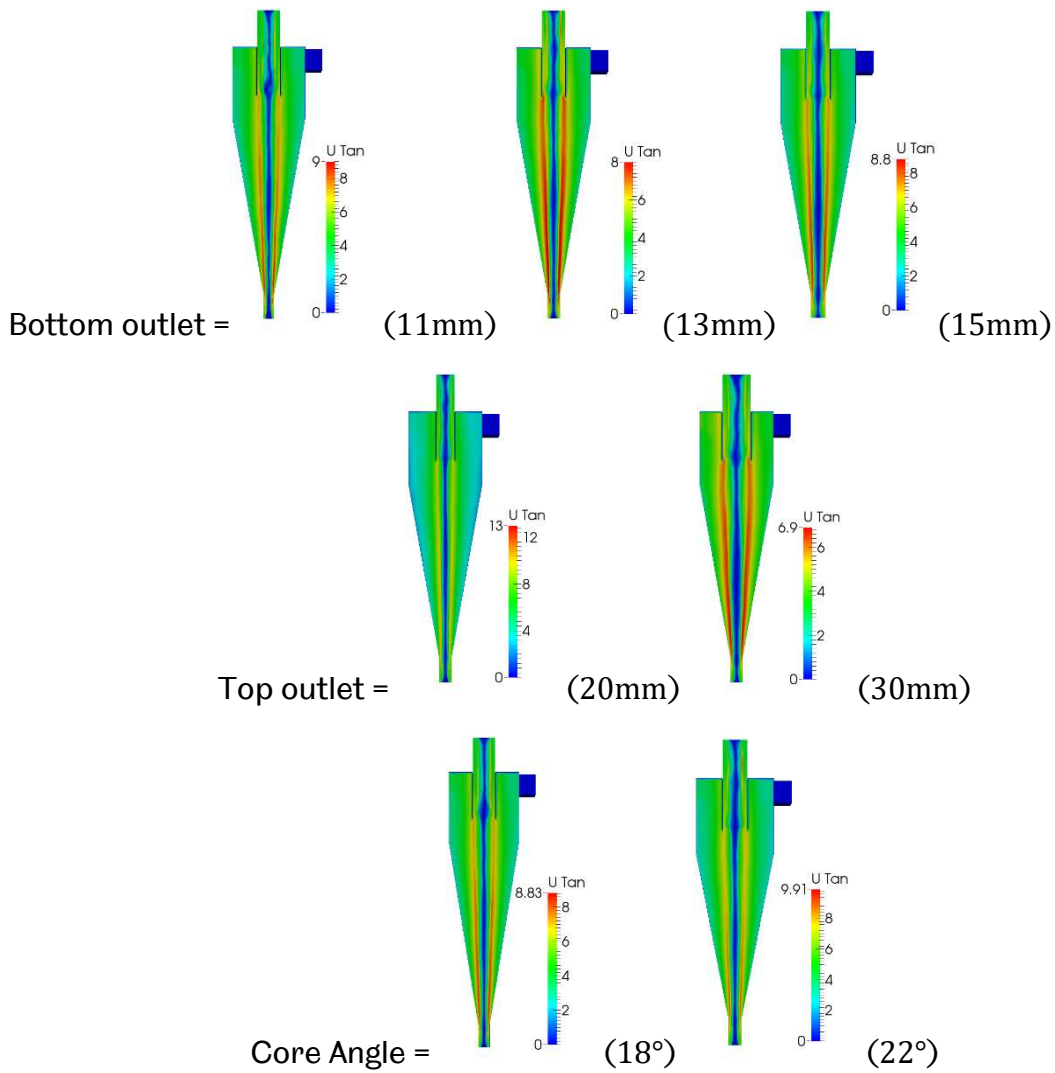
Core Angle =   (18°)   (22°)

Fig. 8.17. Contour plots of the Tangential velocity

Unmodified Geometry:

(Bottom outlet =12.5mm, Top outlet =25mm and Core angle = 20°)

Bottom outlet =   (11mm)   (13mm)   (15mm)

Top outlet =   (20mm)   (30mm)
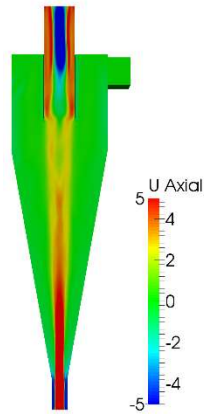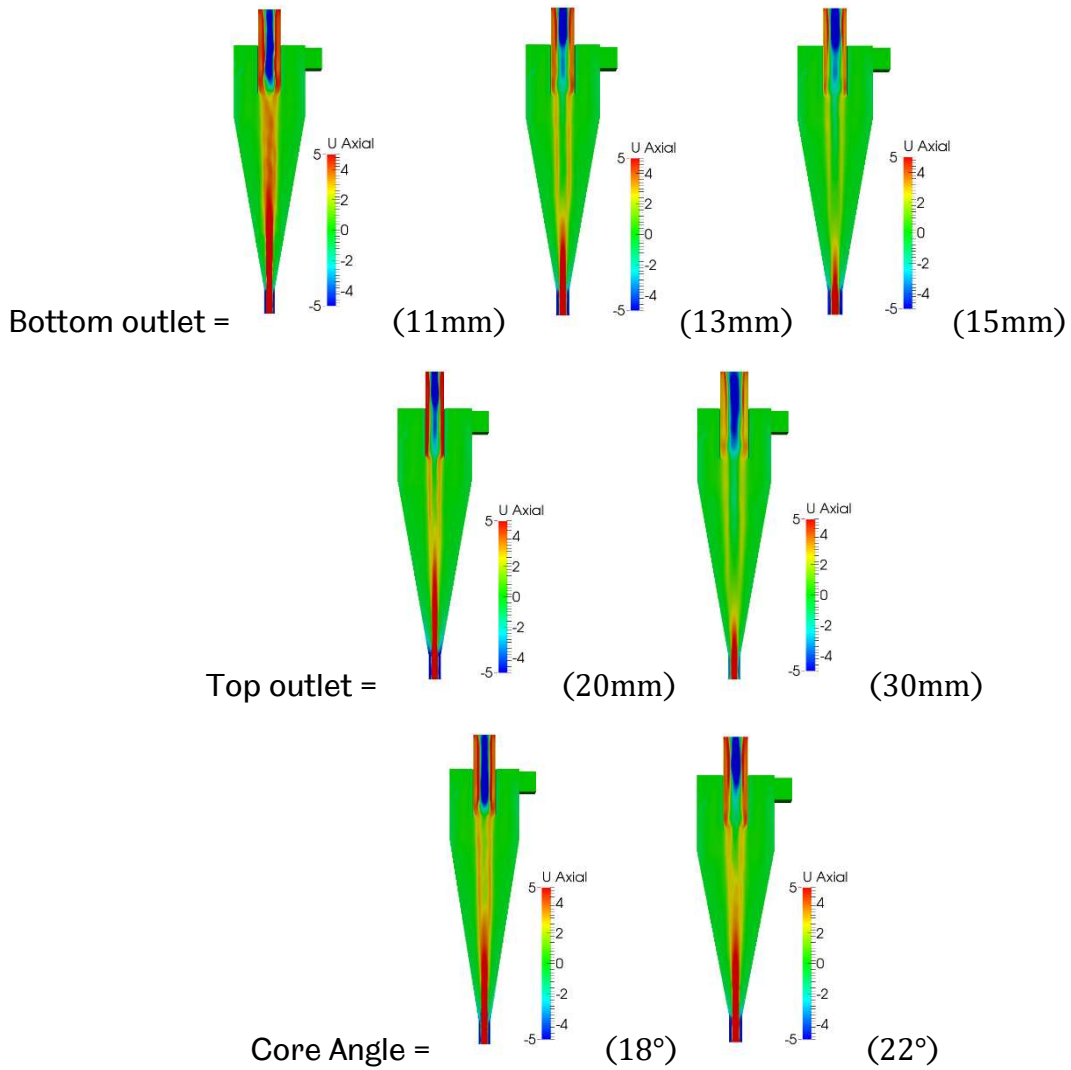
Core Angle =   (18°)   (22°)

Fig. 8.18. Contour plots of the axial velocity

Unmodified Geometry:

(Bottom outlet =12.5mm, Top outlet =25mm and Core angle = 20°)

Bottom outlet =   (11mm)   (13mm)   (15mm)

Top outlet =   (20mm)   (30mm)
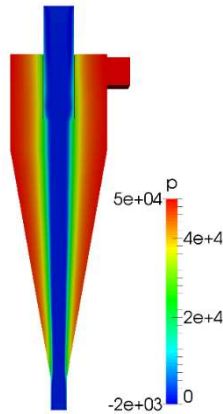
Core Angle =   (18°)   (22°)
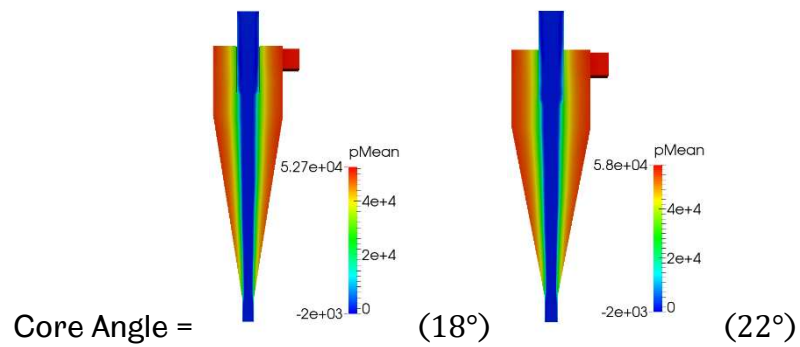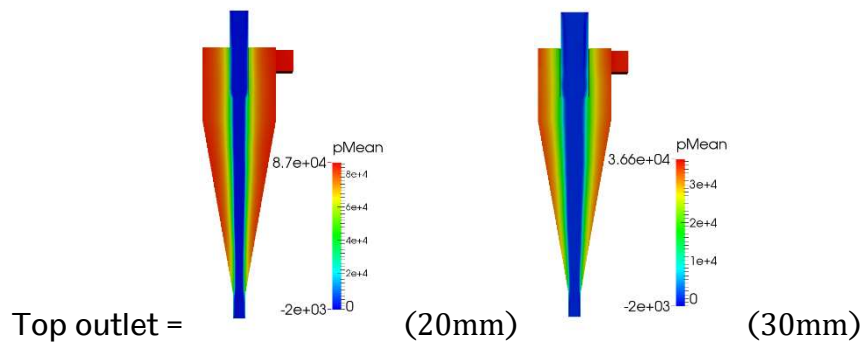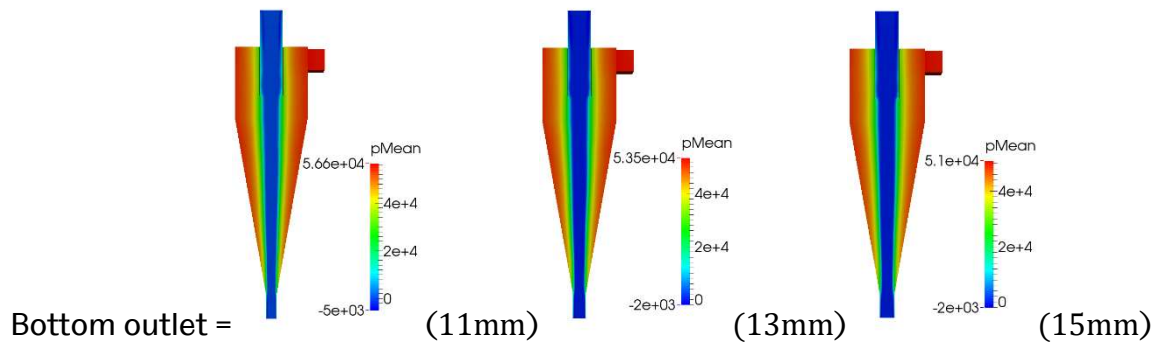
Fig. 8.19. Contour plots of the pressure field
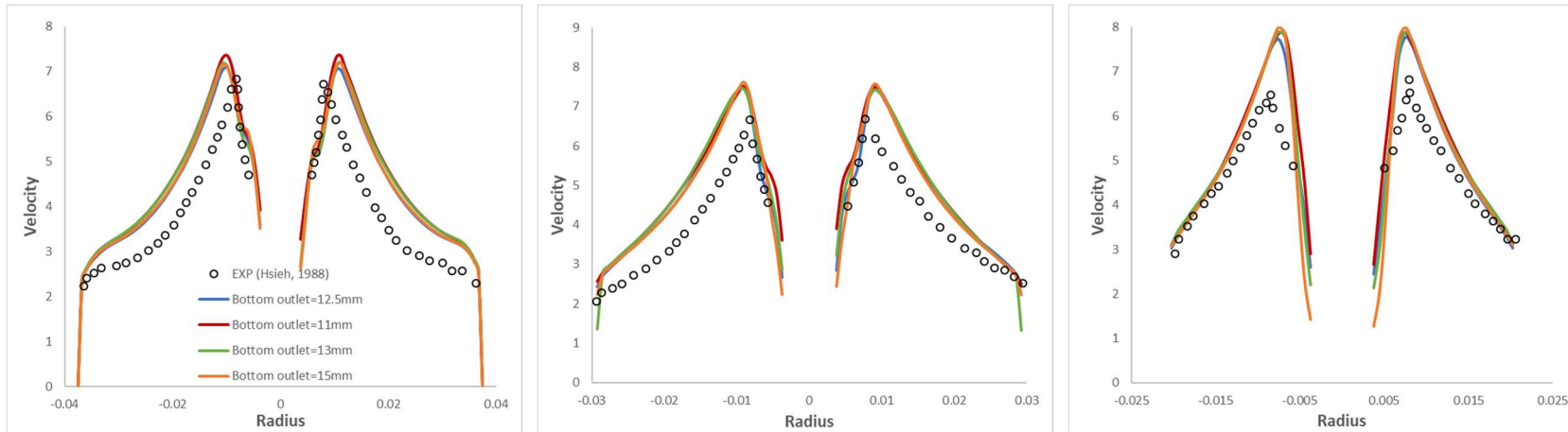
Fig. 8.20. Profile of the tangential velocity curve obtained by hydrocyclone with different Bottom outlet diameter
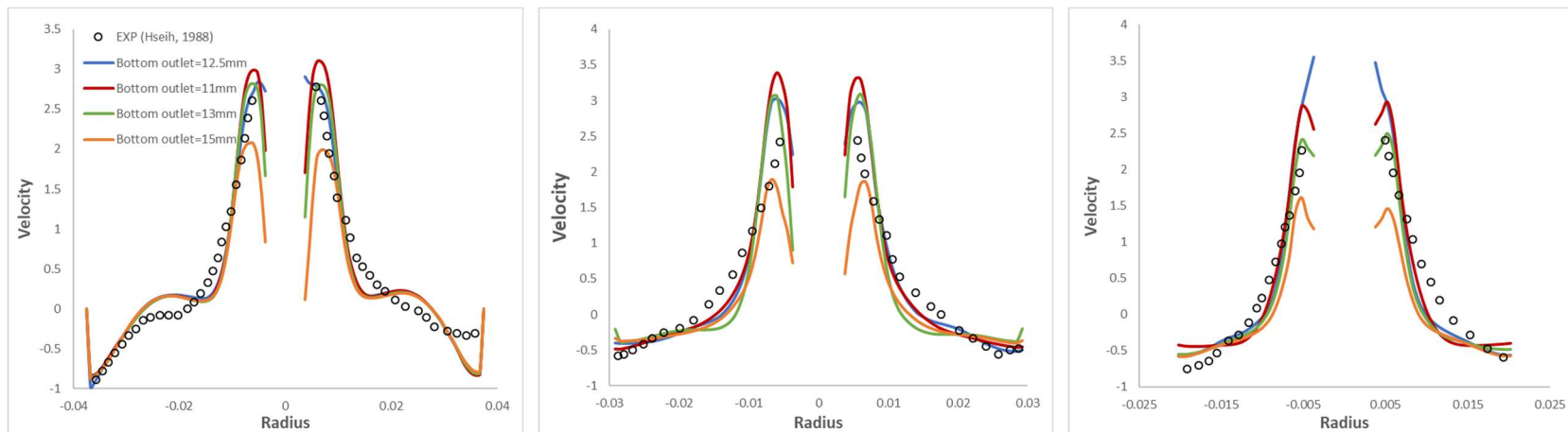
Fig. 8.21. Profile of the axial velocity curve obtained by hydrocyclone with different Bottom outlet diameter
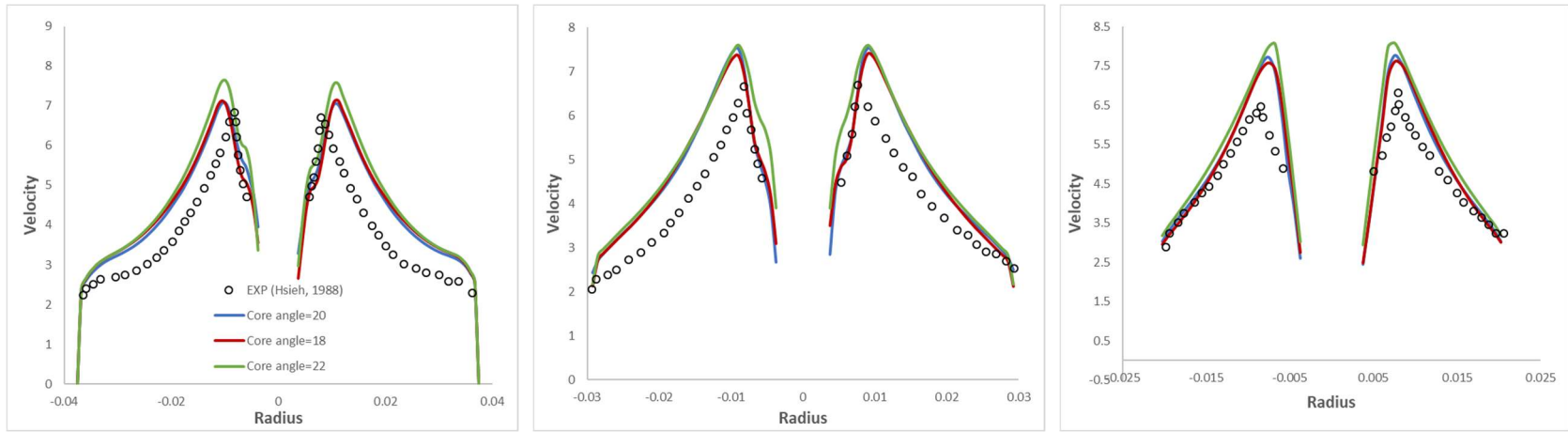
Fig. 8.22. Profile of the tangential velocity curve obtained by hydrocyclone with different Core angle
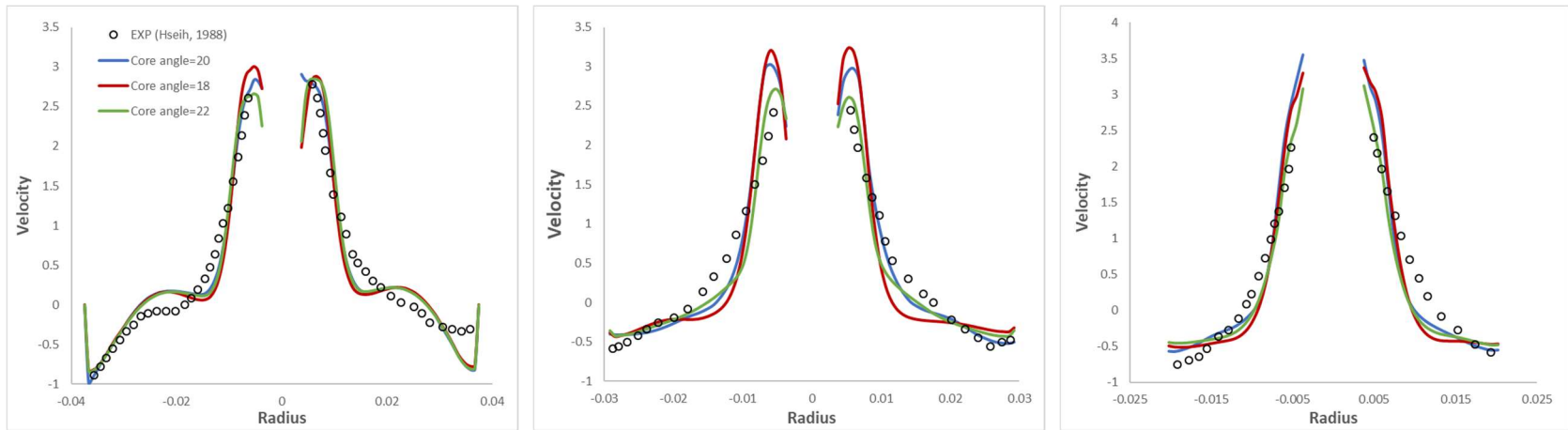
Fig. 8.23. Profile of the tangential velocity curve obtained by hydrocyclone with different Core angle

163
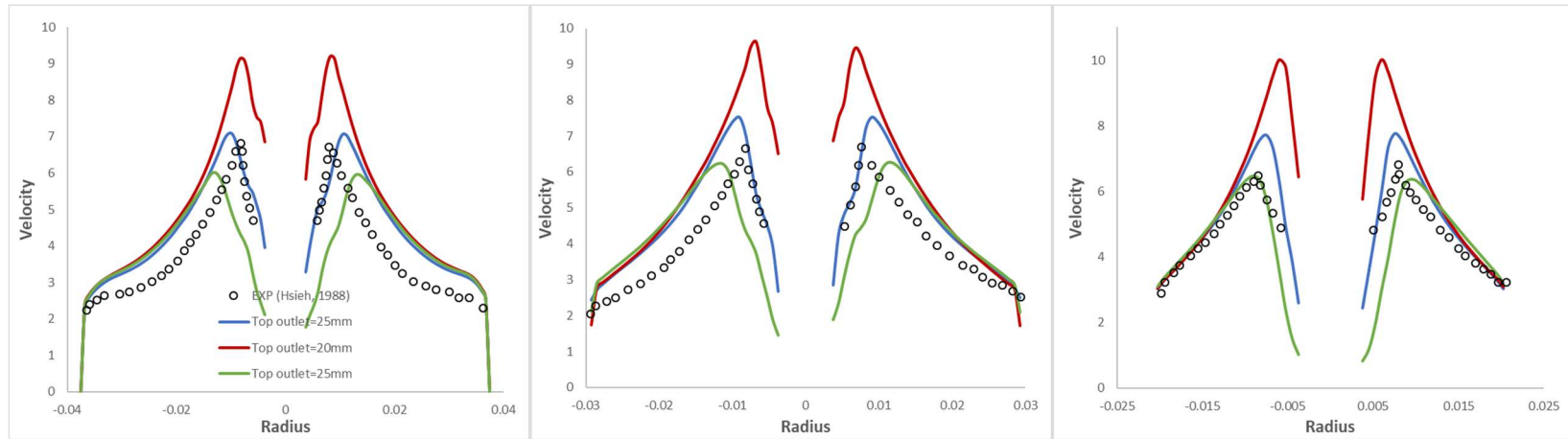
Fig. 8.24. Profile of the tangential velocity curve obtained by hydrocyclone with different Top outlet diameter
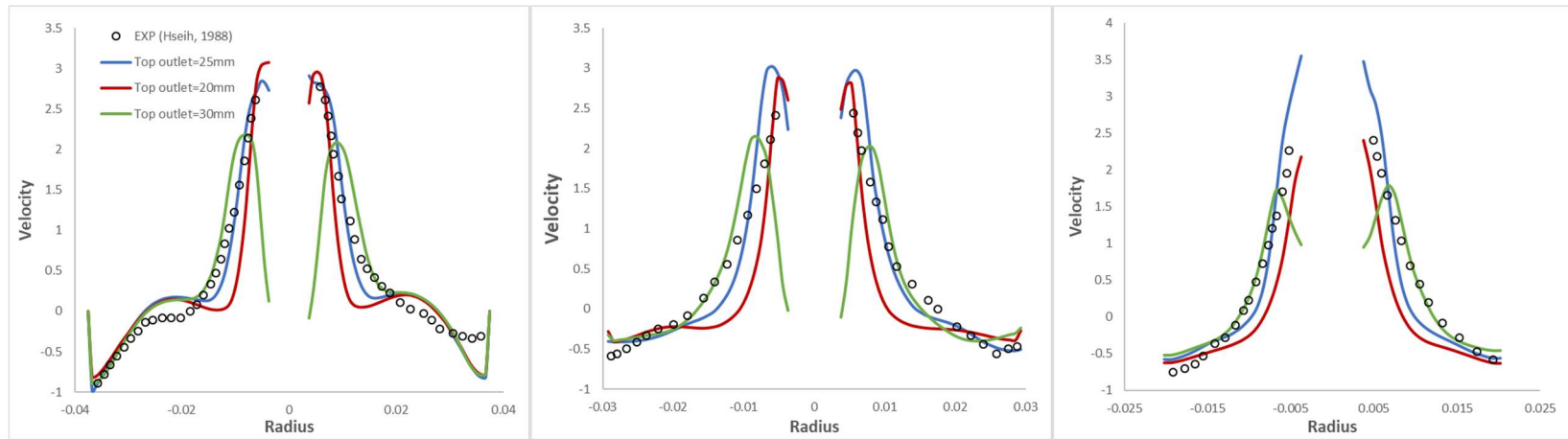
Fig. 8.25. Profile of the tangential velocity curve obtained by hydrocyclone with different Top outlet diameter

Table 8.1. Water split ratio of hydrocyclones in different dimensions (a. Top outlet $= 25$ mm, $Cone\ angle = 20°$)

	Bottom outlet $= 11\ mm$	Bottom outlet $= 12.5\ mm$	Bottom outlet $= 13\ mm$	Bottom outlet $= 15\ mm$
$VOF - RSM$	15.09%	21.11%	24.3%	33.4%
$VOF - LES$		21.02%		
$VOF - KE$		21.16%		

(b. $Bottom\ outlet = 12.5\ mm$, $Cone\ angle = 20°$)

	$Top\ outlet = 20\ mm$	$Top\ outlet = 25\ mm$	$Top\ outlet = 30\ mm$
$VOF - RSM$	39.97%	21.11%	14.46%
$VOF - LES$		21.02%	
$VOF - KE$		21.16%	

(c. $Bottom\ outlet = 12.5\ mm$, $Top\ outlet = 25$ mm)

	$Cone\ angle = 18°$	$Cone\ angle = 20°$	$Cone\ angle = 22°$
$VOF - RSM$	22.10%	21.11%	22.19%
$VOF - LES$		21.02%	
$VOF - KE$		21.16%	

8.4.3 Simulations based on different interface smearing factors

The interface smearing factor is an important element used in the equation of the developed VOF method. This factor, C_α influences the value of the artificial convection term, which is given as

$$\phi_{rf}\gamma_{rf}(1-\gamma)_{rf}$$

(8.1)

And

$$\phi_{rf} = \min\left[C_\alpha \frac{|\phi_f|}{|S_f|}, \max\left(\frac{|\phi_f|}{|S_f|}\right)\right](n_f \cdot S_f)$$

(4.48)

The artificial convection term is used to compress the thickness of the free-surface between different fluids. Thus, the value of the interface smearing factor will influence the magnitude of the artificial convection term and the stability of the simulation. Another potential influence is that the simulation result may be distorted by adding the artificial convection term. It is necessary to find the optimal value of the smearing factor for the current study.

The value of the interface smearing factor used in previous simulations was set using the default value, $C_\alpha = 1$, and the current study using $C_\alpha = 0, 0.5, 1$ and $C_\alpha = 2$ for simulations and comparisons. The contour plots of the volume fraction are given in Fig. 8.26. They illustrate that the thickness of the free-surface increases as the value of the interface smear factor decreases. When the factor, $C_\alpha = 0.5$ or $C_\alpha = 1$, the free-surface is regular and smooth. The pressure, tangential velocity and axial velocity contour plots are given in Fig. 8.27, Fig. 8.28 and Fig. 8.29, respectively. The difference is not conspicuously presented in these plots.

The curve graphs help to amplify the discrepancies between the simulation results. It can be found that the difference appears mainly near the free-surface. The smaller the value of the interface smearing factor, the smoother the gradient of the tangential velocity (see Fig. 8.30). In terms of the axial velocity curve (see Fig. 8.31),

because there are not enough variables of the surface smearing factor used in the current study, the differences between each curve have no obvious rules to follow. All the simulation results are acceptable compared to the experimental results at each observation level.

Finally, due to the simulation being solved using the PIMPLE algorithm, the stability of the simulations is essential and it is influenced by the value of the interface smearing factor. When the value is $C_\alpha = 2$, in order to keep the courant number smaller than 1, the time step needs to be set shorter than $5 \times 10^{-6} s$. When the factor is $C_\alpha \leq 1$, the time step can be set to $1 \times 10^{-5} s$ and the simulation can still remain stable. Thus, the time spent in the simulation is almost halved.

$(C_\alpha = 0)$ $\qquad$ $(C_\alpha = 0.5)$ $\qquad$ $(C_\alpha = 1)$ $\qquad$ $(C_\alpha = 2)$
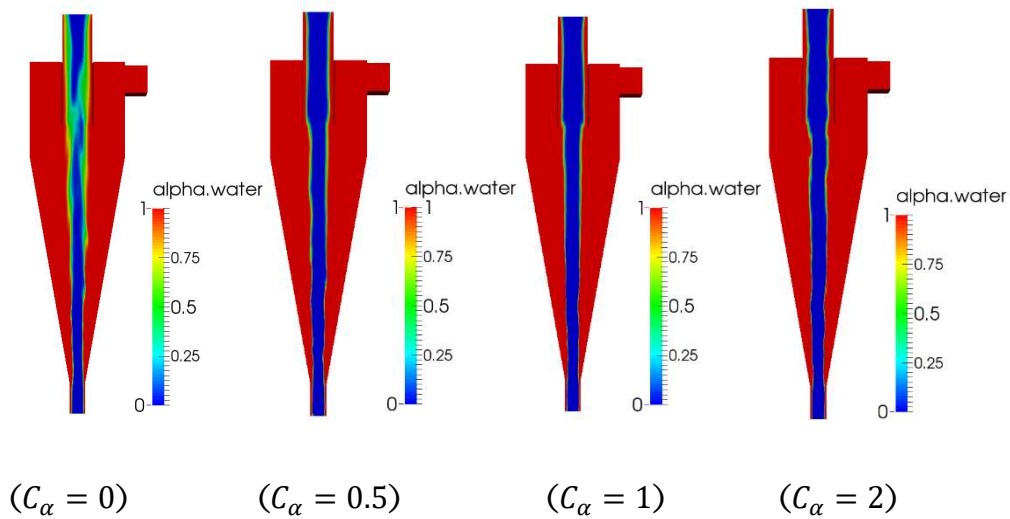
Fig. 8.26. Volume fraction contour plots obtained by simulations using different C_α.

$(C_\alpha = 0)$ $\qquad$ $(C_\alpha = 0.5)$ $\qquad$ $(C_\alpha = 1)$ $\qquad$ $(C_\alpha = 2)$
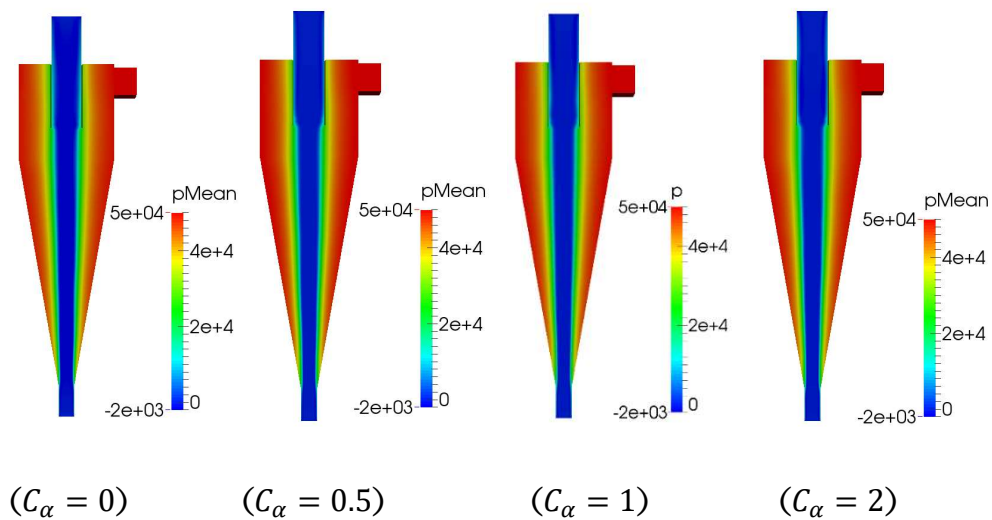
Fig. 8.27. Pressure contour plots obtained by simulations using different C_α.

$(C_\alpha = 0)$ $(C_\alpha = 0.5)$ $(C_\alpha = 1)$ $(C_\alpha = 2)$
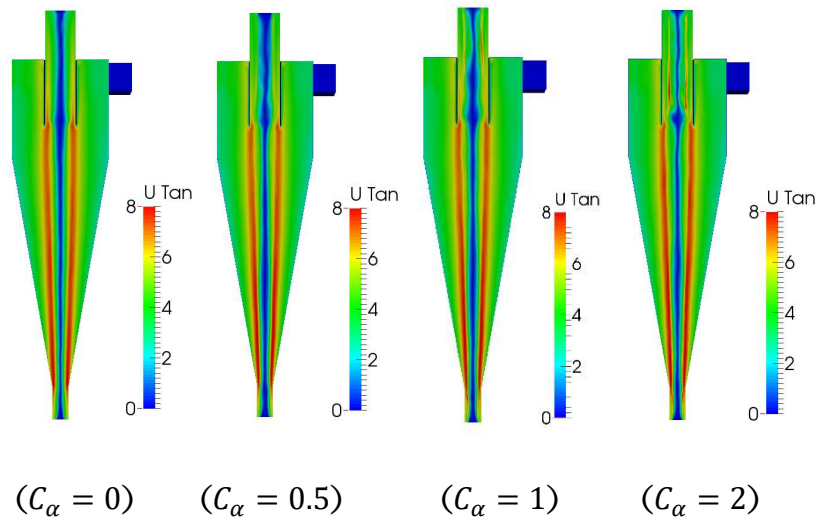
Fig. 8.28. Tangential velocity contour plots obtained by simulations using different C_α.

$(C_\alpha = 0)$ $(C_\alpha = 0.5)$ $(C_\alpha = 1)$ $(C_\alpha = 2)$
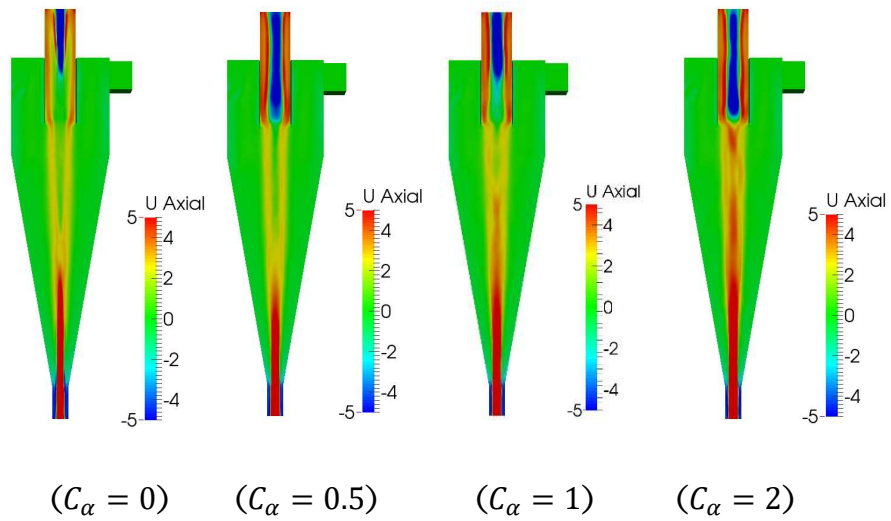
Fig. 8.29. Axial velocity contour plots obtained by simulations using different C_α.
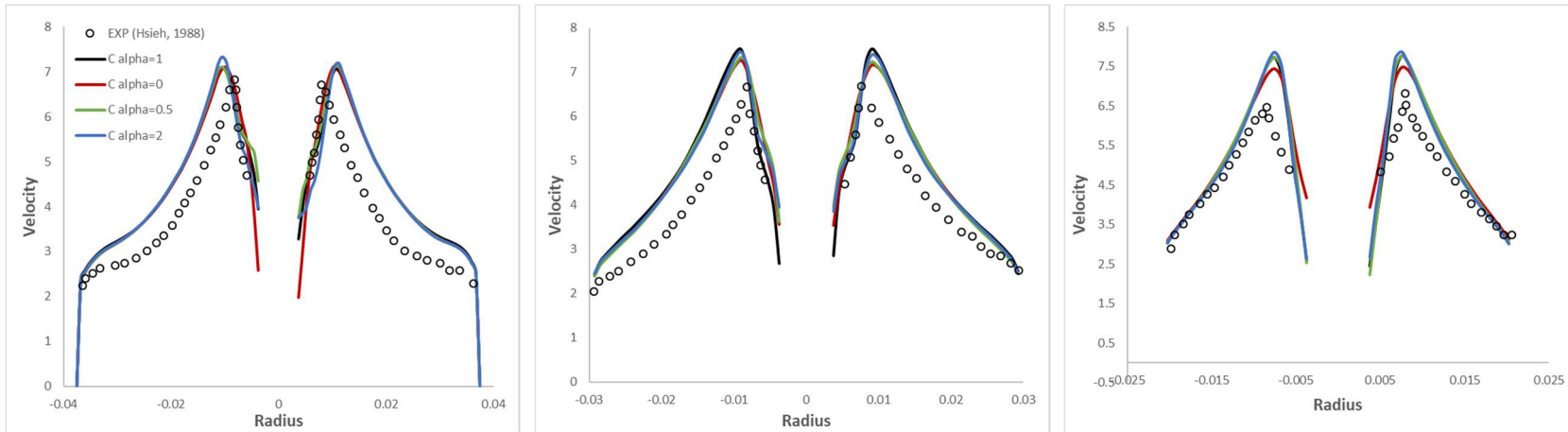
Fig. 8.30. Profile of the tangential velocity curve obtained by simulation using different C_α.
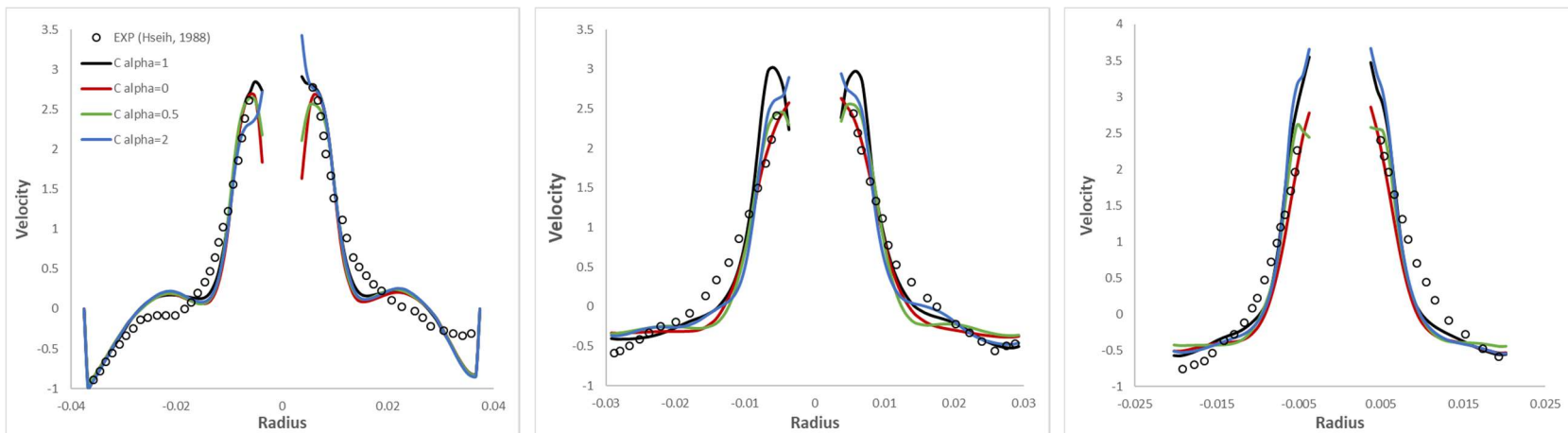
Fig. 8.31. Profile of the axial velocity curve obtained by simulation using different C_α.

169

8.4.4 Simplification of the simulation of the flow in hydrocyclones

The above simulations use the developed VOF method to investigate the phenomena of the air-core in a purely air-water hydrocyclone flow. However, in most situations, the working conditions in the hydrocyclone are complicated. The liquid phase is often mixed with solid particles, or the liquid flow flows through the hydrocyclone as a mixed suspension of high density and high viscosity. In such cases, it should be considered whether it is worth including the air phase in the simulations because the simulation will save much time when only the primary phase is simulated. The process of weighing needs to investigate how the air-core affects the flow fields of the liquid phase. Thus, in the current study, the simulation only considered the liquid phase. In other words, the current simulation is a single-phase flow problem. The properties of the liquid are set consistent with the above simulations, and the RSM turbulence model is used for simulation.

The volume fraction contour plot is unnecessary for the current simulation and contour plots of the pressure, tangential velocity and axial velocity are presented for comparison. The tangential velocity contour plot in Fig. 8.33. presents that the high-velocity area is closer to the centre of the hydrocyclone compared with the plots obtained by the VOF-RSM method. The axial velocity contour plot shown in Fig. 8.34 is similar to the contour plots obtained by the VOF-RSM method. In terms of the pressure contour plot, the low-pressure area in Fig. 8.32 is narrower than the area shown in the plots obtained by the VOF-RSM method. In addition, the pressure values in the low-pressure area in the VOF-RSM plots are almost equal, while the pressure values in the low-pressure area on the left of Fig. 8.32 gradually increase from the centre outwards.

Fig. 8.35 shows the curves of the tangential velocity obtained through the experiment and simulations using the VOF-RSM method, the VOF-LES method and the single-phase RSM method at three observation levels. The curves predicted by the VOF-LES method and the single-phase RSM method are highly consistent with the curves obtained by experiments in the peripheral region of the liquid phase. Moreover, the tangential velocity curve predicted by the single-phase RSM method has a maximum velocity value closer to the experimental value. Nevertheless, in the area near the

free-surface, the curve obtained by the VOF-based solver is more accurate. Regarding the axial velocity curves (see Fig. 8.36), the curves yielded by the single-phase RSM method are acceptable, especially compared with the curve predicted by the VOF-LES method. However, it is not as accurate as the curves predicted by the VOF-RSM method.

- **The collection efficiency predicted by the simplified simulation.**

The simulation result of the collection efficiency is produced by the DPM method. Due to the prediction of the flow fields obtained by the simplified single-phase hydrocyclone flow simulation being acceptable, the Eulerian domain of the continuous phase is assumed to be single-phase. The trajectory of a discrete phase particle is predicted by integrating the force implemented on the particle, as Section 3.6 described. The simulation result is shown in Fig. 8.37 and Fig. 8.38

Compared with the experimental data, the curves obtained by the simulations prove that the simplification of the continuous phase is acceptable. The collection efficiency predicted by the DPM method without considering the effect caused by the air-core is also accurate. The primary influence on the accuracy of the prediction still depends on the turbulence model. The RSM model and the $k - \varepsilon$ RNG Curvature Correction model provide the best result for predicting the curve of the collection efficiency.

From the several simulations above, it can be seen that when the CFD method is used for relatively simple simulation and analysis, the effect of the air-core on the hydrocyclone is negligible. Moreover, in most cases, the air-core phenomenon does not exist, such as with the use of multiple separators for multi-stage separation. As such, a simplified simulation of a hydrocyclone will greatly increase the speed of assisted design using the CFD method.

(Without using VOF)   (VOF-RSM)
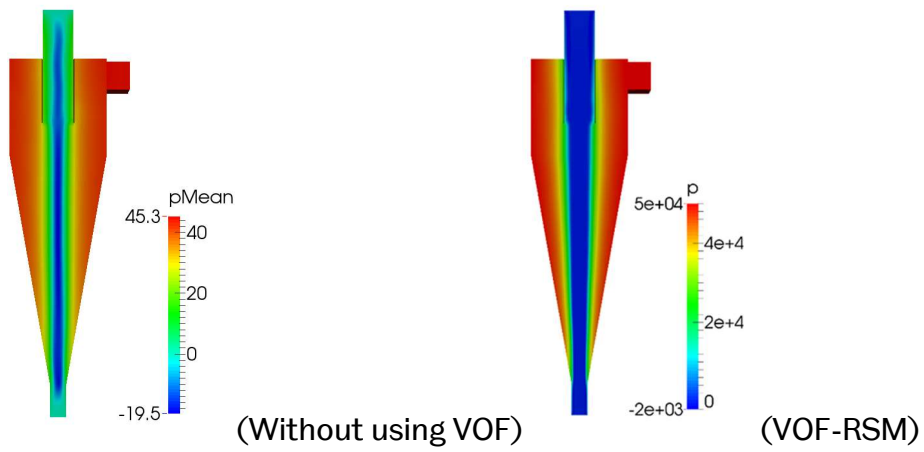
Fig. 8.32. Pressure contour plots of single-phase flow.

(Without using VOF)   (VOF-RSM)
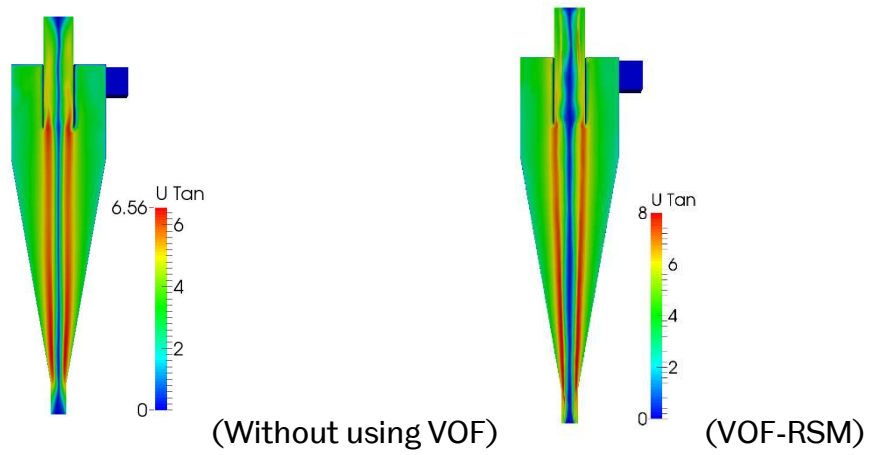
Fig. 8.33. Tangential velocity contour plots of single-phase flow.

(Without using VOF)   (VOF-RSM)
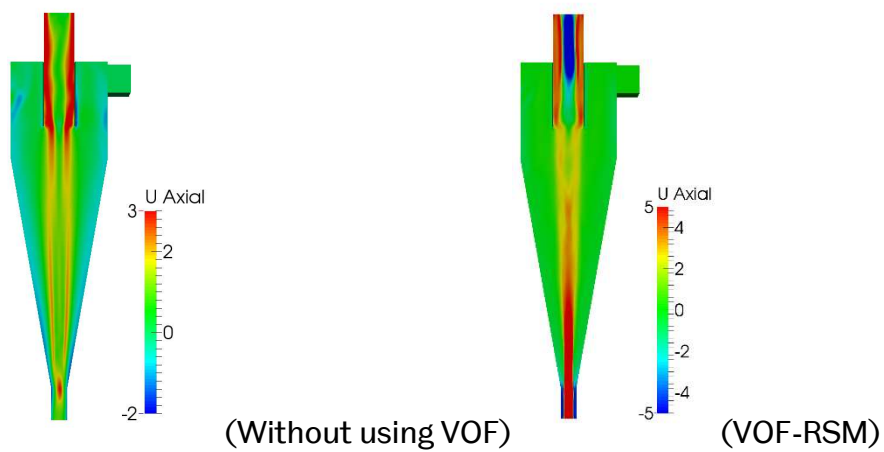
Fig. 8.34. Axial velocity contour plots of single-phase flow.
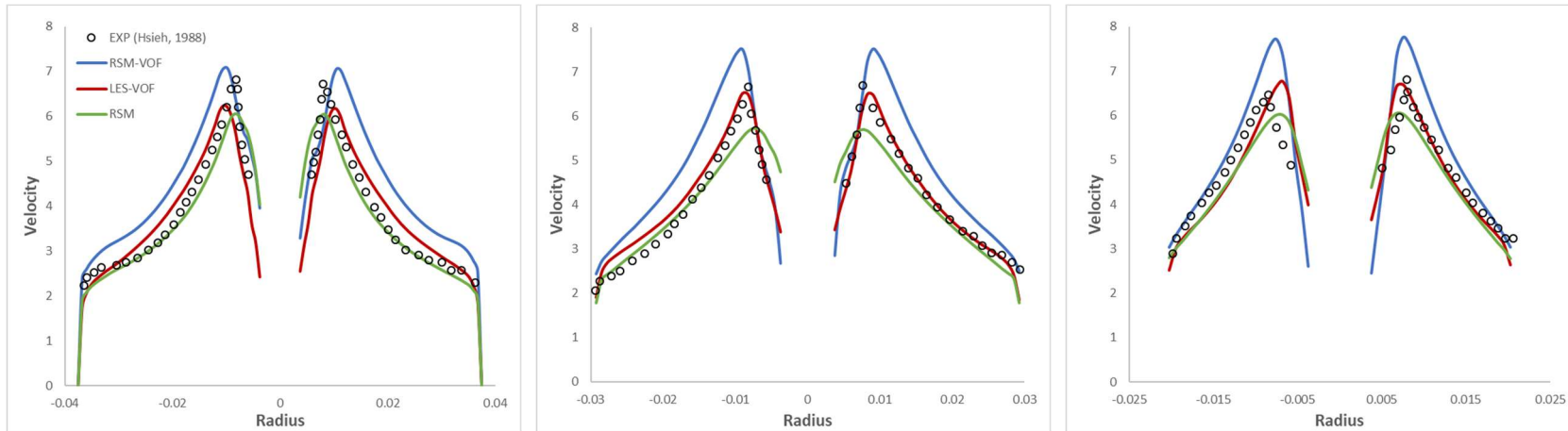
Fig. 8.35. Profile of the tangential velocity curve obtained by simulation using single-phase flow assumption.
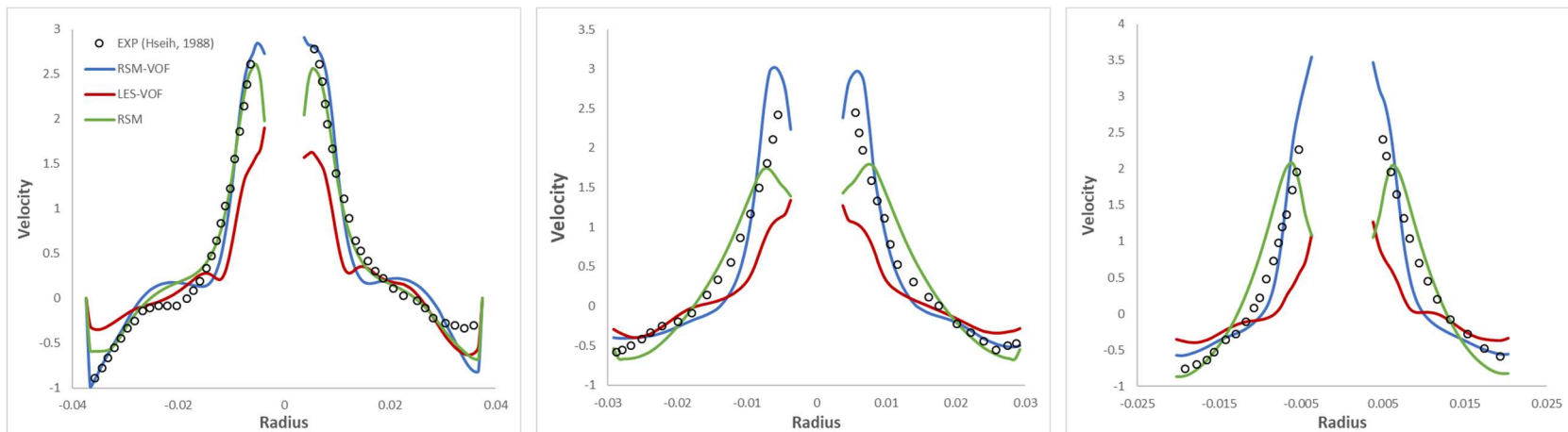
Fig. 8.36. Profile of the axial velocity curve obtained by simulation using single-phase flow assumption.
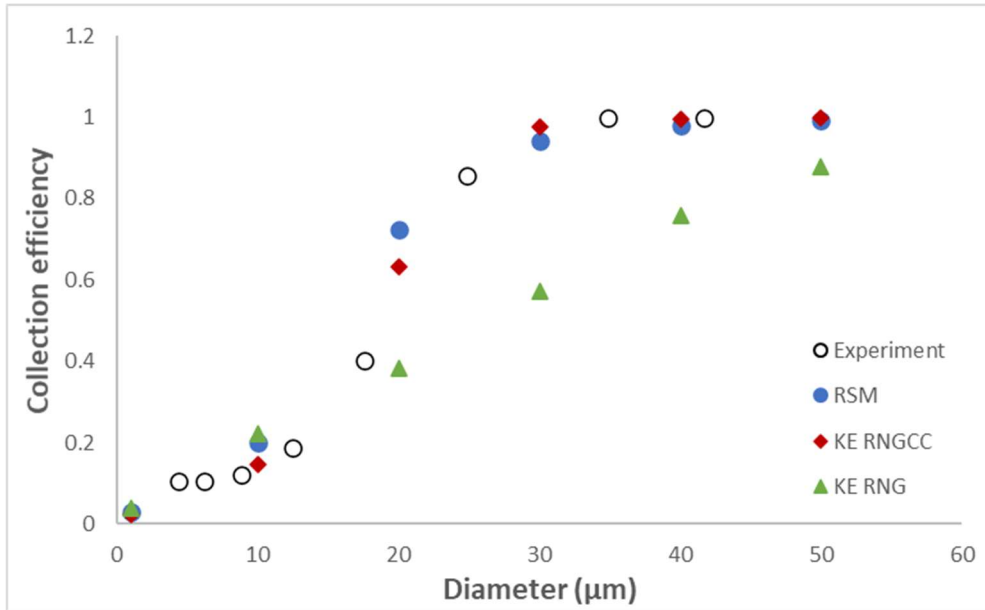
Fig. 8.37. Simulated collection efficiency curves for 4.78% mass loading.
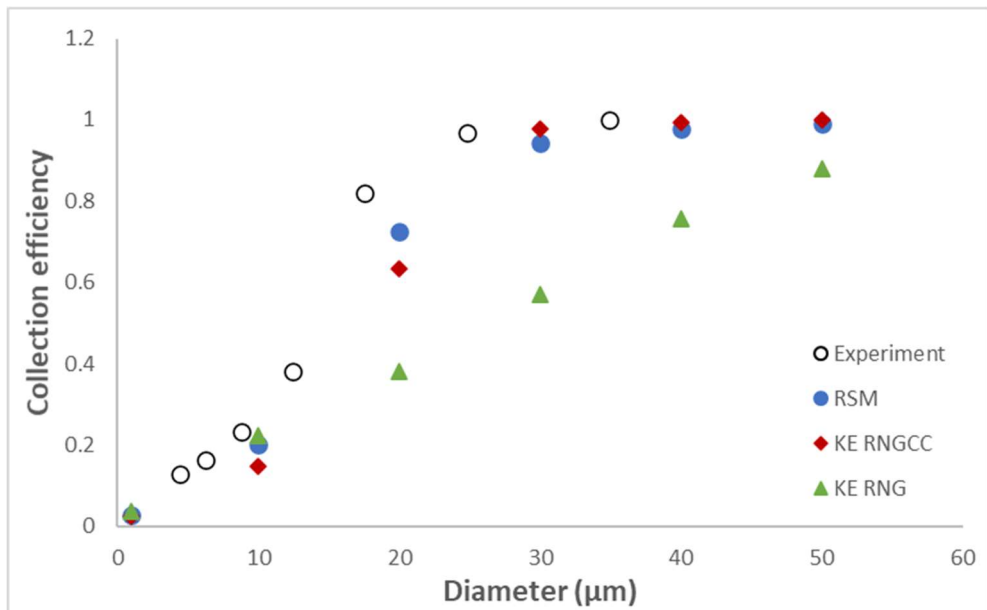
Fig. 8.38. Simulated collection efficiency curve for 10.2% mass loading.

Chapter 9. Conclusion

Having completed the current work, the conclusions of all the studies will be summarised. The primary aim for the current work has been to find a new numerical methodology to analyse the flow fields of the flow with air-core in hydrocyclones. The Reynolds Stress Model (RSM) has been employed to deal with an anisotropic turbulent flow in hydrocyclones. Furthermore, the new method, which is constructed based on the developed-Volume of Fluid method (Weller, 2008) has been used to tackle the problem of the multi-phase flow with a clear free-surface. The modified advection term in the volume fraction equation helps to compress the thickness of the free-surface. The customised MULES solver is an integral part of this novel VOF method, which is derived from the Flux Corrected Transport (FCT) technique that guarantees the accuracy and boundedness. In addition, the High-Resolution Scheme (HRS) has been applied to further optimise the developed VOF method. This technique helps to eliminate unexpected oscillations and dissipation near strong gradients. With such a method, the simulation of multi-phase flow in the cyclone has been further improved. The regions of the multi-phase flow can be predicted, and the free-surface between different phases can be captured accurately and clearly, even during the transient state. The specific achievements and conclusions are given below.

9.1 Conclusions of the work

- This thesis gives a brief introduction to the CFD techniques used in the current work. These include: the discretization technique based on the Finite Volume Method; the governing equations used for numerical simulation; the turbulence model used for predicting the fields of turbulence flow; the algorithm used for solving the problem of pressure-velocity coupling; the principles of the Volume of Fluid method with the Flux Corrected Transport (Multi-dimensional Universal Limiter for Explicit Solution) method; the High Resolution Schemes framework based on the Total Variation Diminishing schemes and the strategies used for geometry modelling and mesh generation.

- The fundamental simulations (simulation of the flow in cyclones and simulation of the dam breaking flow) presented good results and provided sufficient experience for the simulation of the flow with air-core in hydrocyclones. This simulation of the flow proves that the RANS method with the RSM turbulence model is able to predict the flow fields of the flow in cyclones. Owing to the anisotropic character of the turbulent flow with large swirls, the standard $k - \varepsilon$ turbulence model fails to accurately capture the flow fields. As a result, the turbulent kinetic energy is overestimated. The simulation of the dam breaking flow demonstrates that the volume of fluid method is able to capture the movement of the free-surface between different phases. Furthermore, with the FCT and HRS techniques, the thickness of the free-surface can be limited. The PIMPLE algorithm is able to predict the fields of the flow in transient state within an acceptable range, and it helps to investigate the formation process of the air-core. In addition, turbulence models can be applied in multi-phase flow solvers to obtain more accurate simulation results.

- The primary simulation of the flow with air-core in hydrocyclones were carried out using the RSM turbulence model and the develop-VOF method. Acceptable results have been generated compared with the experimental data obtained by Hsieh (1988) and the snapshot taken by Wang et al. (2015). In terms of the tangential velocity, the characteristic of the "Rankine vortex" has been captured by the numerical simulation method and the obtained curves matched the experimental curves within an acceptable range. The numerical simulation results of the axial velocity also provided curves that match the experimentally obtained curves at each observation level. The numerical simulation result of the pressure fields demonstrated that the low-pressure area coincides with the air-core area, which indicates that the air-core is formed due to the low pressure in the hydrocyclone. The process of forming the air-core captured by the numerical simulation method can also be considered reasonable. When the initial state of the hydrocyclone flow is filled with air, the air-core is formed by the rotating water stream, which flows around the air-core located at the centre of the hydrocyclone. When the initial state of the hydrocyclone flow is filled with liquid, the air-core is formed in the low-pressure area, and the pressure in the centre of the separator is lower than the external pressure, which causes air to flow back into the hydrocyclone. The air streams reach the bottom of the vortex

finder, extending until they form an air-core and become steady. This phenomenon is consistent with Davidson's theory (Davidson, 1988).

Further studies have been undertaken to explore the performance of the numerical simulation method with different turbulence models and adjustable coefficients. These have managed to optimise the numerical method to design the hydrocyclones in particular cases.

- The simulation results of the first study demonstrate that the LES method with the subgrid-scale kinetic energy model is able to present an accurate simulation result in terms of the tangential velocity. The phenomena of the air-core can also be predicted by the LES method. However, the $k - \varepsilon$ turbulence model not only cannot capture the air-core phenomenon in the hydrocyclone, but also the flow fields in the hydrocyclone cannot be accurately predicted.

- The second simulations of the further studies have proven that the angle of the conical part and the size of the top outlet and the bottom outlet will affect the prediction of flow fields in hydrocyclones. As the diameter of the top outlet increases, the maximum value of the tangential velocity decreases, and the position where the maximum value appears is shifted to the outward of the hydrocyclone. Furthermore, the value of the axial velocity increases near the free-surface, the size of the upper half of the air-core in the hydrocyclone also becomes larger and the water split ratio decreases.

  As the variation of the bottom outlet diameter is small, the difference in the predicted flow fields is not obvious. This can give the conclusion that the difference in the value of the tangential velocity and axial velocity is insignificant; as the diameter of the bottom outlet becomes smaller, the size of the lower half of the air-core becomes narrower, and the water split ratio decreases.

- Regarding the cone angle, with its increase, the length of the conical part decreases; the maximum value of the tangential velocity increases; the value of the axial velocity near the free-surface barely changes; the water split ratio has a minimum value when the cone angle is $10°$, and the size of the air-core is almost unchanged.

- The interface smearing factor C_α is an important parameter that affects the volume fraction equation in the developed-VOF method. The third simulation in

the further studies demonstrates that the thickness of the free-surface will decrease as the factor increases. However, after the value of the coefficient is greater than 1.0, the change in thickness becomes insignificant, and the simulation becomes unstable, which requires a smaller time step for the simulation. Although the artificial convection term determined by the interface smearing factor are introduced into the volume fraction equation, the simulation results of the flow fields are not greatly affected. Overall, in the current simulations, the interface smearing factor equalling 0.5 is considered the optimal choice.

- The last further study in the current work has attempted to simplify the simulation of the flow in hydrocyclones by ignoring the effect caused by the air-core. The simulation results have proven that the flow fields of the water phase were accurately predicted. Even if an air-core appears in the centre of the hydrocyclone, the liquid phase is still considered the main phase that influences the flow fields inside the cyclone or hydrocyclone. When solid particles flow into the separator, the liquid phase will become the main current-carrying phase, so this simplification is considered reasonable. In addition, the simulation result of the collection efficiency is acceptable, which further proves that in the numerical simulation method, the air-core phenomenon does not play a significant role in the prediction of the separation efficiency of low concentration solid-liquid fluids.

Based on the above conclusions, it has been found that using the new numerical method can successfully simulate the flow with air-core in hydrocyclones. Compared with the previous numerical simulations, the new numerical method more realistically simulates the transient flow state in the hydrocyclone, and provides reasonable prediction values for the flow fields data under steady state. Therefore, after validating that the numerical simulation method is feasible, the design of the cyclone separator can be modified by the numerical simulation method, thereby saving time and money in preparing the experimental equipment. The further studies have also provided useful experience for the design of cyclones and hydrocyclones, which can be used by the petroleum, chemical, materials and other industries.

9.2 Future work

Although the simulation of the flow with air-core in hydrocyclones has presented an acceptable result, there remains work to be investigated and refined in the aspects of the numerical simulations and experiments, for which detailed statements are given below

- The primary task is to build a solver in OpenFOAM® that can simulate a solid-liquid-gas three-phase flow. Although for higher concentration suspensions, solid particles can be assumed to be dissolved in the liquid and impart particular physical properties to the suspension, such as density and viscosity, the flow fields of such a three-phase flow can be directly simulated by the VOF method, mixture-model method and the Eulerian-Eulerian approach. However, when the concentration of solid particles is low, or the particles are large, the mixture of solid particles and liquid cannot be assumed to be multi-continuum. In this case, it is more reasonable to simulate the interaction between solid particles and the continuous phase using the Lagrangian-Eulerian method. Based on the integral of the particle path in the entire computational domain, interaction with the continuous phase and particles can be simulated through one-, two-, or four-way coupling. The VOF or mixture model can be used to predict the flow fields of the continuous phase. Tracking is achieved by writing force equilibrium equations for the solid particles which would afford different types of force based on the complexity of the model (Rudolf, 2013). If this new solver runs smoothly on OpenFOAM® and is verified by benchmarks, then based on experiments performed by Hsieh (1988), new simulations and validations should be implemented.

- Hsieh's experiment used the laser Doppler velocimetry (LDV) technique to measure the fluid velocity inside the hydrocyclone, over 30 years ago. It is believed that the convenience and accuracy of the experimental method will have been further improved in these 30 years. Therefore, a new experiment should be undertaken for the measurement of the fluid flow velocity inside the hydrocyclone. The new experiment can be implemented using the LDV method or using other methods, such as the micro-Particle Image Velocimetry (micro-PIV) or electrical impedance technology (EIT).

- The simulation results in this work's further studies have not been validated by the corresponding experiments. Therefore, the experimental results lack validity. If conditions permit, corresponding experiments still need to be carried out, especially for the simulation of changing the size of the hydrocyclone. Practical simulation results will facilitate the design of the separator.

- The simulation efficiency using the RSM-VOF method is not efficient. This may be caused by the use of a large number of structural grids. The uniformity of the structural grids makes the grids in the bottom outlet pipeline very small. A small time step is required to ensure the stability of the simulation. Therefore, in future work, simulations using unstructured grids or mixed grids should be attempted. If the results are reasonable, this will not only reduce the establishment time of the grids but also greatly reduce the simulation time.

- Since the simulation has been carried out based on Hsieh's experiments, the geometry and boundary conditions used in the simulation are simplified, and they are assumed to be consistent with the experimental equipment and experimental environment. Some details have not been completely modelled by the simulations so that may cause errors in the simulation results. For example, in the experiment, the shape of the tangential inlet pipe is a cylinder, while in the simulation, the shape of the inlet pipe is a rectangular parallelepiped. Therefore, in future simulations, the equipment used in the experimental equipment and the experimental environment should be restored as much as possible so that unnecessary interference can be eliminated.

- In the current study, using the LES-VOF method has been more efficient and stable than the RSM-VOF method. In some specific regions, the simulation results obtained by the LES-VOF method are more in line with the experimental results. More simulations need to be implemented to verify that the LES method is more suitable for the developed-VOF method than the RANS method.

Appendices A

A.1 Publications

- Y. Hu, A. F. Nowakowski. Investigation of the flow with air-core in hydrocyclones (To be submitted)

A.2 Conference presentations

- Hu, Y., Awadh S.A. and Nowakowski, A. F., Air-core formation in hydrocyclones. 14th Workshop on Synthetic Turbulence Models and Fractional Dynamics. Université de Caen, France, 27th-28th June 2019.

- Awadh S.A., Hu Y., Nowakowski, A. F. and Nicolleau. F.C.G.A., High resolution simulation of cyclone flow. 14th Workshop on Synthetic Turbulence Models and Fractional Dynamics. Université de Caen, France, 27th-28th June 2019.

Appendices B

List of reproduced copyrighted materials

(acknowledgements)

- Figure 7.1 reproduced from Computational Mechanics, 39, 2007, 453-476, "Collapse of a Liquid Column: Numerical Simulation and Experimental Validation", Cruchaga, M.A., Celentano, D.J. and Tezduyar, T.E., figure 12, With kind permission of Springer Nature.

- Figure 8.1 reproduced with kind permission from The Canadian Journal of Chemical Engineering, 93-10, 2015, 1802-1811, "Simulation and experiment on transitional behaviours of multiphase flow in a hydrocyclone", Wang, C. Ji, C. and Zou, J., figure 5. Copyright (2015), Canadian Society for Chemical Engineering.

References

Alahmadi, Y.H. and Nowakowski, A.F. (2016): Modified shear stress transport model with curvature correction for the prediction of swirling flow in a cyclone separator. Chemical Engineering Science. 147, pp. 150-165.

Amini Afshar, M. (2010) Numerical wave generation in OpenFOAM®. Master's thesis, Chalmers University of Technology.

Arugonda, R., Vakamalla, T.S.R., Kumar, R. and Mangadoddy, N. (2013): Air-Core Size Measurement of Operating Hydrocyclone by Electrical Resistance Tomography. Chem. Eng. Technol. 37 (5), pp. 795-805.

Azadi, M. and Mohebbi, A. (2010): A CFD study of the effect of cyclone size on its performance parameters. Journal of Hazardous Materials. 182 (1), pp. 835-841.

Bailly, C and Comte-Bellot, G., (2018): Turbulence. National Defense Industry Press. pp. 39-40

Balogh, M. Parente, A and Benocci, C. (2012): RANS simulation of ABL flow over complex terrains applying an Enhanced k-e model and wall function formulation: Implementation and comparison for fluent and OpenFOAM®. Journal of Wind Engineering & Industrial Aerodynamics. 104(106), pp. 360-368.

Berberovic, E., van Hinsberg, N., Jakirlic, S., Roisman, I. and Tropea, C. (2009): Drop impact onto a liquid layer of finite thickness: dynamics of the cavity evolution. Physical Review. E 79.

Bhaskar, K. U., Mur thy, Y. R., Raju, M. R., Tivari, S, Srivastava, J. K. and Ramakrishnan, N. (2007): CFD simulation and experimental validation studies on hydrocyclone. Miner. Eng. 20, pp.60-71.

Brackbill, J.U., Kothe, D.B. and Zemach, C. (1992): A continuum method for modelling surface tension. Comput. Phys. 100, pp. 335–354.

Bogdanov, D. and Poniaev, S., (2014): Numerical Simulation of the Turbulent Flow in a Cyclonic Separator.16th Russian Youth Conference on Physics and Astronomy. IOP, pp. 1-6.

Boris, J. and Book, D. (1973): Flux-corrected transport. I. SHASTA, A fluid transport algorithm that works. Journal of Computational Physics. 11, pp. 38-69

Boysan, F., Ayers, W.H. and Swithenbank, J., (1982): A fundamental mathematical modelling approach to cyclone design. Transactions of the Institution of Chemical Engineers 60, 222–230.

Brennan, M., (2006): CFD Simulations of hydrocyclones with an air-core - Comparison between Large Eddy Simulations and a Second Moment Closure. Chemical Engineering Research and Design. 84(A6), pp. 495–505

Brennan, M.S., Narasimha, M. and Holtham, P.N., (2006): Multi-phase modelling of hydrocyclones - prediction of cut-size. Minerals Engineering. 20 (2007), pp. 395–406

Caretto, L. S., A. D. Gosman, S. V. Patankar, and D. B. Spalding., (1973): Two calculation procedures for steady, three-dimensional flows with recirculation. Lecture Notes in Physics. 19, 60.

Carrica, P., Wilson, R., Stern, F., (2006): An unsteady single-phase level set method for viscous free-surface flows. International Journal for Numerical Methods in Fluids. 53 (2), pp. 229—256

Concha, F., Castro, B., Ovalle, E. and Romero, J., (1998): Numerical simulation of the flow pattern in a hydrocyclone. In Innovation in physical separation technology. pp. 35-60.

Cruchaga, M.A., Celentano, D.J. and Tezduyar, T.E., (2007): Collapse of a liquid column: numerical simulation and experimental validation. Computational Mechanics, Vol. 39 No. 4, pp. 453-476.

Chu, L. and Chen, W., (1999): Numerical Simulation of Turbulence and Its Structure. 9, pp 128-136.

Cullivan, J.C., Williams, R.A. and Cross, C.R., (2003): Understanding the hydrocyclone separator through computational fluid dynamics. Transactions of the IChemE, Part A, Chemical Engineering, Research and Design, 81 (A4), pp. 455-466.

Dai, G.Q., Li, J.M. and Chen, W.M., (1999): Numerical prediction of liquid flow within a hydrocyclone, Chemical Engineering Journal. 74, pp.211-216.

Darwish, M., Moukalled, F. (2003): TVD schemes for unstructured grids. International Journal of Heat and Mass Transfer. 46(4), pp. 599--611

Davailles, A., Climent, E., Bourgeois, F. and Majumder, A.K., (2012): Analysis of swirling flow in hydrocyclones operating under dense region. Minerals Engineering. 31 (2012), pp.   32–41

Davidson, M.R. (1988): Numerical calculations of flow in a hydrocyclone operating without an air-core. Applied Mathematical Modelling. 12, pp.119-128.

Delgadillo, J.A. and Rajamani, R.K. (2005): A comparative study of three turbulence-closure models for the hydrocyclone problem, Int. J. Mineral Process. 77, pp.217-230.

Deshpande, S.S., Anumolu, L. and Trujillo, M.F. (2012): Evaluating the performance of the two-phase flow solver interfoam. Computational Science and Discovery. 5 (1), pp. 014016 (1-36).

Doby, M.J., Nowakowski, A.F. and Dyakowski, T. (2008): Understanding air-core formation in hydrocyclones by studying pressure distribution as a function of viscosity. International Journal of Mineral Processing, In Press.

Dyakowski, T., Williams, R.A. (1993): Modeling turbulent flow within a small-diameter hydrocyclone. Chemical Engineering Science. 6, pp.1143-1152.

Dyakowski, T. and Williams, R.A. (1995): Prediction of air-core size and shape in a hydrocyclone. International Journal of Mineral Processing. 43 (1-2), pp.1-14.

Ferziger, J., Peric, M. (2002): Computational Methods for Fluid Dynamics, vol. I. Springer-Verlag.

Fumiya. (2016): One equation eddy-viscosity SGS model in OpenFOAM®. https://caefn.com/openfoam/keqn-sgs-model.

Gopala, V., van Wachem, B. (2008): Volume of fluid methods for immiscible-fluid and free-surface flows. Chemical Engineering Journal. 141 (1-3), pp. 204-221.

Harlow, F. H. and Nakayama, P. I. (1968): Transport of turbulence energy decay rate, Los Alamos Sci. Lab., LA-3854.

Harten, A. (1983): High resolution schemes for hyperbolic conservation laws. Journal of Computational Physics. 49 (3), pp. 357-393.

He, P., Salcudean, M., Gartshore, I.S. (1999): A numerical simulation of hydrocyclones. Chemical Engineering Research and Design 77 (A5), pp. 429–441.

He, S. (2016): Computational Fluid Dynamics. Lecture slides. Chapter 2 Turbulence Modelling (Part I), p. 28.

Hirsch, C. (2007): Numerical computation of internal and external flows: fundamentals of computational fluid dynamics. vol. 1, Butterworth-Heinemann.

Hirt, C. W. and Nichols, B. D. (1981): Volume of Fluid (VOF) method for the dynamics of free boundaries, J. Comput. Phys. 39, 201-225.

Hoekstra, A.J. (2000): Gas Flow Field and Collection Efficiency of Cyclone Separators. (Ph.D. thesis). TU Delft, Delft University of Technology.

Hoffmann, A.C., De Groot, M., Peng, W., Dries, H. W. and Kater, J. (2001): Advantages and risks in increasing cyclone separator length, AIChE J. 47, pp. 2452–2460.

Hoffmann, A.C. and Stein, L.E., (2008): Gas Cyclones and Swirl Tubes. Springer-Verlag, Berlin, Heidelberg, (ISBN: 978-3-540-74694-2).

Horvath, A., Jordan, C. and Harasek, M., (2008): Influence of vortex-finder diameter on axial gas flow in simple cyclone. Chem. Product Process Model. 3 (1), 2008.

Hsieh, K.T. and Rajamani, R. K., (1991): Mathematical Model of the Hydrocyclone Based on Physics of Fluid flow. AICHE Journal, 37(5), pp. 735-746.

Hsieh, K.T., (1988): Phenomenological model of the hydrocyclone. Ph.D. thesis, University of Utah, Salt Lake City, UT, USA.

Huang, S. and Li, Q. (2010): A new dynamic one-equation subgrid-scale model for large eddy simulations. INTERNATIONAL JOURNAL FOR NUMERICAL METHODS IN ENGINEERING. 81, pp. 835-865.

Issa, R.I., (1984): Solution of the Implicitly Discretised Fluid Flow equations by operator -Splitting. Journal of computational physics, 62, pp. 46-65.

Jasak, H., Weller, H., Gosman, A. (1999): High resolution NVD differencing scheme for arbitrarily unstructured meshes. International Journal for Numerical Methods in Fluids. 31(2), pp. 431-449.

John, D.A., (1995): Computational fluid dynamics: the basics with applications. Maidenhead, Berkshire: McGraw-Hill Education, ISBN: 0071132104.

Kelsall, D.F., (1952): A study of the motion of solid particles in a hydraulic cyclone. Transactions, Institute Chemical Engineers. 30, pp. 87–108.

Kraipech-Evans, W., Suksangpanomr ung, A. and Nowakowski, A. F., (2008): The simulation of the flow within a hydrocyclone operating with an air-core and with an inserted metal rod, Chemical Engineering Journal. 143 (1-3), pp.51-61.

Kuzmin, D., Moller, M., Turek, S. (2003): Multidimensional FEM-FCT schemes for arbitrary time stepping. International Journal for Numerical Methods in Fluids. 42(3), pp. 265-295.

Launder, B. E. and Spalding, D. B. (1974): The numerical computation of turbulent flows. Comput. Methods Appl. Mech. Eng. 3(2), pp. 269-289.

Lee, J.W., Yang, H.J., and Lee, D. Y. (2006): Effect of the cylinder shape of a long-coned cyclone on the stable flow-field establishment, Powder Technol. 165, PP.30–38.

Leonard, B.P. (1991): The ultimate conservative difference scheme applied to unsteady one-dimensional advection. Computer Methods in Applied Mechanics and Engineering. 88, pp. 17-74

Li, Z. (2019): Two-phase spectral wave explicit Navier-Stokes equations method for wave-structure interactions. Ph.D. thesis, L'ÉCOLE CENTRALE DE NANTES COMUE UNIVERSITE BRETAGNE LOIRE, France.

Liu, Z., Zheng, Y., Jia, L., Jiao, J. and Zhang, Q., (2006): Stereoscopic PIV studies on the swirling flow structure in a gas cyclone. Chem. Eng. Sci. 61(13), pp.4252–4261.

Ma, L., Ingham, D.B. and Wen, X., (2000): Numerical modelling of the fluid and particle penetration through small sampling cyclones. Journal of Aerosol Science. 31 (9), pp.1097-1119.

Malhotra, A., Branion, R.M.R., and Hauptman, E.G., (1994): Modelling the flow in a hydrocyclone. The Canadian Journal of Chemical Engineering, 72, 953–960.

Márquez Damián S., Nigro, N. and Buscaglia, G. (2012): Solving the algebraic slip mixture model as a hyperbolic system with restrictions. In: Mecánica Computacional. Vol XXXI, pp. 651-671.

Márquez Damián S. (2013): An extended mixture model for the simultaneous treatment of short and long scale interfaces. Eng.D thesis, Universidad Nacional del Litoral, Spain.

Marzo, A., He, S. and Qin, N. (2015): Computational Fluid Dynamics – Mesh matter. Lecture slides. 15.

Mathur, S., Murthy, J. (1997): A pressure-based method for unstructured meshes. Numerical Heat Transfer. 31 (2), pp. 195-215

Nowakowski, A.F., Kraipech, W., Williams, R.A. and Dyakowski, T., (2000): The hydrodynamics of a hydrocyclone based on a three-dimensional multi-continuum model. Chemical Engineering Journal. 80 1-3, pp.275-282.

Nowakowski, A.F. and Dyakowski, T., (2004): Investigation of swirling flow structure in hydro-cyclones. Chemical Engineering Research and Design. 81(A), pp.862-873

Nowakowski, A.F. and Doby, M.J., (2008): The Numerical Modelling of the Flow in Hydro-cyclones. KONA Powder and Particle Journal, 26, pp.66-80.

OpenCFD, (2008) OpenFOAM®, the Open Source CFD Toolbox, User Guide. OpenCFD Ltd.

OpenCFD, (2012) OpenFOAM®, the Open Source CFD Toolbox, User Guide. OpenCFD Ltd.

OpenCFD, (2018) OpenFOAM®, the Open Source CFD Toolbox, User Guide. OpenCFD Ltd.

Osher, S. and Sethian, J.A., (1988): Fronts Propagating with Curvature-Dependent Speed: Algorithms Based on Hamilton-Jacobi Formulations, Journal of Computational Physics. 79, pp.12-49.

Osher, S. and Fedkiw, R.P., (2001): Level set methods: an overview and some recent results. Journal of Computational Physics. 169 (2). pp. 463-502.

Ovalle, E., Araya, R. and Concha, F., (2005): The role of wave propagation in hydrocyclone operations I: An axisymmetric streamfunction formulation for a conical hydrocyclone Chemical Engineering Journal. 111 (2-3), pp.205-211.

Ovalle, E. and Concha, F., (2005): Role of wave propagation in hydrocyclone operations II. Wave propagation in the air-water interface of a conical hydrocyclone, Chemical Engineering Journal. 111, pp.213-223.

Peng, W., Hoffmann, A., Boot, P., Udding, A., Dries, H., Ekker, A. and Kater, J., (2002): Flow pattern in reverse-flow centrifugal separators. Powder Technol. 127 (3), pp. 212–222.

Petty, C.A. and Parks, S.M., (2001): Flow predictions within hydrocyclones. Filtration and separation, 38, pp.28-34.

Qiana, F. and Wu, Y., (2009): Effects of the inlet section angle on the separation performance of a cyclone, Chem. Eng. Res. Des. 87, pp.1567–1572.

Rudolf, P., (2013): Simulation of multi-phase flow in hydrocyclone. The European Physical Journal Conferences. DOI: 10.1051

Shephered, C. and Lapple, C., (1939): Flow pattern and pressure drop in cyclone dust collectors. Ind. Eng. Chem. 31 (8), pp. 972–984.

Shephered, C. and Lapple, C., (1940): Flow pattern and pressure drop in cyclone dust collectors-Cyclone without inlet vane. Ind. Eng. Chem. 32 (9), pp. 1246–1248.

Slack, M.D., Prasad, R.O., Bakker, A. and Boysan, F., (2000): Advances in cyclone modelling using unstructured grids. Trans IchemE. 78, pp.1098-1104.

Slack, M.D., Boysan, F., (1998): Advances in cyclone modelling using unstructured grids. In: Scandinavian FLUENT UGM Gothenburg.

Spalart, P., Shur, M., (1997): On the sensitization of turbulence models to rotation and curvature. Aerosp. Sci. Technol. 1 (5), pp. 297–302.

Sweby, P. (1984): High resolution schemes using flux limiters for hyperbolic conservation laws. SIAM Journal on Numerical Analysis, pp. 995--1011

Ter Linden, A., (1949): Investigations into cyclone dust collectors. Proc. Inst. Mech. Eng. 160 (1), pp. 233–251.

Wang, B. and Yu, A.B., (2006): Numerical study of particle fluid flow in hydrocyclones with different body dimensions. Miner. Eng. 19, pp.1022-1033.

Wang, C. Ji, C. and Zou, J. (2015): Simulation and Experiment on Transitional Behaviours of Multi-phase Flow in a Hydrocyclone. The Canadian journal of chemical engineering. 93, pp. 1082-1811.

Weller, H., (2008): A new approach to VOF-based interface capturing methods for incompressible and compressible flow. CFD Direct.

Yakhot, V., Orszag, S.A., Thangam, S., Gatski, T.B. and Speziale, C.G., (1992): Development of turbulence models for shear flows by a double expansion technique. Physics of Fluids A, Vol. 4, No. 7, pp. 1510-1520.

Yoshizawa, A. and Horiuti, K. (1985): A Statistically-Derived Subgrid-Scale Kinetic Energy Model for the Large-Eddy Simulation of Turbulent Flows. Journal of the Physical Society of Japan. 54 (8), pp. 2834-2839.

Yoshizawa, A. (1986): Statistical theory for compressible turbulent shear flows, with the application to subgrid modelling. The Physics of Fluids 29, 2152 (1986), pp. 2152-2164.

Zalesak, S.T. (1979): Fully multidimensional Flux-Corrected Transport algorithms for fluids. Journal of Computational Physics. 31, pp. 335—362

Zikanov, O., (2010): Essential Computational Fluid dynamics. John Wiley & Sons, Inc., ISBN 978-0-470-42329-5.

Zhao, X., Huang, B., Chen, T., Wang, G., Gao, D. and Zhao, J. (2017): Numerical simulations and surrogate-based optimization of cavitation performance for an aviation fuel pump. Journal of Mechanical Science and Technology. 31 (2), pp. 705-716.